

Paleoceanography of the Bering Sea across the Mid- to late Pleistocene



Henrieka Detlef

Thesis submitted for the Degree of Doctor of Philosophy

Cardiff University

July 2018

DECLARATION

This work has not been submitted in substance for any other degree or award at this or any other university or place of learning, nor is being submitted concurrently in candidature for any degree or other award.

Signed.....(candidate) Date.....

STATEMENT 1

This thesis is being submitted in partial fulfillment of the requirements for the degree of PhD(insert MCh, MD, MPhil, PhD etc, as appropriate)

Signed.....(candidate) Date.....

STATEMENT 2

This thesis is the result of my own independent work/investigation, except where otherwise stated.

Other sources are acknowledged by explicit references. The views expressed are my own.

Signed.....(candidate) Date.....

STATEMENT 3

I hereby give consent for my thesis, if accepted, to be available for photocopying and for inter-library loan, and for the title and summary to be made available to outside organisations.

Signed.....(candidate) Date.....

STATEMENT 4: PREVIOUSLY APPROVED BAR ON ACCESS

I hereby give consent for my thesis, if accepted, to be available for photocopying and for inter-library loans **after expiry of a bar on access previously approved by the Academic Standards & Quality Committee.**

Signed.....(candidate) Date.....

Paleoceanography of the Bering Sea across the Mid-to late Pleistocene

The Bering Sea represents the gateway between the Pacific and the Arctic Ocean. It is characterized by a seasonal sea ice cycle, which together with upwelling along the continental margin provides nutrients for primary producers. The resulting high sedimentation rates along the margin allow to study Quaternary climate change at an orbital to sub-orbital resolution, ideal to examine the evolution of continental ice volume across the Mid-Pleistocene transition (MPT, 1.2-0.7 Ma), the shift in glacial/interglacial (G/IG) frequency from 41-ka to 100-ka. Additionally, the Bering Sea provides a unique opportunity to study sea ice-ocean/land ice interactions. In the North Pacific, sea ice not only plays a significant role in climatic feedbacks, but also influences the ventilation of mid-depth waters via brine rejection.

This thesis focuses on MPT climate change in the eastern Bering Sea, with particular emphasis on bottom water temperature (BWT), seawater oxygen isotopes ($\delta^{18}\text{O}_w$), sedimentary redox conditions, and sea ice dynamics. The MPT findings are reinforced by examining the same parameters across the last G/IG cycle. Further, the chemical composition of contamination phases in benthic foraminifera in eastern Bering Sea slope sediments is analysed.

Foraminiferal contaminants are primarily composed of authigenic carbonates enriched in Mg, U, Mn, Fe, and Sr with consequences for geochemical proxies, such as Mg/Ca for BWT. Nevertheless, this study also demonstrates the opportunities accompanying authigenic carbonates, such as authigenic U/Mn for sedimentary redox chemistry.

Across the MPT, $\delta^{18}\text{O}_w$ suggests two possible scenarios of continental ice volume history, in line with published records. Together $\delta^{18}\text{O}_w$, BWT, and sedimentary redox chemistry point towards enhanced entrainment of well-ventilated intermediate waters at ~2000 m water depth following the MPT, supported by an increase in the sea ice extent. The reconstructed sea ice dynamics align with published modelling studies, characterised by the emergence of a late glacial/deglacial sea ice maximum in the Bering Sea during the MPT. Increased sea ice extent across early deglaciations could have exerted a negative feedback on the moisture supply to continental ice sheets, highlighting the importance of sea ice dynamics for Quaternary climate change. The MPT results are additionally supported by findings across the last G/IG cycle. A BWT amplitude of ~ 2 °C across the last glacial maximum (LGM) to Holocene transition, is in line with previously published records from across the Pacific, and together with records of sedimentary redox chemistry, $\delta^{18}\text{O}_w$, and sea ice suggest admixture of well-ventilated waters during the LGM and Heinrich stadial 1.

In conclusion, this thesis highlights the importance of the Bering Sea hydrography for environmental reconstructions and emphasises the need to understand the evolution of intermediate water formation in the North Pacific across the MPT. Additionally, it demonstrates the necessity of a globally stacked $\delta^{18}\text{O}_w$ record, to reduce the influence of the regional hydrography on $\delta^{18}\text{O}_w$. Finally, this thesis accentuates the role of sea ice in long-term climate change and indicates the need for additional studies of MPT sea ice dynamics to fully unravel its influence on continental ice sheets.

Author's Note

Chapter 6 of this thesis has partly been published as:

DETLEF, H., BELT, S. T., SOSDIAN, S. M., SMIK, L., LEAR, C. H., HALL, I. R., CABEDO-SANZ, P., HUSUM, K. & KENDER, S. 2018. Sea ice dynamics across the Mid-Pleistocene transition in the Bering Sea. *Nature Communications*, 9, 941.

Author contributions:

H.D., S.M.S., and S.T.B. developed this sea ice study using Arctic biomarkers. K.H. and S.K. sailed on IODP Leg 323 and contributed to developing the MPT study at Site U1343, with valuable sample material provided by K.H.. H.D. performed most of the analyses with support from L.S. and P.C.-S.. H.D. wrote the manuscript with help from S.T.B. and S.M.S. and contributions from L.S., K.H., S.K., C.H.L., and I.R.H..

Acknowledgements

First of all, I would like to thank my supervisory team, Sindia Sosdian, Caroline Lear, Sev Kender, Ian Hall, and Melanie Leng for all the support and the great discussions throughout the last four years. I feel very fortunate for having been part of such a great team.

First and foremost, however, I would like to thank Sindia Sosdian, my main supervisor, for giving me this amazing opportunity. I cannot thank her enough for all the scientific discussions during the course of my PhD. Her expertise and understanding of the climate system is truly inspiring. I am very grateful to Sindia for always encouraging me to pursue my own research ideas and for the guidance and mentorship both scientifically and personally. My PhD has been an amazing experience and Sindia's enthusiasm and optimism have been a great part of that.

This thesis would not have been possible without the technical and laboratory support of many people. In particular, Anabel Morte-Ródenas, who taught me how to process and analyse foraminiferal samples and how to run the ICP-MS during numerous hours in the laboratory. Thanks, as well, to Sandra Nederbragt for all the isotope measurements and to Lukas Jonkers for sharing his EPMA processing technique with me.

I would like to thank the 'Changing Earth and Ocean' research group at Cardiff University for the welcoming and encouraging atmosphere and the always open doors. I am grateful to Paola, Eleanor, Margit, and Anabel for being such inspirational female scientists and friends. A special thanks to Paola for encouraging me to apply to this PhD project in the first place.

Thank you to the entire PhD community at the School of Earth and Ocean Sciences for all the support and fun throughout the last four years. Above all thanks to the 'Paleo-office': Amy, Michael, Emanuela, Ewa, Freya, Anna, Sophie, James and Chris, for all the scientific and non-scientific discussions, the emotional support, the biscuits, and for being such great friends.

I would like to thank my parents Christiane and Heinz, my sister Anne-Mieke, Ann Kristin, Niklas, Tobi and Chloe for the unconditional support throughout my life and for always believing in me. A special thanks to Chloe, my rock, for the patience and empathy during the last couple of months.

Commonly used symbols and abbreviations

[CO ₃ ²⁻]	Carbonate ion concentration
[O ₂]	Oxygen concentration
AMOC	Atlantic meridional overturning circulation
ANSC	Aleutian North Slope Current
AOM	Anaerobic oxidation of methane
APF	Antarctic Polar Front
B/A	Bølling-Allerød
BSC	Bering Slope Current
BWT	Bottom water temperature
CDW	Circum Polar Deep Water
CI	Confidence interval
DCM	Dichloromethane
DIC	Dissolved inorganic carbon
DSDP	Deep Sea Drilling Project
DWBC	Deep Western Boundary Current
E/O	Eocene/Oligocene
EAIS	East Antarctic Ice Sheet
EPMA	Electron probe microanalyser
G/IG	Glacial/interglacial
GLODAP	Global Ocean Data Analysis Project
HBI	Highly branched isoprenoid
HBI III	Tri-unsaturated HBI
HMC	High-Mg calcite
HNLC	High nutrient low chlorophyll
HPLC	High-performance liquid chromatography
HS1	Heinrich stadial 1
ICP-MS	High resolution inductively coupled plasma mass spectrometry
IODP	International Ocean Discovery Program
IRD	Ice rafted debris
IWT	Intermediate water temperature
ka	Thousand years
LA-ICP-MS	Laser ablation inductively coupled plasma mass spectrometry
LGM	Last glacial maximum
LMC	Low-Mg calcite
LOD	Limit of detection
LR	Low resolution mode
m CCSF-A	Meters core composite depth below seafloor
Ma	Million years
MAR _{opal}	Mass accumulation rate of biogenic opal
mbsf	Meters below seafloor

MIS	Marine isotope stage
MIZ	Marginal ice zone
MPT	Mid-Pleistocene transition
MR	Medium resolution mode
NADW	North Atlantic Deep Water
NPDW	North Pacific Deep Water
NPI	North Pacific Index
NPIW	North Pacific Intermediate Water
ODP	Ocean Drilling Program
OMZ	Oxygen minim zone
PIP ₂₅	Index combining phytoplankton biomarkers with IP ₂₅ for semi-quantitative sea ice reconstructions
PMOC	Pacific Meridional Overturning Circulation
r.s.d.	Relative standard deviation
s.d.	Standard deviation
s.e.	Standard error
SEM	Scanning electron microscope
SIS	Sea ice switch hypothesis
SMTZ	Sulphate Methane Transition Zone
SST	Sea surface temperature
TBA	Tetrabutylammonium sulphite reagent
Termination I	LGM-Holocene transition
TOE	Total organic extract
WPWP	West Pacific Warm Pool
YD	Younger Dryas
$\Delta[\text{CO}_3^{2-}]$	Carbonate saturation state
$\delta^{11}\text{B}$	Boron isotope composition
$\delta^{13}\text{C}$	Carbon isotope composition
$\delta^{13}\text{C}_{\text{DIC}}$	Carbon isotope composition of dissolved inorganic carbon
$\delta^{15}\text{N}$	Nitrogen isotope composition
$\delta^{18}\text{O}_b$	Benthic foraminiferal oxygen isotope composition
$\delta^{18}\text{O}_w$	Oxygen isotope composition of seawater
ΔBWT	BWT amplitude across the LGM-Holocene transition
$\Delta\delta^{13}\text{C}_{(849-U1342)}$	Carbon isotope difference of ODP Site 849 and IODP Site U1342
$\Delta\delta^{18}\text{O}_b$	Benthic foraminiferal oxygen isotope amplitude across the LGM-Holocene transition
ϵ_{Nd}	Neodymium isotope composition

Contents

1. Introduction	1
1.1 Cenozoic climate change giving rise to the Mid-Pleistocene Climate Transition .	1
1.2 The Mid-Pleistocene transition	3
1.2.1 Hypothesis to explain the Mid-Pleistocene climate transition	6
1.2.2 Global climate change across the Mid-Pleistocene transition.....	9
1.2.2.1 The North Pacific throughout the Mid-Pleistocene	15
1.3 Climate of the subarctic North Pacific across the last glacial maximum to Holocene	17
1.4 Biogeochemical cycling and ventilation in the North Pacific on glacial/interglacial timescales	19
1.5 Research questions and outline of the thesis.....	23
1.6 Outline of the thesis	25
2. Materials and methods	28
2.1 Oceanography of the Bering Sea.....	28
2.2 International Ocean Discovery Program Site U1343.....	33
2.2.1 Sedimentary properties.....	34
2.2.2 Age model	34
2.3 Methodology	36
2.3.1 Sediment processing for inorganic geochemical analyses	36
2.3.2 Sediment processing for organic geochemical analyses	36
2.3.3 Sea ice and phytoplankton biomarkers for sea ice reconstruction	36
2.3.4 Foraminiferal authigenic U/Mn for sedimentary redox conditions.....	38
2.3.5 Benthic foraminiferal Mg/Ca for bottom water temperatures.....	39
2.3.6 Secondary effects on foraminiferal Mg/Ca values	41
2.3.6.1 Post-mortem alterations of foraminiferal tests during early diagenesis	41

2.3.6.2 Seawater Mg/Ca variations across the Pleistocene.....	43
2.3.6.3 The effect of the carbonate saturation state on foraminiferal Mg/Ca values	44
2.3.7 The effect of different chemical cleaning techniques on foraminiferal trace metal ratios	45
2.3.8 Dysoxic foraminiferal assemblage counts.....	48
2.3.9 Statistical analyses and error propagation	50
3. Foraminiferal diagenesis in sediments underlying high productivity areas.....	52
3.1 Introduction.....	52
3.2 Materials and methods	57
3.2.1 Sedimentary evidence for authigenic carbonates at IODP Site U1343.....	57
3.2.2 Sampling strategy	58
3.2.3 Scanning electron microscope imaging.....	60
3.2.4 Geochemical analyses	60
3.2.4.1 LA-ICP-MS elemental profiles and specimen means.....	60
3.2.4.2 EPMA elemental mapping of Mg/Ca and Fe/Ca	63
3.3 Results.....	64
3.3.1 Visual identification of foraminiferal alteration at Site U1343 under the reflected light microscope and SEM	64
3.3.2 LA-ICP-MS single specimen geochemical analyses.....	66
3.3.3 EPMA elemental mapping of Mg/Ca and Fe/Ca.....	70
3.4 Discussion	74
3.4.1 Multi-element composition of foraminifera-bound authigenic carbonates at Site U1343	74
3.4.2 Dissolution of foraminiferal test at Site U1343.....	78
3.4.3 The origin of foraminifera-bound authigenic calcite within the sediment-pore water system	79
3.4.4 Paleoceanographic implications	82
3.5 Conclusions.....	87

4. Pleistocene bottom water temperature evolution in the eastern Bering Sea	89
4.1 Introduction	89
4.2 Materials and methods	93
4.2.1 Composite benthic foraminiferal Mg/Ca record.....	93
4.2.2 LA-ICP-MS measurements of <i>E. batialis</i> Mg/Ca across the LGM-Holocene transition.....	94
4.2.3 Secondary effects on foraminiferal Mg/Ca	94
4.2.3.1 Early carbonate diagenesis.....	94
4.2.3.2 The effect of salinity on foraminiferal Mg/Ca.....	97
4.2.3.3 The effect of the carbonate saturation state on primary foraminiferal Mg/Ca	98
4.2.3.4 Post-depositional dissolution of foraminiferal tests	100
4.2.3.5 Seawater Mg/Ca variations across the Pleistocene.....	101
4.3 Results	103
4.3.1 Multi-species Mg/Ca ratios at Site U1343	103
4.3.2 Mg/Ca bottom water temperature calibration.....	103
4.4 Discussion	108
4.4.1 Bottom water temperatures in the eastern Bering Sea across the Mid- to late Pleistocene.....	108
4.4.1.1 The Last Glacial Maximum to Holocene bottom water temperature history in the eastern Bering Sea	108
4.4.1.2 Mid-Pleistocene bottom water temperature in the eastern Bering Sea – implications for the Mid-Pleistocene climate transition.....	115
4.5 Conclusions	124
5. Pleistocene variability in sedimentary redox chemistry in the eastern Bering Sea.....	127
5.1 Introduction.....	127
5.2 Materials and methods	131

5.2.1 U/Mn and U/Ca of authigenic foraminiferal coatings.....	131
5.2.2 Low oxygen benthic foraminifera assemblage census counts.....	131
5.3 Results.....	132
5.3.1 Down-core U/Mn and U/Ca of authigenic foraminiferal coatings at IODP Site U1343.....	132
5.3.2 The effect of different cleaning techniques on foraminiferal authigenic U/Mn.....	135
5.3.3 Inter- and intra-species variability of U/Mn.....	137
5.3.4 Low oxygen benthic foraminiferal assemblages.....	138
5.4 Discussion.....	139
5.4.1 Authigenic foraminiferal U/Mn as a proxy for sedimentary redox conditions above and below the SMTZ.....	139
5.4.2 Sedimentary redox chemistry across the last glacial maximum to the Holocene.....	143
5.4.3 Sedimentary redox changes in the deep eastern Bering Sea across the Mid-Pleistocene.....	149
5.4.3.1 Interglacial evolution of sedimentary redox conditions across the Mid-Pleistocene.....	150
5.4.3.2 Glacial variability and long-term trends of sedimentary redox conditions across the Mid-Pleistocene.....	153
5.5 Conclusions.....	157
6. Sea ice dynamics in the Bering Sea across the Mid- to late Pleistocene.....	160
6.1 Introduction.....	160
6.2 Materials and methods.....	165
6.2.1 Biomarker extraction and analysis.....	165
6.3 Results.....	166
6.3.1 Sea ice biomarker variability across the LGM-Holocene and the Mid-Pleistocene in the eastern Bering Sea.....	166
6.3.2 Phytoplankton biomarkers in the eastern Bering Sea.....	170

6.3.2.1 HBI III across the LGM-Holocene and the Mid-Pleistocene	170
6.3.2.2 Brassicasterol across the Mid-Pleistocene.....	171
6.4 Discussion	172
6.4.1 Defining sea ice boundary conditions	172
6.4.2 Sea ice variability in the eastern Bering Sea across the Mid- to late Pleistocene.....	177
6.4.2.1 Marine isotope stages 1 to 3	177
6.4.2.2 Marine isotope stages 10 to 13	178
6.4.2.3 Marine isotope stages 20 to 36	179
6.4.2.4 Marine isotope stages 44 to 51	181
6.4.3 Sea ice dynamics in the eastern Bering Sea across the last glacial cycle..	182
6.4.3.1 Sea ice evolution in the eastern Bering Sea across Termination I....	185
6.4.4 Mid-Pleistocene sea ice dynamics in the eastern Bering Sea.....	188
6.4.4.1 Mechanisms for Mid-Pleistocene sea ice change	194
6.4.4.2 The influence of Bering Sea sea ice on intermediate water formation	196
6.5 Conclusions	198
7. Synthesis and outlook	202
7.1 Diagenetic alterations of foraminifera underlying the high-productivity region of the Green Belt in the eastern Bering Sea – challenges and opportunities.....	202
7.2 Last glacial maximum to Holocene climate change in the eastern Bering Sea – records of bottom water temperature, oxygenation, and sea ice	205
7.3 The Mid-Pleistocene transition from a Bering Sea perspective.....	210
7.3.1 The role of sea ice for the Mid-Pleistocene transition.....	214
7.4 Future work	216
References	219

1. Introduction

1.1 Cenozoic climate change giving rise to the Mid-Pleistocene Climate Transition

The Cenozoic describes the geological era between 65.5 million years ago and the present and is marked by a transition in Earth's climate from a 'greenhouse' to an 'icehouse' state. Cenozoic climate change, primarily determined from the oxygen isotope ratio of benthic foraminifera ($\delta^{18}\text{O}_b$), demonstrates a transition from a mainly ice-free world throughout the Eocene to the modern icehouse climate, characterised by bipolar ice sheets (Zachos et al., 2001) (Figure 1.1). This is accompanied by long-term cooling of the deep global ocean of $\sim 12^\circ\text{C}$ (Shackleton and Kennett, 1975, Miller et al., 1987, Lear et al., 2000, Zachos et al., 2001), a decrease in the atmospheric CO_2 concentrations (Pearson and Palmer, 2000), and prominent changes in the ocean circulation (Thomas, 2004, Motoi et al., 2005, Hague et al., 2012, Thomas et al., 2014). Cenozoic long-term climate trends are primarily governed by changes in the tectonic forcing, including volcanism, paleogeography, and changes in the topography and bathymetry. This influences oceanic gateways (Haug and Tiedemann, 1998, Motoi et al., 2005, Haug et al., 2005, Lyle et al., 2008) and atmospheric circulation (Raymo and Ruddiman, 1992, Molnar et al., 1993), in turn impacting the oceanic overturning, meridional heat and moisture transport, and atmospheric greenhouse gas concentrations. In addition to tectonic mechanisms, driving the climate on timescales of 10^5 to 10^7 years (Zachos et al., 2001), Cenozoic climate change demonstrates distinctive periodic and quasi-periodic oscillations defined by the orbital parameters obliquity (41 thousand years (ka)), precession (19 ka and 23 ka), and eccentricity (100 ka and 413 ka), determining the total and latitudinal seasonal/annual solar energy budget (Milankovitch, 1941, Hays et al., 1976, Zachos et al., 2001) (Figure 1.1). Overall, Earth's boundary conditions, predominantly governed by plate tectonics, determine the sensitivity of climate to orbital modulation. In addition to these long-term and cyclical climate trends, abrupt transient events can be observed throughout the Cenozoic, such as the Palaeocene-Eocene-Thermal-Maximum and the Eocene-Oligocene (E/O) boundary, suggesting a nonlinear response of the climate system (Pearson and Palmer, 2000, Lear et al., 2000, Zachos et al., 2001, DeConto and Pollard, 2003) (Figure 1.1). Traditionally, the E/O boundary is considered to represent

intensive glaciation of the Antarctic continent, as a result of thermal isolation of Antarctica and/or a long-term decrease in atmospheric CO₂ (Zachos et al., 2001, DeConto and Pollard, 2003, Hill et al., 2013, Galeotti et al., 2016), with extensive northern hemisphere ice sheets not appearing until ~2.7 million years (Ma) ago during the Pliocene (Shackleton et al., 1984, Raymo, 1994). The unipolar glaciation throughout the Oligocene and Miocene, however, has recently been challenged by evidence of ice rafted debris (IRD) in the Arctic Ocean since ~45 Ma (Moran et al., 2006), suggesting smaller ice sheets and/or sea ice throughout at least parts of the Middle Cenozoic with some evidence pointing towards perennial and/or seasonal sea ice in the Arctic Ocean during the Miocene (Moran et al., 2006, Krylov et al., 2008, Stein et al., 2016). The modern sea ice extent was established coeval with the intensification of northern hemisphere ice sheets at ~2.7 Ma (Knies et al., 2014). Following the late Miocene cooling the Plio-Pleistocene (5.3-0.012 Ma) is characterised by profound changes in northern hemisphere ice volume and changes in the sensitivity of Earth's climate to external forcing, setting the stage for modern climate variability.

The Mid-Pliocene is the most recent period that was consistently warmer than today, with atmospheric CO₂ concentrations >280 ppm (Martinez-Boti et al., 2015) and sea surface temperatures (SST) up to 3°C warmer. The expansion of northern hemisphere ice sheets around 2.7 Ma is accompanied by a pronounced increase in the IRD content of North Atlantic and North Pacific sediments (Shackleton et al., 1984, Ruddiman and Raymo, 1988), indicating more extensive glacial discharge and larger continental ice sheets surrounding these major ocean basins. Hypotheses explaining northern hemisphere ice sheet expansion include changes in the ocean circulation resulting from the closure of the Mid-American seaway (Haug and Tiedemann, 1998, Lear et al., 2003) or the restriction of the Indonesian throughflow, Tibetan uplift (Raymo and Ruddiman, 1992), the onset of North Pacific stratification with the development of a permanent halocline (Haug et al., 1999, Haug et al., 2005), and/or changes in the deep water circulation influencing the meridional heat and salt transport governed by Antarctic ice sheet growth and Southern Ocean stratification (Woodard et al., 2014). The expansion of northern hemisphere ice sheets is coupled with the onset of a pronounced expression of 41-ka periodicity in glacial/interglacial (G/IG) cycles of the global δ¹⁸O_b stack (LR04) (Lisiecki and Raymo, 2005) around ~3 Ma (Raymo and

Nisancioglu, 2003, Lisiecki and Raymo, 2007), indicative of obliquity modulation (Figure 1.2). Further, from ~2.5 Ma onwards G/IG cycles, as seen from records of $\delta^{18}\text{O}_b$, indicate distinct asymmetry with long glaciations and rapid deglaciations giving rise to the emergence of the prominent saw-tooth pattern of Pleistocene G/IG cycles (Lisiecki and Raymo, 2007) (Figure 1.2). During the Pleistocene together with a pronounced increase in the $\delta^{18}\text{O}_b$ amplitude the dominant frequency of G/IG cycles changed from 41-ka to quasi-periodic 100-ka oscillations that became dominant from ~0.65 Ma (Clark et al., 2006). This transition is called the Mid-Pleistocene transition (MPT) (Figure 1.2).

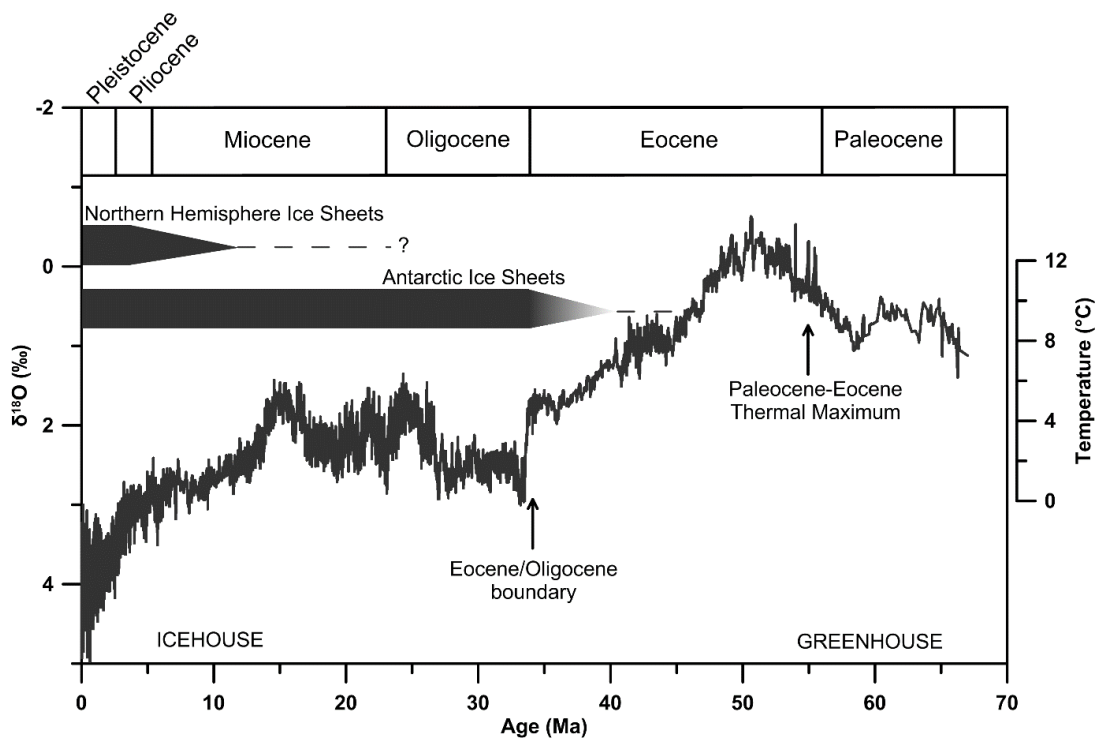


Figure 1.1 Composite Cenozoic benthic $\delta^{18}\text{O}$ curve including the bottom water temperature based on $\delta^{18}\text{O}$ in an ice-free world (Zachos et al., 2001, Zachos et al., 2008). Approximate schematic of Antarctic and northern hemisphere ice sheet evolution from Zachos et al. (2008).

1.2 The Mid-Pleistocene transition

The MPT describes the shift in G/IG frequency from 41-ka cycles to quasi-periodic 100-ka cycles during the Mid-Pleistocene (1.25-0.7 Ma). The 100-ka spectral power first emerged in global records of $\delta^{18}\text{O}_b$ around 1.25 Ma but did not become dominant until 0.65 Ma (Ruddiman et al., 1989, Clark et al., 2006), contradicting other studies

defining the MPT as an abrupt event with an increase in the 100-ka power between 0.9-0.6 Ma (Mudelsee and Schulz, 1997). Simultaneously with the increase in frequency the asymmetry of G/IG cycles strengthened (Lisiecki and Raymo, 2007) and the G/IG amplitude in the global $\delta^{18}\text{O}_b$ record (LR04 stack (Lisiecki and Raymo, 2005)) increased with consistently higher $\delta^{18}\text{O}_b$ during late Pleistocene glacials, indicating either larger continental ice volume, a decrease in deep ocean temperatures, or both (Figure 1.2).

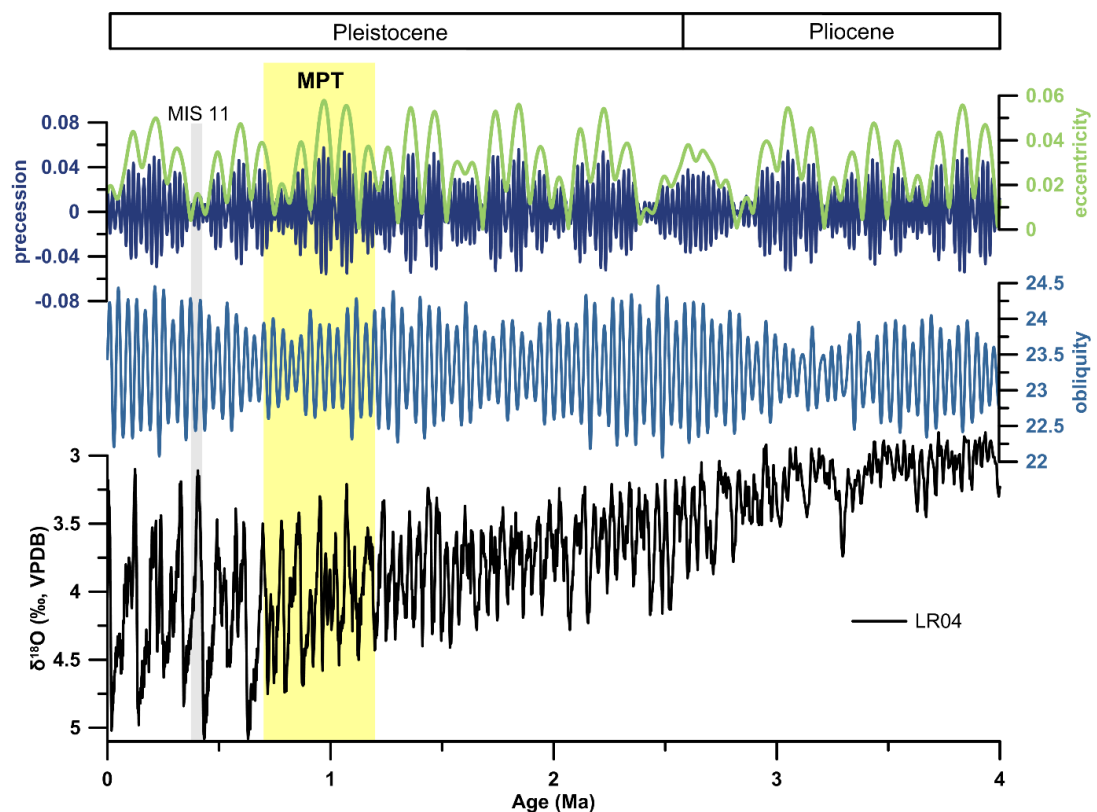


Figure 1.2 Global benthic foraminiferal $\delta^{18}\text{O}$ stack (LR04) (black) (Lisiecki and Raymo, 2005), including the orbital parameters obliquity (light blue), precession (dark blue) and eccentricity (green) (Paillard et al., 1996, Laskar et al., 2004) across the Plio-Pleistocene (0-4 Ma). The vertical yellow bar indicates the Mid-Pleistocene transition (MPT, 0.7-1.2 Ma) and the grey vertical bar marks marine isotope stage (MIS) 11 characterised by a pronounced mismatch in the eccentricity forcing and the $\delta^{18}\text{O}$ response.

Milankovitch's theory indicates that variability in continental ice volume is driven by changes in the caloric summer half-year insolation (amount of energy integrated over the caloric summer half of the year) (Milankovitch, 1941), which at 65°N shows almost equal contribution from precession and obliquity forcing (Tzedakis et al., 2017). Thus, challenges arise to explain Plio-Pleistocene G/IG variability in light of

orbital forcing, as no pronounced ice volume variability at precession periods is observed. Further, the power in the eccentricity band is too low to directly force late Pleistocene climate cycles and a distinct amplitude mismatch between eccentricity forcing and the $\delta^{18}\text{O}_b$ signal is observed, for example during marine isotope stage (MIS) 11 (~400 ka) where the amplitude in eccentricity is low but the $\delta^{18}\text{O}_b$ signal is unusually strong (Parrenin and Paillard, 2003) (Figure 1.2). Additionally, late Pleistocene G/IG cycles vary in duration between 80-120 ka equal to two to three obliquity cycles.

Studies of the Pliocene and early Pleistocene G/IG cycles attribute the mismatch between Milankovitch's theory and the 41-ka frequency to either self-sustained climate variability phase-locked to obliquity (Ashkenazy and Tziperman, 2004) or direct obliquity forcing (Raymo and Nisancioglu, 2003, Huybers, 2006, Raymo et al., 2006, Lisiecki and Raymo, 2007). Whereas, the latter could result from ice sheets being sensitive to variations in the meridional insolation gradient between 25°N and 70°N (Raymo and Nisancioglu, 2003), however climate models have failed to show this relationship (Jackson and Broccoli, 2003), or the insolation integrated over the duration of the summer, insensitive to precession as the summertime length is inversely proportional to Earth's distance from the sun (Kepler's second law) (Huybers, 2006). Huybers and Tziperman (2008) propose that 41-ka ice sheet variability can effectively be generated by climate models, if the ablation zone remains north of 60°N, where obliquity forcing has a greater influence, and if the summer melt season is long enough to balance changes in the insolation intensity, for example by basal sliding of the ice sheet resulting in thinning and lowering of the ice surface to warmer elevations. Raymo et al. (2006), on the other hand, suggest that the precession forcing is simply out of phase between hemispheres and is, thus, cancelled out in globally integrated records of $\delta^{18}\text{O}_b$. However, other more regionally determined climatically sensitive records such as bottom water temperature (BWT), IRD, and SST also vary at 41-ka during the Pliocene and early Pleistocene (Raymo et al., 2006, Sosdian and Rosenthal, 2009, Elderfield et al., 2012, McClymont et al., 2013). Additionally, as aforementioned 41-ka cycles demonstrate distinct asymmetry since at least ~2.5 Ma (Raymo and Nisancioglu, 2003, Lisiecki and Raymo, 2007), suggesting that even if climate cycles are directly forced or paced by obliquity modulation,

nonlinearities internal to the climate system must exist, as no orbital parameter demonstrates any kind of asymmetry.

100-ka climate cycles, on the other hand, have been attributed to either nonlinear amplification of eccentricity (Hays et al., 1976), or to pacing by the external orbital forcing. However, studies disagree on whether the quasi-periodic 100-ka oscillations are paced by eccentricity or two to three obliquity cycles (Ashkenazy and Tziperman, 2004, Huybers and Wunsch, 2005, Ashkenazy, 2006, Lisiecki, 2010, Huybers, 2011), with the timing of glacial terminations most likely being determined by obliquity, precession, or a combination of the two (Hays et al., 1976, Huybers and Wunsch, 2005, Huybers, 2011, Feng and Bailer-Jones, 2015, Tzedakis et al., 2017). Nevertheless, the change from 41-ka to 100-ka climate cycles appears without any attributable change in orbital forcing (Shackleton and Opdyke, 1976, Pisias and Moore Jr, 1981, Imbrie et al., 1993, Raymo and Nisancioglu, 2003), indicating that the MPT is characterised by a shift in the sensitivity of the climate system to external forcing, driven by mechanisms internal to the climate system. However, controversy still exists concerning the nature of feedback mechanisms and teleconnections responsible for MPT climate change.

1.2.1 Hypothesis to explain the Mid-Pleistocene climate transition

Hypotheses explaining MPT climate change can be divided into two broad categories, with the first one invoking a pronounced change in ice sheet dynamics and the second one indicating a threshold response to long-term climate cooling, for example as a result of gradual atmospheric CO₂ decrease, even though records of atmospheric CO₂ across the MPT are scarce.

One hypothesis indicating a fundamental shift in ice sheet dynamics is the ‘regolith hypothesis’ (Clark and Pollard, 1998), suggesting a gradual removal of a thick sediment horizon (regolith) underlying the North American ice sheet by ice erosion, allowing the Laurentide ice sheet to grow in size. Fundamental to their hypothesis Clark and Pollard (1998) argue that ice sheets primarily grew in thickness rather than area during the MPT, as a result of the exposure of high-friction Precambrian bedrock. A thicker ice sheet would imply changes in the response of the ice sheet to solar forcing, with increased ice sheet inertia giving rise to the late Pleistocene 100-ka climate cycles (Clark and Pollard, 1998, Clark et al., 2006). This is supported by

sedimentary evidence, such as thick saprolite layers found in Minnesota and Canada, a change in the geochemical and mineralogical signature of till deposits in North America, and a change in the ocean's strontium and osmium isotope values at ~1.4 Ma and ~1 Ma, respectively (Clark et al., 2006). Both, Sr ($^{87}\text{Sr}/^{86}\text{Sr}$) and Os ($^{187}\text{Os}/^{186}\text{Os}$) isotope ratios, are influenced by rates of continental weathering, however compared to Sr, Os isotopes are unaffected by the erosion of regolith (Clark et al., 2006). Thus, Clark et al. (2006) argue that the increase in Sr isotopes at ~1.4 Ma represents the removal of regolith underlying the North American ice sheet, whereas the increase in Os isotopes at ~1 Ma represents the onset of bedrock weathering. Further, an increase in the silicate weathering rates associated with the bedrock exposure could have promoted atmospheric CO_2 drawdown across the MPT, causing additional cooling (Clark et al., 2006). Tabor and Poulsen (2016) explored the validity of the 'regolith hypothesis' using a complex earth system model and find distinct changes in the ice sheet flow and accumulation/ablation dynamics as a result of crystalline bedrock exposure. Thus, they argue that the 'regolith hypothesis' is a valid mechanism to explain frequency changes across the MPT, as thicker and colder ice sheets require increased insolation forcing to fully retreat (Tabor and Poulsen, 2016). An increase in North American ice sheet size across the Mid-Pleistocene is also proposed by Bintanja and van de Wal (2008a) with the Laurentide and Cordilleran ice sheet merging for the first time around ~1 Ma, however, these authors attribute the larger ice sheets to gradual cooling following the northern hemisphere glaciation around ~2.7 Ma, rather than changes in the underlying geology.

Other hypothesis of changes in ice sheet dynamics invoke an increase in Antarctic ice volume across the MPT (Pollard and DeConto, 2009, Elderfield et al., 2012) as the determining factor to lock Earth's climate in a quasi-periodic 100-ka variability (Elderfield et al., 2012). Elderfield et al. (2012) study $\delta^{18}\text{O}_b$ in conjunction with BWT variability at Ocean Drilling Program (ODP) Site 1123 in the southwestern Pacific, to extract the seawater $\delta^{18}\text{O}$ ($\delta^{18}\text{O}_w$), sensitive to changes in continental ice volume. They find a pronounced increase in $\delta^{18}\text{O}_w$ across the so-called '900-ka event' (MIS 24 to MIS 22), which they interpret as an abrupt increase in Antarctic ice volume resulting from low southern hemisphere summer insolation across this interval (Elderfield et al., 2012). Raymo et al. (2006) also suggest a change in Antarctic ice sheet dynamics across the MPT, however due to long-term cooling, for example as a result of

decreasing atmospheric CO₂ concentration and increased chemical weathering rates (Raymo and Ruddiman, 1992). During the pre-MPT 41-ka world East Antarctic Ice Sheet (EAIS) margins are suggested to remain terrestrial-based, sensitive to summer melting and thus insolation forcing (Raymo et al., 2006). Long-term cooling across the Pleistocene, however, led to EAIS expansion and the formation of marine-based ice margins around 1 Ma, positively influencing EAIS thickness (Raymo et al., 2006). Further, marine-based ice margins would allow for in-phase ice sheet variability between the northern and southern hemisphere (Raymo et al., 2006), as marine-based margins are sensitive to sea level fluctuations controlled by northern hemisphere insolation changes (Thompson and Goldstein, 2005).

Other mechanisms, proposed to drive MPT climate change as a threshold response to long-term cooling, include the sea ice switch (SIS) hypothesis (Gildor and Tziperman, 2001, Tziperman and Gildor, 2003, Sayag et al., 2004). Tziperman and Gildor (2003) use conceptual modelling and attribute a hypothetical long-term decrease in deep ocean temperatures and the resulting changes in the surface ocean heat capacity due to increased stratification, to the activation of the SIS mechanism across the MPT. The model results of Tziperman and Gildor (2003) show that as the climate heads towards a glacial state and atmospheric temperatures start to decrease substantial cooling of the surface ocean allows sea-ice to form. Subsequently, sea-ice extent increases rapidly resulting from a positive albedo-temperature feedback, with an increase in sea ice leading to a decrease in evaporation and moisture supply to continental glaciers (Tziperman and Gildor, 2003). However, sea ice growth is self-limiting as sea ice effectively insulates the surface ocean and thus, when atmospheric temperatures start to rise again, sea ice loss is rapid. The SIS hypothesis makes two critical predictions. The first one being a pronounced increase in the sea ice extent across the MPT (Tziperman and Gildor, 2003), and the second one being land-glacier sea ice hysteresis during post-MPT climate cycles, with the largest sea ice extent when continental ice volume starts to retreat (Sayag et al., 2004). Lee et al. (2017) also demonstrate the importance of sea ice for the MPT using climate models. They propose that the change in G/IG frequency associated with the MPT originated from changes in the inter-hemispheric sea ice growth related to climate cooling (Lee et al., 2017). Whereas sea ice varies in-phase between hemispheres at 41-ka during warm climates, such as the

Pliocene, cold climates are characterised by out-of-phase interhemispheric sea ice growth driven by precession variation modulated by eccentricity (Lee et al., 2017).

Furthermore, a nonlinear response of the Atlantic meridional overturning circulation (AMOC) to Plio-Pleistocene cooling has been proposed to change the redistribution of heat between the southern and northern hemisphere between the 41-ka and the 100-ka world (Bell et al., 2015). Less northward heat transport during the 100-ka world as a result of decreased deep water formation in the North Atlantic could lead to/aid in the build-up of northern hemisphere ice volume across the MPT (Bell et al., 2015). In addition to changes in the oceanic overturning, changes in the atmospheric circulation have also been suggested to increase northern hemisphere ice volume across the MPT (McClymont and Rosell-Melé, 2005). Progressive intensification of the zonal SST gradient in the equatorial Pacific between 1.17-0.9 Ma has been proposed to drive the onset and intensification of the Walker circulation (McClymont and Rosell-Melé, 2005). Together with an increase in the meridional SST gradient across the MPT in both the Atlantic and the Pacific (McClymont et al., 2008), this suggests strengthening of the Hadley Circulation, at least in the northern hemisphere, and decreased heat but increased moisture transport to ice-sheet source regions (McClymont and Rosell-Melé, 2005, McClymont et al., 2008, McClymont et al., 2013). Although, it is unclear whether atmospheric changes were effective in controlling continental ice volume increase (McClymont et al., 2013).

Thus, plenty of hypothesis exist as to what could have caused MPT climate change, however, the evaluation of these hypotheses requires additional records from climatically sensitive regions to paint a complete picture of global climate change across the Pleistocene.

1.2.2 Global climate change across the Mid-Pleistocene transition

The change in frequency of G/IG cycles together with the increase in continental ice volume across the MPT is preceded/accompanied by a variety of atmospheric and oceanic changes. Determining the nature and timing of Mid-Pleistocene climate change is crucial with respect to our understanding of the synchronicity and/or sequential evolution of global climate feedbacks and our understanding of mechanisms driving the MPT frequency change.

McClymont et al. (2013) studied SSTs of 26 globally distributed sediment cores and identified an overall cooling trend during the early Pleistocene that intensified between 1.2 Ma and 0.8 Ma and diminishes at the onset of dominant 100-kyr periodicity (~0.7 Ma). Six sites, among others from the West Pacific Warm Pool (WPWP) (de Garidel-Thoron et al., 2005, Medina-Elizalde and Lea, 2005) and in the Southern Ocean (Crundwell et al., 2008, Martínez-García et al., 2010) deviate from this overall cooling trend and exhibit long-term warming across the mid to late Pleistocene (McClymont et al., 2013). Southern Ocean warming across the mid-Pleistocene disagrees with other studies, indicating a northward shift of the Antarctic Polar Front (APF) by 6° and 7° between 1.3-0.9 Ma and 0.9-0.42 Ma, respectively (Kemp et al., 2010). However, the sites studied by McClymont et al. (2013) are just north of the proposed APF shift, potentially highlighting the local hydrography as a driver of SST warming across the MPT. The lack of a cooling trend in the WPWP across the Pleistocene has been observed in several studies (McClymont and Rosell-Melé, 2005, de Garidel-Thoron et al., 2005, Medina-Elizalde and Lea, 2005, Dyez and Ravelo, 2014, Sun et al., 2017), indicating steady SSTs in the western equatorial Pacific but progressive cooling in the east between ~1.4-0.9 Ma. As aforementioned the inferred increased zonal SST gradient in the equatorial Pacific has been linked to an intensification of the Walker Circulation across the MPT, leading to enhanced upwelling in the east and shoaling of the thermocline (McClymont and Rosell-Melé, 2005, Dyez and Ravelo, 2014), supported by increased dust deposition in the eastern equatorial Pacific from 1.1 Ma suggesting a stronger atmospheric circulation (McClymont and Rosell-Melé, 2005). Together with a strengthening of the zonal SST gradient in the equatorial Pacific an enhanced meridional SST gradient can be observed in both the Pacific and Atlantic Ocean throughout the Mid-Pleistocene (Ruddiman et al., 1989, McClymont et al., 2008, Martínez-García et al., 2010, Lawrence et al., 2010, McClymont et al., 2013), strengthening the Hadley Circulation. Relatively stable SSTs throughout the Pleistocene in the Coral Sea (Russon et al., 2010), north of Australia, suggest that the Hadley circulation may have only increased in the northern hemisphere (McClymont et al., 2013), supported by a strengthening of the East-Asian monsoon and Atlantic and Arabian Sea aeolian dust input at around 1.5 Ma and 1.35 Ma, respectively (Clark et al., 2006). Compared to the ~2 °C SST cooling in the North Atlantic between ~1.4-0.85 Ma (Lawrence et al., 2010), thermocline waters at the Iberian Margin demonstrate relatively stable long-term SSTs with intermittent warming throughout the Mid-

Pleistocene coeval with a southward shift of the North Atlantic subpolar front, indicative of a shift in the predominant thermocline water mass off Iberia (Bahr et al., 2018). Warmer waters off Western Europe could potentially have provided an important moisture source for Alpine glaciers throughout the MPT (Bahr et al., 2018).

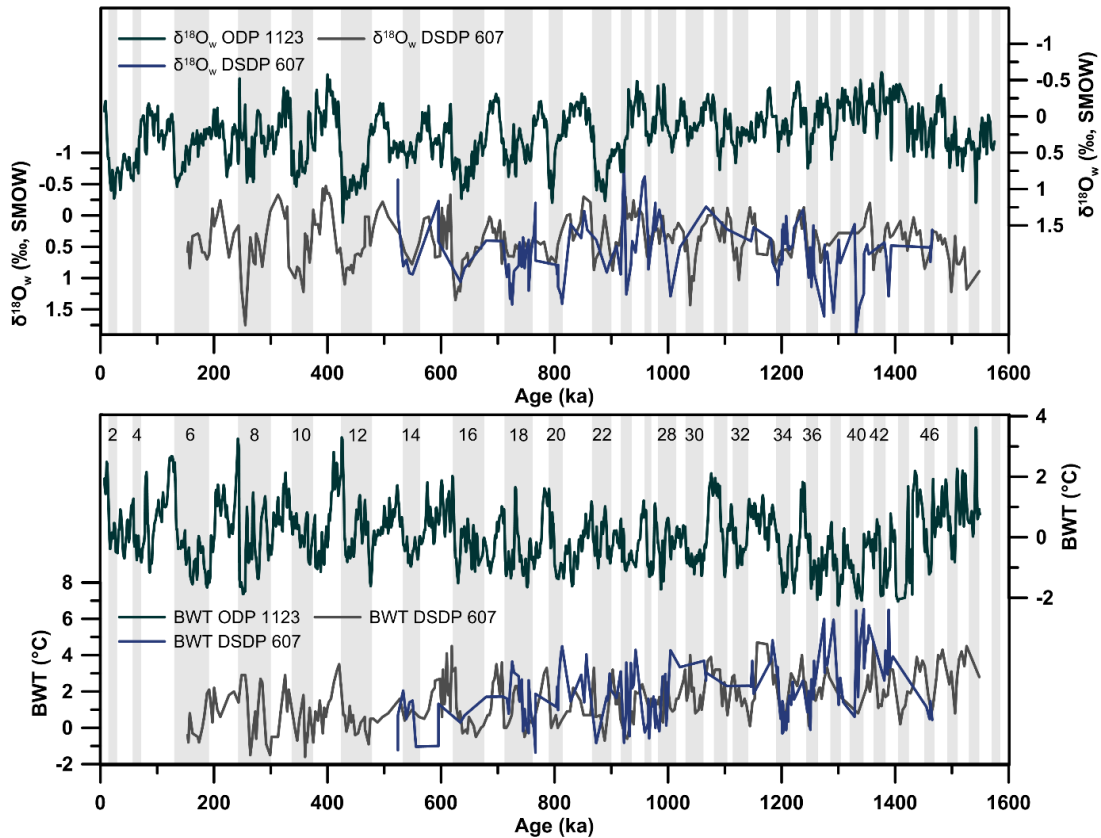


Figure 1.3 Bottom water temperature (BWT) and $\delta^{18}\text{O}_w$ at DSDP Site 607 in the North Atlantic (grey (Sosdian and Rosenthal, 2009) and blue (Ford et al., 2016)) and the southwestern Pacific ODP Site 1123 (Elderfield et al., 2012) across the Mid-Pleistocene.

Compared to the SST records BWT reconstructions across the MPT are scarce and only three high resolution records exist with two from North Atlantic Deep Sea Drilling Project (DSDP) Site 607 (Sosdian and Rosenthal, 2009, Ford et al., 2016) and one from southwestern Pacific ODP Site 1123 (Elderfield et al., 2012). All three studies are based on Mg/Ca ratios of benthic foraminifera, indicating a distinctly different long-term evolution of BWT in the North Atlantic and the South Pacific. Whereas, North Atlantic Site 607 demonstrates a long-term BWT cooling between 1.12-0.85 Ma of ~ 2 °C with cooling observed during both glacial and interglacial intervals (Sosdian and Rosenthal, 2009, Ford et al., 2016) (Figure 1.3), South Pacific

Site 1123 indicates no long-term change in BWT (Elderfield et al., 2012) (Figure 1.3). Instead, glacial BWT at Site 1123 across the last 1.5 Ma consistently approach the freezing point, with a small increase in interglacial BWT from MIS 19 (790 ka) onwards (Elderfield et al., 2012). Similarly consistent glacial BWT in the deep Pacific close to the freezing point of seawater have been inferred by Siddall et al. (2010) using a transfer function between sea level and $\delta^{18}\text{O}_b$ to deconvolve the $\delta^{18}\text{O}_b$ record into its BWT and ice volume component. However, it is debatable if the transfer function of $\delta^{18}\text{O}_b$ derived for the last two G/IG cycles holds true for the entire Pleistocene. Long-term BWT cooling in the North Atlantic has been suggested to result from either surface water cooling in the deep water source regions, as suggested from SST records (Lawrence et al., 2010, McClymont et al., 2013), and/or changes in the mixing ratio of relatively warm northern sourced deep waters and cooler southern sourced deep waters across the MPT (Sosdian and Rosenthal, 2009, Ford et al., 2016). Whilst different BWT histories in the Atlantic and Pacific may be explained by changes in the deep water masses bathing these basins, the three studies also report distinctly different Mid-Pleistocene continental ice volume histories, based on the reconstructed $\delta^{18}\text{O}_w$ (Sosdian and Rosenthal, 2009, Elderfield et al., 2012, Ford et al., 2016). Whereas, $\delta^{18}\text{O}_w$ at DSDP Site 607 suggests no long-term change in continental ice volume across the MPT (Sosdian and Rosenthal, 2009, Ford et al., 2016) (Figure 1.3), ODP Site 1123 indicates a step-like increase across the 900-ka event (Figure 1.3), interpreted to represent an abrupt increase in Antarctic ice volume (Elderfield et al., 2012). Based on the differences in the amplitude of the $\delta^{18}\text{O}_b$ record at ODP Site 1123 and the globally integrated LR04 stack between ~0.9-0.7 Ma, Ford et al. (2016) attribute the increase in $\delta^{18}\text{O}_w$ to the influence of the local hydrography, with Site 1123 likely being sensitive to the mixing ratio of northern and southern sourced deep waters. This highlights the need for further studies of BWT $\delta^{18}\text{O}_w$ and from across the deep ocean to derive a globally integrated continental ice volume signal across the MPT averaging out any regional influences.

As previously mentioned the MPT is associated with a pronounced perturbation in the deep ocean circulation. Early evidence of changes in the deep Pacific and Atlantic carbon isotope values ($\delta^{13}\text{C}$) of benthic foraminifera indicate convergence between these two ocean basins between 0.8-0.7 Ma and 0.5-0.4 Ma, suggesting relatively weak North Atlantic Deep Water (NADW) formation at these times (Raymo et al., 1990,

Raymo et al., 1997). This was further demonstrated by Pena and Goldstein (2014) using neodymium isotopes (ϵ_{Nd}) to track changes in the NADW export throughout the MPT. More positive ϵ_{Nd} values during the 900-ka event (MIS 24 to MIS 22) indicate a prominent decrease in the NADW export during this time. Similarly, post-MPT glacials are also marked by decreased NADW export (Elderfield et al., 2012, Pena and Goldstein, 2014) together with a shoaling of its distinctive ϵ_{Nd} signature in the South Atlantic, whereas interglacial circulation patterns are similar to the pre-MPT interval (Pena and Goldstein, 2014). Pena and Goldstein (2014) further argue that the weak thermohaline circulation during the 900-ka event and post-MPT glacials facilitated atmospheric CO₂ drawdown by reducing the exchange between Antarctic surface and deep waters (Hodell et al., 2003). Increased deep ocean carbon storage across the MPT is inferred from records of benthic foraminiferal B/Ca in the North Atlantic (Lear et al., 2016, Sosdian et al., 2018). A decrease in the carbonate saturation state ($\Delta[CO_3^{2-}]$) at DSDP Site 607 between 1-0.8 Ma is associated with an increased incursion of southern component deep waters into the North Atlantic and potential changes in the air-sea gas exchange around Antarctica, suggesting increased carbon sequestration in the deep ocean (Lear et al., 2016, Sosdian et al., 2018). Additionally, if a larger portion of the deep ocean is bathed in corrosive bottom waters the subsequent dissolution of CaCO₃ in the sediments and increase in total alkalinity lead to further atmospheric CO₂ drawdown (Lear et al., 2016, Sosdian et al., 2018). Moreover, Sosdian et al. (2018), suggest a change in the location of CaCO₃ burial during glacials since the MPT, with increased carbonate dissolution in the Atlantic raising the average ocean carbonate ion concentration ($[CO_3^{2-}]$), leading to the formation of CaCO₃ burial hotspots in the equatorial Pacific, in line with records of Atlantic and Pacific CaCO₃ preservation across the Pleistocene (Sexton and Barker, 2012). The shift in primary location of carbonate burial and the transfer of alkalinity from the Atlantic to the Pacific aids in keeping deep ocean $[CO_3^{2-}]$ low throughout glacial intervals and high across interglacials, as observed from the benthic foraminiferal B/Ca record at Site 607 (Sosdian et al., 2018). Studies of benthic foraminifera-derived productivity changes in the equatorial Pacific support an increase in primary productivity since the MPT, in line with enhanced CaCO₃ burial (Diester-Haass et al., 2018).

In addition to changes in the oceanic carbon cycle, records of atmospheric CO₂, as reconstructed from planktonic foraminiferal boron isotopes ($\delta^{11}B$) and Antarctic ice

cores, suggest prominent changes across the Pleistocene, in line with increased deep ocean carbon storage in the glacial Atlantic Ocean since the MPT (Lear et al., 2016, Sosdian et al., 2018). Continuous records of ancient air trapped in Antarctic ice cores only date back to ~800 ka, with G/IG CO₂ variability between 182-290 ppmv and 176-260 ppmv between 0-400 ka and 400-800 ka, respectively (Bereiter et al., 2015) (Figure 1.4). Beyond 800 ka records of atmospheric CO₂ variations become scarce, complicating the interpretation of the role of CO₂ for MPT climate change. Many hypotheses for the frequency change of G/IG cycles, invoke a threshold response to long-term cooling, for example as a result of a gradual decrease in atmospheric greenhouse gas concentrations. However, Hönisch et al. (2009) suggest a decrease in glacial atmospheric CO₂ of ~31 µatm across the MPT with no long-term trend and relatively stable interglacial CO₂ values (Figure 1.4). Between ~2 Ma and 1 Ma average glacial and interglacial atmospheric CO₂ concentrations were on the order of ~215 µatm and 285 µatm, respectively (Hönisch et al., 2009), in line with an orbitally resolved study of atmospheric CO₂ concentrations across MIS 38 to MIS 32 (1081 ka to 1264 ka) suggesting a similar glacial drawdown in atmospheric CO₂ associated with the MPT (Chalk et al., 2017) (Figure 1.4). Further, reconstructions of disturbed blue ice from Antarctica indicate atmospheric CO₂ concentrations between 221 ppm and 277 ppm around ~1 Ma (Higgins et al., 2015), in line with studies of planktonic δ¹¹B (Figure 1.4). Based on modelling results, Chalk et al. (2017) attribute the post-MPT glacial decrease in atmospheric CO₂ to iron fertilization in the Southern Ocean increasing the efficiency of the biological pump and deep ocean carbon sequestration.

In line with the general global climate cooling observed across the Mid-Pleistocene, records of microfossil assemblages in the Arctic Ocean, suggest a pronounced shift in the sea ice regime. Both foraminifera and ostracod faunal assemblages indicate a transition from more seasonal to perennial sea ice in the central Arctic Ocean at the MPT (DeNinno et al., 2015, Lazar and Polyak, 2016). Additionally, the diatom species *Neodenticula seminae*, typical for the North Pacific (Sancetta and Silvestri, 1986), becomes extinct in the North Atlantic coeval with the MPT, in favour of changes in the Arctic sea ice concentrations and/or circulation (Miettinen et al., 2013).

All in all this demonstrates the extent of climate change associated with the shift in G/IG frequency across the MPT, emphasizing the importance of this transition for our

understanding of climatic feedbacks and the sensitivity of Earth's climate to different forcing mechanisms.

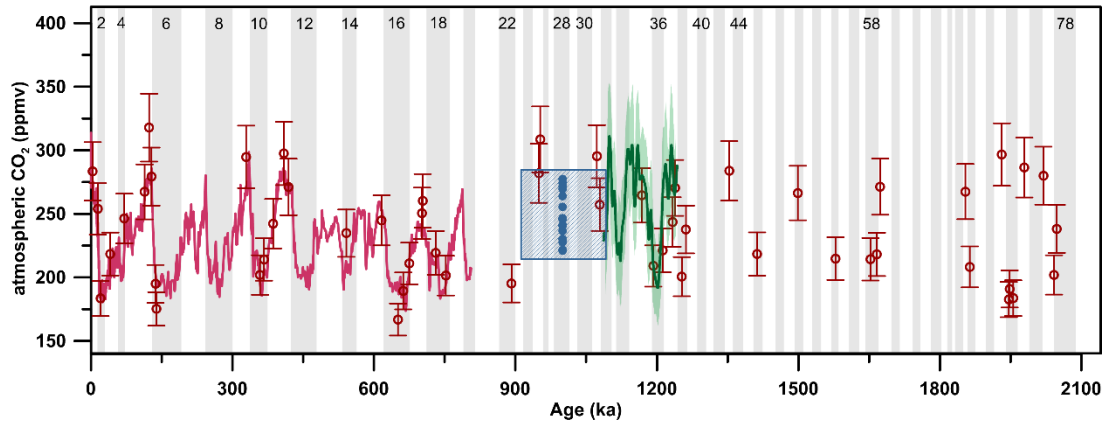


Figure 1.4 Records of atmospheric CO₂ change across the Pleistocene from Antarctic ice cores between ~0-800 ka (pink) (Bereiter et al., 2015 and references herein) and from Antarctic blue ice around ~1 Ma (blue) (Higgins et al., 2015), together with CO₂ records from foraminiferal boron isotopes ($\delta^{11}\text{B}$) from Hönisch et al. (2009) (red) with ± 1 standard error (s.e.) and Chalk et al. (2017) (green) including a 2σ error envelope. Grey vertical bars represent glacial intervals, white vertical bars mark interglacials. Marine isotope stage (MIS) boundaries from Lisiecki and Raymo (2005). Numbers at the top correspond to the respective MIS.

1.2.2.1 The North Pacific throughout the Mid-Pleistocene

Records of North Pacific climate change demonstrate prominent changes on G/IG timescales, highlighting the potential of this region to actively shape climate cycles, however, compared to the North Atlantic it is a highly underrepresented region in paleoclimate research, largely owing to the low preservation potential of calcareous microfossils, hindering the application of traditional foraminiferal paleoclimate proxies.

Nevertheless, some evidence exists for climate change in the North Pacific and its marginal seas across the MPT. As previously mentioned the MPT is marked by an increase in the meridional temperature gradient in the Pacific Ocean, driven by an expansion of polar water masses in the North Pacific from ~1.15 Ma as seen from a decrease in the SST (McClymont et al., 2008, Martínez-García et al., 2010). Gradual increasing SSTs from 0.9-0.5 Ma suggest a subsequent retreat of polar waters in the North Pacific (McClymont et al., 2008). McClymont et al. (2008) suggest that the

southward expansion of polar water masses likely exerted a negative feedback on the moisture supply to continental ice sheet source regions, potentially accounting for the delay in ice sheet response compared to oceanic and atmospheric changes observed from ~1.2 Ma. Further, the expansion of cold waters may have shoaled the thermocline, aiding in the development of the modern eastern equatorial Pacific cold tongue and the intensification of the Walker Circulation (Martínez-García et al., 2010). An expansion of polar water masses and North Pacific cooling from ~1.2 Ma is in line with increased IRD content in sediments of the Gulf of Alaska between 1.2-0.8 Ma and the western North Pacific from ~1 Ma, indicating a highly dynamic Cordilleran ice sheet across the MPT (St. John and Krissek, 1999, Müller et al., 2018).

The Bering Sea represents the northernmost marginal sea of the Pacific, forming the gateway between the Pacific and the Arctic Ocean. Records of Bering Sea climate change across the Mid-Pleistocene demonstrate significant cooling associated with the MPT, as seen from a step-wise expansion of sea ice extent at ~1.9 Ma and ~0.9 Ma, inferred from microfossil assemblages (Teraishi et al., 2016, Ikenoue et al., 2016, Stroynowski et al., 2017). The increase in sea ice extent is accompanied by a decrease in the primary productivity in the Bering Sea (Kim et al., 2014, Iwasaki et al., 2016) and a change in the circulation regime associated with sea level low stands during glacials, restricting the inflow of relatively warm North Pacific waters into the southern Bering Sea (Kim et al., 2014, Teraishi et al., 2016, Stroynowski et al., 2017). Records of $\delta^{13}\text{C}$ and microfossils in the Bering Sea, also suggest the presence of well-ventilated intermediate waters throughout glacials of the last ~1.2 Ma, likely indicating increased brine rejection during sea ice freezing (Knudson and Ravelo, 2015b, Ikenoue et al., 2016). Knudson and Ravelo (2015b) suggest that intermediate water ventilation was enhanced during glacials characterised by a closed Bering Strait, however, it is unclear whether intermediate waters originated in the Bering Sea or in the neighbouring Sea of Okhotsk throughout this interval. Further, records of nitrate utilisation in the Bering Sea indicate increased nutrient utilisation across all glacials of the last 1.2 Ma, likely as a result of enhanced stratification limiting the nutrient-supply from below (Knudson and Ravelo, 2015a). Increased stratification during late Pleistocene glacials might have aided in glacial atmospheric CO_2 drawdown, restricting the evasion of CO_2 from old deep waters outcropping in the North Pacific (Knudson and Ravelo, 2015a).

1.3 Climate of the subarctic North Pacific across the last glacial maximum to Holocene

The environment of the last glacial maximum (LGM) in the North Pacific and the Bering Sea differs significantly from present day conditions by means of geomorphology, surface currents, SST, and sea-ice extent. Resulting from the large sea level fall of ~120 m associated with the LGM (Spratt and Lisiecki, 2016), the Bering land bridge was exposed with large parts of the Bering shelf being submerged (Elias et al., 1996). Further, the drastic change in sea level restricted the inflow of relatively warm and nutrient-rich Alaskan Stream waters through the Aleutian Arc into the southern Bering Sea (Tanaka and Takahashi, 2005). Both the North Pacific and the Bering Sea are characterised by decreased SSTs throughout the LGM, as inferred from microfossil assemblages, organic, and inorganic geochemistry (Tanaka and Takahashi, 2005, Kiefer and Kienast, 2005, Martínez-García et al., 2010, Meyer et al., 2016). Absolute temperatures, however, vary based on the proxy potentially indicating different water depths of the proxy carriers and/or seasonal bias. Low SSTs and low salinity surface conditions together with prevailing northerly winds during the LGM (Muhs et al., 2003, Tanaka and Takahashi, 2005) likely favoured sea ice formation in the Bering Sea. Evidence from both microfossil and geochemical studies suggests extended sea ice during the LGM at the Umnak Plateau and in the western Bering Sea (Caissie et al., 2010, Méheust et al., 2016). Seasonal to extended sea ice is also observed throughout the eastern and western subarctic North Pacific at this time (Méheust et al., 2018), however, microfossil assemblages in the Bowers Ridge region, do not support sea ice cover in this area (Katsuki and Takahashi, 2005), potentially as a result of sustained Alaskan Stream inflow around the Bowers Ridge.

Climate evolution across the last deglacial in the Bering Sea and the North Pacific realm has experienced recurrent attention in the past decade. Available modelling and proxy studies show divergent results with regard to the North Pacific response to millennial-scale climate change in the North Atlantic, most prominently seen in $\delta^{18}\text{O}$ of Greenland ice cores (Heinrich, 1988, Bond et al., 1993, Dansgaard et al., 1993, North Greenland Ice Core Project Members 2007). Across the LGM-Holocene transition (Termination I) two cold stadial events, Heinrich stadial 1 (HS1, ~14.7-18 ka) and the Younger Dryas (YD, ~12.9-11.7 ka), separated by the warm Bølling-Allerød (B/A, ~12.7 ka to 14.7 ka) interstadial, are linked to freshwater perturbations

and changes in the AMOC flow (Heinrich, 1988, McManus et al., 2004). Slowdown and/or shutdown of the AMOC leads to pronounced cooling in the North Atlantic, modifying the atmospheric circulation and SSTs downstream (Okumura et al., 2009). Whilst some studies indicate warming in the North Pacific in response to North Atlantic cooling (Sarnthein et al., 2004, Kiefer and Kienast, 2005, Sarnthein et al., 2006, Okazaki et al., 2010), for example as a result of the onset of a Pacific Meridional Overturning Circulation (PMOC) and increased heat transport (Saenko et al., 2004, Okazaki et al., 2010), other studies suggest in-phase climate change of the North Atlantic and North Pacific as a result of atmospheric and/or oceanic teleconnections (Kienast and McKay, 2001, Piasias et al., 2001, Okumura et al., 2009, Caissie et al., 2010, Max et al., 2012, Chikamoto et al., 2012, Meyer et al., 2016). Discrepancies in the subarctic Pacific proxy records, primarily SST, could potentially arise from either seasonal signals and/or differences in the water depth of proxy carriers or different regional oceanographic responses (Max et al., 2012, Meyer et al., 2016).

Sea ice extent in the Bering Sea and the North Pacific across the deglaciation varied in-phase with millennial-scale climate change in the North Atlantic. The onset of the deglaciation, associated with cold conditions during HS1 is marked by an extensive sea ice cover in the Bering Sea and the subarctic North Pacific (Caissie et al., 2010, Méheust et al., 2016, Méheust et al., 2018). Around ~15 ka, towards the end of HS1, the sea ice regime shifted towards seasonal sea ice/ice free conditions in the Bering Sea and predominantly ice free conditions in the subarctic North Pacific (Caissie et al., 2010, Méheust et al., 2016, Méheust et al., 2018), with reduced sea ice and/or ice free conditions prevailing throughout all of the B/A (Caissie et al., 2010, Méheust et al., 2016, Méheust et al., 2018). High resolution records of sea ice related biomarkers in the western and northern Bering Sea indicate a re-establishment of seasonal sea ice during the YD cold reversal, whilst the sea ice edge likely did not extend as far south as the subarctic North Pacific (Méheust et al., 2016, Méheust et al., 2018). Coeval with the early Holocene climate warming following the YD, diatom assemblages at the Umnak Plateau indicate ice free conditions in conjunction with increased SSTs and enhanced influence of the warm Alaskan Stream waters in the southern Bering Sea (Caissie et al., 2010). Likewise, the western and northern Bering Sea are characterised by ice free conditions during the early Holocene, whereas seasonal sea ice re-emerges during the mid-Holocene (Méheust et al., 2016, Méheust et al., 2018). The North

Pacific, on the other hand, remained largely ice free since the onset of the Holocene (Méheust et al., 2016, Méheust et al., 2018).

Based on studies of foraminiferal $\delta^{18}\text{O}$, $\delta^{13}\text{C}$, and ϵ_{Nd} , it has been suggested that intermediate water formed in the Bering Sea during times of increased sea ice cover, such as the LGM and HS1 (Horikawa et al., 2010, Rella et al., 2012, Knudson and Ravelo, 2015b, Cook et al., 2016). Today, North Pacific Intermediate Water (NPIW) forms primarily via brine rejection during sea ice freezing in the Sea of Okhotsk and mixing with nutrient-rich subsurface waters in the subarctic gyre (300-700 m) (Talley, 1993, Shcherbina et al., 2003). Nevertheless, evidence of chlorofluorocarbon suggests the formation of trace amounts of deep water in the Bering Sea today (Warner and Roden, 1995). Based on more radiogenic ϵ_{Nd} isotopes at intermediate depth along the Bowers Ridge during cold periods of the last G/IG cycle, Horikawa et al. (2010) concluded subduction of radiogenic surface waters along the Aleutian Arc to intermediate depth. Additional studies, on the other hand, suggest that the Sea of Okhotsk remained the primary source of NPIW during cold events, such as the HS1 (Max et al., 2014). Thus, further research is needed to determine the source region of NPIW during northern hemisphere cold events. Additionally, the extent and depth of NPIW during glacial intervals is poorly constrained. $\delta^{18}\text{O}_b$ from across the Bering Sea suggests a divide of well-ventilated intermediate and poorly-ventilated deep waters around ~1000 m water depth for the LGM (Cook et al., 2016), whereas other studies from the Gulf of Alaska demonstrate decreased ventilation ages during HS1 at ~3500 m water depth (Rae et al. 2014). Further, a larger extent of glacial NPIW has been proposed to foster primary productivity in the equatorial Pacific, important for oceanic carbon sequestration (Max et al., 2017).

Overall, LGM climate change in the Bering Sea and the North Pacific illustrates the sensitivity of the region to G/IG cycles and highlights its potential to actively shape Pleistocene climate cycles via oceanographic and carbon cycle feedbacks.

1.4 Biogeochemical cycling and ventilation in the North Pacific on glacial/interglacial timescales

Late Pleistocene G/IG cycles are accompanied by pronounced changes in the atmospheric CO_2 concentration (~180-280 ppmv), observed in Antarctic ice cores (Bereiter et al., 2015) (Figure 1.4), indicating a large scale re-distribution of carbon

between different reservoirs, including the ocean, the biosphere, and the atmosphere (Broecker, 1982). The deep ocean is the largest reservoir accessible on orbital timescales, suggesting that large amounts of carbon were stored in the deep ocean during glacials and released across the deglaciation (Boyle, 1988, Galbraith et al., 2007, Jaccard et al., 2009, Yu et al., 2010a, Skinner et al., 2010, Burke and Robinson, 2012). Proposed mechanisms of deep ocean carbon storage include expansion of more corrosive southern-sourced bottom waters and associated dissolution of CaCO_3 at the seafloor, raising the whole ocean alkalinity (Boyle, 1988, Skinner, 2009), changes in the air-sea gas exchange, as a result of changes in the ocean circulation/stratification (Toggweiler et al., 2006, Schmittner and Galbraith, 2008, Anderson et al., 2009, Jaccard et al., 2013, Billups et al., 2018) and/or increased sea ice extent around Antarctica causing decreased CO_2 outgassing (Stephens and Keeling, 2000, Ferrari et al., 2014), and changes in the efficiency of the biological pump as indicated by a change in the regenerated to preformed nutrient inventory of the deep ocean (Martin, 1990, Jaccard et al., 2009, Jaccard and Galbraith, 2012, Ziegler et al., 2013, Jaccard et al., 2013, Martínez-García et al., 2014, Gottschalk et al., 2016).

Thus, biogeochemical cycling and ventilation, the subduction of atmospherically-equilibrated waters, are important components of the oceanic carbon cycle. Dynamic changes have been proposed for the North Pacific on G/IG timescales, as a result of variations in the primary productivity, the ventilation of North Pacific Deep Water (NPDW), and the influence of NPIW, suggesting that the North Pacific and Bering Sea carbon cycle may have played an active role in G/IG atmospheric CO_2 variability.

Vast areas of the modern North Pacific are considered High Nutrient Low Chlorophyll (HNLC) regions (Moore et al., 2001, Lam and Bishop, 2008), with iron representing the limiting micronutrient (Moore et al., 2001, Lam and Bishop, 2008). Along the eastern Bering Sea slope, however, eddy-driven upwelling (Mizobata et al., 2002, Mizobata and Saitoh, 2004, Mizobata et al., 2008, Ladd et al., 2012), the inflow of nutrient-rich Pacific waters (Walsh et al., 1989, Expedition 323 Scientists 2010), tidal mixing, and transverse circulation (Springer et al., 1996, Hurst et al., 2010, Tanaka et al., 2012) sustain one of the most productive ecosystems in the world's ocean (Springer et al., 1996). Resulting from enhanced primary productivity and remineralisation of organic matter settling through the water column, a pronounced

oxygen minimum zone (OMZ) is found in mid-depth waters (600-1000 m) (Whitledge and Luchin, 1999, Expedition 323 Scientists, 2010) (Figure 1.5).

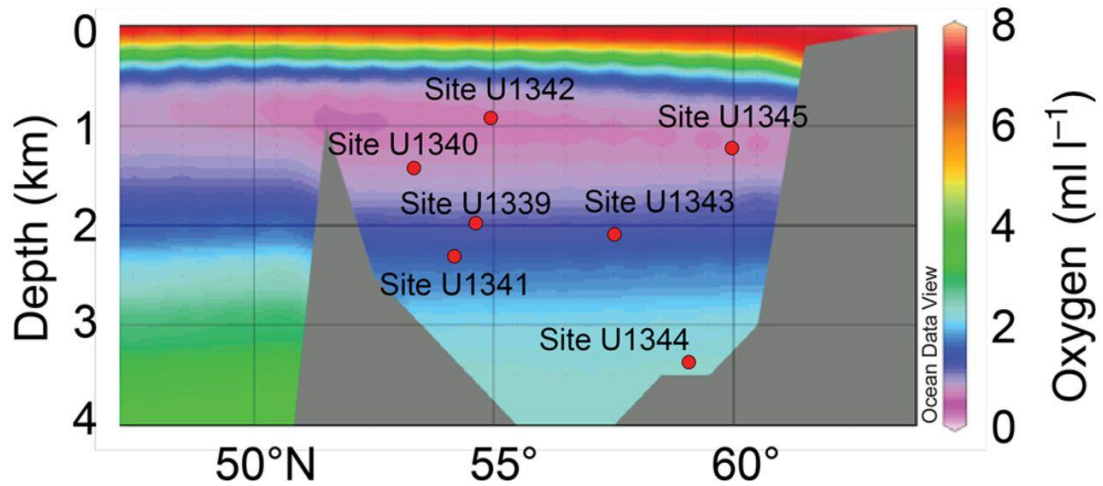


Figure 1.5 Dissolved oxygen concentrations in the Bering Sea and the North Pacific, including all Sites cored as part of International Ocean Discovery Program (IODP) expedition 323. The pink area with dissolved oxygen concentrations $< 1 \text{ ml L}^{-1}$ represents the mid-depth oxygen minimum zone (OMZ). Figure from Expedition 323 Scientists (2010).

Evidence suggests that primary productivity in the North Pacific and its marginal seas has varied on G/IG timescales. This is expressed with a widespread decrease in primary productivity observed across the LGM (Jaccard et al., 2005, Brunelle et al., 2007, Jaccard et al., 2009, Brunelle et al., 2010, Kohfeld and Chase, 2011, Kim et al., 2014, Knudson and Ravelo, 2015a), ascribed to a decrease in the light availability in areas of extensive sea ice formation together with enhanced stratification of the subpolar water column, decreasing the nutrient-supply to the surface ocean (Jaccard et al., 2005, Brunelle et al., 2007, Brunelle et al., 2010, Kim et al., 2014, Knudson and Ravelo, 2015a). Records of opal mass accumulation rates (Kim et al., 2014) and nutrient utilisation in the Bering Sea (Knudson and Ravelo, 2015a), indicate that decreased glacial productivity together with enhanced stratification may have been a consistent feature across the Mid-Pleistocene ($\sim 1.2 \text{ Ma}$). This likely infers dynamic changes in the mid-depth OMZ in the Bering Sea in response to enhanced/reduced primary productivity during interglacial and glacial intervals, respectively. This is also seen from laminated sediments along the Bering Sea continental margins, which have been reported from up to $\sim 2000 \text{ m}$ water depth across the last deglaciation (Cook et al., 2005, Expedition 323 Scientists 2010, Caissie et al., 2010, Aiello and Ravelo,

2012, Kuehn et al., 2014, Pelto et al., 2018), suggesting OMZ expansion in conjunction with deglacial warm events characterised by enhanced primary productivity (Brunelle et al., 2007, Jaccard et al., 2009, Aiello and Ravelo, 2012, Kim et al., 2014, Kuehn et al., 2014).

In addition to expansion/contraction of the OMZ in the Bering Sea bottom water oxygenation is also influenced by the contribution and ventilation of different water masses. Whereas the modern deep Bering Sea is ventilated by NPDW, originating in the Southern Ocean, primarily ventilated by deep water formation around Antarctica (Killworth, 1983, Broecker et al., 1998, Kawabe and Fujio, 2010), the mid-depth Bering Sea is ventilated by NPIW, originating locally from brine formation during sea ice freezing in the Sea of Okhotsk and mixing with subsurface waters (Talley, 1993, Yasuda, 1997, Shcherbina et al., 2003).

Enhanced ventilation of the mid-depth Bering Sea (~800 m water depth) has been observed across glacial intervals of the last 1.2 Ma (Knudson and Ravelo, 2015b), whilst a pronounced deepening of well-ventilated intermediate waters to ~2000 m (potentially even ~3500 m (Rae et al., 2014)) is suggested from records across the North Pacific for the LGM and cold intervals of the last deglaciation, such as HS1 (Duplessy et al., 1989, Ahagon et al., 2003, Galbraith et al., 2007, Sagawa and Ikehara, 2008, Jaccard et al., 2009, Lund et al., 2011, Okazaki et al., 2012, Jaccard and Galbraith, 2013, Rae et al., 2014, Max et al., 2014, Cook et al., 2016). Hence, deepening of atmospherically-equilibrated O₂-enriched intermediate waters during glacials may have influenced intermediate to bottom water oxygenation in the Bering Sea throughout the Pleistocene, however no records exist as of yet, documenting the evolution of NPIW across the MPT.

On the other hand, NPDW which ventilates the deep Bering Sea today, likely also experienced prominent changes in oxygenation on G/IG timescales, linked to enhanced deep ocean carbon storage during glacial intervals. Records of bottom water oxygenation in the North Pacific across the last ~150 ka, suggest a pronounced decrease in the oxygen concentrations of NPDW during glacials, as a result of a change in the ratio of preformed to regenerated nutrients, facilitating deep ocean carbon storage (Jaccard et al., 2005, Galbraith et al., 2007, Jaccard et al., 2009, Jaccard and Galbraith, 2012).

Considering recent studies from the North Atlantic, indicating an increase in the deep ocean carbon storage associated with the MPT (Lear et al., 2016, Sosdian et al., 2018), together with records of CaCO₃ accumulation in the deep North Pacific, in support of poorly ventilated more corrosive deep waters prevailing across glacial intervals of the last ~2.7 Ma (Haug et al., 1995, Jaccard et al., 2005, Burls et al., 2017), this suggests that lower NPDW oxygen concentrations could have been a consistent feature of glacial intervals across the Pleistocene. Further this is supported by records of magnetite preservation in the deep western North Pacific, suggesting decreased oxygen concentrations below 5000 m during MIS 22, 12, 10, 8, 6, and 2 (Korff et al., 2016). Although, absolute oxygen concentrations in NPDW across Pleistocene glacials likely varied in response to changes in the deep ocean carbon sequestration and ventilation.

Thus, both biogeochemical cycling, linked to primary productivity, and ventilation demonstrate dynamic behaviour on G/IG timescales in the North Pacific, most prominently expressed as changes in the oxygen concentration. Whereas, remineralisation of organic matter in the water column likely played a pronounced role during interglacials, marked by increased primary productivity, lower rates of primary productivity during glacials potentially caused OMZ contraction. On the other hand, changes in the ventilation and water mass structure of the North Pacific on G/IG timescales, with enhanced ventilation and formation of NPIW together with increased carbon storage in NPDW during glacial intervals, are expected to influence the oxygenation of the North Pacific and the Bering Sea.

1.5 Research questions and outline of the thesis

The North Pacific is a highly underrepresented region in paleoceanographic studies, largely owing to the poor preservation potential of calcareous microfossils, one of the main proxy carriers in paleoceanography, in the relatively corrosive bottom waters. Nonetheless, dynamic behaviour, such as changes in the primary productivity, deep ocean carbon storage, and enhanced intermediate water formation have been proposed on orbital timescales, important for the oceanic carbon cycle. However, many open questions remain regarding the potential of this region to actively shape Pleistocene climate cycles.

International Ocean Discovery Program (IODP) Expedition 323 to the Bering Sea cored along the high productivity area of the eastern Bering Sea slope, with Site U1343 reaching back to ~2.3 Ma, covering most of the Pleistocene (Expedition 323 Scientists 2010, Asahi et al., 2016). The high sedimentation rates along the continental margin indicate the potential to study Mid-Pleistocene climate change at a sub-orbital resolution.

The overall aim of this study is to add a North Pacific perspective on climate change across the MPT. Further, I explore changes across the last glacial to Holocene cycle to provide context with respect to this comparatively well understood time period. Particular emphasis is placed on disentangling the evolution of continental ice volume across the MPT, to explore dynamic changes in the North Pacific oceanography, and to examine potential forcing mechanisms driving climate change across this critical transition. Especially, the development of sea ice across the MPT is of major interest, as modelling studies suggest fundamental changes of sea ice dynamics, actively driving global climate change. A multi-proxy approach is employed, combining organic geochemistry for sea ice reconstructions with inorganic geochemistry of calcareous microfossils to study the evolution of bottom water temperatures and sedimentary redox chemistry in the eastern Bering Sea to help unravel continental ice volume, North Pacific circulation patterns, and biogeochemical cycling across the Pleistocene. Furthermore, I am exploring the influence of high surface ocean productivity on diagenesis of calcareous microfossils in the continental margin of the eastern Bering Sea and the implications for paleoclimate studies.

Specifically, the scientific objectives of this study are:

- To develop a comprehensive understanding of authigenic carbonate geochemistry precipitated on foraminiferal tests in sediments underlying high productivity areas.
 - Establish the trace metal composition of foraminiferal authigenic carbonates in sediments along the eastern Bering Sea slope both above and below the Sulphate-Methane Transition Zone (SMTZ).
 - Determine the role of organoclastic sulphate reduction versus anaerobic oxidation of methane for authigenic carbonate formation on foraminiferal tests.

- Understand the spatial distribution of authigenic carbonates within foraminiferal tests and examine the applicability of diagenetically altered foraminiferal tests for paleoclimate reconstructions.
- To investigate the relationship of BWT history and $\delta^{18}\text{O}_b$ in the eastern Bering Sea and its implications for the $\delta^{18}\text{O}_w$ across the MPT and LGM-Holocene. This will provide insights into continental ice volume history, but also offer the opportunity to explore the contribution of NPDW versus NPIW to the deep Bering Sea on G/IG timescales.
- To examine changes in the sedimentary redox chemistry along the eastern Bering Sea slope in order to infer changes in bottom water oxygenation in light of primary productivity and water masses contributing to the deep Bering Sea across the MPT and LGM-Holocene.
- To explore the role of sea ice for the LGM-Holocene and MPT climate change on a regional to global scale, studying the dynamic changes of the Bering Sea sea ice regime under consideration of the sea ice switch hypothesis (Gildor and Tziperman, 2001, Tziperman and Gildor, 2003) and potential NPIW formation across the Mid-Pleistocene and the last deglaciation.

1.6 Outline of the thesis

Chapter 2 of this thesis comprises a detailed description of the modern Bering Sea oceanography, together with an in-depth Site description of IODP Site U1343. Further, the paleoceanographic proxies and statistical approaches utilised throughout the study are elucidated and discussed.

The following four chapters comprise the description and discussion of the scientific findings of this study. Chapter 3 focuses on the diagenetic alterations of foraminiferal tests in sediments from IODP Site U1343. Reconstructing past climate using foraminifera, relies on the assumption that foraminifera calcify in equilibrium with the surrounding seawater and the geochemical integrity of calcareous tests, preserved in the sediments for thousands to millions of years. This chapter explores foraminiferal alterations in conjunction with early diagenesis driven by an active microbial community within the sediments underlying a high productivity area. The results comprise a suite of single-specimen imaging and geochemical analyses to examine the

trace metal composition and spatial variability of authigenic foraminiferal carbonates and their applicability for paleoceanographic studies.

Building upon these findings Chapter 4 encompasses a composite record of benthic foraminiferal Mg/Ca for BWT reconstructions across the LGM-Holocene and the Mid-Pleistocene. Independent BWT reconstructions are a powerful tool to deconvolve the $\delta^{18}\text{O}_b$ record into its temperature and $\delta^{18}\text{O}_w$ component, driven by changes in continental ice volume and regional hydrography. In the Bering Sea and North Pacific fluctuations in the depth and ventilation of NPIW have been proposed on orbital timescales. NPIW is a low $\delta^{18}\text{O}_w$ water mass indicating the potential to influence the mid-depth to deep Bering Sea $\delta^{18}\text{O}_w$ record across the Pleistocene. Thus, inferences of continental ice volume based on $\delta^{18}\text{O}_w$ in this region always need to take local changes in the water mass contribution into account. Nonetheless, this offers a potentially unique opportunity to study continental ice volume together with the Mid- to late Pleistocene evolution of NPIW in the Bering Sea.

Changes in the contribution and ventilation of the different water masses in the deep Bering Sea additionally have the potential to cause pronounced fluctuations in the bottom water oxygenation. Chapter 5 explores dynamic changes in sedimentary redox chemistry across the LGM-Holocene and the MPT, inferred from U/Mn and U/Ca of authigenic foraminiferal coatings. Sedimentary redox chemistry varies in relation to bottom water oxygenation and organic carbon export from the sea surface. Thus, in conjunction with records of primary productivity at Site U1343, sedimentary redox chemistry provides a qualitative tool to investigate changes in bottom water oxygenation linked to changes in the water mass contribution and/or deep ocean carbon storage.

Subsequently, Chapter 6 focuses on the evolution of sea ice in the eastern Bering Sea across the Mid-Pleistocene and the LGM-Holocene. Sea ice reconstructions are based on organic geochemistry, utilising biomarkers produced by sea ice diatoms to track changes in the seasonal sea ice extent. Across the LGM-Holocene the sea ice dynamics will be discussed together with previously published records from across the Bering Sea and the North Pacific painting a regionally consistent picture of deglacial sea ice variability. The Mid-Pleistocene sea ice evolution, on the other hand, is the first of its

kind looking at orbital-scale variability and allows the assessment of previously proposed mechanisms for MPT climate change.

Chapter 7 summarises and brings together the conclusions from the individual chapters of this thesis. Additionally, an outlook is provided with potential future work to reinforce the key findings and to further develop the proposed hypotheses.

2. Materials and methods

2.1 Oceanography of the Bering Sea

The Bering Sea represents the northernmost marginal Sea of the North Pacific, forming the gateway between the Pacific and Arctic Ocean. Its area of $2.29 \times 10^6 \text{ km}^2$ and volume of $3.75 \times 10^6 \text{ km}^3$ make it the third largest marginal sea in the world (Takahashi et al., 2011), comprising a wide neritic shelf area in the east up to 200 m deep and the Aleutian Basin to the west reaching depths over 3.5 km (Figure 2.1).

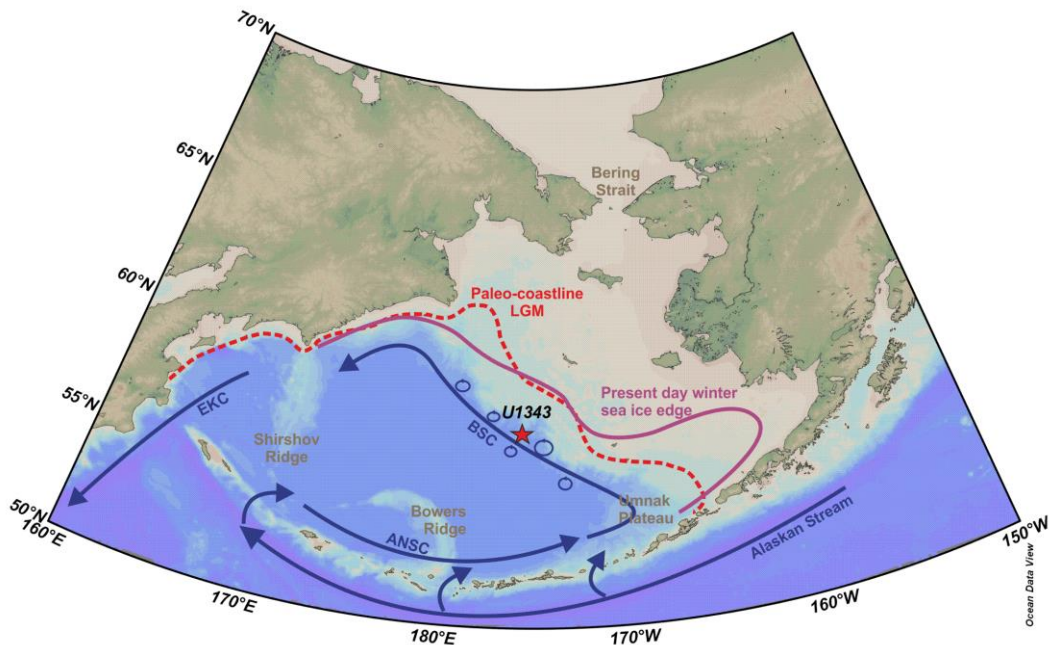


Figure 2.1 Map of the Bering Sea showing the location of IODP Site U1343 (red star). The pink solid line represents the present day winter sea ice edge, the red dashed line is the last glacial maximum (LGM) coastline (PALE Beringian Working Group, , 1999), and the blue arrows show the cyclonic surface circulation in the Bering Sea. The Alaskan Stream enters the Bering Sea in the south through several Aleutian passes to form the Aleutian North Slope Current (ANSC) that feeds into the Bering Slope Current (BSC), which in turn feeds into the East Kamchatka Current (EKC) (modified from Stabeno et al. (1999)). Eddy formation along the eastern Bering slope brings nutrients to the surface resulting in high primary productivity, called the 'Green Belt' (Springer et al., 1996, Mizobata and Saitoh, 2004). Map created with Ocean Data View (Schlitzer, 2011).

The surface circulation in the Bering Sea is fed via inflow of the relatively warm and nutrient-rich Alaskan Stream, the northern boundary current of the subarctic North Pacific gyre, through several passes of the Aleutian Arc (Stabeno et al., 1999). The sill

depth of the different passes constrains the influx of Alaskan Stream waters, with the main flow occurring through Amukta Pass in the central Aleutian Arc east of Bowers Ridge (Ladd, 2014) (Figure 2.1). In addition to the sill depth, the flow through the passes can be obstructed by eddy formation, such as observed for the Amchitka Pass west of the Bowers Ridge (Stabeno et al., 1999). Within the Bering Sea the cyclonic gyre circulation is comprised of the southward flowing Kamchatka Current representing the western boundary current, the north-westward flowing Bering Slope Current (BSC) as the eastern boundary current, and the eastward flowing Aleutian North Slope Current (ANSC) to the south (Figure 2.1) (Stabeno et al., 1999). The main surface outflow in the Bering Sea occurs through the Kamchatka Strait in the west, however, some surface water (0.85 Sverdrup (Sv) (Coachman, 1993)) flows northward and leaves the Bering Sea through the 50 m deep Bering Strait – the gateway between the Pacific and the Arctic Ocean. The northward transport through the Bering Strait is driven by a sea level difference of 0.4 m between the Bering Sea and the Arctic Ocean (Stabeno et al., 1999) and it is thought to influence the heat equilibrium and salt balance of the Pacific and Atlantic Ocean on long time scales (Takahashi, 2005). At International Ocean Discovery Program (IODP) Site U1343, the surface ocean is characterised by the BSC (Figure 2.1), flowing along the eastern Bering Sea shelf break. It exhibits a pronounced seasonal cycle with enhanced flow speed closer to the shelf break during winter and a reduced flow speed during summer (Ladd, 2014). The average flow speed of the BSC is $>10 \text{ cm s}^{-1}$ with maximum speed around 14 cm s^{-1} (Ladd, 2014). The BSC is characterised by mesoscale cyclonic and anticyclonic eddies measuring up to 10-200 km horizontally and $>1 \text{ km}$ vertically (Paluszkiwicz and Niebauer, 1984, Stabeno et al., 1999, Mizobata et al., 2002, Ladd, 2014) (Figure 2.1). Eddies form primarily along the major canyons of the eastern shelf slope during spring and are important for the spring phytoplankton bloom (Ladd et al., 2012). A chlorophyll a maximum has been observed within eddies (Mizobata et al., 2002, Mizobata et al., 2008, Ladd et al., 2012), as a result of upwelling within or along the eddies (Mizobata et al., 2002), transporting nutrient and CO_2 -rich deep waters to the surface, resulting in occasional CO_2 outgassing (Kelley et al., 1971). Further, horizontal water mass transport within eddies (Mizobata et al., 2006, Ladd et al., 2012) is enhancing the exchange of nitrogen-rich basin waters and iron-rich shelf waters (Aguilar-Islas et al., 2007), fostering primary productivity. Eddy activity is negatively correlated with the North Pacific Index (NPI), with a negative NPI, characterized by

a strong Aleutian Low, resulting in an enhanced subarctic gyre in the North Pacific and increased inflow into the Bering Sea (Ladd et al., 2012, Ladd, 2014).

Deep water in the Bering Sea today originates in the North Pacific and is marginally influenced by small amounts of deep water forming in situ within the Bering Sea (Warner and Roden, 1995, Takahashi et al., 2011). Deep water renewal takes place via inflow of North Pacific Deep Water (NPDW) into the Bering Sea through the Kamchatka Strait below 2500 m (Coachman et al., 1999, Stabeno et al., 1999). As it progresses north- and eastward through the Aleutian Basin it slowly freshens and is displaced upward, exiting the Bering Sea via outflow through Kamchatka Strait at depth <2500 m (Stabeno et al., 1999). However, data on the Bering Sea deep water is scarce so more information is needed to constrain its flow and origin (Riethdorf et al., 2013b).

The Bering Sea has a subarctic water column structure with a warm surface layer (0-50 m) during summer, a cold subsurface dicothermal layer (50-200 m) (cold layer between two warmer layers) (Tanaka and Takahashi, 2005) overlying the strong halocline (100-200 m) (Miura et al., 2002) (Figure 2.2). During winter when the surface layer cools the thermocline deepens (150 m) (Tanaka and Takahashi, 2005) and vertical mixing is promoted forming a winter mixed layer with the depth restricted by the permanent halocline (Miura et al., 2002). These cold waters remain throughout summer forming the dicothermal layer (Figure 2.2).

The surface layers are underlain by North Pacific Intermediate Water (NPIW) 300-700 m (Talley, 1993, Yasuda, 1997) (Figure 2.2), and NPDW. Modern NPIW is produced by mixing of Okhotsk Sea Mode Water, formed via brine rejection during winter sea ice freezing (Talley, 1993, Yasuda, 1997, Shcherbina et al., 2003), with the relatively warm and salty Western Subarctic Gyre, to form the Oyashio Current (Yasuda, 1997). A large part of this current then flows south cabbeling with the Kuroshio Extension, forming new NPIW (Yasuda, 1997). NPDW is one of the oldest deep water masses throughout the oceans, characterised by relatively low oxygen and high nutrient concentrations. Whereas the nitrate and phosphate concentrations in the deep Bering Sea are similar (Garcia et al., 2006b), the silicate concentrations are enriched compared to the deep North Pacific (Garcia et al., 2006b), in line with the deep Bering Sea having the highest concentrations of silica throughout the world's

ocean. This is likely caused by extraordinary high production of siliceous phytoplankton in the surface ocean, high regeneration rates at the sediment-water interface and accumulation in the bottom water due to very low flushing rates (Coachman et al., 1999).

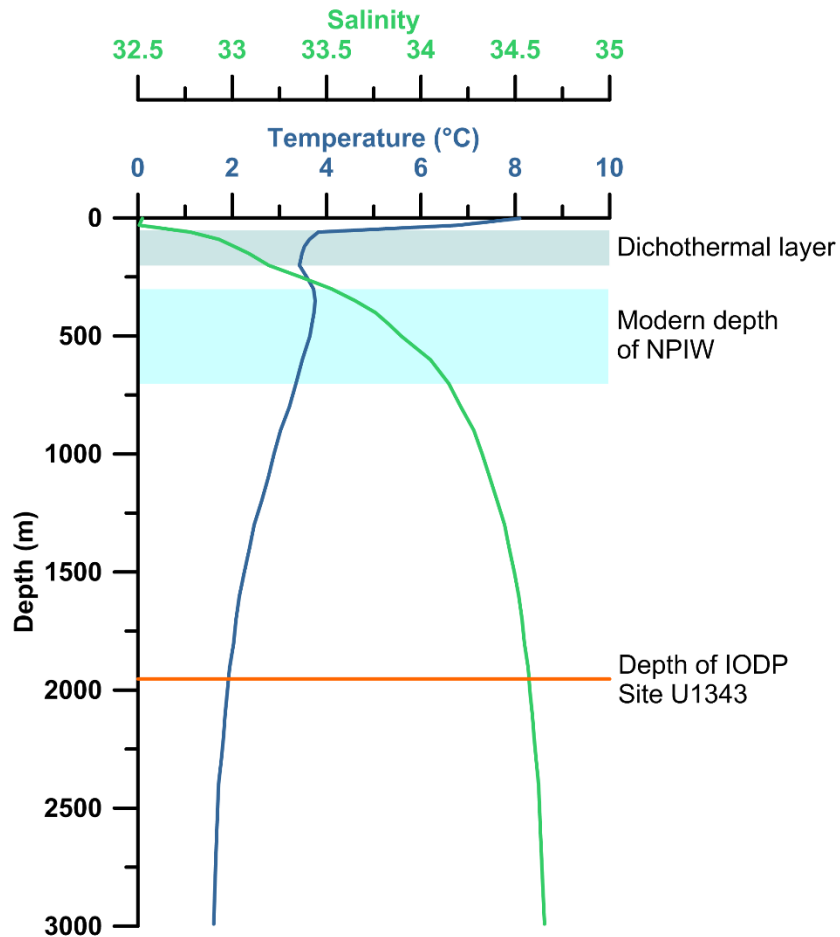


Figure 2.2 Water column temperature (blue) and salinity (green) at GLODAP v2 station 41047-3 (B) (58°00'N, 174°87'W) (Olsen et al., 2016), close to IODP Site U1343 in the eastern Bering Sea. The dark blue box indicates the dichothermal layer (Tanaka and Takahashi, 2005) and the light blue box marks the modern depth of North Pacific Intermediate Water (NPIW) in the Bering Sea (Talley, 1993).

The ecosystem in the Bering Sea is among the most productive in the world, particularly along the eastern Bering slope, also called the ‘Green Belt’ with productivity rates of 175-275 g C m⁻² yr⁻¹ (Springer et al., 1996). As a result of enhanced primary productivity along the shelf break, depleted oxygen concentrations are pervasive in mid-depth waters, forming a pronounced oxygen minimum zone (OMZ) between 600-1000 m (Expedition 323 Scientists 1999, Expedition et al., 2010)

(Figure 1.5). The oxygen content within the OMZ core ranges from 0.43-1.57 mg L⁻¹ (Whitledge and Luchin, 1999) and is highly variable between seasons, with lowest concentrations during winter.

Large parts of the remaining Bering Sea, especially the deep Aleutian Basin, are considered a High Nutrient Low Chlorophyll (HNLC) zone with iron representing the limiting micronutrient (Springer et al., 1996, Leblanc et al., 2005, Aguilar-Islas et al., 2007). However, a pronounced spring phytoplankton bloom can be observed on the 500 km wide eastern shelf, partly sustained by the seasonal sea ice cycle, providing an important seed population, releasing nutrients during melting, and facilitating water column stratification (Goes et al., 2014, Wang et al., 2014).

Seasonal sea ice formation in the Bering Sea is important for both the physical properties of the water column and the ecosystem. Formation and extent are driven by the air and water temperature together with the direction of storm tracks during the winter months (Rodionov et al., 2007). Today, sea ice originates in the Chukchi Sea and in polynyas on the southward facing coastlines on the eastern Bering shelf and is advected south-westward (Niebauer et al., 1999). Polynyas are areas of extensive heat exchange between the ocean and the atmosphere, therefore ice and brine formation take place. Niebauer et al. (1999) calculated an average sea ice and brine formation for Bering Sea polynyas of 10-12 cm day⁻¹ and 0.006-0.042 Sv, respectively. According to studies by Cavalieri and Martin (1994), who used a combination of satellite, weather, and oceanographic data together with an ocean box model to investigate brine flow in the Arctic Ocean marginal seas, the brine formed on the eastern Bering shelf flows northward across the shelf and through the Bering Strait into the Arctic Ocean, where it helps to maintain the Arctic halocline. The maximum seasonal sea ice extent is reached in March/April close to the Bering Sea slope (Figure 2.1) (Niebauer et al., 1999, Expedition 323 Scientists 2010). Recent years, however, are marked by a pronounced retreat of the sea ice edge in the Bering Sea (Grebmeier et al., 2006, Douglas, 2010, Brown and Arrigo, 2013), with important implications for the marine ecosystem (Hunt Jr et al., 2002, Grebmeier et al., 2006, Mueter and Litzow, 2008, Brown et al., 2011b, Brown and Arrigo, 2013).

2.2 International Ocean Discovery Program Site U1343

This study is focused on the IODP Site U1343, retrieved during IODP Leg 323 in 2009 (Expedition 323 Scientists 2010). The Site is located on a topographic high off the eastern Bering Sea slope (57°33.4'N, 176°49.0'W at 1953 m water depth (Expedition 323 Scientists 2010)) (Figure 2.1). In total five holes (A-E) were drilled using an Advanced Piston Corer and an Extended Core Barrel system, to compile a composite core and depth scale (Expedition 323 Scientists 2010). The cores vary in length between 8.5 m below sea floor (mbsf) (U1343D) to 744.3 mbsf (U1343E) (Expedition 323 Scientists 2010). The composite depth scale was constructed by correlating the physical properties of U1343A, U1343C, and U1343E (Asahi et al., 2016). From the mudline down to 235 mbsf the splice is composed of a continuous interval. Below 235 mbsf, however, sections from U1343E are appended with unknown gaps (Asahi et al., 2016).

IODP Site U1343 is bathed in NPDW (Expedition 323 Scientists 2010). Data from Global Ocean Data Analysis Project version 2 (GLODAP v2) (Olsen et al., 2016) station 41047-3 (B) (58°00'N, 174°87'W) show a present day water temperature at ~2000 m depth in the eastern Bering Sea of ~1.95 °C with a salinity of 34.58 (Practical Salinity Scale – 1978) (Figure 2.2). The nitrate concentration is 41 $\mu\text{mol kg}^{-1}$, with phosphate and silicate having concentrations of 3.06 $\mu\text{mol kg}^{-1}$ and 199.8 $\mu\text{mol kg}^{-1}$, respectively (Olsen et al., 2016). The total carbon concentration at ~2000 m water depth in the eastern Bering Sea is 2392 $\mu\text{mol kg}^{-1}$ with a pH of 7.6 (Olsen et al., 2016). By means of the software CO2calc (Robbins et al., 2010) other CO₂ system parameters were calculated, using the dissociation constants from Mehrbach et al. (1973) refit by Dickson and Millero (1987). This yields a bottom water carbonate saturation state ($\Delta[\text{CO}_3^{2-}]$) (Equation 2.1) at Site U1343 around -14 $\mu\text{mol kg}^{-1}$ with an Ω of 0.8, suggesting undersaturated waters with respect to CaCO₃.

$$\Delta[\text{CO}_3^{2-}] = [\text{CO}_3^{2-}] - [\text{CO}_3^{2-}]_{\text{saturation}} \quad (\text{Equation 2.1})$$

Today, IODP Site U1343 underlies the mid-depth OMZ (Expedition 323 Scientists 2010), with modern oxygen concentrations at ~2000 m water depth of ~52 $\mu\text{mol kg}^{-1}$ (1.2 ml L⁻¹) (Olsen et al., 2016).

2.2.1 Sedimentary properties

The sediment at Site U1343 is primarily composed of dark/very dark greenish-grey to dark/very dark grey silt (Expedition 323 Scientists 2010). It contains varying amounts of clay and diatoms, whilst sand, foraminifera, ash, calcareous nannofossils, and sponge spicules constitute only minor components (Expedition 323 Scientists 2010). Frequent authigenic carbonate crystals are found in all holes at Site U1343 (Expedition 323 Scientists 2010). Compared to Sites drilled at the Bowers Ridge during IODP expedition 323, U1343 has a higher ratio of siliciclastic versus biogenic components, as a result of its proximity to the Bering slope (Expedition 323 Scientists 2010), with a total organic carbon content at Site U1343 between 0.5-1 wt% (Wehrmann et al., 2011). Additionally, a smaller amount of volcanoclastic material is found in U1343 compared to Sites further south, resulting from its more distal position from the Aleutian Arc (Expedition 323 Scientists 2010).

Overall the sediments are characterized by slight to moderate rates of bioturbation, however, six narrow intervals of laminations occur at Site U1343 above 130 mbsf that can be correlated between different holes, indicating episodes of drastically decreased bottom water oxygen concentration ($[O_2]$) ($<0.1 \text{ ml L}^{-1}$) (Moffitt et al., 2015). Below 130 mbsf there are no laminated intervals in IODP sediment core U1343 either indicating that the OMZ did not expand to ~2000 m water depth or the loss of laminations due to sediment compaction (Expedition 323 Scientists 2010).

2.2.2 Age model

The age model of sediment core U1343 is based on benthic foraminiferal oxygen isotope ($\delta^{18}O_b$) stratigraphy, constructed by tuning the $\delta^{18}O_b$ record to the global LR04 stack (Lisiecki and Raymo, 2005, Asahi et al., 2016, Kender et al., in review). The composite $\delta^{18}O_b$ records are based on multiple benthic foraminifera species (*Elphidium batialis*, *Uvigerina* spp., *Globobulimina pacifica*, *Nonionella labradorica*, *Islandiella norcrossi*, *Valvulineria auracana*, *Lenticulina* spp., *Cassidulina* spp., *Cibicidoides* spp., *Planulina wuellerstorfi*), normalized to *E. batialis*, the most abundant species at Site U1343 (Asahi et al., 2016, Kender et al., in review). Asahi et al. (2016) measured $\delta^{18}O_b$ at an average depth resolution of 0.3 m between 0-170 m core composite depth below seafloor (CCSF-A), 1.4 m between 170-423 m CCSF-A, and 5.1 m between 423-770 m, yielding a highly refined age model between 0-1.2 Ma

and a refined age model between 1.2-2.4 Ma (Figure 2.3). Kender et al. (in review) measured $\delta^{18}\text{O}_b$ at a temporal resolution of ~ 250 years between ~ 0.84 -1.02 Ma, to refine the previous age model across this climatically important time period (Figure 2.3). The $\delta^{18}\text{O}_b$ stratigraphy at Site U1343 is consistent with the biostratigraphy, with 19 out of 21 biostratigraphic datum events (Takahashi et al., 2011, Teraishi et al., 2016) agreeing with the $\delta^{18}\text{O}_b$ stratigraphy published in Asahi et al. (2016). The age model reveals very high sedimentation rates of 26 cm ka^{-1} in the uppermost 400 m CCSF-A and 56 cm ka^{-1} in the remaining 350 m CCSF-A (Expedition 323 Scientists 2010). Spectral analysis of the $\delta^{18}\text{O}_b$ record at Site U1343 indicates a change in the glacial/interglacial (G/IG) frequency from 41-ka to 100-ka associated with the Mid-Pleistocene transition (MPT) (Asahi et al., 2016). The 100-ka power first emerges at 1.2 ka but does not become dominant until 0.7 Ma (Asahi et al., 2016).

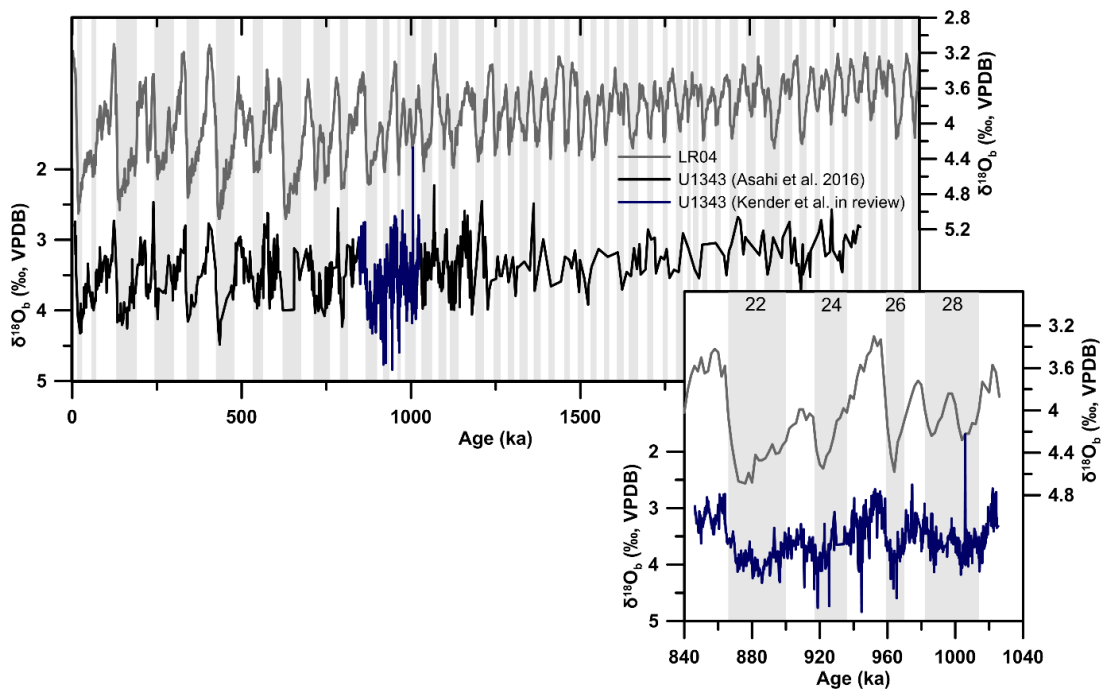


Figure 2.3 Benthic foraminiferal oxygen isotopes ($\delta^{18}\text{O}_b$) at IODP Site U1343 in black (Asahi et al., 2016) and in blue (Kender et al., in review) together with the global $\delta^{18}\text{O}_b$ stack (LR04) (Lisiecki and Raymo, 2005). The box in the bottom right corner shows the Kender et al. (in review) (blue) together with the LR04 stack (grey) (Lisiecki and Raymo, 2005). Grey vertical bars represent glacial intervals. The numbers at the top represent marine isotope stages (MIS). MIS boundaries from Lisiecki and Raymo (2005).

2.3 Methodology

2.3.1 Sediment processing for inorganic geochemical analyses

In total 336 samples (2-3 cc) were processed for inorganic geochemical analyses, with $n = 115$ for the final Mg/Ca bottom water temperature (BWT) record and $n = 140$ for benthic U/Mn and $n = 47$ for planktonic U/Mn and $n = 6$ for planktonic U/Ca. The samples were weighed and wet-sieved over a $63 \mu\text{m}$ sieve. The fraction $<63 \mu\text{m}$ was left to settle, siphoned off, dried, weighed, and archived. The fraction $>63 \mu\text{m}$ was dried in the oven over night at $40 \text{ }^\circ\text{C}$. Subsequently the coarse fraction was weighed and dry-sieved using narrow size fraction intervals. Foraminifera were picked from the size fractions $>250 \mu\text{m}$ and $150\text{-}250 \mu\text{m}$.

2.3.2 Sediment processing for organic geochemical analyses

In total 157 samples were processed for biomarker analyses with 1-2 cc of wet sediment per sample. The sediment was freeze dried at -45°C and 0.2 mbar for 48 hours using a Thermo Savant Modulyo D freeze drier and an Edwards K4 Modulyo freeze drier at Plymouth and Cardiff University, respectively. After freeze drying samples were homogenized using a Dichloromethane (DCM)-cleaned agate pestle and mortar and 3 g of sediment was weighed into 7 ml glass vials with aluminium-lined polypropylene screw caps for biomarker extraction.

2.3.3 Sea ice and phytoplankton biomarkers for sea ice reconstruction

Resulting from its transient nature, accurately reconstructing past sea ice dynamics is challenging. In recent years a source-specific biomarker produced by sea ice diatoms has received recurrent attention. IP₂₅ (Ice Proxy with 25 carbon atoms) (Belt et al., 2007), a mono-unsaturated highly branched isoprenoid (HBI) alkene produced by certain sea ice diatoms (Brown et al., 2011a, Brown et al., 2014), provides proxy evidence for past seasonal sea ice in the Arctic and subarctic realm. The sea ice diatoms grow in brine channels at the bottom surface of seasonal sea ice, with a maximum of IP₂₅ concentrations observed during spring, coinciding with the ice algal bloom (Brown et al., 2011a). Sedimentary IP₂₅ abundance has been shown to reflect variations in the spring sea ice extent as determined from surface sediment studies in comparison to satellite derived sea ice variability (Müller et al., 2009, Xiao et al., 2013, Méheust et al., 2013, Stoyanova et al., 2013, Navarro-Rodriguez et al., 2013, Müller

and Stein, 2014, Xiao et al., 2015, Smik et al., 2016). Further, IP₂₅ has been readily identified in sediments from the northern Bering Sea shelf, characterised by a seasonal sea ice cover (Méheust et al., 2013), whereas IP₂₅ is absent in sediments along the eastern Bering Sea slope (Méheust et al., 2013), south of the modern maximum sea ice extent, suggesting accurate representation of Bering Sea sea ice dynamics.

However, IP₂₅ alone does not provide a robust measure of sea ice dynamics, resulting from absent IP₂₅ observed under both ice free and perennial sea ice conditions (Belt and Müller, 2013). Hence, further proxies and or a combination with other biomarkers is needed to distinguish between these two extreme scenarios in sea ice extent. Additionally, caveats, such as lateral transport, degradation of IP₂₅ within the sediments, and changes in the sea ice diatom ecosystem structure could affect sedimentary IP₂₅ concentrations (Belt and Müller, 2013). However, further research is needed to fully constrain these influences.

Traditionally, semi-quantitative reconstructions of seasonal sea ice extent are based on the combination of IP₂₅ with phytoplankton biomarkers (PIP₂₅), such as dinosterol and brassicasterol, found in year-round ice free settings (Equation 2.2) (Müller et al., 2011). Recent studies, suggest calculating the PIP₂₅ index by combining IP₂₅ with a tri-unsaturated HBI (HBI III) (Smik et al., 2016), produced by diatoms characteristic of the spring bloom within the marginal ice zone (MIZ) (Belt et al., 2015), which provides a better correlation of satellite-derived sea ice conditions and biomarker-based sea ice reconstructions from surface sediments.

$$PIP_{25} = IP_{25} / (IP_{25} + (\text{Phytoplankton marker} * c)) \quad (\text{Equation 2.2})$$

$$c = \text{mean } IP_{25} \text{ concentration} / \text{mean phytoplankton marker concentration}$$

The calculation of PIP₂₅, however, includes a balance term (c-factor) needed to account for significant differences in the sedimentary concentrations of IP₂₅ and the applied phytoplankton biomarker (Müller et al., 2011, Smik et al., 2016). The c-factor can be calculated from the downcore data, or from a regional surface sediment calibration (Müller et al., 2011, Belt and Müller, 2013). Thus, the c-factor may vary based on the core section studied, significantly altering the interpretations of past sea ice dynamics.

Other approaches to determine past sea ice dynamics include the combination of IP₂₅ with productivity proxies. Extended seasonal sea ice is thought to reduce primary productivity, by limiting the light availability for phytoplankton growth. Hence, reduced IP₂₅ concentrations in combination with reduced primary productivity likely point towards extended/perennial sea ice, whereas reduced IP₂₅ together with high primary productivity is more characteristic of ice free conditions. Potential caveats, however, include other parameters besides sea ice significantly influencing the local primary productivity. Méheust et al. (2016) use threshold values of IP₂₅ and biogenic opal concentrations to distinguish ice free, extended, and seasonal sea ice cover in the western Bering Sea across the last ~18 ka. This indicates that a combinatory approach of IP₂₅ with primary productivity proxies may provide valuable insights with respect to sea ice dynamics in the Bering Sea.

2.3.4 Foraminiferal authigenic U/Mn for sedimentary redox conditions

In the modern ocean, uranium has a concentration of 13-14 nmol kg⁻¹ (McManus et al., 2005) and acts conservatively with a residence time of >400 ka (Boiteau et al., 2012). It forms highly soluble U⁶⁺ carbonate complexes under oxic conditions, whilst under anoxic conditions soluble U⁶⁺ is removed from the pore water and precipitated as U⁴⁺ (Boiteau et al., 2012). Thus, the bulk sedimentary content of authigenic uranium has been proposed as a proxy for sedimentary redox conditions in the past, related to changes in the oxygenation of overlying bottom waters and the remineralization of organic carbon in the sediments (Calvert and Pedersen, 1993, Rosenthal et al., 1995, Morford and Emerson, 1999, Morford et al., 2007). A novel approach using authigenic uranium in foraminiferal coatings was developed by Boiteau et al. (2012). Both planktonic and benthic foraminiferal tests act as a low uranium substrate (3-23 nmol mol⁻¹) (Russell et al., 2004, Raitzsch et al., 2011, Boiteau et al., 2012, Chen et al., 2017) in reducing sediments and can accumulate authigenic uranium. As the ionic radius of U⁴⁺ is similar to that of Ca²⁺ cations, U⁴⁺ can be readily incorporated into authigenic carbonates forming in the sediment during early diagenesis (Sturchio et al. 1998, Zhao et al. 2016). The accumulation of authigenic uranium in sediments has been shown to be sensitive to re-oxidation ('burn-down') if previously anoxic sediments are re-exposed to oxygen, for example following a drastic decrease in the sedimentation rates, an increase in bottom water [O₂], and/or a decrease in the organic carbon flux (Crusius and Thomson, 2000, Zheng et al., 2002, McManus et al., 2005).

Considering the high sedimentation rates at Site U1343 ($34 \pm 11 \text{ cm ka}^{-1}$ (Asahi et al., 2016)) the influence of re-oxidation effects on precipitated uranium is likely to be insignificant for the interpretation of U/Ca and U/Mn ratios.

Building on the approach outlined in Boiteau et al. (2012), Gottschalk et al. (2016) proposed to normalise authigenic foraminiferal uranium to manganese (U/Mn) rather than calcium (U/Ca), to avoid species-specific differences based on the test surface-to-mass ratio. Manganese precipitates as Mn^{4+} in sediments under oxic conditions in form of Mn-oxides or Mn-carbonates and is re-dissolved into pore waters as Mn^{2+} under reducing conditions (Froelich et al., 1979). The dissolved Mn^{2+} either migrates upwards until it reaches the depth of oxygen penetration where it re-precipitates or is removed from pore waters by the formation of diagenetic carbonates (Froelich et al., 1979, Pedersen and Price, 1982). Primary foraminiferal carbonate is typically low in Mn $< 100 \mu\text{mol mol}^{-1}$ (Boyle, 1983, Barker et al., 2003), however, several studies report increased foraminiferal Mn concentrations in conjunction with prominent diagenetic alterations (Pena et al., 2005, Hasenfratz et al., 2017a), suggesting the incorporation of Mn into authigenic mineral phases. Hence, normalisation of authigenic uranium to manganese is independent of the test matrix variations, reducing the species-specific variability (Gottschalk et al., 2016, Chen et al., 2017). Applied studies demonstrate that authigenic U/Mn sensibly tracks sedimentary redox changes, linked to the oxygenation of overlying bottom waters (Gottschalk et al., 2016, Chen et al., 2017).

Recent studies have shown that chemical cleaning of foraminifera, can remove authigenic foraminiferal coatings, of interest for studies of authigenic U/Mn (Boiteau et al., 2012, Chen et al., 2017). Thus, a chemical cleaning test is needed to determine the appropriate procedures.

2.3.5 Benthic foraminiferal Mg/Ca for bottom water temperatures

Mg is a conservative element in seawater, with relatively constant oceanic Mg/Ca ratios on timescales of $\sim 1 \text{ Ma}$ (Li, 1982, Evans and Müller, 2012). Mg^{2+} is among the various positive divalent ions that can substitute for Ca^{2+} in CaCO_3 . At equilibrium this substitution is endothermic, suggesting a higher incorporation of Mg^{2+} into CaCO_3 at increased temperatures. In line with inorganic CaCO_3 experiments (Katz, 1973, Mucci, 1987, Oomori et al., 1987), biologically precipitated CaCO_3 , such as the tests

of planktonic and benthic foraminifera, demonstrates an increase in Mg/Ca in correlation with the ambient temperature at calcification (Nürnberg et al., 1996, Rosenthal et al., 1997, Lea et al., 1999). Early laboratory culturing experiments of planktonic foraminifera, however, showed that foraminiferal calcite is undersaturated with respect to seawater Mg^{2+} , suggesting a lower partition coefficient of Mg for biologically compared to inorganically precipitated calcite (Nürnberg et al., 1996). Thus, the incorporation of Mg into biologically precipitated calcite is different from the reaction kinetics of precipitation of inorganic calcite. Mg uptake into foraminiferal calcite is likely controlled by temperature-dependent physiological processes (Nürnberg et al., 1996). This highlights the importance of vital effects on Mg^{2+} incorporation into foraminiferal carbonate, emphasizing the need for species-specific Mg/Ca-temperature calibrations.

Compared to Mg/Ca paleothermometry on planktonic foraminifera, the use of benthic foraminifera has been developed more recently and the respective processes of Mg uptake are less constrained. Sensitivities of 10-11 % per 1 °C (*Cibicidoides pachyderma*) (Rosenthal et al., 1997, Lear et al., 2002), ~6 % per 1 °C (*Uvigerina* spp.) (Lear et al., 2002), and 11 % per 1 °C (*Oridorsalis umbonatus*) (Lear et al., 2002) have been proposed for different benthic foraminiferal species.

In addition to species-specific vital effects, secondary effects on the incorporation of Mg^{2+} into foraminiferal calcite have been reported for the $pH/\Delta[CO_3^{2-}]$, salinity, and the Mg/Ca composition of seawater (Rosenthal et al., 1997, Elderfield et al., 2006, Rosenthal et al., 2006, Yu and Elderfield, 2008, Hasiuk and Lohmann, 2010, Elderfield et al., 2010, Dissard et al., 2010, Evans and Müller, 2012, Geerken et al., 2018). A potential salinity effect on benthic foraminiferal Mg/Ca, however, has only been determined for one species, *Ammonia tepida* characteristic of brackish waters, suggesting increased Mg incorporation at higher salinities, proposed to bias paleotemperature reconstructions by 1 °C per 2 practical salinity unit (psu) (Dissard et al., 2010, Geerken et al., 2018).

Furthermore, several post-depositional processes, such as dissolution, recrystallization, authigenic mineral precipitation, and contamination with silicate minerals can alter the primary Mg/Ca ratio of foraminiferal tests and introduce bias to the temperature reconstruction (Rosenthal et al., 2000, Barker et al., 2003, Pena et al.,

2005, Edgar et al., 2013, Edgar et al., 2015, Schneider et al., 2017, Panieri et al., 2017, Hasenfratz et al., 2017a). To address some of these post-depositional effects different chemical cleaning procedures have been developed, aiming to remove silicate contamination, remnant organic matter, and oxide coatings (Boyle, 1983, Boyle and Keigwin, 1985, Barker et al., 2003).

2.3.6 Secondary effects on foraminiferal Mg/Ca values

2.3.6.1 Post-mortem alterations of foraminiferal tests during early diagenesis

Reconstructing past climate using foraminifera relies on the assumption that foraminifera calcify in equilibrium with the surrounding seawater and that the geochemical integrity of calcareous tests is preserved in the sediments for thousands to millions of years. Detailed studies of the microstructure and geochemistry of fossil foraminifera tests, increasingly reveal diagenetic alteration, as a result of dissolution, recrystallization, or precipitation of authigenic mineral phases (Rosenthal et al., 2000, Barker et al., 2003, Pena et al., 2005, Sexton et al., 2006, Sexton and Wilson, 2009, Edgar et al., 2013, Edgar et al., 2015, Schneider et al., 2017, Panieri et al., 2017, Hasenfratz et al., 2017a). Post-mortem interactions with the sea or pore water can alter or reset the geochemistry of the foraminiferal calcite (Pearson et al., 2001, Edgar et al., 2013, Edgar et al., 2015). Partial dissolution of test material, for example, can lead to preferential loss of trace elements, such as Mg, Cd, Ba, and Sr (Murray, 1989, McCorkle et al., 1995, Brown and Elderfield, 1996, Edgar et al., 2013), whereas authigenic overgrowth can lead to contamination and bias in the trace metal record and shifts in the isotopic signal (Millo et al., 2005, Pena et al., 2005, Hasenfratz et al., 2017a, Schneider et al., 2017, Panieri et al., 2017). The influence of recrystallization on foraminiferal isotope and trace metal values depends on the mode of the sediment-pore water system (open versus closed system), the lithology, the burial history/sedimentation rates, and the original habitat of the life foraminifera (Sexton and Wilson, 2009, Edgar et al., 2013).

Whereas diagenetic alteration of planktonic foraminiferal calcite has received recurrent attention over the past decade (Norris and Wilson, 1998, Pearson et al., 2001, Wilson and Norris, 2001, Pena et al., 2005, Edgar et al., 2013, Edgar et al., 2015),

benthic foraminiferal calcite is often assumed to be less impacted by diagenesis. This is likely a result of the greater robustness of the more heavily calcified benthic foraminiferal tests and the supposedly smaller effect of recrystallization on benthic foraminifera, as it proceeds in pore waters with similar temperatures and chemical composition to the habitat experienced during the life of the organism.

Whilst recrystallization of Oligocene benthic foraminifera has been shown to only marginally influence the oxygen and carbon isotope values (Edgar et al., 2013), benthic foraminiferal trace metal ratios can be severely impacted by authigenic overgrowth (Hasenfratz et al., 2017a, Schneider et al., 2017, Panieri et al., 2017). Hasenfratz et al. (2017a) studied benthic and planktonic foraminifera from the Southern Ocean, where large shifts in the oxygenation of bottom waters are expected on G/IG timescales resulting from changes in the ventilation of deep waters and biological productivity. They find a distinct overgrowth on the inner surface of foraminiferal tests, enriched in Mn (Hasenfratz et al., 2017a). Mn-rich coatings, most likely Mn-rich carbonates, form following the formation of reductive microenvironments within the foraminiferal tests (Hasenfratz et al., 2017a), able to bias foraminiferal trace metal ratios. Specifically, Hasenfratz et al. (2017a) demonstrate increased Mg/Ca ratios in foraminifera with Mn-rich carbonate overgrowth.

Further, microbial activity in sediments underlying high productivity areas has been shown to fundamentally alter the pore water geochemistry, which can lead to authigenic carbonate formation. Panieri et al. (2017) and Schneider et al. (2017) investigated the influence of microbial reactions within the Sulphate-Methane Transition Zone (SMTZ) on foraminiferal Mg/Ca and isotope ratios. They find characteristically low carbon isotope ($\delta^{13}\text{C}$) ratios in authigenic carbonates, resulting from carbon released during the remineralisation of organic matter and/or methane-derived carbon (Schneider et al., 2017, Panieri et al., 2017). Additionally, increased Mg concentrations are observed in foraminifera with authigenic carbonate contamination (Schneider et al., 2017, Panieri et al., 2017).

Thus, a lot of progress has been made in recent years to understand the influence of early diagenesis on foraminiferal isotope and Mg/Ca ratios. However, a detailed understanding of the trace metal composition and formation mechanisms of authigenic

carbonates is still missing. Abundant, authigenic carbonates in the sediments of IODP Site U1343, co-occurring with discoloured foraminiferal specimens (Expedition 323 Scientists 2010), indicate the need to study the implications of authigenic carbonate formation for paleoenvironmental studies at this Site.

2.3.6.2 Seawater Mg/Ca variations across the Pleistocene

Recent studies demonstrate that secular changes in seawater Mg/Ca ratios over time may influence the incorporation of Mg into foraminiferal calcite (Fantle and DePaolo, 2006, Medina-Elizalde et al., 2008, Evans and Müller, 2012). Both, Mg and Ca have a relatively long residence time in seawater of 12 million years (Ma) and 1 Ma, respectively (Li, 1982). Mg and Ca are supplied to the ocean by rivers, where the supply depends on the strength of continental weathering and the composition of the weathered rocks (Billups and Schrag, 2002). The major sink for Mg in the oceans is hydrothermal alteration of newly formed oceanic crust at Mid-Ocean Ridges (Billups and Schrag, 2002). Other sinks include ion exchange reactions with clay, low-temperature alteration of basalts, and carbonate deposition, which is also the only sink for Ca in the ocean (Billups and Schrag, 2002). This indicates, that the Mg/Ca ratio of seawater has likely varied in the past on timescales longer than ~1 Ma (Medina-Elizalde et al., 2008, Evans and Müller, 2012).

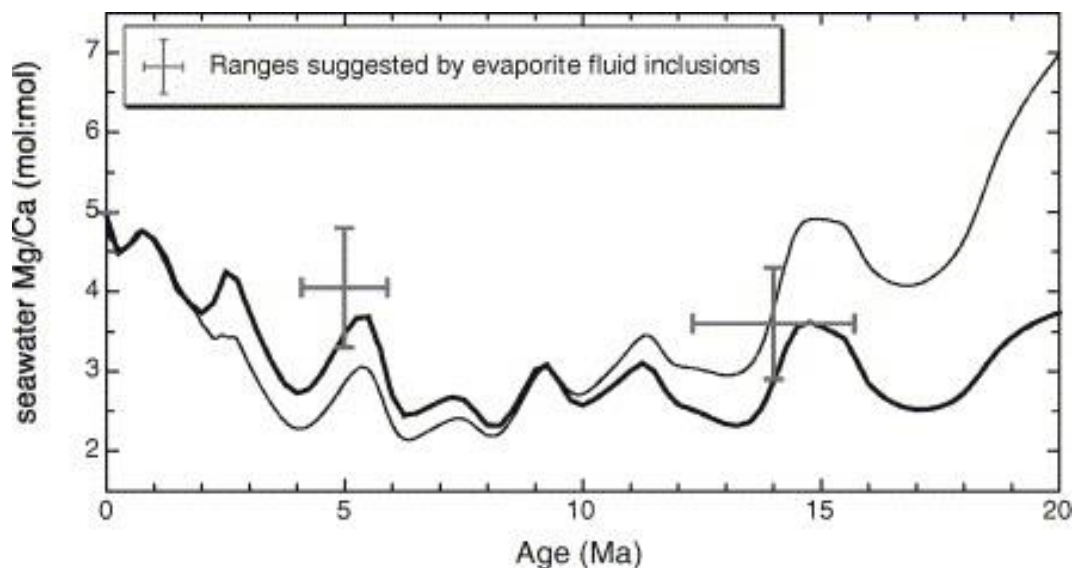


Figure 2.4 Seawater Mg/Ca variability over the last 20 million years (Ma) based on evaporite fluid inclusions (Lowenstein et al., 2001, Horita et al., 2002) and numerical modelling studies (Fantle and DePaolo, 2005, Fantle and DePaolo, 2006). Figure from (Fantle and DePaolo, 2006).

A modelling study by Fantle and DePaolo (2006) demonstrates a change in seawater Mg/Ca over the past ~2 Ma of $\sim 1 \text{ mol mol}^{-1}$, with potential implications for Pleistocene reconstructions of foraminiferal Mg/Ca ratios (Figure 2.4). However, most studies examining Pleistocene temperature variability based on foraminiferal Mg/Ca do not take Mg/Ca seawater variability into account, whereas it becomes more important for studies further back in time such as the Pliocene or the Neogene/Paleogene.

2.3.6.3 The effect of the carbonate saturation state on foraminiferal Mg/Ca values

The concentration of carbonate ions ($[\text{CO}_3^{2-}]$) in seawater has been shown to influence the incorporation of Mg into biologically precipitated calcium carbonate (Rosenthal et al., 1997, Elderfield et al., 2006, Rosenthal et al., 2006, Yu and Elderfield, 2008, Elderfield et al., 2010). Martin et al. (2002) first noted that abyssal Mg/Ca ratios of the epifaunal foraminifera species *Cibicidoides wuellerstorfi* from temperatures $<3 \text{ }^\circ\text{C}$ fall on a steeper slope than predicted by the global temperature calibration for this species, indicating the influence of the $\Delta[\text{CO}_3^{2-}]$ on Mg/Ca values of *C. wuellerstorfi*. BWT changes in abyssal waters are comparably small, thus the effect of $\Delta[\text{CO}_3^{2-}]$ on foraminiferal Mg/Ca ratios is proportionally enhanced (Elderfield et al., 2006). Comparison studies of Rose Bengal stained living specimens of *C. wuellerstorfi* and the post-mortem assemblage confirmed that $\Delta[\text{CO}_3^{2-}]$ affects Mg incorporation into the foraminiferal calcite, rather than influencing Mg/Ca ratios via post-mortem dissolution (Elderfield et al., 2006). Empirical quantification of the carbonate ion effect on Mg/Ca ratios in *C. wuellerstorfi* and *Cibicidoides mundulus* yields values of $0.0087 \pm 0.0007 \text{ mmol mol}^{-1} \mu\text{mol}^{-1} \text{ kg}^{-1}$ and $0.017 \text{ mmol mol}^{-1} \mu\text{mol}^{-1} \text{ kg}^{-1}$, respectively (Elderfield et al., 2006, Raitzsch et al., 2008). This indicates that there may be subtle differences in the $\Delta[\text{CO}_3^{2-}]$ sensitivity of different species as a result of vital effects and/or microhabitat preferences. Elderfield et al. (2010) demonstrate no or only a very small $\Delta[\text{CO}_3^{2-}]$ effect on Mg/Ca ratios of shallow infaunal *Uvigerina* spp., as pore waters come to rapid equilibrium with calcium carbonate. This suggests that the use of infaunal benthic foraminifera for Mg/Ca is favourable as the $\Delta[\text{CO}_3^{2-}]$ effect is reduced in pore waters compared to bottom waters. However, due to

differences in the habitat depth and migration within the sediment site/species specific variations might occur.

2.3.7 The effect of different chemical cleaning techniques on foraminiferal trace metal ratios

Abundant authigenic carbonate crystals in sediments of IODP Site U1343 co-occurring with discoloured foraminiferal specimens, suggest the presence of authigenic foraminiferal carbonate contaminant phases (Expedition 323 Scientists 2010). Hence, a cleaning study was conducted to assess the impact of different chemical cleaning techniques on foraminiferal trace metal ratios.

There are two frequently used cleaning protocols, the Cd-cleaning (Boyle, 1983, Boyle and Keigwin, 1985) and the Mg-cleaning protocol (Barker et al., 2003). Each cleaning protocol comprising of several steps, including: (i) a clay removal step with repeated rinses in UHQ water and methanol with intervals of ultrasonication, to remove adhered clay particles (ii) an oxidative step in a hot solution of alkali (0.1 M NaOH) buffered 1% H₂O₂ to remove organic material and (iii) one dilute acid leach in 0.001 M HNO₃ to remove remaining contaminants adsorbed to the surface of the foraminifera fragments. The Cd-protocol additionally includes a reductive treatment, prior to the oxidative step, aimed to remove Mn-Fe-oxides. Performed in a hot solution of 1200 µl hydrous hydrazine in a citric acid (10 mL)/ammonia (10 mL) buffer for 30 minutes, including several intervals of short (~5 seconds) ultrasonication followed by extensive rinsing with UHQ water and a sample transfer to fresh acid-cleaned micro-centrifuge tubes.

Recently, partial dissolution of foraminiferal shell material has been reported during the reductive step, most likely as a result of chelate complex formation of the metal cations with the citric acid, reducing the primary foraminiferal Mg/Ca ratio by up to 10 % (Barker et al., 2003, Yu et al., 2007). Pena et al. (2005), on the other hand, demonstrate that Mn-rich authigenic carbonates from samples in the Panama basin could only be removed by the addition of the reductive step. This could be associated with the structure of the authigenic carbonate, making it more prone to dissolution and/or the removal of Mn-Fe oxides in between the authigenic carbonate crust and the foraminiferal test wall (Pena et al., 2005). Thus, careful examination of foraminiferal test contamination and the effects of different cleaning techniques is needed, to ensure

that the cleaning protocols are adapted to the contaminant phases present in the respective foraminifera samples.

In order to test the influence of different chemical cleaning protocols on foraminiferal Mg/Ca, Mn/Ca, U/Ca, and Sr/Ca ratios five large (>300 μg) samples (2 *E. batialis*, 3 *Uvigerina* spp.) were evenly split after the foraminiferal tests had been gently crushed between two glass plates and the fragments were homogenized. The two aliquots of each sample were treated according to the ‘Mg-cleaning’ (Barker et al., 2003) and the ‘Cd-cleaning’ (Boyle, 1983, Boyle and Keigwin, 1985) protocol, respectively.

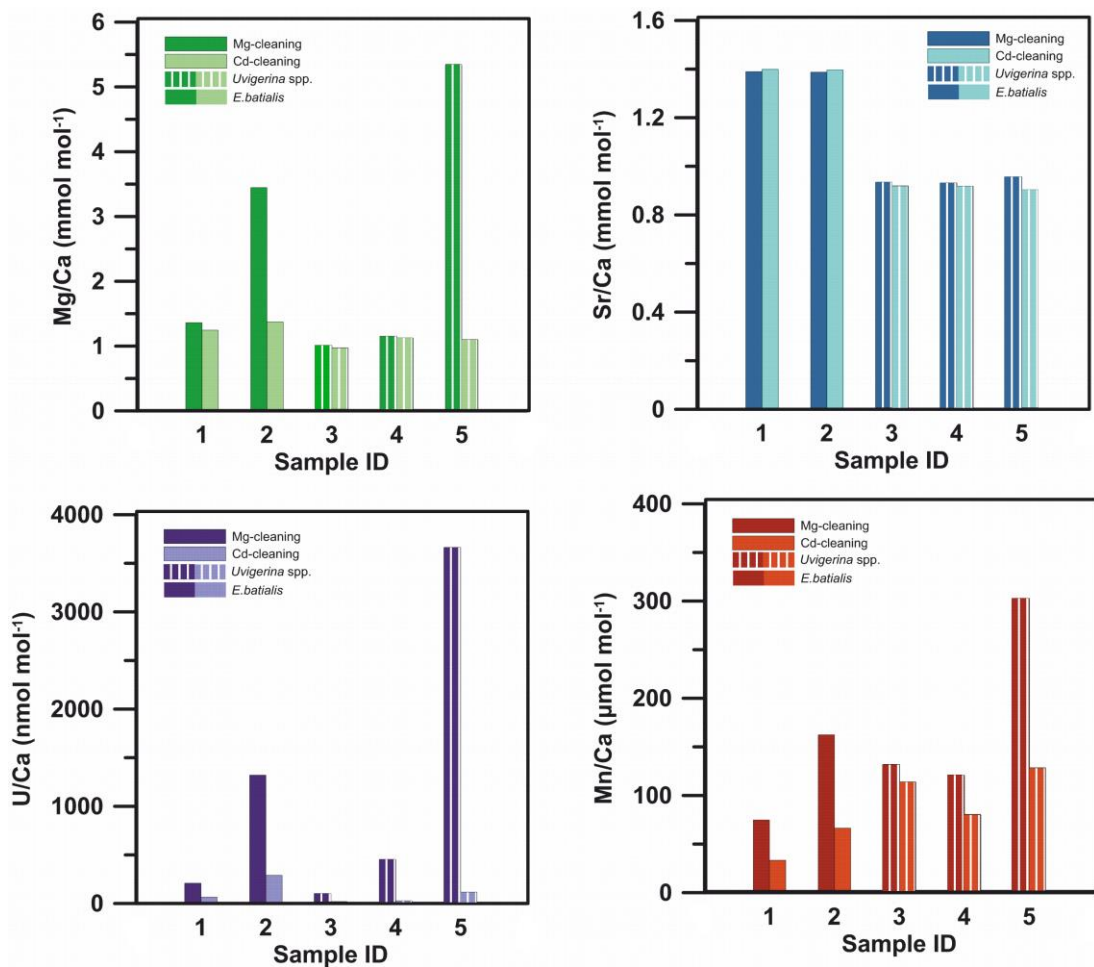


Figure 2.5 Mg/Ca (green), Sr/Ca (blue), U/Ca (purple), and Mn/Ca (red) of five samples (3 *Uvigerina* spp. (striped), 2 *E. batialis* (solid)) cleaned using the Cd-cleaning protocol (light colour) (Boyle, 1983, Boyle and Keigwin, 1985) and the Mg-cleaning protocol (dark colour) (Barker et al., 2003), respectively.

All samples cleaned using the Cd-protocol show a reduction in Mg/Ca, Mn/Ca, and U/Ca compared to the Mg-protocol (Figure 2.5). The change in Sr/Ca between the

cleaning protocols is inconsistent (Figure 2.5), in support of previous studies demonstrating no influence of the reductive treatment on Sr/Ca ratios (Barker et al., 2003, Yu et al., 2007). Three samples (sample ID 1, 3, and 4) show a Mg/Ca reduction <10 % between the aliquot cleaned using the Mg-protocol and the Cd-protocol (Figure 2.5). Barker et al. (2003) demonstrate that a reduction in Mg/Ca of up to 10 % can result from dissolution of the primary test calcite during the reductive step. If this was the case, U/Ca and Mn/Ca ratios typical of primary foraminiferal calcite (<23 nmol mol⁻¹ and <100 μmol mol⁻¹, respectively (Barker et al., 2003, Chen et al., 2017)) would be expected for both aliquots of each sample. U/Ca ratios of the samples with <10 % reduction in Mg/Ca vary between 99-449 nmol mol⁻¹ after the Mg-cleaning, and between 17-64 nmol mol⁻¹ after the Cd-cleaning (Figure 2.5), indicating a reduction of 69-94 % between cleaning techniques. The same is true for Mn/Ca ratios, ranging between 75-300 μmol mol⁻¹ and 33-128 μmol mol⁻¹ after the Mg- and Cd-cleaning, respectively (Figure 2.5), suggesting a reduction of 13-55 % between cleaning protocols. Removal of large amounts of U and Mn, together with a small reduction in Mg/Ca, suggests either the presence of an additional non-calcareous high-U and Mn, but low-Mg, contamination phase, preferential leaching of U and Mn during the reductive treatment, or variable amounts of Mg in the authigenic carbonate phase.

A commonly reported non-calcareous contamination phase are Mn-Fe-oxides, with Mg/Mn and U/Mn values of around 0.2 ± 0.03 mol mol⁻¹ (De Lange et al., 1992, Pattan, 1993) and 0.01 ± 0.008 mmol mol⁻¹ (Kunzendorf et al., 1983, Lugovskaya et al., 2007), respectively. Assuming that all the reduction in Mn between the Mg- and Cd-cleaning is a result of Mn-Fe-oxide removal, a decrease in Mg/Ca for all five samples of 0.004-0.035 mmol mol⁻¹ and 0.18-1.75 nmol mol⁻¹ in U/Ca would be expected, much smaller than the observed reduction of 0.03-4.2 mmol mol⁻¹ for Mg/Ca and 81-3545 nmol mol⁻¹ for U/Ca (Figure 2.6). Thus, even though a contribution of Mn-Fe-oxides to the reduction in the metal/Ca values cannot be ruled out, it does not act as a main non-calcareous high-U and Mn/low-Mg contamination phase. Another possibility is the preferential leaching of U and Mn compared to Mg, from the primary/authigenic foraminiferal calcite during reductive cleaning. However, this does not explain the differences in Mg-reduction observed in the five samples analysed. Further, Yu et al. (2007) demonstrate that partial dissolution of foraminiferal tests during reductive cleaning is most likely caused by the formation of chelate-complexes

of the metal cations with citric acid. Thus, selective leaching of metals is highly unlikely, as these metals are uniformly distributed within the calcite shell, and solid diffusion rates are slow at low temperatures (Yu et al., 2007). In conclusion, the different patterns in element/Ca reduction between the Mg- and Cd-cleaning protocols are most likely related to varying Mg contents in the authigenic carbonate contaminants.

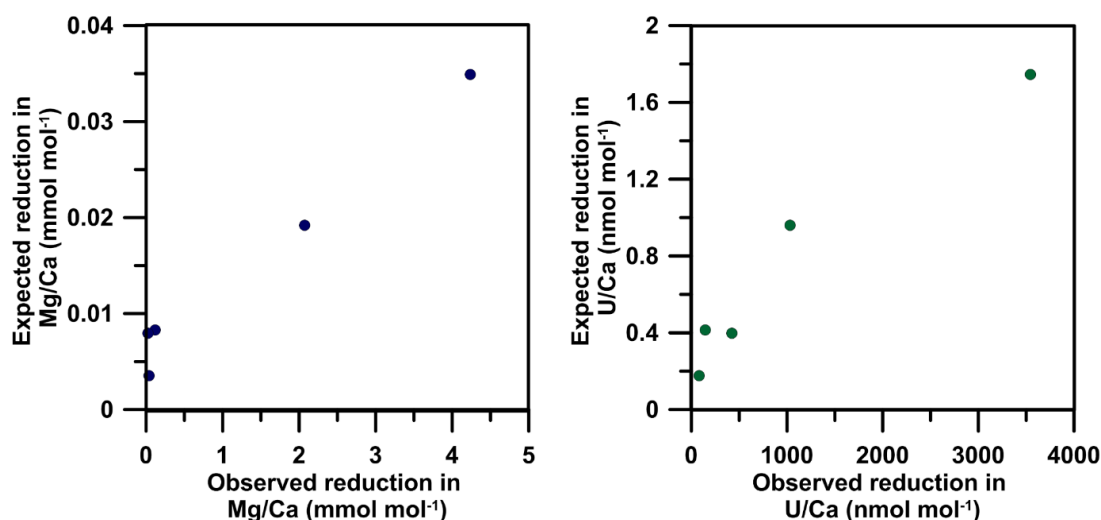


Figure 2.6 Observed versus expected reduction in Mg/Ca (left) and U/Ca (right) if all the authigenic contamination at Site U1343 was a result of Mn-Fe-oxide coatings with Mg/Mn and U/Mn values of around $0.2 \pm 0.03 \text{ mol mol}^{-1}$ (De Lange et al., 1992, Pattan, 1993) and $0.01 \pm 0.008 \text{ mmol mol}^{-1}$ (Kunzendorf et al., 1983, Lugovskaya et al., 2007), respectively.

Even though minor dissolution of primary foraminiferal calcite cannot be ruled out, all in all, the cleaning study supports the presence of a Mg, U, Mn, and Sr-rich authigenic carbonate phase. Further, the Cd-cleaning protocol is more successful at removing the authigenic carbonates, compared to the Mg-cleaning protocol. However, even reductively cleaned U/Ca ratios are still elevated compared to reported U/Ca ratios of primary foraminiferal calcite (up to 23 nmol mol^{-1} (Russell et al., 2004, Raitzsch et al., 2011, Boiteau et al., 2012, Chen et al., 2017)), indicating that some contamination might still be present.

2.3.8 Dysoxic foraminiferal assemblage counts

The ecology of calcareous benthic foraminifera has long been used as a powerful tool to qualitatively reconstruct past environmental conditions at the seafloor (Corliss,

1985, Jorissen et al., 1995, Jorissen et al., 2007, Bubenshchikova et al., 2010, Ovsepyan et al., 2013, McKay et al., 2016, Ovsepyan et al., 2017). This is related to the microhabitat preferences of species, where the relative abundance correlates with the optimum in living conditions (Jorissen et al., 2007). In particular, benthic foraminiferal faunal assemblages can provide insights into oxygenation, organic carbon export, and deep water mass changes (Jorissen et al., 2007). The benthic habitat has been divided into epifaunal, living at or very close to the sediment-water interface, and infaunal, living below the sediment-water interface, with the oxygen penetration depth and organic carbon flux to the seafloor exerting the primary control mechanisms on the assemblage composition (Figure 2.7) (Jorissen et al., 1995, Jorissen, 1999, Gooday and Rathburn, 1999).

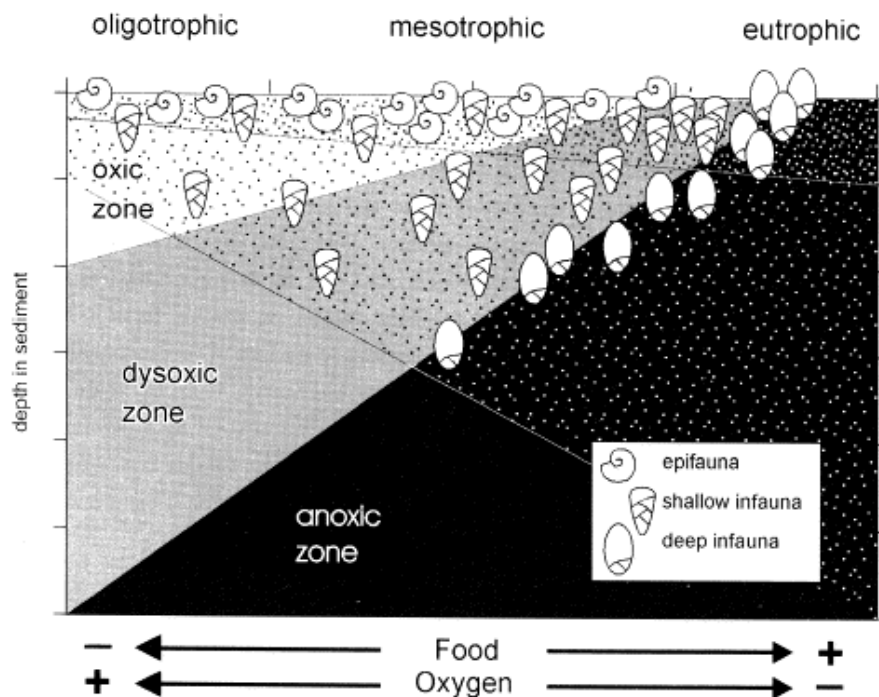


Figure 2.7 TROX (TRophic OXYgen) model for benthic foraminiferal microhabitats after (Jorissen et al., 1995). Figure from Van der Zwaan et al. (1999).

Characteristic low-oxygen foraminiferal assemblages are typically composed of deep infaunal taxa and/or epi-/infaunal taxa adapted to low oxygen conditions (Jorissen et al., 2007). However, the benthic foraminiferal assemblage responds to multiple environmental parameters, such as bottom water oxygenation and the organic carbon flux simultaneously (Gooday and Rathburn, 1999, Jorissen et al., 2007) and numerous

species classified as low-oxygen indicators also occur under high organic carbon flux (Gooday and Rathburn, 1999, Jorissen et al., 2007). Continental margins sediments, characterised by increased input of organic carbon, are typically dominated by infaunal taxa tolerant to low oxygen conditions (Gooday and Rathburn, 1999). This is also observed in sediments of the mid-depth Bering Sea, with calcareous infaunal benthic taxa tolerant to low-oxygen conditions dominating the assemblage (Khusid et al., 2006, Setoyama and Kaminski, 2015).

Typically, faunal census counts rely on a representative subset of the sample. However, the calcareous foraminifera abundance at Site U1343 is generally low (Expedition 323 Scientists 2010). Thus, all foraminifera from the 150-250 μm size fraction were picked, identified, and counted to get a representation of assemblage changes through time.

2.3.9 Statistical analyses and error propagation

Statistical analyses conducted throughout this study comprise analyses of variance and correlation, together with the identification of long-term trends. Long-term trends of downcore records were determined using ordinary least squares regression analyses.

Analyses of correlation were performed using the Pearson correlation coefficient (R^2). Where possible, the correlation of two time series was determined using PearsonT3 (Mudelsee, 2003). PearsonT3 automatically performs mean detrending and estimates the persistence time of both variables (Mudelsee, 2003). The confidence intervals (CI) of the Pearson correlation coefficient are students t CIs based on nonparametric bootstrapping (Mudelsee, 2003). However, PearsonT3 requires a minimum of 10 data points, thus correlation analyses for timeseries ($n < 10$) and non-timeseries datasets were performed in RStudio (RStudio Team, 2015). Correlations of individual foraminiferal trace metal ratios measured by laser ablation inductively coupled plasma mass spectrometry (LA-ICP-MS) (Chapter 3) were calculated using non-parametric bootstrapping where R^2 is based on random sampling ($n = 10,000$) of each elemental ratio within their respective uncertainties as represented by normal distributions. The CI reported for the bootstrapped R^2 values represent bias-corrected accelerated bootstrap CIs.

To test for a significant difference in the variance ($p < 0.05$) of two datasets a Wilcoxon-Mann-Whitney test or a two-sample t-test was performed for non-normally and normally distributed data, respectively. To test for normality the Shapiro-Wilk test was used. Analyses of variance were performed in RStudio (RStudio Team, 2015).

Gaussian error propagation was followed to propagate the analytical and procedural uncertainty of foraminiferal Mg/Ca ratios to derive an estimate for BWT uncertainty. The reported uncertainties for BWT represent standard errors (s.e.), whilst the uncertainties for foraminiferal trace metal ratios measured using LA-ICP-MS are given as standard deviations (s.d.), to represent the full spread of the data.

3. Foraminiferal diagenesis in sediments underlying high productivity areas

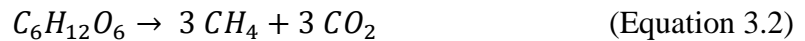
3.1 Introduction

Continental margins offer a unique opportunity to study Quaternary climate change at millennial-scale resolution, owing to high siliciclastic and organoclastic sedimentation rates. Riverine input from the nearby continents, downslope sediment transport, and high rates of primary productivity, resulting from upwelling of nutrient-rich deep waters especially along western continental margins, together with ice rafted debris (IRD) in high latitudes, constitute prized climate archives. Marine carbonates, such as the calcareous tests of planktonic and benthic foraminifera that accumulate in the sediments over time, represent valuable proxies to study both global and regional paleoceanographic changes.

Elemental and isotopic ratios in planktonic and benthic foraminifera are important and established tools in paleoceanography, used to understand past changes in marine biogeochemical cycling, hydrography, the terrestrial cryosphere, and ocean circulation (e.g. Shackleton, 1967, Nürnberg et al., 1996, Lynch-Stieglitz, 2006). Mg/Ca of benthic foraminifera, for example, is a powerful proxy to determine changes in the bottom water temperature (BWT) at any given location (e.g. Rosenthal et al., 1997, Lear et al., 2002, Elderfield et al., 2006, Lear et al., 2010). When coupled with the oxygen isotope composition of benthic foraminifera ($\delta^{18}\text{O}_b$), this allows reconstructing the evolution of continental ice volume through time, vital to understand long-term climate evolution across the Cenozoic (Zachos et al., 2001), the sensitivity of Earth's climate to external and internal forcing mechanisms (e.g. Lear et al., 2000, Billups and Schrag, 2002, Sosdian and Rosenthal, 2009, Elderfield et al., 2012), and relative sea level changes through time (e.g. Lea et al., 2002, Sosdian and Rosenthal, 2009, Elderfield et al., 2012, Shakun et al., 2015). Accurate knowledge of post-mortem alterations in foraminiferal geochemistry is hence crucial for the application of these tools, our understanding of past climate change, and the reconstruction of an array of environmental changes in Earth's history.

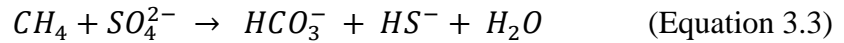
However, continental margin archives often remain untapped for paleoclimate reconstructions, because abundant reservoirs of hydrocarbons, specifically methane, in active and passive continental margin sediments alter the geochemistry of calcareous microfossils (Panieri et al., 2017, Schneider et al., 2017, Wan et al., 2018). Methane in continental margin sediments can have a thermogenic origin or originate from microbial degradation of organic carbon (Judd et al., 2002).

Sub-seafloor carbon cycling and organic carbon remineralization are driven by an active microbial community, exploiting different metabolic pathways, leading to a staggering of reactions in the sediment column according to their metabolic efficiency (Froelich et al., 1979). Oxidic respiration, being the most efficient, takes place in the upper millimetres to meters of the sediment column, whereas the depth of oxygen depletion is a function of the supply of oxygen from the overlying bottom waters by diffusion and the amount of organic carbon exported to the seafloor (Boudreau and Jørgensen, 2001). In the suboxic zone nitrate (NO_3^-) and manganese (Mn^{3+}) are reduced, followed by iron (Fe^{3+}) and sulphate (SO_4^{2-}) reduction (Equation 3.1) (D'Hondt et al., 2002, Hong et al., 2013).



When all energetically more favourable terminal electron acceptors have been depleted, organic carbon remineralisation occurs via methanogenesis (Equation 3.2) and fermentation (Bernier, 1980). Where the upward diffusive flux of methane, caused by sediment compaction, meets the zone of sulphate reduction a Sulphate-Methane Transition Zone (SMTZ) forms and anaerobic oxidation of methane (AOM) occurs (Equation 3.3) (Boetius et al., 2000, Wehrmann et al., 2011). The depth of the SMTZ is variable and depends primarily on the flux of methane from below, which in turn is driven by the availability of labile organic matter for methanogenesis and/or the supply of methane of thermogenic origin (Gaurav et al., 2008, Wehrmann et al., 2011). Along the continental slope of the eastern Bering Sea a shallower SMTZ is found in sediments underlying the mid-depth oxygen minimum zone (OMZ), even though organic carbon accumulation rates are lower compared to other locations along the slope with a deeper SMTZ (Wehrmann et al., 2011). Persistently lower bottom water oxygen concentrations ($[\text{O}_2]$) and an associated shallow oxygen penetration depth

cause a rapid shift from oxic to anoxic remineralization of organic carbon, leaving more labile organic carbon for methanogenesis in deeper sediments (Wehrmann et al., 2011).



Both organoclastic sulphate reduction and AOM release HCO_3^- into the pore waters, increasing the alkalinity and facilitating authigenic carbonate formation. Calcareous foraminifera tests can act as a template for authigenic carbonate precipitation (Panieri et al., 2017, Schneider et al., 2017), altering the geochemistry of the foraminiferal tests, with important implications for paleoclimate reconstructions.

Most studies investigating the influence of authigenic carbonate precipitation on foraminiferal geochemistry in areas of high methane flux or even methane seepage at the seafloor have focused on the carbon isotopic composition (Hill et al., 2003, Hill et al., 2004, Cook et al., 2011, Panieri et al., 2017, Schneider et al., 2017, Wan et al., 2018). Compared to foraminiferal calcite, methane-related authigenic carbonates have a distinct isotopic signature, resulting from methane-derived ^{13}C -depleted dissolved inorganic carbon (e.g. Roberts and Aharon, 1994, Hill et al., 2003, Hill et al., 2004, Pierre and Fouquet, 2007, Pierre et al., 2016). Additionally, SMTZ-related authigenic carbonates are typically enriched in Mg (Aloisi et al., 2000, Aloisi et al., 2002, Crémière et al., 2012, Teichert et al., 2014), resulting from the effect of sulphate on carbonate precipitation, with high-Mg calcite (HMC) being favoured in sulphate-free solutions (Walter, 1986, Burton, 1993, Aloisi et al., 2002).

Recent studies of foraminiferal diagenesis in relation to SMTZ precipitation noticed elevated Mg/Ca ratios, indicating the presence of authigenic HMC on foraminifera tests (Panieri et al., 2017, Schneider et al., 2017, Wan et al., 2018). However, a detailed understanding of early diagenetic processes and their influence on the alteration of primary foraminiferal geochemistry beyond Mg/Ca awaits analysis of a full suite of elemental ratios to elucidate dynamic processes in relation to organic carbon remineralization and the formation of a SMTZ in the sediments.

Sediment cores retrieved from the eastern Bering Sea continental margin as part of International Ocean Discovery Program (IODP) Expedition 323, offer a unique opportunity to gain comprehensive insight into early diagenetic processes. Sedimentation rates of $34 \pm 11 \text{ cm ka}^{-1}$ (Asahi et al., 2016) at IODP Site U1343

(57°33.4'N, 176°49.0'W; 1953 m) (Figure 2.1), located on a topographic high off the eastern continental margin, indicate the potential to examine Quaternary climate change at a millennial to orbital resolution, in a region highly underrepresented in paleoclimate studies.

Methane in Bering Sea margin sediments is predominantly of microbial origin, related to high primary productivity in the surface ocean, also called the 'Green Belt' (Springer et al., 1996). The present day SMTZ, at Site U1343, is located at ~8 meters below seafloor (mbsf), clearly seen in pore water profiles of dissolved sulphate and methane (Figure 3.1) (Wehrmann et al., 2011). The modern burial rate of organic carbon at Site U1343 is 171 mmol m⁻² y⁻¹, similar to other continental margins characterized by upwelling and increased primary productivity (Wehrmann et al., 2011). Intense rates of organic carbon remineralization are reflected in the carbon isotope composition ($\delta^{13}\text{C}$) of dissolved inorganic carbon (DIC), decreasing throughout the zone of organoclastic sulphate reduction towards a pronounced minimum at the SMTZ (Figure 3.1) (Wehrmann et al., 2011).

Analyses of authigenic carbonate crystals in the sediments of Site U1343 revealed high- and low-Mg calcite (LMC), Fe-rich calcite, and dolomite (Pierre et al., 2016). Depending on the mode of formation diagenetic carbonates at Site U1343 have a distinctive $\delta^{13}\text{C}$ signature between 10 ‰ and -20 ‰ (Pierre et al., 2016). As a result of bicarbonate formation during sulphate reduction ($\delta^{13}\text{C}$: -22 ‰ to -26 ‰) and AOM ($\delta^{13}\text{C}$: -50 ‰ to -90 ‰) (Schrage et al., 2013), early diagenetic carbonates are typically associated with low $\delta^{13}\text{C}$ values (Pierre et al., 2016). Further, the drawdown of dissolved Ca and Mg in the upper meters of the sediment column with a minimum in pore water concentrations at the SMTZ (Figure 3.1), supports the formation of LMC and HMC authigenic phases in this zone (Wehrmann et al., 2011, Pierre et al., 2016). On the other hand, authigenic carbonate crystals, mainly Fe-rich carbonates and dolomite, which form in a deeper diagenetic zone (~260 mbsf), are enriched in ¹³C, characteristic of bicarbonate formed during silicate weathering within the sediments, promoted by CO₂ released during methanogenesis (Pierre et al., 2016). Other common diagenetic mineral phases in sediments from Site U1343 include barite and pyrite, typically precipitated during organoclastic sulphate reduction and AOM (Pierre et al., 2016).

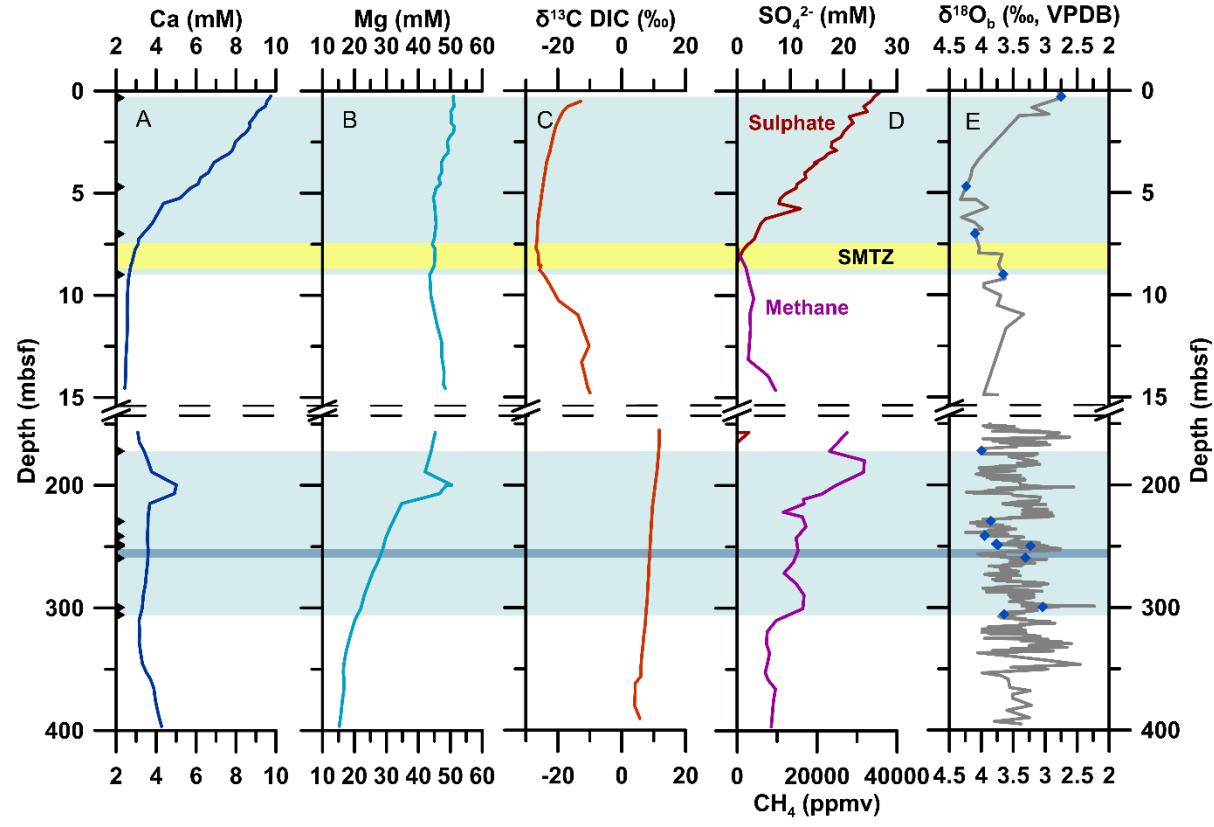


Figure 3.1 Pore water profiles of dissolved (A) Ca (blue), (B) Mg (teal), (C) $\delta^{13}\text{C}$ of dissolved inorganic carbon (DIC) (Wehrmann et al., 2011), and (D) sulphate (orange), and methane (purple) (dissolved Ca, Mg, CH_4 , and SO_4^{2-} data from LIMS (<http://web.iodp.tamu.edu/LORE/>) at IODP Site U1343 at 1953 m water depth in the eastern Bering Sea. (E) $\delta^{18}\text{O}_b$ record at Site U1343 across the LGM-Holocene (grey) (Asahi et al., 2016), together with the 5-point running mean of $\delta^{18}\text{O}_b$ across the Mid-Pleistocene (grey) (Asahi et al., 2016, Kender et al., in review) including the samples used for this study (dark blue diamonds). The blue shaded areas indicate the study intervals with the black triangles on the left indicating the respective sample depth. The light yellow shaded area demonstrates the Sulphate-Methane Transition Zone (SMTZ) and the dark blue shaded area indicates the deeper zone of authigenic carbonate formation at ~260 mbsf (Pierre et al., 2016).

Here I present the trace metal composition (Mg/Ca, Sr/Ca, Mn/Ca, Fe/Ca, U/Ca, Al/Ca) of shallow infaunal foraminiferal species *Elphidium batialis*, the most abundant benthic foraminifera at IODP Site U1343. I use a suite of single-specimen visual and geochemical evidence, including scanning electron microscope (SEM) imaging, laser ablation inductively coupled plasma mass spectrometry (LA-ICP-MS), and electron probe microanalyser (EPMA) elemental mapping, to explore the trace metal composition of both primary foraminiferal calcite and authigenic carbonates. Further, this study explores the applicability of geochemical proxies for paleoenvironmental studies in continental margin sediments characterized by abundant methane of microbial origin. Careful examination of foraminiferal tests using a range of approaches, suggests authigenic carbonate formation both above and within the SMTZ along the eastern Bering Sea margin. Whereas samples from below the SMTZ demonstrate primarily HMC contamination, dissolved sulphate in pore waters above the SMTZ, may hinder the formation of HMC, leading to LMC contamination of foraminiferal calcite. Even though abundant authigenic carbonates were found, this study suggests that after careful examination of foraminiferal tests, traditional proxies for paleoenvironmental reconstructions can be applied. Using a suite of single-specimen geochemical analyses trace metal thresholds, related to authigenic carbonate contamination, need to be established to distinguish primary versus diagenetically altered foraminiferal samples, offering a chance to reconstruct past environmental changes from largely under-utilized continental margin sediments.

3.2 Materials and methods

3.2.1 Sedimentary evidence for authigenic carbonates at IODP Site U1343

Sediments at IODP Site U1343 are primarily composed of dark/very dark greenish-grey to dark/very dark grey silt (Expedition 323 Scientists 2010). Visually lighter and more yellowish authigenic carbonate layers can be identified in all holes below 35 mbsf (Expedition 323 Scientists 2010). Compared to other Sites in the Bering Sea, carbonate concretions are less pronounced at Site U1343 (Expedition 323 Scientists 2010). High rates of sediment accumulation along the eastern Bering Sea slope (21-58 cm ka⁻¹) (Expedition 323 Scientists 2010) likely indicate that the SMTZ did not persist at a given sediment depth long enough for distinct authigenic carbonate nodules

to form (on timescales of centuries (Ussler and Paull, 2008)) (Expedition 323 Scientists 2010). Authigenic carbonate crystals comprise of rhombs, acicular and globular crystals, as identified in smear slides (Expedition 323 Scientists 2010) and are comprised of LMC, HMC, Fe-rich carbonates and dolomite (Pierre et al., 2016).

3.2.2 Sampling strategy

This study is focused on two narrow depth intervals of Holocene ($n = 4$) to Pleistocene ($n = 9$) age between 0.33-8.99 m core composite depth below seafloor (CCSF-A) and 172.02-305.63 m CCSF-A, respectively (Figure 3.1) from IODP Site U1343 to study the influence of diagenesis on benthic foraminifera buried along the continental margin of the eastern Bering Sea. The samples represent both glacial and interglacial intervals (Table 3.1, Figure 3.1), as bottom water conditions and primary productivity in the eastern Bering Sea are likely to vary on these timescales (Kim et al., 2014, Asahi et al., 2016), impacting the nature/magnitude of authigenic carbonate formation. Further, I explore diagenetic alterations in samples from above and below the SMTZ, to elucidate the influence of both organoclastic sulphate reduction and AOM on foraminiferal diagenesis. Samples from a greater sediment depth can provide information regarding a deeper zone of authigenic carbonate formation and its influence on foraminiferal geochemistry, as proposed by Pierre et al. (2016).

Based on the abundances of infaunal foraminiferal species, *Elphidium batialis* was chosen to study the effects of diagenesis on benthic foraminiferal trace metal ratios (Figure 3.2). Other abundant infaunal foraminifera include *Uvigerina* spp. and *Islandiella norcrossi* (Figure 3.2). *E. batialis* is a shallow infaunal benthic foraminifera, forming a hyaline LMC test. In the neighbouring Sea of Okhotsk *E. batialis* has a habitat depth of 0.5-1.7 cm (Bubenshchikova et al., 2008). It precipitates a test of medium size that is involute planispiral with nine to twelve chambers in the final whorl (Figure 3.2). The wall is finely perforate and the aperture appears as a peripheral arch. It has a rounded to lobulated outline and the chambers increase gradually in size (Figure 3.2). The most distinct feature are the depressed sutures with slightly backwards curved sutural bridges (Figure 3.2). The specimens for this study were picked from the two size fractions 150-250 μm and $> 250 \mu\text{m}$. Specimens $> 250 \mu\text{m}$ from Site U1343 have been previously utilized for paleoclimate reconstructions

(Asahi et al., 2016), however, overall benthic foraminiferal abundance is larger in the size fraction 150-250 μm .

Table 3.1 Sample information regarding the depth within the core, the age, the size fraction, and the general climate state for all samples utilised in this study.

Sample ID	Depth (m CCSF-A)	Age (ka)	Size fraction	Glacial (G)/ Interglacial (IG)
U1343C-1H-1 (32-34 cm)	0.3	8.5	>250 μm	IG
U1343C-1H-4 (19-21 cm)	4.7	20.8	>250 μm	G
U1343E-1H-3 (50-52 cm)	7.0	30.1	>250 μm	IG
U1343E-1H-4 (100-102 cm)	9.0	38.3	>250 μm	IG
U1343A-17H-5 (84-86 cm)	172.0	634.6	>250 μm , 150-250 μm	G
U1343E-25H-2 (132-134 cm)	229.4	877.5	>250 μm , 150-250 μm	G
U1343C-24H-7 (109-111 cm)	241.5	925.6	>250 μm	G
U1343C-25H-5 (37-39 cm)	248.2	942.6	>250 μm	IG
U1343C-25H-5 (126-128 cm)	249.1	944.9	>250 μm	IG
U1343C-25H-6(46-48 cm)	249.8	946.7	>250 μm	IG
U1343C-26H-5 (126-128 cm)	259.5	970.9	>250 μm	IG
U1343E-32H-2 (42-44 cm)	299.6	1070.1	>250 μm , 150-250 μm	IG
U1343E-32H-6 (142-144 cm)	305.6	1086.0	>250 μm	G



Figure 3.2 Images of specimens of *E. batialis*, *I. norcrossi*, and *U. bifurcata* (left to right). Images taken from Usami et al. (2017). Scale bars (white) represent 100 μm .

3.2.3 Scanning electron microscope imaging

SEM imaging was conducted on nine *E. batialis* samples, exhibiting different degrees of diagenetic alteration, as determined by reflected light microscope inspection. The samples are from above and below the SMTZ and from around 250 ± 10 m CCSF-A, to cover all stages of carbonate diagenesis at Site U1343. For each sample a whole specimen together with crushed fragments was imaged. Prior to imaging all samples were ultrasonicated in UHQ water for ~10 seconds to remove clay minerals and other particles loosely stuck to the foraminiferal tests. The specimens and fragments were then mounted on SEM stubs using carbon adhesive tape. All samples were gold/palladium coated and imaged on a FEI XL30 Field Emission Gun Environmental SEM at Cardiff University in high vacuum mode with a beam voltage of 10-20 kV using a Secondary Electron Detector.

3.2.4 Geochemical analyses

3.2.4.1 LA-ICP-MS elemental profiles and specimen means

LA-ICP-MS measurements were performed at Cardiff University using an ArF excimer 193 nm laser ablation system with dual volume laser ablation cell (RESOLUTION S-155 ASI) coupled to a Thermo Scientific™ ELEMNT XR™ magnetic sector field ICP-MS. In total 13 samples, from two depth intervals (0.33-8.99 m CCSF-A and 172.02-305.63 m CCSF-A) (Figure 3.1), were analysed with six specimens per sample and six laser spots on consecutive chambers per specimen. Based on previous work using the same instrumental setup at Cardiff University this was found to yield statistically good results when averaging over the natural and diagenetic heterogeneity of foraminiferal tests (Michael Nairn, personal communication 2018), also demonstrated in other studies (Rathmann et al., 2004). As a result of low abundance of *E. batialis* two samples only contained two and five specimens, respectively. The tests were collected from two different size fractions (150-250 μm , >250 μm) (Table 3.1) and LA-ICP-MS operating conditions varied accordingly (Table 3.2). All samples were analysed for the isotopes ^{25}Mg , ^{26}Mg , ^{27}Al , ^{43}Ca , ^{48}Ca , ^{55}Mn , ^{87}Sr , ^{88}Sr , ^{238}U with the magnetic sector field ICP-MS operating in low resolution (LR) mode, as no spectral interference was expected for these isotopes in the sample. ^{48}Ca , however, did show spectral interference with ^{48}Ti for both glass standards, the NIST SRM 610 and

NIST SRM 612 (see below), hampering quantification of this isotope. ^{56}Fe cannot be resolved in LR mode as a result of spectral interference with ArO (May and Wiedmeyer, 1998). Thus, a combination of LR and medium resolution (MR) mode was used to analyse all isotopes of interest. In total four samples from the size fraction $>250\ \mu\text{m}$ were analysed for ^{56}Fe , with two sample from above and two samples from below ~ 260 mbsf (second zone of carbonate diagenesis (Pierre et al., 2016)). For each specimen all isotopes were acquired on six consecutive chambers in LR, followed by re-ablation of each chamber in MR, allowing for direct comparison of ^{56}Fe with all other isotopes.

Table 3.2 LA-ICP-MS analytical settings for foraminifera specimens between 150-250 μm , $>250\ \mu\text{m}$ and the NIST 610/612 silicate glass reference standards.

	150-250 μm	$>250\ \mu\text{m}$	Silicate glass reference standards NIST SRM 620 and 612
Mode	Spot analysis	Spot analysis	Raster analysis
Spot size (μm)	20	30	64
Laser fluence (J cm^{-2})	2.5	3.5	4.5
Laser pulse repetition rate (Hz)	2	4	4

NIST SRM 612 and NIST SRM 610 silicate glass standards were used as consistency and quantification standards, respectively. NIST SRM 612 was acquired at the beginning and end of every sequence and calibrated using NIST SRM 610 for external reproducibility (Table 3.3). NIST SRM 612 was also used to tune the magnetic sector field ICP-MS to minimize oxide formation and elemental fractionation ($\text{ThO}/\text{Th} < 0.3\%$, $\text{Th}/\text{U} \sim 1$). NIST SRM 610 was measured every six laser ablation spots and used for sample calibration. Reference values for elemental concentrations in NIST SRM 610 and 612 are from Jochum et al. (2011). Samples were calibrated using R Studio (RStudio Team 2015) following the method outlined in Longerich et al. (1996), using ^{43}Ca as the internal standard, assuming 40 wt% for CaCO_3 . Prior to sample calibration the limit of detection was calculated ($\text{LOD} = \text{mean gas blank} + 3.3 * \text{s.d.}$, s.d. = standard deviation on the gas blank) for each isotope and spot and all values below the

LOD were removed (Petersen et al., 2018). The high gas blank for ^{55}Mn , resulting from polyatomic interference with $^{40}\text{Ar}^{15}\text{N}$ (Evans and Müller, 2018), causes a relatively high LOD for ^{55}Mn measurements. Thus, ^{55}Mn could only be quantified for 22 out of 91 specimens.

Table 3.3 Absolute elemental values and external reproducibility for the duration of this study (relative standard deviation (r.s.d.)) of NIST 612 silicate glass reference standard in LR and MR mode in comparison to absolute values from Jochum et al. (2011).

Isotope	NIST SRM 612 - LR			NIST SRM 612 - MR		
	This study (ppm)	External reproducibility (r.s.d.)	Jochum et al. (2011) (ppm)	This study (ppm)	External reproducibility (r.s.d.)	Jochum et al. (2011) (ppm)
^{25}Mg	56	3.1	68 ± 5	59	8.1	68 ± 5
^{26}Mg	58	2.0	68 ± 5	58	1.7	68 ± 5
^{27}Al	12961	1.4	10743 ± 212	12983	0.5	10743 ± 211
^{43}Ca	Internal Standard		85060 ± 715	Internal Standard		85060 ± 715
^{48}Ca	37148	2.3	85060 ± 715	33817	2.9	85060 ± 715
^{55}Mn	39	5.2	39 ± 1	39	0.9	39 ± 1
^{57}Fe	n.a.	n.a.	51 ± 2	55	1.7	51 ± 2
^{87}Sr	51	1.7	78 ± 0.2	50	1.5	78 ± 0.2
^{88}Sr	83	3.5	78 ± 0.2	82	2.0	78 ± 0.2
^{238}U	41	4.5	37 ± 0.08	38	0.8	37 ± 0.08

Additionally, signal sections classified as ‘instrumental’, as determined by the $^{48}\text{Ca}/^{43}\text{Ca}$ ratio, were removed. Sample calibration includes a gas blank and drift correction of reference materials, sample gas blank correction, and sample data reduction. Subsequently an outlier correction was performed using the Hampel identifier (Davies and Gather, 1993). Lastly, the average and standard deviation was calculated of all laser profiles per specimen. ^{27}Al was primarily used to screen for silicate contamination and most profiles show an initial peak of Al/Ca, interpreted to represent contamination on the outside of the foraminifera test. Specimen means are integrated only for signal sections with Al/Ca below the LOD, to minimize the risk of

silica contribution to the sample signal. Further, specimen means were only calculated from profiles with >10 data points of Al/Ca below the LOD. The standard deviation for single specimen means is based on the variance of the elemental ratio across the average of all laser profiles taken per specimen.

3.2.4.2 EPMA elemental mapping of Mg/Ca and Fe/Ca

EPMA elemental mapping was used to study the spatial cross-sectional distribution of Mg/Ca and Fe/Ca in three *E. batialis* specimens, representing minor, moderate, and major diagenetic alteration (see below), respectively. Foraminiferal cross sections were prepared at the British Geological Survey in Keyworth, mounting the foraminiferal tests on separate glass slides and embedding them in epoxy (RT154). To expose the foraminiferal cross sections small amounts of resin were taken off at a time using a Logitech LP50 polisher with 10 µm Al-oxide powder. Subsequently the slides were polished using a sequence of 6 µm, 3 µm, 1 µm, and 0.25 µm polycrystalline diamond paste on Logitech CL50 polisher units for 30 minutes each.

The elemental maps were acquired on a JEOL 8530F field-emission electron microprobe equipped with 5 wavelength dispersive spectrometers at the University of Bristol. All samples were silver coated, to ensure carbonate stability and to mitigate thermally driven beam damage on the sample (Smith, 1986, Kearns et al., 2014). The calibration standards were silver coated together with the samples. Calcium carbonate (CaCO₃) was used as a standard for Ca, Diopside (MgCaSi₂O₆) was used for Mg, and Fe-rich Olivine ((Mg²⁺, Fe²⁺)₂SiO₄) was used for Fe. Ca was measured for 10 ms on one (PETL crystal) spectrometer, whereas Mg and Fe were measured for 300 ms each on two (2 TAP crystals and one TAPH crystal) and one (LIFH/PETH crystal) spectrometers, respectively. The maps were acquired at an accelerating voltage of 15 kV, a beam current of 40 nA, and a step size of 0.5 µm. The analytical resolution, the area over which 75 % of the X-rays are emitted, however, is 0.9 µm (Jonkers et al., 2016), indicating that the measured intensity for features <0.9 µm (~2 pixels) is a convolution of the actual intensity and the intensity of surrounding material. The detection limit for an average of 4 pixels is 97 ppm, 650 ppm, and 355 ppm for Mg, Ca, and Fe, respectively. Raw data were reduced to wt% according to the Armstrong/Love-Scott matrix correction (Armstrong, 1988). As the maps were acquired on pre-defined rectangular areas of the foraminiferal cross section, not only

shell material, but also parts of the resin and other minerals were measured. Following the method outlined in Jonkers et al. (2016) Ca values under 35 wt% were masked, with the same mask applied to the Mg and Fe concentration maps, before creating the Mg/Ca and Fe/Ca maps, thus only elemental values associated with the carbonate phases are displayed in the EPMA maps. Negative Mg and Fe values were replaced with half the minimum positive value (Jonkers et al., 2016). The ratio maps were created and plotted using the RStudio software package (RStudio Team 2015).

3.3 Results

3.3.1 Visual identification of foraminiferal alteration at Site U1343 under the reflected light microscope and SEM

Foraminiferal tests from IODP Site U1343 were grouped into three classes of minor, moderate, and major alteration, based on morphological features, following the approach outlined by Schneider et al. (2017). The classification includes the test colour, ranging from white to orange/brown, the translucency of the test, with increasing opaqueness indicating more alteration, and features such as a ‘sugary’ texture, indicating crystal growth on the outside of the foraminiferal tests, obscuring the original test structure. Minor diagenetic alteration is characterized by little or no discolouration, translucent test walls, and prominent morphological features, such as sutural bridges for *E. batialis*. Specimens with moderate diagenetic alteration usually have a yellow test with both translucent and opaque areas, whereas discoloured orange/brown specimens with an opaque test wall, a ‘sugary’ texture, and obscured morphological features are classified as having major diagenetic alteration. Reflected light microscopy also shows a large inter-species and inter-sample heterogeneity, with *E. batialis* usually displaying stronger discolouration compared to other abundant infaunal benthic foraminiferal species at Site U1343, such as *Uvigerina* spp. and *Islandiella norcrossi*. This either indicates the importance of species-specific morphological features for post-mortem diagenetic alteration and/or different ecological preferences, which cause them to occur at times of different organic carbon fluxes and microbial activity. The latter, however, requires rapid post-mortem formation of discolouration and subsequent mixing of different communities by bioturbation.

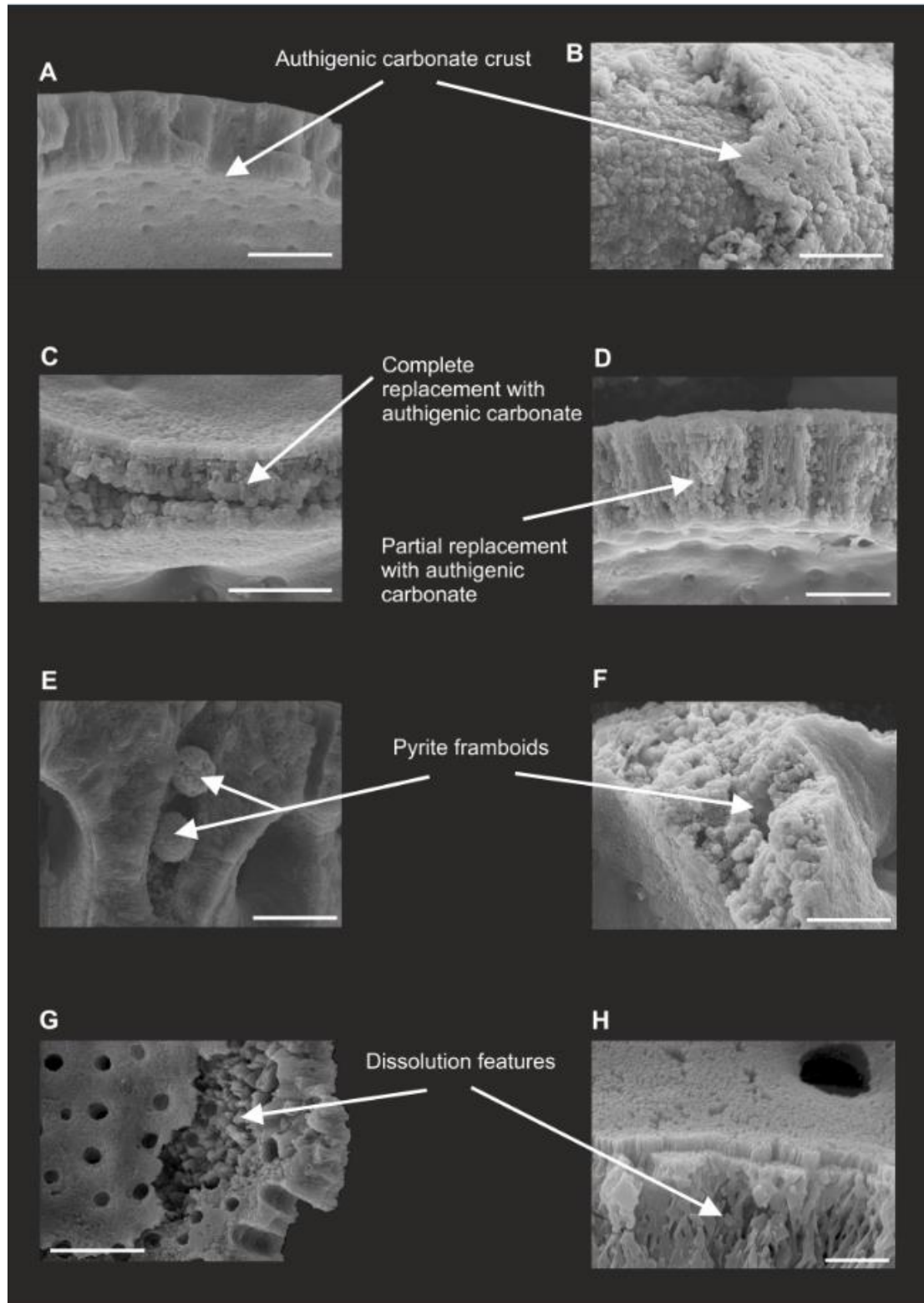


Figure 3.3 SEM images of *E. batialis* wall cross sections from IODP Site U1343. (A) Primary foraminiferal calcite wall with authigenic carbonate crust. (B) Authigenic carbonate crust on the outside of foraminiferal test. (C) Recrystallized test wall with authigenic crust. (D) Partially recrystallized test wall. (E) Pyrite framboids in *E. batialis* suture. (F) Pyrite framboids inside recrystallized test wall. (G) Etched inner surface of foraminifera test. (H) Lattice-like calcite wall with authigenic carbonate crust. Scale bars (white) indicate 10 μm .

In support of light microscopy results, SEM imaging reveals abundant authigenic carbonates and other authigenic minerals, such as pyrite, in correlation with the degree of alteration. This is in line with observations during IODP cruise 323, indicating the co-occurrence of discoloured foraminiferal tests with sedimentary authigenic carbonate crystals at Site U1343 (Expedition 323 Scientists 2010). Authigenic carbonates can occur encrusting on the outside and/or inside of the foraminiferal tests or in form of part or full recrystallization of the test walls (Figure 3.3). Stacks of tabular crystals with gaps in between characterize authigenic carbonates, compared to the dense calcite layers of primary foraminiferal calcite (Figure 3.3). However, authigenic carbonates can also be the subject of dissolution, obscuring the original crystal structure, making identification more difficult. Pyrite framboids occur inside the test chambers, sutures, and even within recrystallized test walls (Figure 3.3). Typically, samples with a higher degree of alteration also have more pyrite framboids. In addition to authigenic minerals, SEM images also show distinctive dissolution features, including broken chambers, etched surfaces, and lattice-like calcite structures inside the test walls (Figure 3.3).

3.3.2 LA-ICP-MS single specimen geochemical analyses

LA-ICP-MS single specimen analyses are used to record profiles of elemental change throughout the foraminiferal tests and for overall specimen elemental means. Table 3.4 contains the range of single specimen mean elemental ratios. The relatively high Mn gas blank (section 2.4.1) and the resulting high LOD, hampered the quantification of Mn/Ca ratios for 69 out of 91 specimens. Mg concentrations for *E. batialis* varied between 0.04 ± 0.025 wt% to 3.08 ± 0.39 wt%, with increasing Mg concentrations for a higher degree of diagenetic alteration (Figure 3.4). There is a significant difference in the variance of Mg concentrations of samples with minor, moderate and major diagenetic alteration ($p < 0.05$).

Representative LA-ICP-MS profiles (Figure 3.5) and boxplots of specimen means (Figure 3.6) demonstrate the difference in trace metal composition of *E. batialis* tests according to the degree of diagenetic alteration. There is a significant difference in the population median ($p < 0.05$) at the 95% confidence level for minor/moderate diagenetic alteration for Sr/Ca and minor/moderate and moderate/major diagenetic alteration for Mg/Ca and U/Ca (Table 3.5). Also supported by a positive correlation

of Mg/Ca with U/Ca and Sr/Ca single specimen means ($R^2 = 0.58$ [0.32; 0.63], $n = 91$ and ($R^2 = 0.53$ [0.33; 0.72], $n = 91$, respectively) (Figure 3.7), indicating that U and Sr, in conjunction with Mg, are increased in the authigenic carbonates.

Table 3.4 Overall range of elemental ratios in LA-ICP-MS samples for both depth intervals including the standard deviation (s.d.).

Isotope ratio	0.3-9.0 m CCSF-A		172.0-305.6 m CCSF-A	
	Minimum \pm s.d.	Maximum \pm s.d.	Minimum \pm s.d.	Maximum \pm s.d.
$^{25}\text{Mg}/^{43}\text{Ca}$ (mmol mol ⁻¹)	1.04 \pm 0.11	64.67 \pm 13.43	1.08 \pm 0.08	116.38 \pm 12.88
$^{55}\text{Mn}/^{43}\text{Ca}$ ($\mu\text{mol mol}^{-1}$)	2160.19 \pm 857.64	3625.74 \pm 554.27	957.97 \pm 205.51	13891.08 \pm 7260.84
$^{238}\text{U}/^{43}\text{Ca}$ (nmol mol ⁻¹)	337.29 \pm 91.80	16231.03 \pm 3023.81	281.91 \pm 33.10	33678.40 \pm 10636.70
$^{88}\text{Sr}/^{43}\text{Ca}$ ($\mu\text{mol mol}^{-1}$)	1.23 \pm 0.04	1.72 \pm 0.04	1.12 \pm 0.04	2.09 \pm 0.13
$^{56}\text{Fe}/^{43}\text{Ca}$ ($\mu\text{mol mol}^{-1}$)	n.a.	n.a.	1808.34 \pm 396.40	93709.67 \pm 170415.71

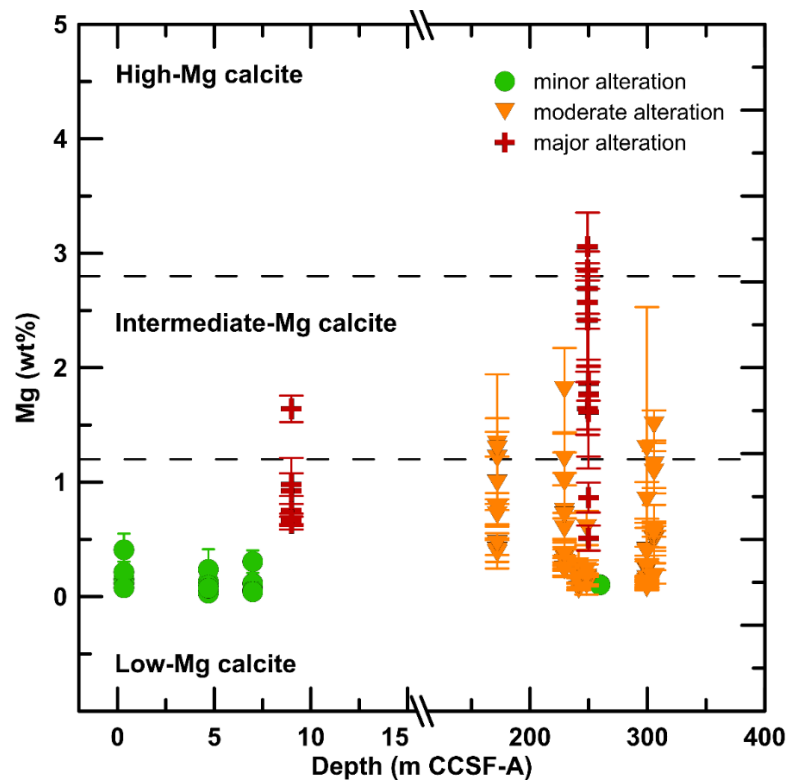


Figure 3.4 Mg concentrations (wt%) in *E. batialis* measured by LA-ICP-MS from IODP Site U1343 including one standard deviation (s.d.) versus depth in the core. The classification of diagenetic alteration is based on the morphological appearance of foraminiferal tests under the reflected light microscope.

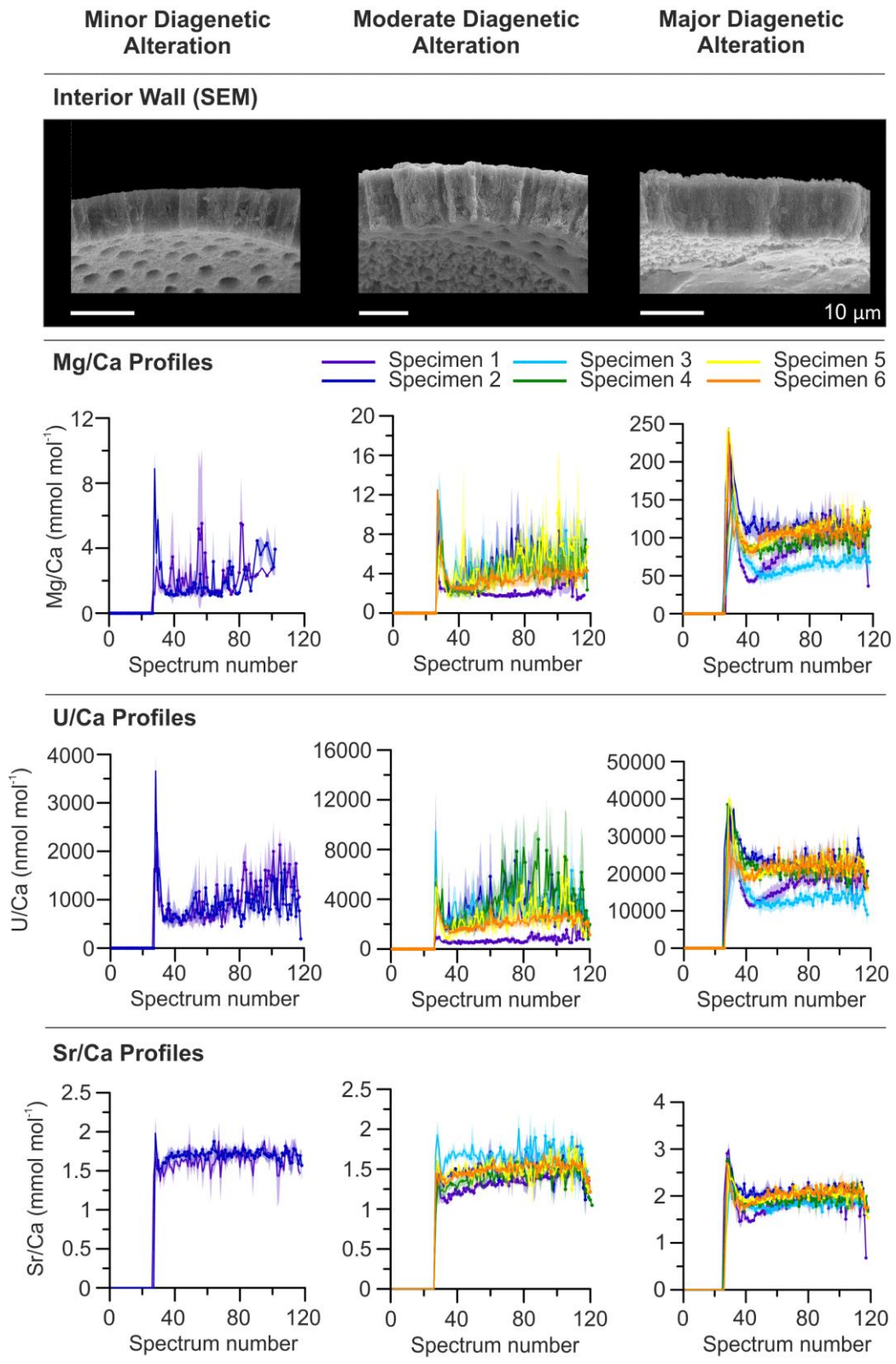


Figure 3.5 SEM images of wall cross sections of specimens with minor, moderate, and major diagenetic alteration together with representative LA-ICP-MS profiles of Mg/Ca, U/Ca, and Sr/Ca. Each specimen has 2 to 6 laser points (colour coded) with the shaded regions representing one standard deviation (s.d.).

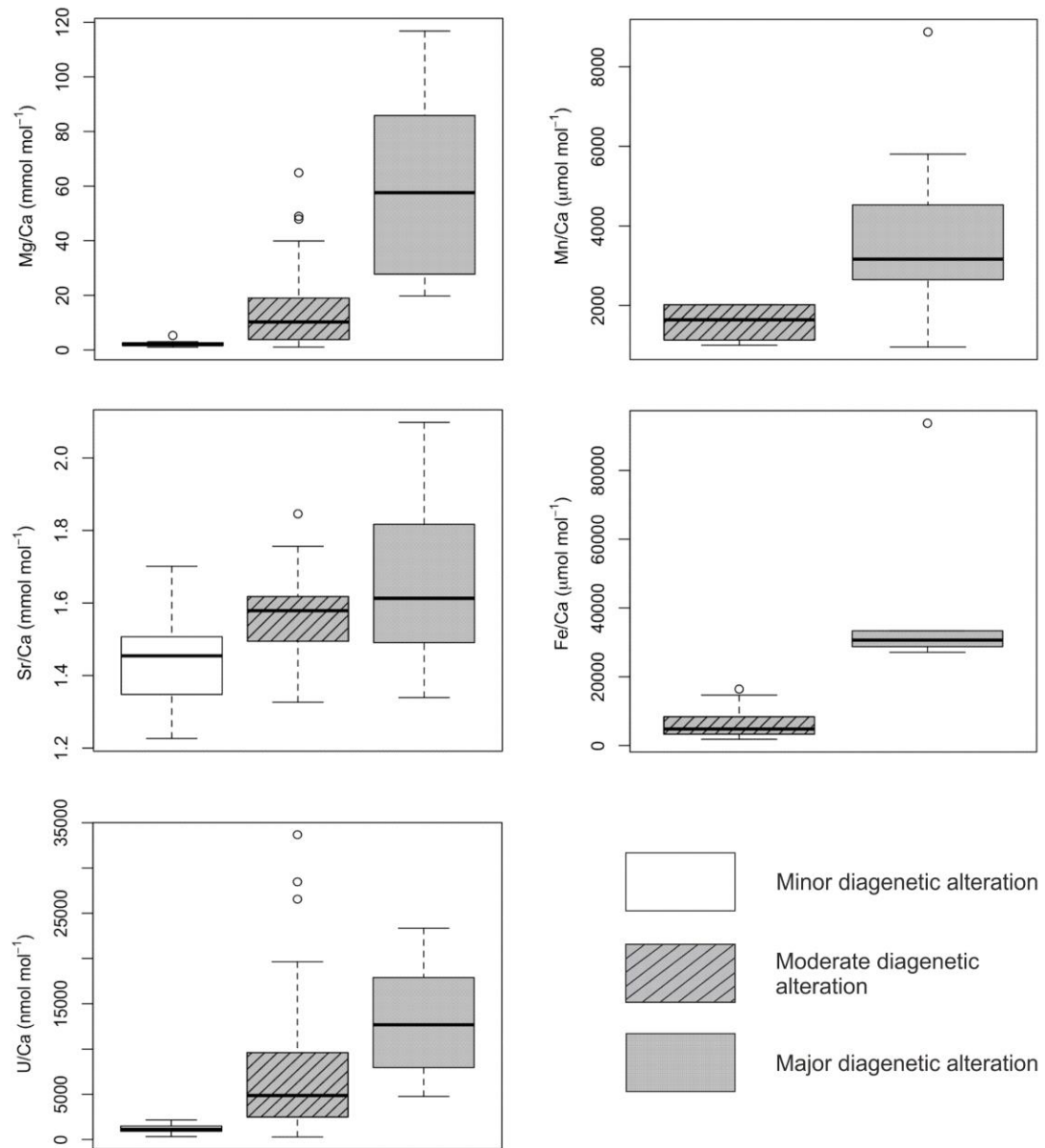


Figure 3.6 Boxplots of Mg/Ca, Sr/Ca, U/Ca, Mn/Ca, and Fe/Ca of *E. batialis* specimens measured by LA-ICP-MS separated according to their degree of diagenetic alteration as determined from morphological evidence under the reflected light microscope.

Additionally there is a significant difference in the population mean ($p < 0.05$) at the 95% confidence level for moderate/major diagenetic alteration for Fe/Ca and Mn/Ca (Table 3.5) (Figure 3.6). Mn/Ca and Mg/Ca show a positive relationship ($R^2 = 0.64$ [0.17; 0.83], $n = 21$) (Figure 3.7), when one data point with anomalously high Mn/Ca ratios, of $\sim 9000 \mu\text{mol mol}^{-1}$ is excluded, in support of Mn incorporation into authigenic carbonates. This indicates that visual classification of alteration stages provides a good first estimate of the microfossil preservation at Site U1343.

Table 3.5 Statistical results of Mann-Whitney and 2 sample t-tests for elemental ratios according to their degree of diagenetic alteration.

	p-value for minor/moderate	p-value for moderate/major	Statistical analysis
Mg/Ca	4.56E-08	7.37E-08	Mann-Whitney test
Sr/Ca	0.02	0.03	2 sample t-test
U/Ca	3.03E-09	6.100E-05	Mann-Whitney test
Fe/Ca	n.a.	0.0002	Mann-Whitney test
Mn/Ca	n.a.	0.02	Mann-Whitney test

3.3.3 EPMA elemental mapping of Mg/Ca and Fe/Ca

EPMA elemental mapping of three *E. batialis* specimen cross-sections was used to determine the spatial variability of Mg/Ca and Fe/Ca in differently altered foraminiferal tests. The samples represent minor, moderate, and major diagenetic alterations as identified by light microscope inspection (Figure 3.8).

EPMA maps of the sample with minor diagenetic alteration show a thin layer of authigenic carbonate on the inside of the chamber walls, characterized by Mg/Ca ratios up to $\sim 210 \text{ mmol mol}^{-1}$ and Fe/Ca ratios up to $\sim 80,000 \text{ } \mu\text{mol mol}^{-1}$ (Figure 3.8). This is in line with SEM images of the same sample, showing a thin crust of authigenic carbonate on the inside, but not the outside of the test (Figure 3.8). The moderately altered sample only has Mg/Ca up to $\sim 37 \text{ mmol mol}^{-1}$. However, compared to the sample with minor alteration, increased Mg/Ca values are found throughout the entire test, indicative of recrystallization (Figure 3.8). SEM images of the wall cross-section reveal isolated authigenic carbonate crystals and preservation of the organic lining on the inside of the chamber (Figure 3.8). Dissolution features, including etched surfaces on the inside and outside of the test and gaps within the test wall are common (Figure 3.3, Figure 3.9). Fe/Ca ratios are also increased throughout the entire test, again suggesting recrystallization, and reach up to $\sim 65,000 \text{ } \mu\text{mol mol}^{-1}$ (Figure 3.8). EPMA maps of the sample with major diagenetic alteration, demonstrate the highest Mg/Ca and Fe/Ca values encountered during EPMA analyses, of up to $\sim 270 \text{ mmol mol}^{-1}$ and $\sim 160,000 \text{ } \mu\text{mol mol}^{-1}$, respectively (Figure 3.8). Mg/Ca and Fe/Ca are not uniformly distributed throughout the test, but rather show high Mg/Ca, Fe/Ca banding along lines of dissolution within the test wall (Figure 3.8).

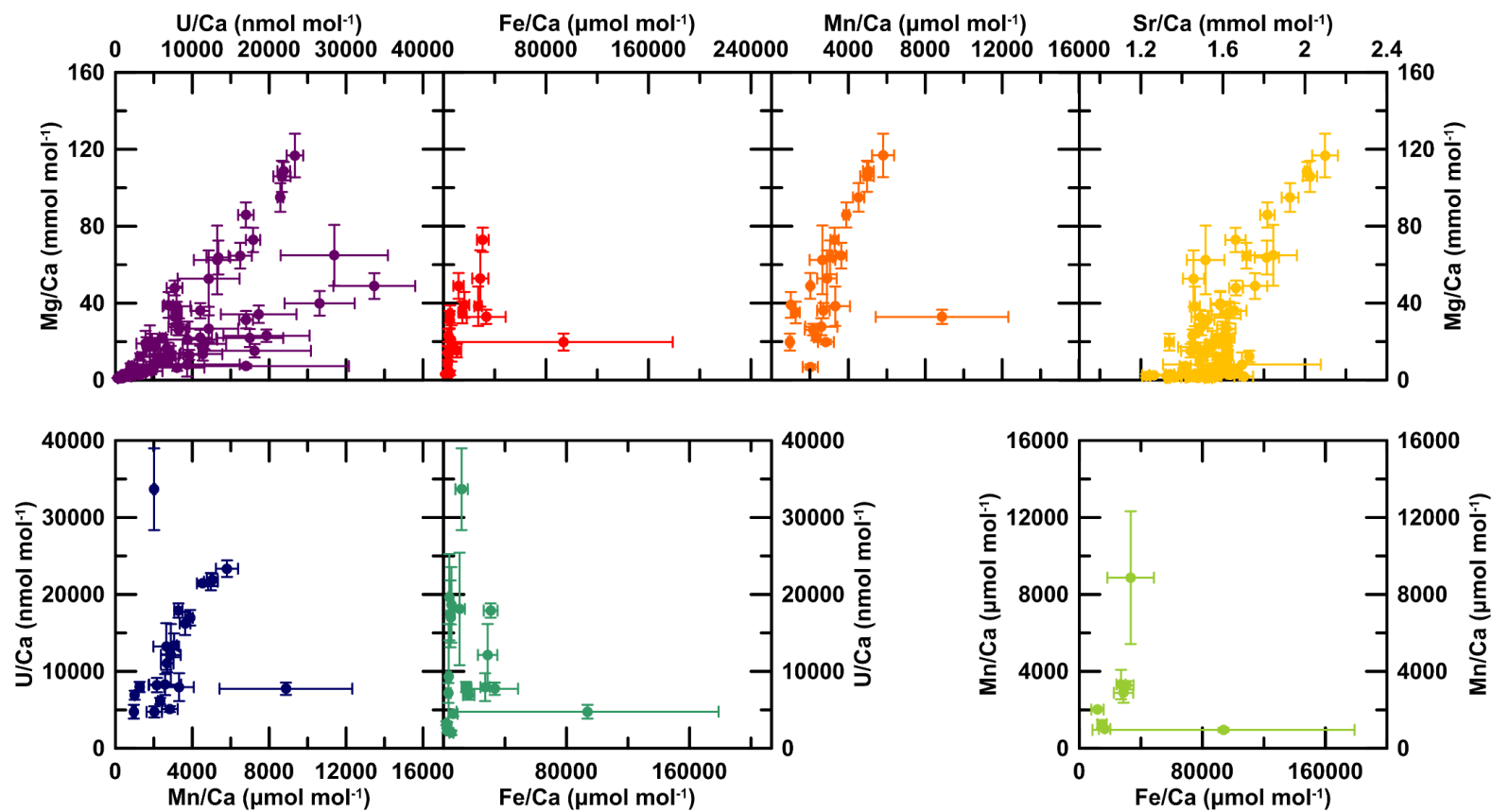


Figure 3.7 Correlations of single specimen LA-ICP-MS mean values, including the standard deviation (s.d.). Mg/Ca shows a positive correlation with U/Ca ($R^2 = 0.58$ [0.32; 0.63], $n = 91$), Sr/Ca ($R^2 = 0.53$ [0.33; 0.72], $n = 91$), and Mn/Ca ($R^2 = 0.64$ [0.17; 0.83], $n = 21$) after removing one data point with anomalously high Mn/Ca ($\sim 9,000 \mu\text{mol mol}^{-1}$).

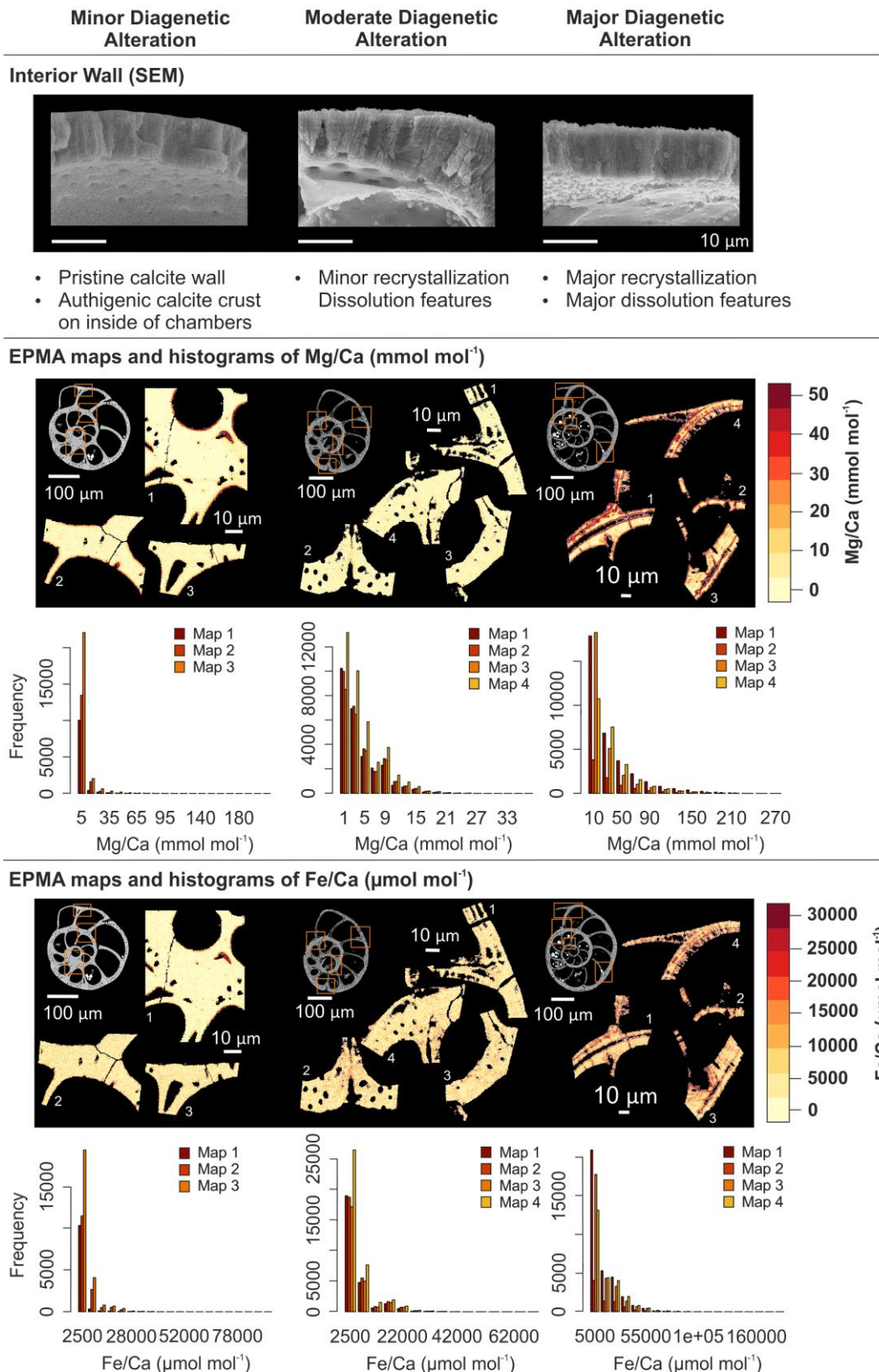


Figure 3.8 SEM images of foraminiferal wall cross sections and EPMA maps of Mg/Ca and Fe/Ca for three specimens of *E. batialis* representative of minor, moderate, and major diagenetic alteration. Mg/Ca and Fe/Ca maps have been capped at 50 mmol mol^{-1} and $30,000 \mu\text{mol mol}^{-1}$, respectively, to ensure good visual representation of the authigenic carbonate phases. Histograms below the maps, however, demonstrate the full range of elemental ratios.

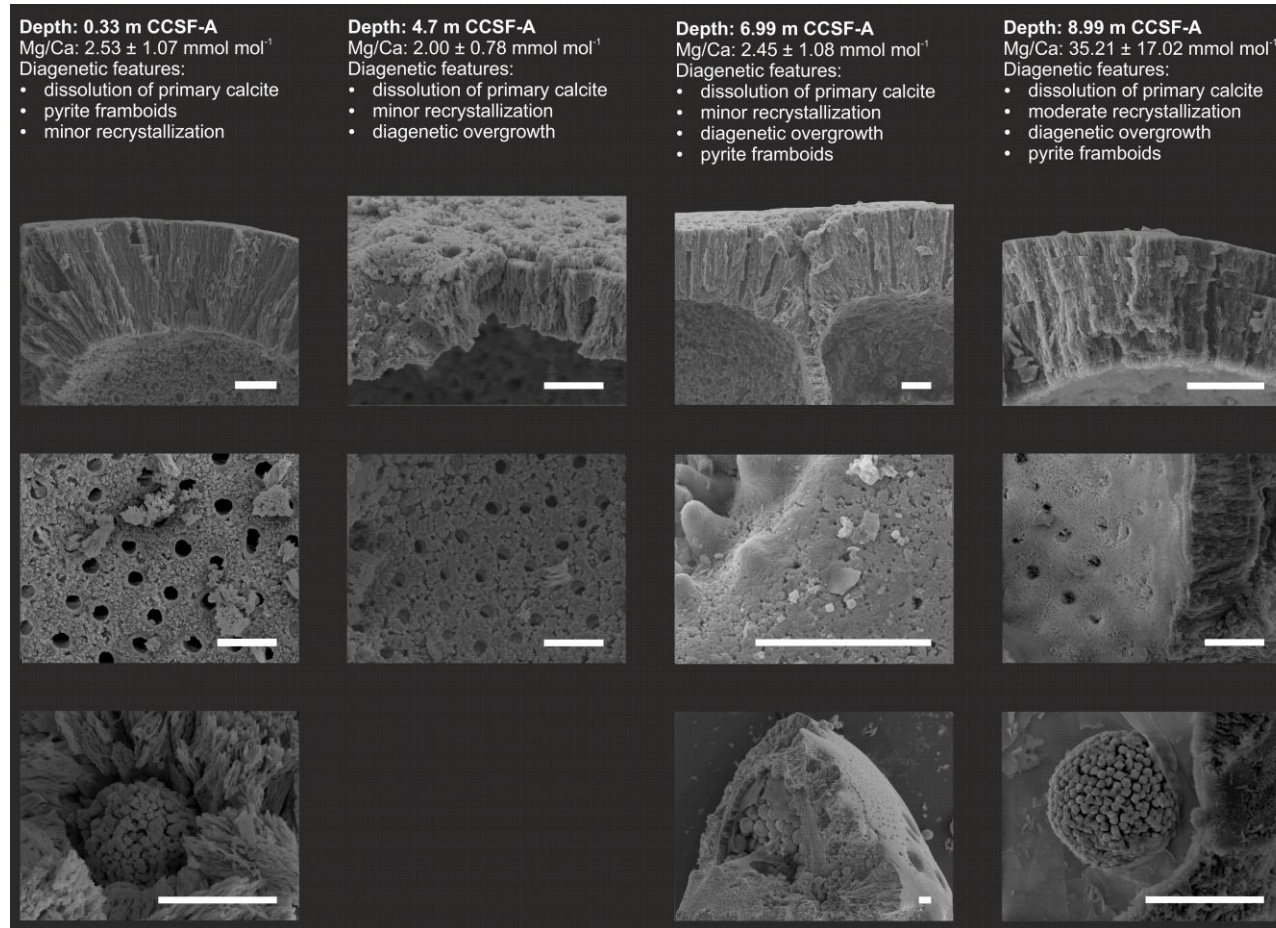


Figure 3.9 SEM images of *E. batialis* specimens across the upper 9 m CCSF-A, spanning the present day SMTZ (~8 mbsf) (Wehrmann et al., 2011), showing the wall cross sections (top row), the inside or outside surface of the tests (middle row), and pyrite framboids within the tests (bottom row). The images demonstrate distinct dissolution features but also some precipitation of authigenic carbonates. Scale bars (white) represent 10 μ m.

3.4 Discussion

3.4.1 Multi-element composition of foraminifera-bound authigenic carbonates at Site U1343

Morphological evidence and geochemical analyses of shallow infaunal benthic foraminiferal species *E. batialis* at IODP Site U1343 reveal visually altered tests in conjunction with prominent changes to the elemental composition. *E. batialis* forms a hyaline test, characterized by layered, perforate walls made of interlocking LMC microcrystals. Hence, increased Mg concentrations, observed in foraminifera from Site U1343, likely result from contamination with carbonates containing larger amounts of Mg. This is in agreement with the authigenic carbonate crystal assemblage found at Site U1343 composed of LMC to HMC, Fe-rich calcite, and dolomite (Pierre et al., 2016). Studies from other methane seep sites, also demonstrate the presence of HMC, aragonite, and dolomite (Aloisi et al., 2002, Pierre et al., 2016, Panieri et al., 2017, Schneider et al., 2017), with aragonite being associated with faster rates of authigenic carbonate formation and precipitation close to the sediment-water interface, whereas HMC typically precipitates deeper in the sediments, when AOM is weaker (Aloisi et al., 2002, Bayon et al., 2009).

Dolomite usually has Mg concentrations of ~12.6 wt% (Lingling and Min, 2005), higher than the observed Mg concentrations in diagenetically altered *E. batialis* tests from Site U1343 (0.04 ± 0.025 wt% (s.d.) to 3.08 ± 0.39 wt% (s.d.)). However, if the foraminiferal tests fall along a mixing line of primary LMC and dolomite and ~0.5 wt% Mg is assumed for primary foraminiferal calcite, a contribution of up to 20.5 % dolomite could explain the observed Mg-concentrations. SEM images of tests with major diagenetic alteration show almost complete replacement of the original foraminiferal calcite with authigenic carbonate (Figure 3.3), indicating that contributions of >20.5 % are likely. Additionally, Pierre et al. (2016) demonstrate that dolomite crystals are primarily associated with a deeper zone of authigenic carbonate formation at ~260 mbsf, whereas LMC and HMC crystals are more characteristic of early diagenesis. Only two samples in this study are from below 260 mbsf, with no significant increase in Mg/Ca ratios across this zone (Figure 3.10), indicating that dolomite is unlikely to be the predominant foraminifera-bound authigenic carbonate phase.

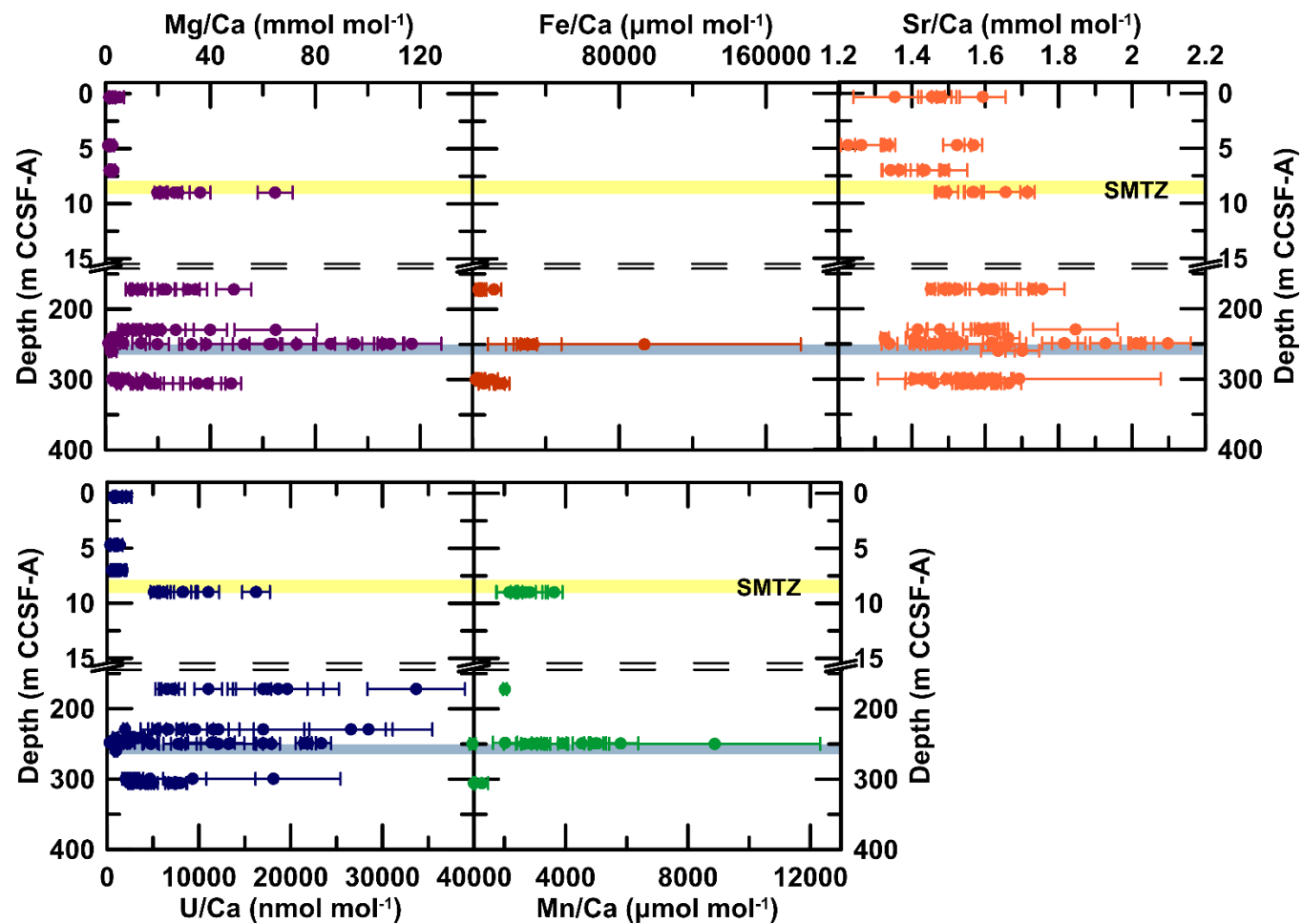


Figure 3.10 Single specimen LA-ICP-MS mean values of *E. batialis*, including the standard deviation (s.d.) versus depth across both study intervals, indicating the geochemical change associated with redox horizons at Site U1343. The SMTZ is shaded in light yellow and the deeper zone of authigenic carbonate formation (~260 mbsf) is shaded in blue.

In comparison to calcite, aragonite has a higher partition coefficient of Sr, reflected by higher Sr/Ca ratios of $\sim 30 \text{ mmol mol}^{-1}$ (Bayon et al., 2007). Sr/Ca values of single specimen LA-ICP-MS analyses vary between 1.2-1.8 mmol mol^{-1} (typical values of hyaline tests: 0.75-1.25 mmol mol^{-1} (Gussone et al., 2016)), with one sample ($\sim 250 \text{ m CCSF-A}$) showing higher Sr/Ca values between 1.8-2.2 mmol mol^{-1} (Figure 3.10). During carbonate diagenesis, aragonite is replaced with more stable carbonate species (Pierre et al., 2016), suggesting that increased Sr/Ca ratios are either a relic of aragonite formation during early diagenesis or related to the incorporation of Mg into the authigenic carbonates. The latter is supported by a positive correlation of Mg/Ca and Sr/Ca of single specimen LA-ICP-MS analyses ($R^2 = 0.53 [0.33; 0.72]$, $n = 91$) and likely results from a distortion of the calcite crystal lattice due to higher concentrations of Mg^{2+} cations, leaving more space for the relatively large Sr^{2+} cations (Mucci and Morse, 1983). Thus, elemental data of foraminiferal-bound authigenic carbonates suggest that LMC to HMC are the most likely contaminant phases in foraminifera from Site U1343.

In addition to Sr/Ca, U/Ca ratios are positively correlated with Mg/Ca, indicating incorporation of U into authigenic calcite. Uranium in oxygenated seawater exists in form of uranyl (U^{6+}) and uranyl carbonate complexes (Klinkhammer and Palmer, 1991) with a low partition coefficient into marine calcite, as a result of its large ionic radius (Zhao et al., 2016). The largest sink for uranium in the oceans is the diffusion across the sediment-water interface and removal of soluble uranium by reduction to U^{4+} and subsequent precipitation in suboxic to anoxic environments (Klinkhammer and Palmer, 1991, Zhao et al., 2016). As the ionic radius of U^{4+} is similar to that of Ca^{2+} cations, U^{4+} can be readily incorporated into carbonates forming within the sediment (Sturchio et al., 1998, Zhao et al., 2016). Typical U/Ca values of primary foraminiferal calcite are on the order of 3-23 nmol mol^{-1} (Russell et al., 2004, Raitzsch et al., 2011, Boiteau et al., 2012, Chen et al., 2017), whereas U/Ca ratios in foraminifera from Site U1343 vary between $299 \pm 111 \text{ nmol mol}^{-1}$ to $29098 \pm 13826 \text{ nmol mol}^{-1}$ (s.d.), in support of U incorporation into authigenic carbonates during foraminiferal diagenesis (Boiteau et al., 2012, Gottschalk et al., 2016, Chen et al., 2017).

Statistical analysis of Mn/Ca versus Mg/Ca of samples with Mn counts above the LOD also shows a significant correlation ($R^2 = 0.64 [0.17; 0.83]$, $n = 21$), if one data point

with high Mn/Ca values is excluded (Figure 3.7). This indicates that Mn^{2+} is incorporated into the authigenic calcite, as well, in line with previous studies, showing incorporation of Mn into carbonates formed within the sediments under reducing conditions (Pena et al., 2005, Torres et al., 2010, Groeneveld and Filipsson, 2013, Hasenfratz et al., 2017a). Apart from authigenic carbonate phases Mn can also be incorporated into Mn-Fe-oxides coatings on foraminiferal tests (Pena et al., 2005, Pena et al., 2008). Mn-Fe-oxides form within the sediments above the oxygen penetration depth and Mn can be re-dissolved into pore waters as Mn^{2+} under reducing conditions (Froelich et al., 1979). If all the Mn was derived from Mn-Fe-oxide contamination, Mg/Mn ratios close to that of global Mn-Fe-oxide crusts/nodules (0.2 mol mol^{-1} (De Lange et al., 1992, Pattan, 1993)) would be expected. All specimens have an Mg/Mn ratio higher than that of global Mn-Fe-oxide crust/nodules (2.47 to $26.10 \text{ mol mol}^{-1}$), indicating that Mn-Fe-oxides are not the main contaminant phase in foraminifera from Site U1343. However, the possibility that Mn-Fe-oxides contribute to contamination of foraminifera cannot be fully eliminated, even though they are unlikely to be the sole contaminant phase. In particular high Mn/Ca ratios ($\sim 8,500 \text{ } \mu\text{mol mol}^{-1}$) at low Mg/Ca in one specimen, in conjunction with relatively high Fe/Ca of $\sim 35,000 \text{ } \mu\text{mol mol}^{-1}$ (Figure 3.7), could point towards contribution of Mn-Fe-oxides. One possibility is that Mn-Fe-oxides forming on foraminiferal tests above the oxygen penetration depth become covered by authigenic carbonates in deeper sediments, hindering the dissolution and resumption of Mn into pore waters under reducing conditions (Pena et al., 2005).

Fe/Ca values have only been measured for 4 samples (20 specimens) mainly to test whether there is a significant change across the deeper zone of Fe-rich carbonate and dolomite precipitation, as identified by Pierre et al. (2016). There is no significant correlation of Fe/Ca and Mg/Ca in the analysis of single specimen means. However, Mn-Fe-oxide and especially pyrite contamination are likely to bias LA-ICP-MS analyses. Fe/Ca ratios of EPMA maps, on the contrary, cannot be associated with pyrite framboids or Mn-Fe-oxides, as areas with Ca concentrations $< 35 \text{ wt\%}$ have been masked in order to only display the carbonate phases. Fe/Ca values in EPMA maps of foraminiferal cross sections are elevated in conjunction with increased Mg/Ca ratios (Figure 3.8), indicating that Fe, as well, is incorporated into the authigenic calcite.

In line with previous work, indicating increased Mg concentrations in methane-related foraminiferal-bound authigenic carbonates from the western Svalbard margin (Schneider et al., 2017, Panieri et al., 2017) single specimen LA-ICP-MS and EPMA geochemical analyses of *E. batialis* at Site U1343 demonstrate abundant authigenic LMC to HMC. In addition, LA-ICP-MS and EPMA analyses at Site U1343 reveal increased U, Mn, Fe, and Sr values in authigenic carbonates compared to primary foraminiferal calcite, important for paleoclimate reconstructions utilizing these elements.

3.4.2 Dissolution of foraminiferal test at Site U1343

SEM images of foraminiferal fragments reveal abundant dissolution features, including etched surfaces, loss of chambers, and lattice-like calcite walls (Figure 3.3, Figure 3.9). Imaging of foraminiferal cross-sections also shows large gaps within the test walls along biologically-defined laminae. During test formation, foraminifera use a primary organic membrane as a template for calcite precipitation (Erez, 2003). Calcite is precipitated both on the inside and outside of the membrane, with the outside layer covering the entire test (Erez, 2003). Thus, natural laminations form within the test walls representing weak points where pore waters are able to penetrate the test and cause alteration of the foraminiferal calcite.

Typically, dissolution or partial dissolution of foraminiferal tests in the sediment is primarily controlled by changes to the bottom water carbonate saturation state ($\Delta[\text{CO}_3^{2-}]$) and the supply and oxic respiration of labile organic matter producing metabolic acids that cause carbonate dissolution (Martin and Sayles, 1996, Rosenthal and Lohmann, 2002, Martin and Sayles, 2006). However, at Site U1343 anoxic respiration, such as organoclastic sulphate reduction, also needs to be considered as it can cause the formation of metabolic acids (Walter and Burton, 1990). Further, the samples in this study are derived from both glacial and interglacial intervals (Figure 3.1), thus, changes in the primary productivity (Kim et al., 2014) and $\Delta[\text{CO}_3^{2-}]$ (Lear et al., 2016, Sosdian et al., 2018) on orbital timescales need to be considered in order to infer the primary control on foraminiferal test dissolution. In the eastern Bering Sea primary productivity, as inferred from mass accumulation rates of biogenic opal (MAR_{opal}) at Site U1343, varies on glacial/interglacial (G/IG) timescales with increased productivity during interglacials and vice versa (Kim et al., 2014). Increased

productivity during interglacials could lead to an earlier shift from oxic to anoxic organic carbon remineralisation pathways and enhanced rates of sulphate reduction, suggesting less carbonate dissolution by metabolic acids during interglacials as the zone of oxic respiration in the sediments is contracted.

Additionally, $\Delta[\text{CO}_3^{2-}]$ likely changes on G/IG timescales. At present day the Bering Sea at 2000 m water depth is undersaturated with respect to CaCO_3 ($\Omega = 0.8$, $\Delta[\text{CO}_3^{2-}] = -14 \mu\text{mol kg}^{-1}$) (Robbins et al., 2010, Olsen et al., 2016). During the last glacial maximum, the deep ocean is thought to have sequestered large amounts of respired CO_2 (Marchitto et al., 2005, Yu et al., 2014), seen in the North Pacific from decreased deep water $[\text{O}_2]$ concentrations (Galbraith et al., 2007, Jaccard et al., 2009), likely lowering its $\Delta[\text{CO}_3^{2-}]$ even further. If larger deep ocean carbon storage was a common feature during glacial intervals of the Mid- to late Pleistocene (Lear et al., 2016, Sosdian et al., 2018) and Site U1343 was continuously bathed in North Pacific Deep Water (NPDW), dissolution of marine carbonates along the eastern Bering Sea margin is likely enhanced during glacial intervals related to increased corrosiveness of glacial deep waters and changes in the organic carbon supply.

In order to fully elucidate the control of organic carbon export versus carbonate saturation on calcareous test dissolution on orbital timescales, however, additional SEM studies on foraminifera from the eastern Bering Sea margin are necessary to enable statistically relevant inferences.

3.4.3 The origin of foraminifera-bound authigenic calcite within the sediment-pore water system

Previous studies of authigenic carbonate crystals at Site U1343 demonstrate two zones of carbonate formation within the sediments. The upper zone is related to bicarbonate ion formation during organoclastic sulphate reduction and AOM in the upper meters of the sediment column (Wehrmann et al., 2011, Pierre et al., 2016), whereas the second zone is related to CO_2 release during methanogenesis and subsequent silicate weathering (Pierre et al., 2016). At Site U1343 Fe-rich carbonates occur primarily below ~260 mbsf (Pierre et al., 2016). To test the influence of sulphate reduction, AOM, and silicate weathering on foraminiferal-bound authigenic carbonates at Site U1343, samples from two depth intervals were analysed spanning the upper 9 mbsf,

including the present day SMTZ, and between 172-305.6 mbsf, spanning the deeper zone of carbonate formation.

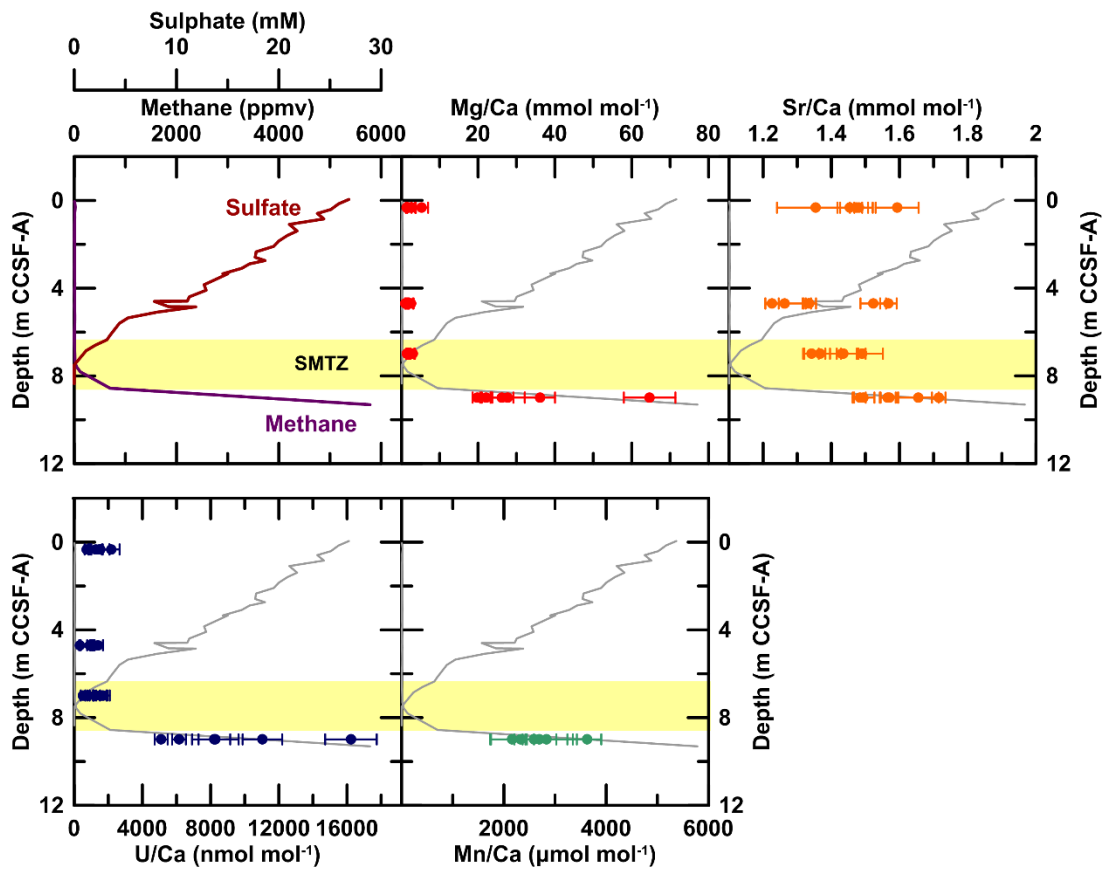


Figure 3.11 Single specimen LA-ICP-MS mean values of *E. batialis* of Mg/Ca, Sr/Ca, U/Ca, and Mn/Ca including their standard deviation (s.d.) across the present day SMTZ (light yellow) at IODP Site U1343, including pore water profiles of sulphate (dark red/grey) and methane (purple/grey) (dissolved pore water constituent data from LIMS (<http://web.iodp.tamu.edu/LORE/>)).

Across the SMTZ there is a significant increase in Mg/Ca and U/Ca of single specimen LA-ICP-MS analyses ($p < 0.05$) (Figure 3.11). Mn/Ca above the SMTZ is below the LOD, but above the LOD just below the SMTZ (Figure 3.11), indicating that Mn/Ca in foraminifera also increases within this redox horizon. This supports that foraminiferal tests are significantly altered during early diagenesis within the SMTZ, where AOM causes the formation of bicarbonate ions, increasing the alkalinity of pore waters causing authigenic HMC to precipitate. This is in line with previous studies of benthic foraminiferal diagenesis in methane seep areas (Schneider et al., 2017, Panieri et al., 2017), suggesting high-Mg authigenic carbonate formation within the SMTZ.

Additionally, Mg and Ca pore water profiles at Site U1343 indicate precipitation of Mg-calcite during early diagenesis (Figure 3.1) (Wehrmann et al., 2011).

U/Ca ratios of single specimen LA-ICP-MS analyses at Site U1343, on the other hand, demonstrate increased values ($>3\text{-}23\text{ nmol mol}^{-1}$ (Russell et al., 2004, Raitzsch et al., 2011, Chen et al., 2017)) even above the SMTZ (Figure 3.11). SEM images of foraminifera above the present day SMTZ primarily show dissolution of the tests, but also provide some evidence for authigenic carbonate precipitation (Figure 3.9). Above the SMTZ organoclastic sulphate reduction releases bicarbonate ions into the pore water, available for authigenic carbonate formation. However, sulphate effectively complexes Mg^{2+} cations (Walter, 1986), indicating that the formation of LMC might be favoured above the SMTZ, supported by lower Mg/Ca ratios (Figure 3.11). Authigenic carbonate formation above the SMTZ is supported by Ca^{2+} pore water profiles, showing a decrease in Ca^{2+} in conjunction with organoclastic sulphate reduction (Figure 3.1) (Wehrmann et al., 2011). Previous studies of methane-related carbonate pavements on the seafloor suggest aragonite precipitation in sulphate-rich environments (Aloisi et al., 2002, Bayon et al., 2009). However, Sr/Ca ratios of foraminifera above the SMTZ are similar to those of foraminifera below the SMTZ, contradicting aragonite formation and supporting LMC precipitation instead. Lower U/Ca and Mn/Ca ratios in foraminifera from above the SMTZ, compared to those below the SMTZ, could result from either differences in the pore water U and Mn concentration or result from less authigenic carbonate formation in the zone of sulphate reduction, compared to the SMTZ, as suggested by pore water Ca^{2+} profiles that reach their minimum within the SMTZ (Wehrmann et al., 2011).

In further support of authigenic calcite formation, SEM images of foraminifera both from above and below the SMTZ at Site U1343 demonstrate the presence of abundant pyrite framboids, within the foraminiferal tests. Notably, some foraminifera even show precipitation of pyrite framboids within the test walls (Figure 3.3, Figure 3.9), suggesting co-precipitation of authigenic carbonates and pyrite framboids. Abundant pyrite and authigenic carbonate precipitation in the sediments typically occurs within the zone of organoclastic sulphate reduction, producing H_2S and HCO_3^- (Berner, 1984, Peckmann et al., 2001, Lin et al., 2016), and in the SMTZ, where AOM leads to the formation of HCO_3^- and HS^- readily available for authigenic mineral formation (Lin et al., 2016).

Across the deeper zone of carbonate formation (~260 mbsf), as proposed by Pierre et al. (2016), there is no significant change in the foraminiferal geochemistry (Figure 3.10), suggesting that foraminiferal trace metal ratios are primarily influenced by authigenic calcite formation during early diagenesis linked to sulphate reduction and AOM.

3.4.4 Paleooceanographic implications

Mg/Ca of benthic foraminifera is a widely applied and accepted proxy in paleoceanography. Mg^{2+} can substitute for Ca^{2+} in $CaCO_3$ as part of an endothermic reaction controlled by temperature-dependent physiological processes during foraminiferal test calcification (Nürnberg et al., 1996) enabling researchers to determine BWTs through time (Nürnberg et al., 1996, Rosenthal et al., 1997, Lea et al., 1999, Lear et al., 2002).

Additionally, in conjunction with $\delta^{18}O_b$, independent measurements of BWT allow to deconvolve the $\delta^{18}O_b$ record into its temperature and continental ice volume components. Such climate reconstructions rely on the geochemical integrity of foraminiferal tests, but detailed diagenetic studies increasingly reveal alterations affecting their trace element and isotope composition (Pena et al., 2005, Pena et al., 2008, Panieri et al., 2017, Schneider et al., 2017, Hasenfratz et al., 2017a).

Common hyaline LMC benthic foraminiferal species in the arctic to subarctic realm, such as *Cassidulina neoteretris*, *Nonionella labradorica*, *Elphidium clavatum*, *Uvigerina* spp., and *Melonis barleeanum* have Mg/Ca ratios on the order of 0.84-1.38 $mmol\ mol^{-1}$, 1.11 -1.69 $mmol\ mol^{-1}$, 0.52-1.06 $mmol\ mol^{-1}$, 0.68-1.42 $mmol\ mol^{-1}$, and 0.7-1.5 $mmol\ mol^{-1}$, respectively (Lear et al., 2002, Elderfield et al., 2006, Kristjánssdóttir et al., 2007, Skirbekk et al., 2016, Hasenfratz et al., 2017b, Barrientos et al., 2018). Average Mg/Ca ratios of *E. batialis* from IODP Site U1343, acquired by LA-ICP-MS, on the other hand, vary between $1.1 \pm 0.3\ mmol\ mol^{-1}$ and $116.4 \pm 12.9\ mmol\ mol^{-1}$ (Figure 3.10), as a result of methane-related authigenic Mg-calcite contamination. To date, no Mg/Ca BWT calibration exists for *E. batialis*. However, if a similar Mg/Ca BWT sensitivity of *E. batialis* and *E. clavatum* is assumed (Chapter 4) (Barrientos et al., 2018), Mg/Ca LA-ICP-MS values of $\sim 116\ mmol\ mol^{-1}$ yield highly unrealistic BWT values.

Typically, studies of foraminiferal trace metal ratios include rigorous chemical cleaning of the lightly crushed foraminiferal tests, including a clay removal step, oxidative treatment to remove remnant organic matter, reductive treatment to remove Mn-Fe-oxides, and a weak acid leach to remove adsorbed contaminants on the foraminiferal fragments (Boyle, 1983, Barker et al., 2003). Pena et al. (2005) demonstrated that the reductive step is able to remove Mn-Mg-rich carbonates on foraminifera from the Panama Basin, as a result of the thinner, more fragile structure of authigenic carbonates and/or the removal of Mn-Fe-oxides in-between the primary foraminiferal calcite and the authigenic carbonates. Yu et al. (2007), on the other hand, show that the reductive step can cause partial dissolution of the primary foraminiferal calcite and reduction of Mg/Ca, due to the formation of chelate complexes of metals, such as Mg, with citrate in the reducing reagent. This demonstrates that it is crucial to determine the chemical composition and nature of contamination phases prior to climate reconstructions using foraminiferal tests, in order to adjust the methodology accordingly.

EPMA analyses of *E. batialis* specimens from Site U1343 show the spatial variability of authigenic carbonates within the foraminiferal test. Whilst tests with moderate to major alterations show high Mg/Ca values throughout the test, resulting from either recrystallization or dissolution and precipitation of HMC along natural laminations within the test walls, tests with minor diagenetic alteration are characterized by an HMC crust (Figure 3.8), which could potentially be removed during chemical cleaning. This indicates, that studies of trace metal ratios in primary foraminiferal calcite at methane bearing continental margin sites are possible for foraminifera displaying minor diagenetic alteration (little or no discolouration, translucent test walls, and prominent morphological features) following a rigorous chemical cleaning study.

Additional approaches to remove the contamination signal in foraminiferal Mg/Ca records, include mathematical corrections for diagenetic Mg (Lea et al., 2005, Hasenfratz et al., 2017a) and the application of thresholds values of trace metal ratios primarily associated with the contamination phases (Barker et al., 2003). Mathematical corrections of foraminiferal Mg/Ca ratios can be applied using a regression of Mg/Ca and trace metal calcium ratios associated primarily with the contamination phase (Lea et al., 2005) or determination of the Mg/metal ratios in the

contaminant (Hasenfratz et al., 2017a). Both approaches assume constant Mg/metal ratios in the contamination phase (Lea et al., 2005, Hasenfratz et al., 2017a), if the former is based on a linear regression of Mg/Ca and trace metal calcium ratios associated with the contamination phase. At Site U1343, Mg/metal ratios, such as Mg/Mn and Mg/U of single specimen analyses are highly variable, most likely as a result of changes to the redox-chemistry in the sediment-pore water system, affecting the distribution coefficients of trace metals between the solid and the liquid phase.

Measured U/Ca ratios in this study are up to ~1500 times higher compared to typical U/Ca ratios of primary foraminiferal calcite (3-23 nmol mol⁻¹ (Russell et al., 2004, Raitzsch et al., 2011, Boiteau et al., 2012, Chen et al., 2017)), indicating that uranium is primarily associated with the authigenic overgrowth and primary foraminiferal U/Ca only marginally influence the measured values. U/Ca, thus potentially offers an opportunity to correct Mg/Ca ratios for authigenic carbonate contributions at continental margin sites. Uranium accumulation in marine deep sea sediments demonstrates a nonlinear relationship with the oxygen penetration depth, but a linear correlation with the organic carbon accumulation rates (McManus et al., 2005). Considering, that the depth of the SMTZ is mainly governed by the bottom water [O₂] (Wehrmann et al., 2011), the oxygen penetration depth may exert the primary control on the sedimentary redox-chemistry along the eastern Bering Sea continental margin. Thus, a non-linear accumulation of Uranium in the sediments and incorporation into authigenic carbonates may be expected.

The relationship of Mg/Ca and U/Ca in foraminifera from IODP Site U1343 is best described by an exponential fit ($R^2 = 0.60$, $n = 91$), which has a y-axis intercept of ~3 mmol mol⁻¹ Mg/Ca (Figure 3.12). The approach outlined in Lea et al. (2005) proposes to correct Mg/Ca values using the slope of the regression at each point, here measured Mg/Ca values would have to be divided by the slope of the regression, resulting from the exponential relationship (Equation 3.4).

$$Mg/Ca_{corrected} = \frac{Mg/Ca_{measured}}{e^{(0.0001 * U/Ca_{measured})}} \quad (\text{Equation 3.4})$$

However, corrected Mg/Ca values at Site U1343 using the method outlined above still yield unrealistically warm BWTs of Mg/Ca values up to 15 mmol mol⁻¹ using the Mg/Ca BWT calibration for *E. clavatum* (Barrientos et al., 2018). This is likely related to the large uncertainty associated with the LA-ICP-MS measurements as a result of

the spatial variability of authigenic carbonates within the foraminifera test walls and the resulting uncertainty in the regression of Mg/Ca and U/Ca. Further, high U/Ca and Mg/Ca values seem to be less well represented by the exponential regression compared to lower U/Ca and Mg/Ca values (Figure 3.12), indicating that more studies are needed to fully understand the incorporation mechanism of Mg and U into authigenic carbonates in methane-bearing sediments.

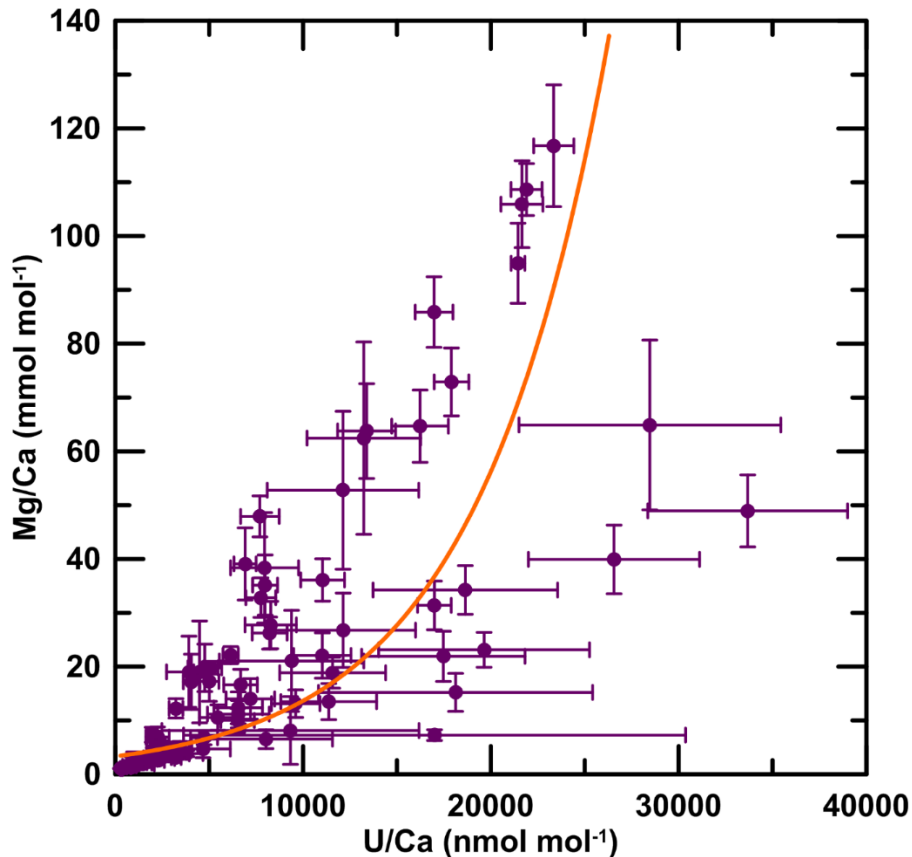


Figure 3.12 Mg/Ca versus U/Ca of single specimen LA-ICP-MS mean values (s.d.) with the best fit exponential regression (orange) ($\text{Mg/Ca} = 3.3 * e^{(0.0001 * \text{U/Ca})}$, $R^2 = 0.60$, $n = 91$).

Another approach of correcting foraminiferal Mg/Ca records for contamination phases is based on threshold values of trace metal ratios primarily associated with the authigenic carbonates. LA-ICP-MS measurements of *E. batialis* specimens at Site U1343 demonstrate that U/Ca ratios are a valuable tool to determine methane-related authigenic carbonate contamination in continental margin settings, as U/Ca is primarily associated with the authigenic carbonates and only small amounts of U are incorporated into primary foraminiferal calcite. However, the U/Ca threshold is likely

to vary between studies, depending on the analytical tools, applied chemical cleaning methods, and the study site, whilst the absolute threshold ultimately depends on the associated Mg contribution of authigenic calcite to the measured foraminiferal Mg/Ca ratios. Thus, instead of using a correction, I propose that foraminiferal samples exerting moderate to major diagenetic alterations can be used in paleoclimate reconstructions if trace metal thresholds for authigenic carbonate contamination are established.

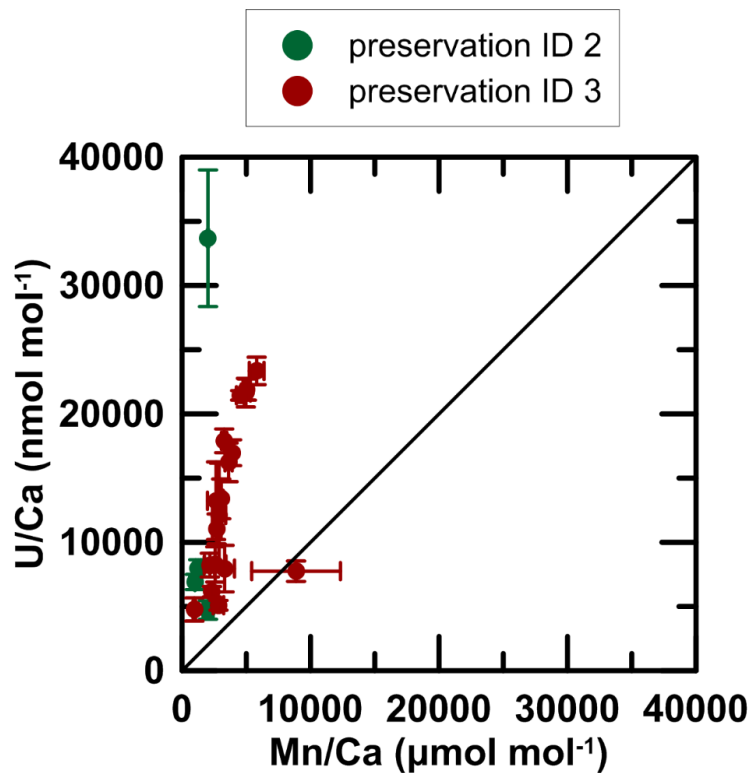


Figure 3.13 U/Ca versus Mn/Ca of LA-ICP-MS single specimen analyses, colour-coded according to the respective preservation ID, with 2 indicating moderate and 3 indicating major diagenetic alterations. This suggests a proportionally larger incorporation of U into authigenic carbonates compared to Mn at IODP Site U1343.

Nevertheless, authigenic carbonates also bear unique opportunities for new approaches to study environmental change through time. Recent studies suggest authigenic foraminiferal U/Mn as a proxy to reconstruct sedimentary redox conditions, linked to bottom water oxygenation and sedimentary carbon burial (Gottschalk et al., 2016, Chen et al., 2017). At IODP Site U1343 an increase in U/Ca and Mn/Ca ratios can be observed in foraminifera with a higher degree of diagenetic alteration (Figure

3.6), likely associated with stronger microbial activity and more reducing conditions in the sediment. Even though both U/Ca and Mn/Ca are positively correlated with diagenetic alterations, the increase in U/Ca is proportionally larger (Figure 3.13), in line with higher U/Mn ratios reflecting more reducing conditions. Thus, although the presence of authigenic carbonates complicates the use of traditional proxies in paleoceanography, their trace metal composition may provide valuable information with respect to changes in the sedimentary redox chemistry through time.

3.5 Conclusions

Visual and geochemical evidence of foraminiferal species *E. batialis* at IODP Site U1343, underlying the high productivity region of the ‘Green Belt’ in the eastern Bering Sea, demonstrate the occurrence of abundant authigenic calcite and authigenic pyrite framboids. Foraminifera-bound authigenic calcite is of early diagenetic origin and forms as a result of bicarbonate production during organoclastic sulphate reduction and AOM. Whereas authigenic calcite within the SMTZ is most likely HMC, LMC forms in the zone of sulphate reduction, as a result of the inhibiting effect of pore water sulphate concentrations on Mg incorporation into inorganically precipitated carbonates.

In addition to increased Mg concentrations, authigenic calcite is characterised by increased U/Ca, Mn/Ca, Fe/Ca, and Sr/Ca ratios. Whereas U, Mn, and Fe incorporation is likely controlled by the redox-chemistry in the sediment-pore water system, indicating precipitation under suboxic conditions, in line with an early diagenetic origin, Sr incorporation likely results from changes to the calcite crystal structure caused by the higher concentrations of Mg.

EPMA maps of foraminifera with minor to major diagenetic alterations demonstrate the spatial distribution of authigenic calcite within the foraminiferal tests, including crust formation, recrystallization, and HMC banding along biologically defined laminations within the test wall. This indicates that samples with minor diagenetic alterations (little or no discolouration, translucent test walls, and prominent morphological features), associated with authigenic carbonates crusts can be utilised in paleoclimate reconstructions following a chemical cleaning study, to target the removal of authigenic coatings. In the case of moderate and major diagenetic

alteration, chemical cleaning of foraminifera test is unlikely to completely remove the authigenic calcite. However, Mg/Ca of benthic foraminifera can be applied for BWT reconstructions when thresholds of elements primarily associated with the authigenic carbonates are established. Resulting from the enhanced incorporation of U into authigenic carbonates, compared to primary foraminiferal calcite, U/Ca provides a suitable means to determine appropriate contamination thresholds. The threshold should be based on a minimum contribution of authigenic Mg/Ca to the measured Mg/Ca ratios. However, the thresholds are likely to vary between studies, based on the chemical cleaning procedures, analytical instruments used, and the study site.

Additionally, the geochemistry of authigenic carbonates at Site U1343 suggests an increase in the U/Mn ratio associated with a higher degree of diagenetic alteration, most likely resulting from enhanced microbial activity, indicating more reducing conditions in the sediments. This is in line with previous studies utilising authigenic foraminiferal U/Mn as a proxy for bottom water oxygen concentrations (Gottschalk et al., 2016, Chen et al., 2017).

All in all, this study indicates distinct changes in the foraminiferal geochemistry in relation to early diagenesis in methane-bearing continental margin sediments. However, it also demonstrates the potential to use traditional and new paleoclimate proxies, such as Mg/Ca for BWT reconstructions and the deconvolution of the $\delta^{18}\text{O}_b$ signal into its temperature and ice volume components and U/Mn for sedimentary redox conditions, in continental margin settings, often associated with high sedimentation rates, representing valuable archives to study past environmental changes at millennial to orbital resolution.

4. Pleistocene bottom water temperature evolution in the eastern Bering Sea

4.1 Introduction

Earth's climate underwent fundamental changes across the mid to late Pleistocene, as seen most prominently in records of benthic foraminiferal oxygen isotopes ($\delta^{18}\text{O}_b$). The Mid-Pleistocene transition (MPT, 1.2-0.7 Ma) is characterized by a lengthening of the glacial/interglacial (G/IG) frequency from 41 ka to 100 ka, together with an increase in the amplitude of $\delta^{18}\text{O}_b$, and a more prominent sawtooth pattern during late Pleistocene climate oscillations (Shackleton and Opdyke, 1976, Pisias and Moore Jr, 1981, Ruddiman et al., 1989, Mudelsee and Schulz, 1997, Clark et al., 2006). Our understanding of climate dynamics across this important time period revolves around high-resolution records of global to regional climate change from climatically sensitive areas to decipher the role of internal climate feedbacks for the MPT. Mechanisms proposed to drive MPT climate change invoke shifts in ice sheet dynamics (Clark and Pollard, 1998, Clark et al., 2006, Raymo et al., 2006, Elderfield et al., 2012), thermohaline circulation reorganization (Raymo et al., 1990, Schmieder et al., 2000, Sexton and Barker, 2012, Pena and Goldstein, 2014, Lear et al., 2016), or a change in climate boundary conditions, such as a threshold response to global cooling potentially associated with atmospheric CO_2 drawdown (Oerlemans, 1984, Raymo et al., 1997, Berger et al., 1999, Tziperman and Gildor, 2003, Rial, 2004, Hönisch et al., 2009, Lear et al., 2016).

Understanding ice sheet dynamics across the Pleistocene hinges on our ability to deconvolve the $\delta^{18}\text{O}_b$ record into its ice volume (oxygen isotope composition of seawater ($\delta^{18}\text{O}_w$)) and bottom water temperature (BWT) component. Three records of paired $\delta^{18}\text{O}_b$ and benthic foraminiferal Mg/Ca BWT exist across the MPT, reporting distinctly different ice volume histories across the Pleistocene (Sosdian and Rosenthal, 2009, Elderfield et al., 2012, Ford et al., 2016). Whereas North Atlantic records from Deep Sea Drilling Project (DSDP) Site 607 (41.0 °N, 33.0 °W, 3427 m water depth) show no pronounced long-term trend in continental ice volume across the MPT

(Sosdian and Rosenthal, 2009, Ford et al., 2016), southwestern Pacific Ocean Drilling Program (ODP) Site 1123 (41.8 °S, 171.5 °W, 3290 m water depth) indicates a step-like increase of continental ice volume during marine isotope stage (MIS) 22 (866-900 ka) (Elderfield et al., 2012). Whilst the earlier record at Site 607 (Sosdian and Rosenthal, 2009) has been challenged, based on the potential carbonate saturation state ($\Delta[\text{CO}_3^{2-}]$) effect on Mg/Ca of epifaunal benthic foraminiferal species (Yu and Broecker, 2010, Elderfield et al., 2012), re-analysis of infaunal benthic foraminiferal species at the same Site, yield very similar results with no long-term trend in continental ice volume across the MPT (Ford et al., 2016). These differences in the reconstructed $\delta^{18}\text{O}_w$ highlight the importance of circulation and water mass changes for the local $\delta^{18}\text{O}_w$ (Ford et al., 2016) and call upon additional high resolution records of paired $\delta^{18}\text{O}_b$ and BWT to reconcile the MPT ice volume evolution.

Resulting from its sheer size, holding more than 50% of Earth's surface water, the Pacific Ocean is often considered to reflect whole ocean changes on timescales longer than the ocean's overturning circulation (>1000 years), making it ideal to study the history of bottom water temperature and global $\delta^{18}\text{O}_w$ changes. Further, high sedimentation rates at International Ocean Discovery Program (IODP) Site U1343 in the eastern Bering Sea of $34 \pm 11 \text{ cm ka}^{-1}$ (Asahi et al., 2016), suggest the potential to study MPT BWT evolution at sub-orbital to orbital resolution.

BWT at any given location in the deep ocean is influenced by the temperature of different contributing water masses, which in turn is driven by surface ocean processes in the areas of deep water formation. Today, the deep Bering Sea is bathed in North Pacific Deep Water (NPDW), one of the oldest water masses in the modern ocean, fed by southern sourced waters entering the deep Pacific via the Deep Western Boundary Current (DWBC) (Hall et al., 2001), consisting mainly of Circum Polar Deep Water (CDW) with some entrainment of North Atlantic Deep Water (NADW) (Venuti et al., 2007). Southern sourced deep waters form around the Antarctic continent, primarily in the Weddell and Ross Sea (Killworth, 1983, Broecker et al., 1998), as a result of brine rejection during sea ice freezing, producing dense and cold water masses ($\sim 0\text{-}1^\circ\text{C}$, $\sim 34.7 \text{ psu}$) (Locarnini et al., 2006, Antonov et al., 2006). NADW, on the other hand, is formed in the North Atlantic, where vigorous heat exchange between the ocean and the atmosphere causes buoyancy loss of relatively warm and saline water masses, promoting thermohaline overturning (Killworth, 1983, Kuhlbrodt et al., 2007)

forming comparatively warm and saline deep water (~ 2.5 °C, ~ 34.9 psu) (Antonov et al., 2006, Locarnini et al., 2006). In addition to surface ocean processes, aging deep water masses are influenced by the geothermal heat flux at the seafloor (Adcroft et al., 2001). Consequently, Bering Sea BWT today is influenced by surface ocean processes in the North Atlantic and primarily around Antarctica, together with the influence of water mass aging.

On G/IG timescales, however, the oceans have experienced distinctive changes in the thermohaline overturning circulation and BWT. BWT records from the last glacial maximum (LGM) in the Pacific Ocean between 1000 m and 3500 m, demonstrate temperatures between -1.5 °C and 0 °C, with an LGM-Holocene BWT amplitude (Δ BWT) of ~ 2 °C (Waelbroeck et al., 2002, Adkins et al., 2002, Martin et al., 2002, Gorbarenko et al., 2002, Elderfield et al., 2010, Woodard et al., 2014, McClymont et al., 2016). Across the Pleistocene, BWT at ODP Site 1123 in the southwestern Pacific, reconstructed from Mg/Ca of *Uvigerina* spp., shows glacial values between -0.5 °C and -1.75 °C, with no long-term trend over the past 1.5 Ma (Elderfield et al., 2012). Interglacial BWT, on the other hand, increases from ~ 1 °C to ~ 2 °C starting during MIS 21 (Elderfield et al., 2012). In comparison, North Atlantic BWT, as reconstructed from *Cibicidoides wuellerstorfi/Oridorsalis umbonatus* and *Uvigerina* spp. at DSDP Site 607 demonstrates long-term cooling between 1.5-0.5 Ma of $1-3$ °C, during both glacial and interglacial intervals (Sosdian and Rosenthal, 2009, Ford et al., 2016). Considering, that these Sites are from different ocean basins, differences in the BWT history likely arise from changes in the water mass contribution, associated with changes in the thermohaline overturning circulation and/or changes in the source water properties across the Pleistocene.

The MPT is associated with a pronounced perturbation in the thermohaline circulation, particularly between MIS 24 and MIS 22 (866-936 ka) characterised by a decrease in the NADW production and enhanced influence of southern sourced bottom waters (Pena and Goldstein, 2014). Further, post-MPT glacials are marked by similarly weak Atlantic deep water formation, whereas the interglacial thermohaline circulation seems to recover following the pronounced perturbation around 900 ka (Raymo et al., 1990, Raymo et al., 1997, Pena and Goldstein, 2014). Both northern and southern high latitudes are characterised by sea surface temperature (SST) cooling prior to and across the MPT (McClymont et al., 2008, Lawrence et al., 2009, Martínez-García et al., 2010,

McClymont et al., 2013), suggesting cooling in deep water source regions during both glacials and interglacials (McClymont et al., 2013). Additionally, foraminiferal carbon isotope ($\delta^{13}\text{C}$) and neodymium isotope (ϵ_{Nd}) evidence across the last glacial cycle and the late Pleistocene, argue for a strengthened intermediate-depth overturning (Curry and Oppo, 2005, Horikawa et al., 2010, Max et al., 2012, Knudson and Ravelo, 2015b, Howe et al., 2016). In the modern North Pacific intermediate waters (300-700 m) form via mixing of nutrient-rich subsurface waters with brines formed through sea ice freezing in the Sea of Okhotsk (Talley, 1993, Shcherbina et al., 2003). Evidence from the Bering Sea suggests increased formation of North Pacific Intermediate Water (NPIW) during glacial of the last 1.2 Ma (Knudson and Ravelo, 2015b), potentially coinciding with a deepening of this water mass, as suggested for the LGM. Whilst $\delta^{18}\text{O}_b$ from across the Bering Sea suggests a divide of intermediate and deep waters around ~1000 m water depth during MIS 2 (Cook et al., 2016), other studies from the Gulf of Alaska demonstrate decreased ventilation ages during Heinrich stadial 1 (HS1, 14.7 ka to 18 ka) at ~3500 m water depth. As the maximum depth of NPIW during glacial intervals remains elusive, changes in the contribution of NPIW versus NPDW to the deep Bering Sea could have influenced the BWT on G/IG timescales across the mid to late Pleistocene.

Here I present records of BWT from IODP Site U1343 in the deep eastern Bering Sea ($57^{\circ}33.4'\text{N}$, $176^{\circ}49.0'\text{W}$, 1953 m water depth), based on a composite Mg/Ca record of infaunal benthic foraminiferal species to add a North Pacific perspective to BWT and ice volume changes across the MPT. The BWT record demonstrates distinctive G/IG variability and long-term changes in the deep Bering Sea, indicating potential changes in the water mass contribution across the Pleistocene. Further, BWT in conjunction with previously published $\delta^{18}\text{O}_b$ at Site U1343 (Asahi et al., 2016, Kender et al., in review), is in line with two possible scenarios of Pleistocene ice volume history. The observed trends can be explained by either no long-term increase in continental ice volume across the MPT with a pronounced event centred on MIS 22 (866-900 ka) characterised by a relatively warm and high $\delta^{18}\text{O}_w$ water mass in the deep Bering Sea, or increased continental ice volume during/prior to MIS 22 with post-MPT glacials being characterised by increased contribution of NPIW to the deep Bering Sea.

4.2 Materials and methods

4.2.1 Composite benthic foraminiferal Mg/Ca record

The calcareous benthic foraminiferal assemblage at Site U1343 is dominated by species tolerant to oxygen-depleted conditions, often found in high productivity areas (Setoyama and Kaminski, 2015, Asahi et al., 2016). This includes primarily elongated, tapered, and/or flattened planispiral typically infaunal species, including the genera *Elphidium*, *Islandiella*, *Uvigerina*, *Eubuliminella*, and *Globobulimina*. For the purpose of this study, the three most abundant and consistently occurring shallow infaunal foraminiferal species *Elphidium batialis*, *Islandiella norcrossi*, and several species of the genus *Uvigerina*, including *Uvigerina bifurcata*, *Uvigerina senticosa*, and *Uvigerina peregrina*, grouped as *Uvigerina* spp. were chosen. Foraminifera were picked from the 150-250 μm and $>250 \mu\text{m}$ size fractions. As a result of the higher abundance, mono-specific foraminiferal samples from the 150-250 μm fraction with a weight $>80 \mu\text{g}$ were used for down-core geochemical analyses. In total 80 *E. batialis*, 89 *I. norcrossi*, and 29 *Uvigerina* spp. samples were gently crushed between two glass plates, homogenised, and transferred to acid-cleaned micro-centrifuge tubes. At this point visible contaminants, primarily pyrite framboids were removed. Often, however, the pyrite framboids disintegrated making a complete removal impossible, resulting in elevated Fe/Ca ratios in some samples. Following an extensive cleaning study (Chapter 2 section 2.3.7) the samples were cleaned according to the Cd-cleaning protocol (Boyle, 1983, Boyle and Keigwin, 1985). Subsequently, the cleaned samples were dissolved in 120 μl of 0.065M HNO_3 and centrifuged to remove any potential remaining particulate contaminants, before splitting and transferring the samples for analysis.

All samples were analysed on a Thermo Element XR High Resolution Inductively Coupled Plasma Mass Spectrometer (ICP-MS) at Cardiff University. Each sample was analysed twice, with the first analysis aimed at determining the Ca concentration in the sample, to enable matrix matching of the standards for elemental ratio calculation. At the beginning and the end of every run a set of two consistency standards was analysed containing $1.24 \text{ mmol mol}^{-1}$ and $7.15 \text{ mmol mol}^{-1}$ Mg/Ca, respectively. Across the time period of this study the external reproducibility was $\pm 0.70 \%$ and $\pm 0.64 \%$ (relative standard deviation (r.s.d.)), respectively. The analytical precision for

Mg/Ca was ± 1.01 % on average (± 3.20 % maximum, r.s.d.), ± 0.85 % on average (± 2.70 % maximum, r.s.d.), and ± 1.09 % on average (± 2.13 % maximum, r.s.d.) for *E. batialis*, *I. norcrossi* and *Uvigerina* spp., respectively.

4.2.2 LA-ICP-MS measurements of *E. batialis* Mg/Ca across the LGM-Holocene transition

To understand the BWT sensitivity of *E. batialis*, two samples from the size fraction >250 μm were measured across the LGM-Holocene transition using laser ablation inductively coupled plasma mass spectrometry (LA-ICP-MS). Measurements were performed at Cardiff University using an ArF excimer 193 nm laser ablation system with dual volume laser ablation cell (RESOLUTION S-155 ASI) coupled to a Thermo Scientific™ ELEMNT XR™ magnetic sector field ICP-MS (Table 3.2). LA-ICP-MS ablation was performed on five to six specimens per sample with six laser spots per specimen. Sample preparation, calibration, and contamination screening was performed as outlined in Chapter 3 section 2.4.1.

Compared to LA-ICP-MS samples, ICP-MS samples were measured on foraminiferal tests from the size fraction 150-250 μm , thus a size-fraction test was performed, to test for a size-specific offset in foraminiferal Mg/Ca. In total four samples (172.02 m core composite depth below seafloor (CCSF-A), 229.42 m CCSF-A, 299.57 m CCSF-A, 305.63 m CCSF-A) were ablated from both the 150-250 μm and >250 μm size fraction. No significant difference in the variance of Mg/Ca ratios of the two size fractions was found ($p > 0.25$, $n = 21$), indicating that LA-ICP-MS studies on foraminifera from >250 μm are applicable to the 150-250 μm size fraction.

4.2.3 Secondary effects on foraminiferal Mg/Ca

4.2.3.1 Early carbonate diagenesis

As discussed in Chapter 3 detailed single specimen imaging and geochemical analyses revealed abundant authigenic carbonates on foraminifera specimens from IODP Site U1343, associated with increased Mg/Ca, Sr/Ca, U/Ca, Mn/Ca, and Fe/Ca ratios in diagenetically altered tests. This is supported by an extensive cleaning test (Chapter 2 section 2.3.7) indicating that even after rigorous cleaning according to the Cd-protocol (Boyle, 1983, Boyle and Keigwin, 1985), some samples show elevated Mg/Ca, U/Ca,

and Mn/Ca compared to expected values for primary foraminiferal calcite. It is thus necessary to establish threshold values of trace metals primarily associated with contamination phases, in order to distinguish ‘pristine’ and contaminated foraminifera samples.

Fe/Ca values in samples measured using ICP-MS are likely to be influenced by pyrite contamination, which is why Fe/Ca ratios are not included in the authigenic carbonate screening process, however pyrite does not contain Mg (Pearson et al., 2009). In addition to trace metals associated with the authigenic carbonates, Al/Ca was also monitored, typically associated with clay contamination. Most samples were found to be below the proposed threshold of $100 \mu\text{mol mol}^{-1}$ (Barker et al., 2003) and there is no correlation of Al/Ca and Mg/Ca down-core (Figure 4.1). However, the lack of correlation could result from authigenic carbonate formation, influencing the Mg/Ca but not the Al/Ca ratios. Thus, to avoid potential bias by silicate minerals all samples with $\text{Al/Ca} > 100 \mu\text{mol mol}^{-1}$ were rejected from the down-core record.

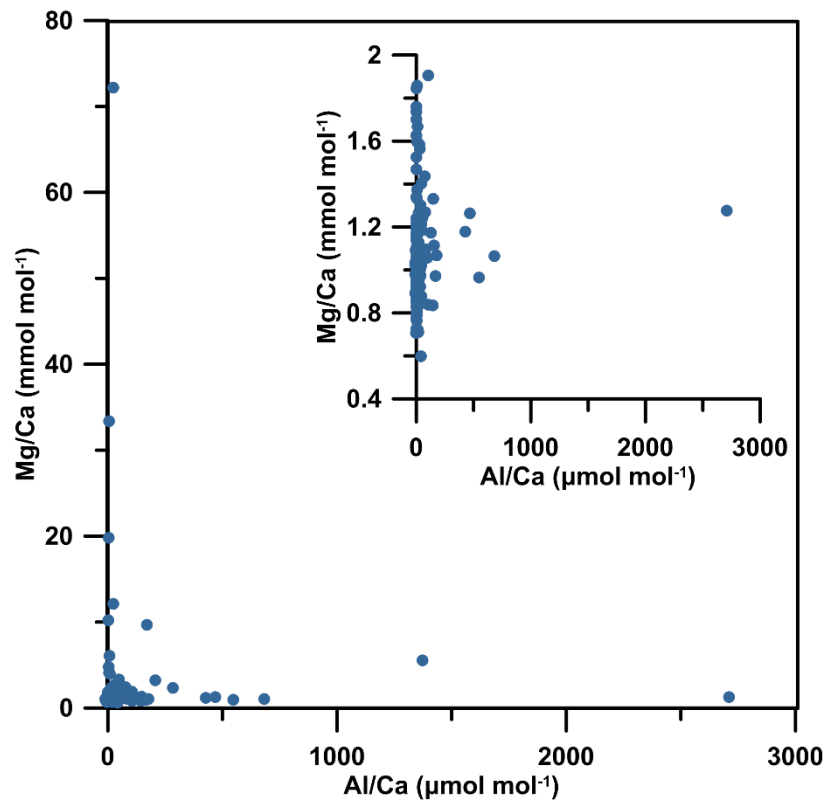


Figure 4.1 Al/Ca versus Mg/Ca of all samples (bottom left) measured for trace elements on the ICP-MS (80 *E. batialis*, 89 *I. norcrossi*, and 29 *Uvigerina* spp.), together with Al/Ca versus Mg/Ca for $\text{Mg/Ca} < 2 \text{ mmol mol}^{-1}$ (top right corner).

Mn/Ca values of foraminiferal samples cleaned according to the Cd-protocol (Boyle, 1983, Boyle and Keigwin, 1985) are mainly below $100 \mu\text{mol mol}^{-1}$, indicating little or no contribution of Mn-Fe-oxides to the measured foraminiferal trace metal values (Barker et al., 2003). Instead, increased Mn/Ca is typically associated with increased U/Ca ratios, indicative of authigenic carbonate contamination. U/Ca was used as the primary trace metal ratio to monitor the effect of authigenic carbonates on Mg/Ca values. U/Ca of reductively cleaned foraminiferal samples at Site U1343 varies between $6\text{-}5751 \text{ nmol mol}^{-1}$, $4\text{-}1405 \text{ nmol mol}^{-1}$, and $5.5\text{-}1494 \text{ nmol mol}^{-1}$ for *E. batialis*, *I. norcrossi*, and *Uvigerina* spp., respectively, with a strong positive correlation of Mg/Ca and U/Ca for the entire dataset ($R^2 = 0.93$, $p < 0.01$, $n = 173$) and the individual species (*E. batialis*: $R^2 = 0.95$, $p < 0.01$, $n = 70$; *I. norcrossi*: $R^2 = 0.90$, $p < 0.01$, $n = 78$; *Uvigerina* spp.: $R^2 = 0.93$, $p < 0.01$, $n = 25$). At U/Ca values below $200 \text{ nmol mol}^{-1}$ the positive correlation of Mg/Ca and U/Ca subsides, with only *E. batialis* displaying a weak positive correlation ($R^2 = 0.34$, $p < 0.05$, $n = 41$). I thus adopted $200 \text{ nmol mol}^{-1}$ U/Ca as the threshold for authigenic carbonate contamination.

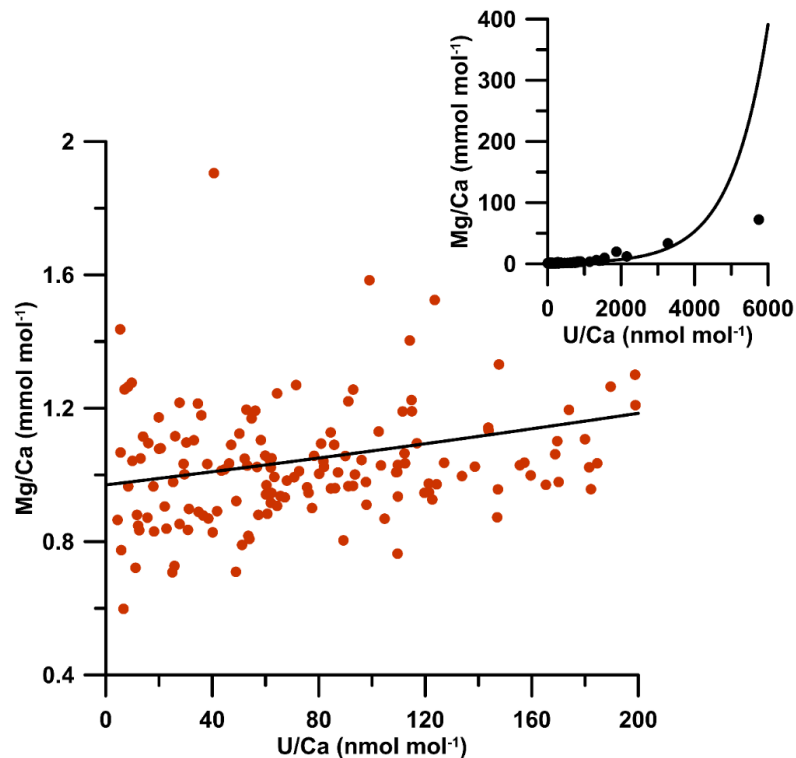


Figure 4.2 U/Ca versus Mg/Ca of all samples measured for trace metals on the ICP-MS (*E. batialis* $n = 70$, *I. norcrossi* $n = 78$, and *Uvigerina* spp. $n = 25$) (black, top right corner) including the exponential regression ($y = 0.97e^{0.001x}$) (black line). On the bottom left (orange) are all Mg/Ca values with $U/Ca < 200 \text{ nmol mol}^{-1}$ together with the same exponential regression (black line).

The overall relationship of Mg/Ca and U/Ca is best described by an exponential regression ($R^2 = 0.85$, $y = 0.97e^{0.001x}$), that yields a particularly good fit within the lower range of Mg/Ca and U/Ca ratios and, compared to a linear regression, has a positive y-intercept similar to expected Mg/Ca ratios of primary foraminiferal calcite (Figure 4.2). Following this regression a U/Ca ratio of 200 nmol mol⁻¹ suggest a maximum contribution of authigenic carbonate to the measured Mg/Ca ratio of 0.22 ± 0.03 mmol mol⁻¹ (s.e.), with the uncertainty based on the reported range of U/Ca values in primary foraminiferal calcite of up to 23 nmol mol⁻¹ (Russell et al., 2004, Raitzsch et al., 2011, Boiteau et al., 2012, Chen et al., 2017). An uncertainty of 0.22 ± 0.03 mmol mol⁻¹ (s.e.) is close to the procedural uncertainty associated with the Mg/Ca record down-core, supporting 200 nmol mol⁻¹ U/Ca as a valuable threshold for authigenic carbonate contamination. For error propagation of BWT values 0.22 mmol mol⁻¹ was adopted as the procedural uncertainty of all Mg/Ca values.

4.2.3.2 The effect of salinity on foraminiferal Mg/Ca

To date, a potential effect of salinity on benthic foraminiferal Mg/Ca has only been determined for one species (Dissard et al., 2010, Geerken et al., 2018). *Ammonia tepida* is characteristic of brackish waters and a salinity effect on Mg/Ca has been proposed altering paleotemperature reconstructions by 1 °C per 2 psu (Dissard et al., 2010), with a positive correlation of Mg/Ca and salinity (Dissard et al., 2010, Geerken et al., 2018).

At Site U1343 salinity changes may arise from changes in the water mass contribution of NPDW versus NPIW on orbital timescales. Modern NPIW is defined as a salinity minimum in the North Pacific near the 26.8 σ_θ isopycnal surface (Yasuda, 1997), with a salinity of 33.9 at GLODAP v2 station 41047-3 (B) (Olsen et al., 2016). At ~2000 m water depth the eastern Bering Sea has a salinity of 34.6 (Olsen et al., 2016), suggesting a salinity difference of 0.7 between NPIW and NPDW bathing Site U1343 today. Hence, entrainment of NPIW at Site U1343 could potentially increase benthic foraminiferal Mg/Ca ratios, if a similar salinity sensitivity of *E. batialis*, *I. norcrossi*, and *Uvigerina* spp. to *A. tepida* is assumed. An inferred salinity change of 0.7, however, would entail a temperature bias <0.5 °C, within the uncertainty of BWT reconstructions at Site U1343 (see below). Hence, no salinity correction is performed for Mg/Ca ratios of *E. batialis*, *I. norcrossi*, and *Uvigerina* spp., as further research is

needed to determine the sensitivity of deep sea infaunal benthic foraminiferal Mg/Ca to salinity changes.

4.2.3.3 The effect of the carbonate saturation state on primary foraminiferal Mg/Ca

Modern benthic foraminifera seem to discriminate against Mg at low $\Delta[\text{CO}_3^{2-}]$, suggesting a $\Delta[\text{CO}_3^{2-}]$ effect on Mg/Ca ratios (Rosenthal et al., 1997, Elderfield et al., 2006, Rosenthal et al., 2006, Yu and Elderfield, 2008, Elderfield et al., 2010). $\Delta[\text{CO}_3^{2-}]$ at ~2000 m water depth close to Site U1343 (GLODAP v2 station 41047-3 (B) (Olsen et al., 2016)) is $-14 \mu\text{mol kg}^{-1}$, highly undersaturated with respect to CaCO_3 . Depending on the contribution of different water masses on G/IG timescales, glacial bottom waters in the Bering Sea may have had even lower $\Delta[\text{CO}_3^{2-}]$, as suggested from increased concentrations of remineralised carbon in NPDW during glacials of the last 150 ka (Jaccard et al., 2009). Typically, infaunal benthic foraminifera are favoured over epifaunal species for Mg/Ca analyses, as the $\Delta[\text{CO}_3^{2-}]$ effect is reduced in pore waters compared to bottom waters (Mawbey and Lear, 2013). However, due to differences in the habitat depth and migration within the sediment site/species specific variations might occur.

E. batialis in the neighbouring Sea of Okhotsk has an average habitat depth of 0.5-1.7 cm (Bubenshchikova et al., 2008), characterising it as a shallow infaunal foraminiferal species, similar to the proposed depth habitat of *Uvigerina* spp. of 1-2 cm (Tachikawa and Elderfield, 2002). *I. norcrossi* also has an infaunal habitat, however may be migrating between shallower and deeper layers in search of a preferred microhabitat (Hunt and Corliss, 1993, Ivanova et al., 2008, Ishimura et al., 2012).

One possible way to examine the effect of $\Delta[\text{CO}_3^{2-}]$ on Mg/Ca ratios is by co-examining Li/Ca and Mg/Ca ratios (Mawbey and Lear, 2013). Benthic foraminiferal Li/Ca ratios have been shown to positively co-vary with $\Delta[\text{CO}_3^{2-}]$ (Lear and Rosenthal, 2006, Lear et al., 2010), whereas a negative relationship with temperature is observed (Marriott et al., 2004). Thus co-variation of Li/Ca and Mg/Ca down-core could indicate a $\Delta[\text{CO}_3^{2-}]$ effect on Mg/Ca ratios (Mawbey and Lear, 2013). Both *E. batialis* and *Uvigerina* spp. Mg/Ca ratios show covariation with Li/Ca between 600 ka to 450 ka, just prior to 800 ka, and around 1100 ka (Figure 4.3), indicating a potential effect of $\Delta[\text{CO}_3^{2-}]$ on Mg/Ca ratios across this interval. *I. norcrossi*, on the other hand, does

not demonstrate covariation across these intervals, in line with a potentially deeper habitat of this migratory infaunal species. This is further supported by a larger amplitude variation in Li/Ca of *Uvigerina* spp. and *E. batialis* compared to *I. norcrossi*, suggesting an increased influence of $\Delta[\text{CO}_3^{2-}]$ on the former two species.

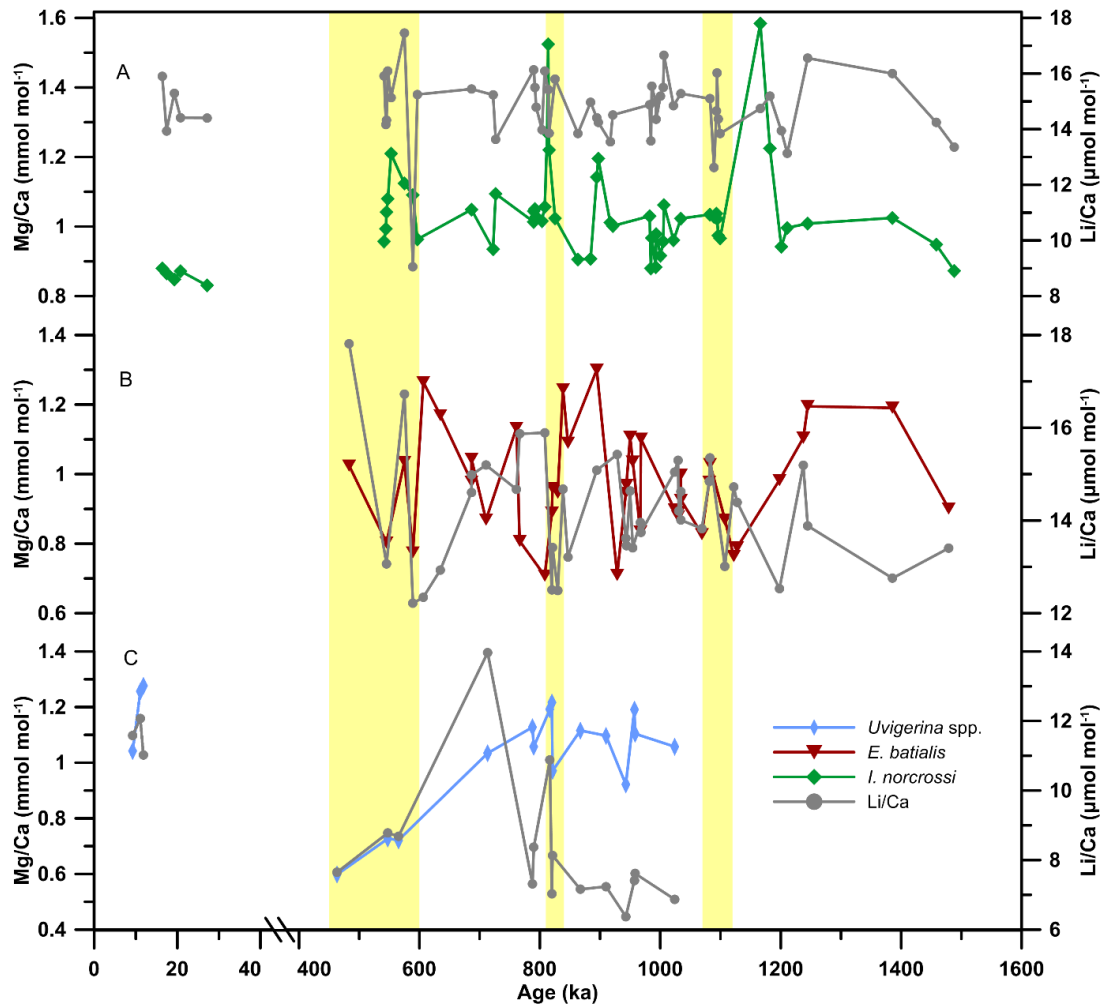


Figure 4.3 Li/Ca (grey) versus Mg/Ca of (A) *I. norcrossi* (green), (B) *E. batialis* (red), and (C) *Uvigerina* spp. (blue) down-core. The yellow vertical bars indicate intervals of visually identifiable covariation for one or more species.

Do to the lack of records of past $\Delta[\text{CO}_3^{2-}]$ in the North Pacific across this time interval a definite influence of $\Delta[\text{CO}_3^{2-}]$ on shallow infaunal Mg/Ca ratios cannot be determined. For the purpose of this study I am assuming that the influence of $\Delta[\text{CO}_3^{2-}]$ on Mg/Ca of *E. batialis*, *I. norcrossi*, and *Uvigerina* spp. is minimal.

4.2.3.4 Post-depositional dissolution of foraminiferal tests

Scanning electron microscope (SEM) images of *E. batialis* specimens from IODP Site U1343 demonstrate dissolution features, such as broken chambers, etched surfaces, and lattice-like calcite structures inside the test walls (Figure 3.3), indicating the importance to test the effect of dissolution on foraminiferal Mg/Ca ratios. Mg/Ca in planktonic foraminifera has been shown to be sensitive to post-depositional dissolution (Brown and Elderfield, 1996, Regenberg et al., 2006), likely as a result of the inhomogeneous distribution of Mg in planktonic foraminiferal species (Brown and Elderfield, 1996, Regenberg et al., 2006, Jonkers et al., 2016). Compared to planktonic foraminifera, Mg in benthic foraminifera has been suggested to be more homogeneously distributed (Curry and Marchitto, 2008), also seen in Electron probe microanalyser (EPMA) Mg/Ca maps of well-preserved foraminiferal species from Site U1343 (Figure 3.8).

To test the influence of post-depositional dissolution on benthic foraminifera (150-250 μm) from Site U1343, Mg/Ca ratios were monitored against the average shell weight of a representative subset of samples comprising all species. However, shell weights at Site U1343 may be influenced by authigenic carbonate formation, thus only shell weights of samples with U/Ca $< 200 \text{ nmol mol}^{-1}$, thought to represent minor authigenic carbonate contribution, were considered. If dissolution would lead to preferential loss of Mg from the foraminiferal carbonate, a positive correlation of shell weight and Mg/Ca is to be expected. Mg/Ca ratios of all three species show no correlation with average shell weights ($R^2 = -0.16$, $p > 0.45$, $n = 25$; $R^2 = 0.12$, $p > 0.5$, $n = 33$; $R^2 = -0.11$, $p > 0.5$, $n = 6$ for *E. batialis*, *I. norcrossi*, and *Uvigerina* spp., respectively) (Figure 4.4), indicating no or only little bias of benthic foraminiferal Mg/Ca ratios by post-depositional dissolution at Site U1343.

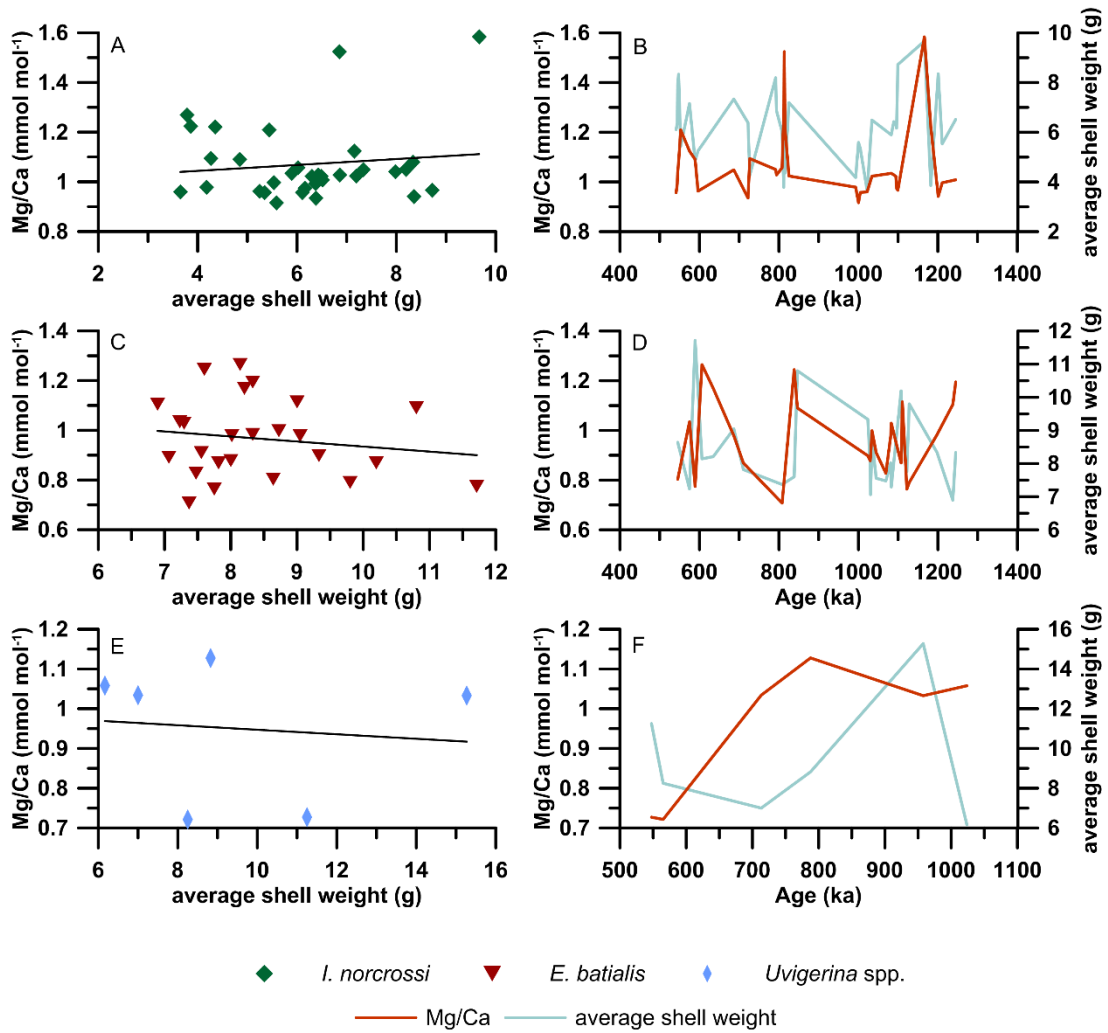


Figure 4.4 Cross plots of the shell weight of a subset of (A) *I. norcrossi* (green diamonds), (C) *E. batialis* (red triangles), and (E) *Uvigerina* spp. (blue diamonds) versus Mg/Ca, together with Mg/Ca (orange) and shell weight (light blue) of (B) *I. norcrossi*, (D) *E. batialis*, and (F) *Uvigerina* spp. downcore. There is no significant correlation of the shell weight with Mg/Ca for any of the three species ($R^2 = -0.16$, $p > 0.45$, $n = 25$; $R^2 = 0.12$, $p > 0.5$, $n = 33$; $R^2 = -0.11$, $p > 0.5$, $n = 6$ for *E. batialis*, *I. norcrossi*, and *Uvigerina* spp., respectively).

4.2.3.5 Seawater Mg/Ca variations across the Pleistocene

Changes in the Mg/Ca composition of seawater have been shown to influence the partition coefficient of Mg into foraminiferal calcite (Hasiuk and Lohmann, 2010, Evans and Müller, 2012). Even though only small changes are expected on time periods < 1 Ma (the residence time of Ca in seawater), the Mg/Ca seawater curve established in Fantle and DePaolo (2006) was used to test the effect of changing Mg/Ca seawater values on measured Mg/Ca at Site U1343 across the Pleistocene

modifying (Equation 2.1), following the approach outlined in Evans and Müller (2012) and McClymont et al. (2016).

$$Mg/Ca_{corrected} = (0.86 + 0.125 \times BWT) \times [(Mg/Ca_{seawater}^{t=t})^H / (Mg/Ca_{seawater}^{t=0})^H] \quad (\text{Equation 2.1})$$

Where $t=0$ is the modern, $t=t$ is the given sample age, and H is the species-specific power component of the relationship between foraminiferal Mg/Ca and the Mg/Ca of seawater.

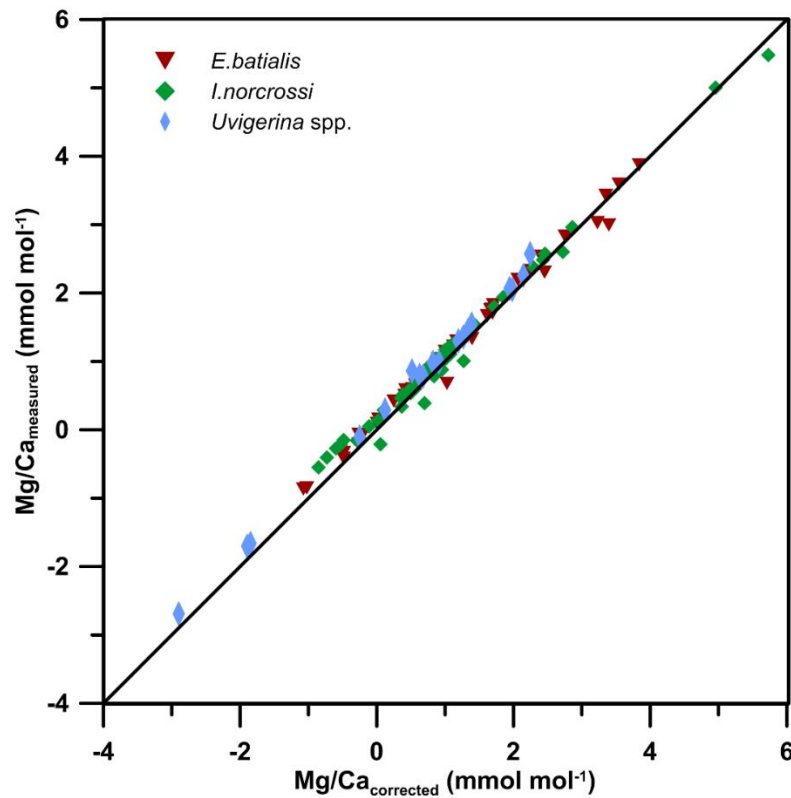


Figure 4.5 Measured Mg/Ca versus Mg/Ca corrected for variations in seawater Mg/Ca across the Pleistocene using the $Mg/Ca_{seawater}$ curve published in Fantle and DePaolo (2006), according to the equation: $Mg/Ca_{corrected} = (0.86 + 0.125 \times BWT) \times [(Mg/Ca_{seawater}^{t=t})^H / (Mg/Ca_{seawater}^{t=0})^H]$, where $t=0$ is the modern, $t=t$ is the given sample age, and H is the species-specific power component.

As no species-specific estimate of H is available for any of the three foraminiferal species used in this study, I adopt the approach outlined in Woodard et al. (2014) (*Uvigerina* spp.), assuming $H = 0.41$ (Delaney et al., 1985) (Figure 4.5), which is also within the range of a H value of 0.2-0.5, as predicted for the epifaunal benthic foraminiferal species *Oridorsalis umbonatus* (Lear et al., 2015). Following this

approach, BWT corrected for changes in seawater Mg/Ca are slightly lower in the early Pleistocene and higher during the late Pleistocene. The maximum offset in corrected versus uncorrected BWT across the entire interval is 0.4 °C, which is within the error of the temperature calibration (± 1.1 °C standard error (s.e.)) and together with the large uncertainty associated with the seawater Mg/Ca reconstructions led to the conclusion to report uncorrected values of BWT across the Pleistocene for the eastern Bering Sea.

4.3 Results

4.3.1 Multi-species Mg/Ca ratios at Site U1343

After applying the trace metal thresholds, established in section 2.3.1, Mg/Ca values of the remaining 41 *E. batialis*, 56 *I. norcrossi*, and 18 *Uvigerina* spp. samples range between 0.70-1.30 mmol mol⁻¹, 0.83-1.58 mmol mol⁻¹, and 0.60-1.26 mmol mol⁻¹, respectively. These values are in line with previously reported Mg/Ca ratios of *I. norcrossi* and *Uvigerina* spp. in the high-latitude deep ocean of 1.01-1.47 mmol mol⁻¹ and 0.68-1.42 mmol mol⁻¹, respectively (Lear et al., 2002, Kristjánssdóttir et al., 2007). There are no reported Mg/Ca values for *E. batialis*, however, a study from the Arctic Ocean reports Mg/Ca ratios of *Elphidium clavatum*, which is of the same genus as *E. batialis*, of 0.52-1.06 mmol mol⁻¹ (Barrientos et al., 2018).

4.3.2 Mg/Ca bottom water temperature calibration

To date no Mg/Ca bottom water temperature calibration exists for *E. batialis*, the most abundant foraminiferal species in IODP core U1343. However, a recent calibration of *E. clavatum* from the nearby Herald Canyon and Laptev Shelf in the Arctic Ocean suggests a Mg/Ca temperature sensitivity of 0.13 ± 0.05 mmol mol⁻¹ °C⁻¹ (Barrientos et al., 2018). To test whether *E. batialis* has a similar Mg/Ca bottom water temperature sensitivity to *E. clavatum*, LA-ICP-MS measurements of *E. batialis* and the $\delta^{18}\text{O}_b$ record at Site U1343 across the LGM-Holocene transition are used. Published $\delta^{18}\text{O}_b$ at IODP Site U1343 (Asahi et al., 2016) suggests a $\Delta\delta^{18}\text{O}_b$ across the LGM-Holocene transition of 1.58 ± 0.23 ‰ (s.e.). Measured foraminiferal $\delta^{18}\text{O}_b$ is influenced by changes in the $\delta^{18}\text{O}_w$, driven by changes in continental ice volume and regional patterns of evaporation/precipitation and deep water formation, and changes in the bottom water temperature (Shackleton, 1967, Schrag et al., 2002, LeGrande and

Schmidt, 2006). Across the LGM-Holocene transition mean ocean $\Delta\delta^{18}\text{O}_w$ is thought to have changed by 1.05 ± 0.20 ‰ (Duplessy et al., 2002). No regional estimate for the deep North Pacific exists, the closest is ODP Site 1123 in the SW Pacific, indicating a $\Delta\delta^{18}\text{O}_w$ of 1.10 ± 0.10 ‰ (Adkins et al., 2002), similar to that of the mean ocean estimate. Thus the mean ocean estimate of 1.05 ± 0.20 ‰ (Duplessy et al., 2002) was adopted to determine the contribution of bottom water temperature changes to the measured foraminiferal $\delta^{18}\text{O}_b$ at Site U1343, which is 0.53 ± 0.21 ‰ (s.e.). Assuming a similar bottom water temperature $\delta^{18}\text{O}_b$ relationship of *E. batialis* compared to other cosmopolitan benthic foraminiferal species (*Uvigerina* spp., *Cibicidoides* spp., *Planulina* spp.) of 0.22 ± 0.03 ‰ °C⁻¹ (Marchitto et al., 2014), this yields an estimated bottom water temperature difference across the LGM-Holocene of 2.42 ± 0.30 °C (s.e.) at Site U1343.

ICP-MS analysis of *E. batialis* samples in the size fraction 150-250 µm across the LGM-Holocene did not yield statistically significant results, due to the low numbers of foraminiferal tests per sample. Instead, LGM-Holocene Mg/Ca ratios of *E. batialis* are based on LA-ICP-MS measurements of two samples from 8.5 ka and 20.8 ka. LA-ICP-MS measurements were performed on *E. batialis* specimens >250 µm. The LGM-Holocene samples are exclusively from above the SMTZ, thus no high-Mg calcite contamination is expected (Chapter 3). However, low-Mg calcite can precipitate following increased pore water alkalinity as a result of organoclastic sulphate reduction (Chapter 3), characterised by increased U/Ca ratios. U/Ca ratios of LA-ICP-MS samples across the LGM-Holocene (*E. batialis*) are generally higher (300-2165 nmol mol⁻¹) compared to U/Ca of ICP-MS samples (*I. norcrossi* and *Uvigerina* spp.) from above the SMTZ (4.4-10.0 nmol mol⁻¹). This suggests, that there is contamination by low-Mg calcite in the uncleaned LA-ICP-MS samples, however, there also seems to be an offset between LA-ICP-MS and ICP-MS samples, related to either the methodology or the sample preparation (cleaning versus no cleaning), leading to higher elemental ratios in samples measured by LA-ICP-MS. Unfortunately there are no standards and/or foraminiferal samples demonstrating minor diagenetic alteration with both LA-ICP-MS and ICP-MS Mg/Ca ratios to calculate a methodological/procedural offset. For the purpose of this study I am assuming that the Mg/Ca offset between LA-ICP-MS and ICP-MS is constant, however, further analyses

are needed to fully understand the nature and origin of the methodological/procedural offset.

One specimen from 8.45 ka displayed increased U/Ca ratios ($2165 \text{ nmol mol}^{-1}$), compared to the other LA-ICP-MS samples across this depth interval, and has been excluded from further analyses. Average Mg/Ca values from 8.45 ka and 20.8 ka are $2.16 \pm 0.31 \text{ mmol mol}^{-1}$ (s.e.) and $1.83 \pm 0.22 \text{ mmol mol}^{-1}$ (s.e.), respectively. Using the calculated BWT difference across the LGM-Holocene transition of $2.42 \pm 0.30 \text{ }^{\circ}\text{C}$ (s.e.), this yields an *E. batialis* Mg/Ca bottom water temperature sensitivity of $0.14 \pm 0.13 \text{ mmol mol}^{-1} \text{ }^{\circ}\text{C}^{-1}$ (s.e.), within error of the Mg/Ca bottom water temperature sensitivity of *E. clavatum* of $0.13 \pm 0.05 \text{ mmol mol}^{-1} \text{ }^{\circ}\text{C}^{-1}$ as reported for the Arctic Ocean (Barrientos et al., 2018). I therefore propose that the Mg/Ca temperature calibration for *E. clavatum* is suitable for *E. batialis*, as well.

There are two possible routes to derive BWT estimates for the multi-species Mg/Ca record. The first approach would be to use previously published species-specific temperature calibrations, whereas the second approach includes normalisation to *E. batialis* Mg/Ca values allowing the use of a single temperature calibration for all samples.

Table 4.1 Benthic foraminiferal Mg/Ca BWT calibrations for *Elphidium clavatum*, *Uvigerina* spp., and *Islandiella norcrossi*.

Species	BWT calibration	Reference
<i>E. clavatum</i>	$BWT = (Mg/Ca - 0.816 \pm 0.06)/0.125 \pm 0.05$	Barrientos et al. (2018)
<i>Uvigerina</i> spp.	$BWT = (Mg/Ca - 0.9)/0.1$	Elderfield et al. (2010)
<i>I. norcrossi</i>	$BWT = (Mg/Ca - 1.044)/0.075$	Kristjánadóttir et al. (2007)

Firstly, the BWT for *Uvigerina* spp., *I. norcrossi*, and *E. batialis* were calculated based on the temperature calibrations published in Elderfield et al. (2010) adjusted for reductively cleaned samples, Kristjánadóttir et al. (2007), and Barrientos et al. (2018), respectively (Table 4.1). Following this approach, the Δ BWT across the LGM-Holocene is $\sim 5 \text{ }^{\circ}\text{C}$, much larger than the expected Δ BWT of $2.42 \pm 0.30 \text{ }^{\circ}\text{C}$ (s.e.) determined from the $\delta^{18}\text{O}_b$ record and published benthic foraminiferal Mg/Ca bottom

water temperature records from across the Pacific between 1000-3300 m suggesting a LGM Holocene Δ BWT of ~ 2 °C (Shackleton, 2000, Waelbroeck et al., 2002, Gorbarenko et al., 2002, Martin et al., 2002, Elderfield et al., 2010, McClymont et al., 2016). The LGM-Holocene transition at Site U1343 is associated with a change in the faunal assemblage, with *I. norcrossi* occurring exclusively during MIS 2, and *Uvigerina* spp. exclusively during MIS 1. A larger than expected Δ BWT could potentially result from a Δ [CO₃²⁻] effect on either *I. norcrossi* or *Uvigerina* spp.. However, there is no correlation of Mg/Ca and Li/Ca across the LGM-Holocene for either species (Figure 4.3), suggesting that changes in the Δ [CO₃²⁻] associated with G/IG cycles likely did not affect the Mg/Ca-based BWT reconstruction. Instead, the large Δ BWT across the LGM-Holocene likely results from very low BWT values based on *I. norcrossi* across MIS 2 (-2.5 °C on average), suggesting that further research is needed to establish a robust BWT calibration for *I. norcrossi* Mg/Ca. Thus, instead of using individual BWT calibrations, Mg/Ca ratios of *I. norcrossi* and *Uvigerina* spp. were normalised to *E. batialis*, enabling the application of a single BWT calibration based on Barrientos et al. (2018). This yields an LGM-Holocene Δ BWT of 2.03 ± 0.78 °C, within the error of a Δ BWT of 2.42 ± 0.30 °C derived from the $\delta^{18}\text{O}_b$ record.

The species-specific Mg/Ca offsets to *E. batialis* are -0.08 ± 0.06 mmol mol⁻¹ (n = 9, s.e.) on average for *I. norcrossi* and -0.12 ± 0.08 mmol mol⁻¹ (n = 4, s.e.) on average for *Uvigerina* spp.. As a result of the low sample size, the offsets have a relatively large uncertainty, however, it is smaller than the uncertainty of 0.22 mmol mol⁻¹ associated with the contribution of Mg from authigenic carbonates for a U/Ca threshold of 200 nmol mol⁻¹. Thus, 0.22 mmol mol⁻¹ was adopted as the procedural uncertainty for BWT error propagation for all samples. Normalized Mg/Ca ratios were converted to BWT using the temperature calibration for *E. clavatum* (Barrientos et al., 2018) (Equation 2.2), yielding an overall bottom water temperature range of -2.7 °C to 5.7 °C and an average temperature uncertainty of ± 1.1 °C (s.e.) for the down-core record (Figure 4.6).

$$BWT (\text{°C}) = (Mg/Ca_{normalised} - 0.816 \pm 0.06) / 0.125 \pm 0.05 \quad (\text{Equation 2.2})$$

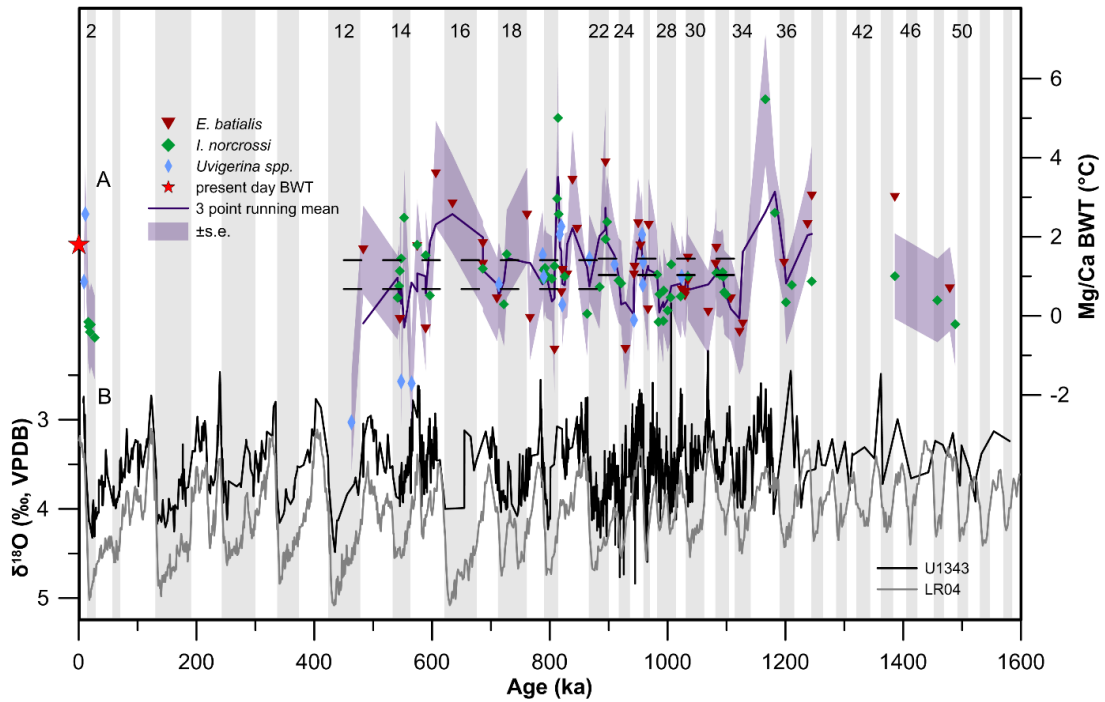


Figure 4.6 (A) BWT across the LGM-Holocene and the Mid-Pleistocene of Mg/Ca ratios of *I. norcrossi* (green diamonds), *Uvigerina* spp. (blue diamonds), and *E. batialis* (red triangle) normalised to *E. batialis* and calculated according to the BWT calibration for *E. clavatum* from the Arctic Ocean (Barrientos et al., 2018) including the \pm s.e. envelope (light purple). The dashed horizontal lines represent the interglacial and glacial mean between 1000-1500 ka and 450-850 ka. The thick purple line is the 3-point running mean and the red star represents present day BWT at ~2000 m water depth in the eastern Bering Sea (Olsen et al., 2016). (B) The $\delta^{18}\text{O}_e$ curve at IODP Site U1343 (Asahi et al., 2016, Kender et al., in review) (black) together with the LR04 stack (grey) (Lisiecki and Raymo, 2005). The grey vertical bars represent glacial intervals, numbers at the top correspond to marine isotope stages (MIS boundaries from (Lisiecki and Raymo, 2005)).

The large uncertainty, associated with the species-specific offsets, leads to differences in the reconstructed BWT for samples with multiple species. Additionally, there are three anomalously cold *Uvigerina* spp. samples during MIS 12, 14, and 15 (Figure 4.6). These samples have an Mg/Ca ratio normalised to *E. batialis* of 0.48-0.61 mmol mol⁻¹ much lower compared to the remaining *Uvigerina* spp. samples that have Mg/Ca varying between 0.8-1.14 mmol mol⁻¹. Comparison of the Mg/Ca and Li/Ca records across this interval suggests a potential effect of $\Delta[\text{CO}_3^{2-}]$ on *Uvigerina* spp. Mg/Ca ratios (Figure 4.3).

4.4 Discussion

4.4.1 Bottom water temperatures in the eastern Bering Sea across the Mid- to late Pleistocene

The multi-species benthic foraminiferal Mg/Ca record indicates orbital variations in BWT in the eastern Bering Sea across the LGM-Holocene and long-term changes during the Mid-Pleistocene. BWT at ~2000 m depth in the Bering Sea is controlled by changes in the contribution of different water masses to the Site and/or changes in the source region of the deep water masses. Today, Site U1343 is bathed in NPDW with a modern BWT of 1.95 °C (GLODAP v2 station 41047-3 (B) (Olsen et al., 2016)), originating from primarily southern sourced water masses sinking around the Antarctic continent. On G/IG timescales, however, NPIW may have played a fundamental role for the Bering Sea, originating locally from brine rejection during sea ice freezing. Bering Sea SST and sea ice extent, important precursors for NPIW formation, across the last deglaciation have been shown to vary in accordance with millennial-scale climate change in the North Atlantic, with increased NPIW formation during the HS1 (~14.7-18 ka) and the Younger Dryas (YD, ~11.7-12.9 ka) (Max et al., 2012, Max et al., 2014, Méheust et al., 2016). Particularly during extreme glacials of the Mid- to late Pleistocene, NPIW has been proposed to form, at least partly, in the Bering Sea (Horikawa et al., 2010, Rella et al., 2012, Max et al., 2012, Knudson and Ravelo, 2015b). Southern sourced deep water temperatures, on the other hand, have been shown to vary coeval with Antarctic climate change across the late Pleistocene (Elderfield et al., 2012).

In order to best understand Pleistocene BWT history in the Bering Sea and its implications for regional and global climate change the LGM to Holocene and the Mid-Pleistocene are discussed separately below.

4.4.1.1 The Last Glacial Maximum to Holocene bottom water temperature history in the eastern Bering Sea

Across the LGM-Holocene transition (Termination I) the multi-species Mg/Ca BWT reconstruction from Site U1343 shows a Δ BWT of 2.03 ± 0.78 °C (s.e.) with colder BWT during the LGM (Figure 4.7), in line with published benthic foraminiferal Mg/Ca bottom and intermediate water temperature records from across the Pacific

between 800-3500 m suggesting a LGM-Holocene Δ BWT of 1-3 °C (Shackleton, 2000, Waelbroeck et al., 2002, Gorbarenko et al., 2002, Martin et al., 2002, Elderfield et al., 2010, Woodard et al., 2014, Knudson and Ravelo, 2015b, McClymont et al., 2016).

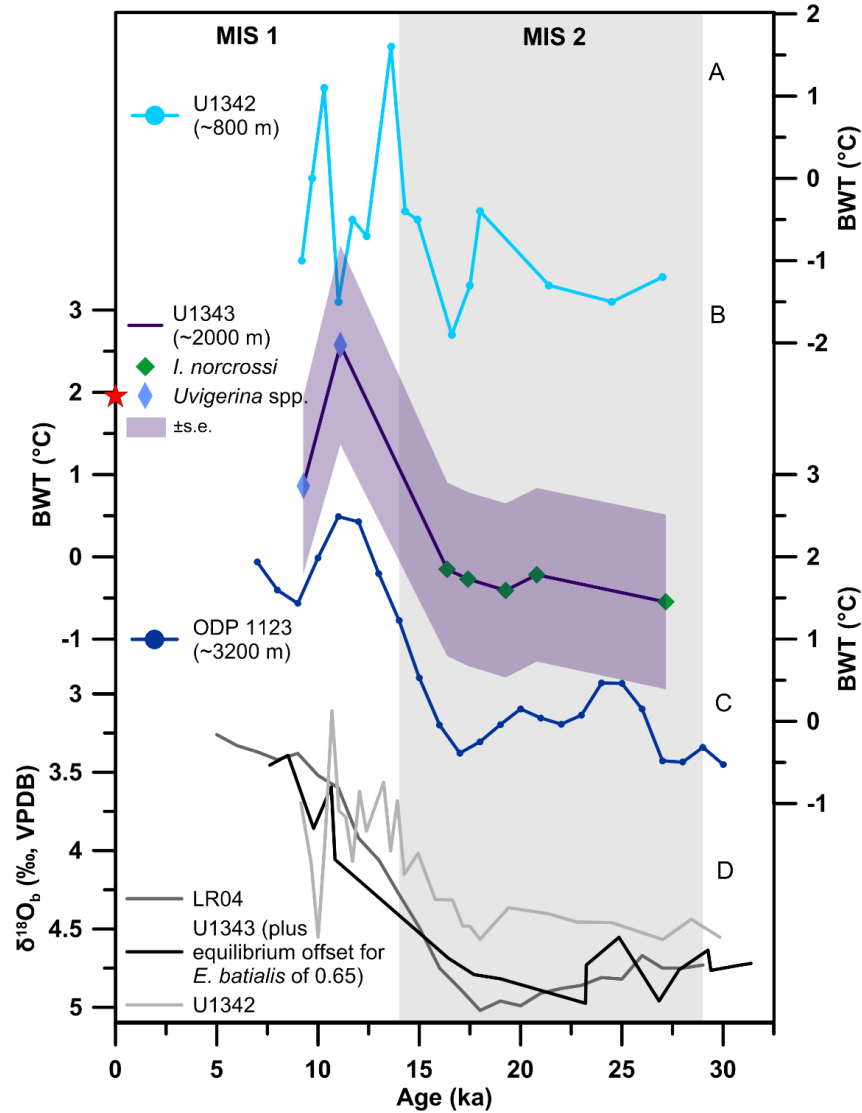


Figure 4.7 (A) LGM-Holocene BWT (light blue) evolution based on *Uvigerina peregrina* Mg/Ca at IODP Site U1342 at ~800 m water depth on the Bowers Ridge in the southern Bering Sea (Knudson and Ravelo, 2015b). (B) BWT at IODP Site U1343 (purple) across Termination I based on *I. norcrossi* (green diamonds) and *Uvigerina* spp. (blue diamonds) including the \pm s.e. envelope (light purple). The red star represents present day BWT at ~2000 m water depth in the eastern Bering Sea (Olsen et al., 2016). (C) BWT at ODP Site 1123 (~3200 m water depth) on Chatham Rise in the southwestern Pacific based on *Uvigerina* spp. (Elderfield et al., 2010). (D) $\delta^{18}\text{O}_b$ records from U1343 adjusted for the *E. batialis* equilibrium offset (+0.65 ‰) (black) (Asahi et al., 2016) and U1342 (light grey) (Knudson and Ravelo, 2015b) together with the LR04 stack (middle grey) (Lisiecki and Raymo, 2005). The grey vertical bar represents the last glacial interval, numbers at the top correspond to marine isotope stages (MIS boundaries from (Lisiecki and Raymo, 2005)).

Even though the Mg/Ca temperature calibration used to calculate BWT is for the species *E. clavatum*, rather than *E. batialis*, LGM-Holocene Δ BWT suggest that absolute reconstructed temperature values are representative of local BWT. This is supported by the modern BWT at ~2000 m water depth at the nearest GLODAP v2 station (58°00'N, 174°87'W, station 41047-3 (B)) (Olsen et al., 2016), of 1.95 °C, falling right in between the two Holocene Mg/Ca BWT values of 0.86 ± 1.07 °C (9.3 ka, s.e.) and 2.6 ± 1.2 °C (11.1 ka, s.e.) (Figure 4.7). Further, a previously published BWT record from the southwestern Pacific (ODP Site 1123 (171.50 °W, 41.78 °S, 3290 m)) demonstrate a parallel BWT history and very similar absolute BWT values across Termination I (Elderfield et al., 2010, Elderfield et al., 2012) (Figure 4.7), supported by a strong positive correlation ($R^2 = 0.96$, $p < 0.001$, $n = 7$) of the two records.

Today Site U1343 is bathed in NPDW with a BWT of 1.95 °C, compared to ODP Site 1123 in the southwestern Pacific that is bathed in CDW and has a modern BWT of 1.3 °C (Elderfield et al., 2010). CDW is the precursor of NPDW and thus warmer temperatures are expected for NPDW, as aging deep water is affected by the geothermal heat flux at the seafloor. Further, Site U1343 is ~1000 m shallower than Site 1123. Hence, if the two Sites are continuously bathed in the same water mass, this relationship would be expected to hold true for both glacials and interglacials.

The approach outlined in Siddall et al. (2010) provides a first opportunity to estimate expected BWT at Site U1343 across late Pleistocene G/IG cycles (Figure 4.8). The average glacial and interglacial $\delta^{18}O_b$ at Site U1343 (Asahi et al., 2016) together with the respective average sea level estimates (Spratt and Lisiecki, 2016) are scaled to the modern BWT of 1.95 °C and plotted together with isotherms (Figure 4.8). The slope of the isotherms is based on the LGM-Holocene mean ocean $\delta^{18}O_w$ change (1.05 ± 0.20 ‰ (Duplessy et al., 2002)) and the LGM-Holocene sea level change of 125 ± 8 m (Spratt and Lisiecki, 2016), whilst the x-axis offset between the isotherms of 0.54 ‰ is based on the temperature (T) $\delta^{18}O$ relationship outlined in (Shackleton, 1974) (Equation 2.3) (Figure 4.8).

$$T = 16.10 - 4.38 * (\delta^{18}O_b - \delta^{18}O_w) + 0.1 * (\delta^{18}O_b - \delta^{18}O_w)^2 \quad (\text{Equation 2.3})$$

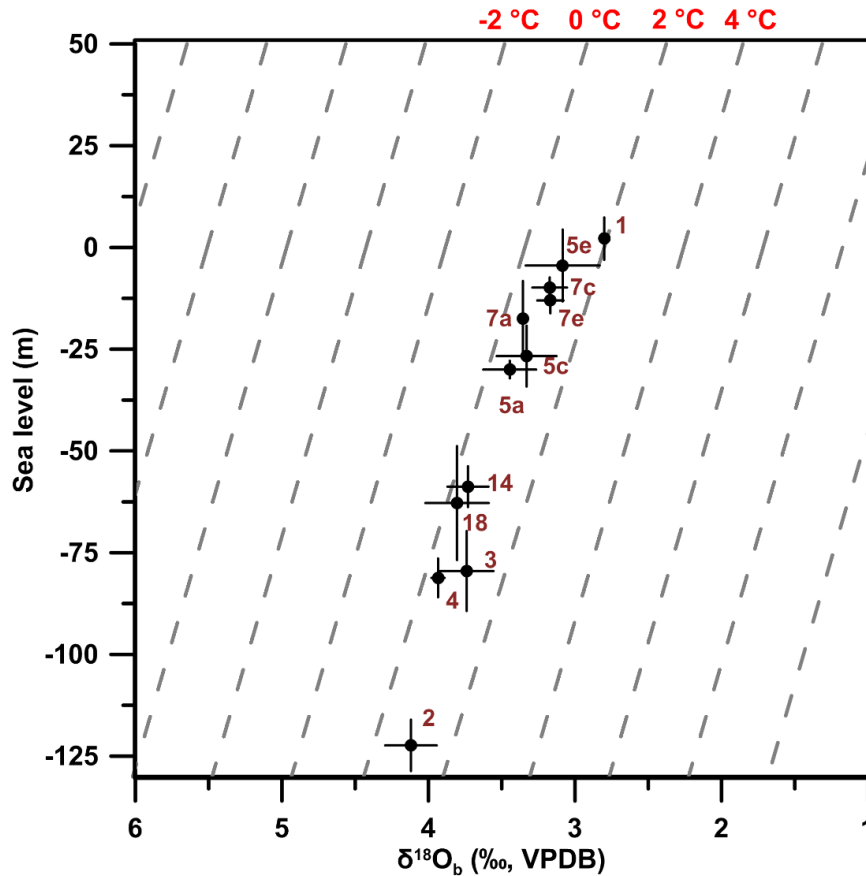


Figure 4.8 Cross plot of $\delta^{18}\text{O}_b$ at Site U1343 (Asahi et al., 2016) versus sea level (Spratt and Lisiecki, 2016), together with isotherms (dashed grey lines) following the approach outlined in Siddall et al. (2010). The slope of the isotherms is determined by the LGM-Holocene mean ocean $\delta^{18}\text{O}_w$ change (1.05 ± 0.20 ‰ (Duplessy et al., 2002)) and the LGM-Holocene sea level change of 125 ± 8 m (Spratt and Lisiecki, 2016), whilst the x-axis offset between the isotherms of 0.54 ‰ is based on the temperature $\delta^{18}\text{O}$ relationship outlined in (Shackleton, 1974). The numbers represent the respective marine isotope stages. Error bars represent the standard error.

Based on an LGM sea level estimate of -123 ± 2 m (s.e.) (Spratt and Lisiecki, 2016) and an average LGM $\delta^{18}\text{O}_b$ of 4.32 ‰ (18-25 ka) (Asahi et al., 2016) in combination with an average $\delta^{18}\text{O}_b$ of 2.74 ‰ (7.6-10.8 ka) for the Holocene (Asahi et al., 2016) this yields an estimated LGM BWT >0 °C (Figure 4.8). The average reconstructed LGM Mg/Ca BWT is -0.3 ± 0.7 °C (s.e.), indicating slightly colder than expected BWT at Site U1343 (Figure 4.7), supported by similar absolute temperatures to those at ODP Site 1123 (Figure 4.7), which is ~ 1000 m deeper and upstream from Site U1343.

Using interpolated $\delta^{18}\text{O}_b$ values (Asahi et al., 2016) together with the reconstructed BWT yields an LGM Holocene seawater oxygen isotope difference ($\Delta\delta^{18}\text{O}_w$) of 0.89 ± 0.30 ‰ (s.e.), calculated according to (Equation 2.4) (Elderfield et al., 2010):

$$\delta^{18}O_w = (\delta^{18}O_b + 0.27) - 0.25 * (16.10 - BWT) \quad (\text{Equation 2.4})$$

A $\Delta\delta^{18}O_w$ of 0.89 ± 0.30 ‰ (s.e.) is smaller but within the error of the proposed mean ocean changes across the LGM-Holocene of 1.05 ± 0.2 ‰ (Duplessy et al., 2002). Potential explanations for the slightly smaller observed change in $\Delta\delta^{18}O_w$ at Site U1343 are either uncertainty associated with the multi-species record and interpolation of the $\delta^{18}O_b$ signal, or, taken at face value, changes in the local hydrography across the LGM-Holocene. A possible mechanism, includes changes in the contribution of NPIW to waters at Site U1343. Glacial NPIW in the Bering Sea is formed via brine rejection during sea ice freezing, able to produce dense waters with little oxygen isotope fractionation, carrying the low $\delta^{18}O_w$ signature of high-latitude surface waters to greater depth (Knudson and Ravelo, 2015b, Cook et al., 2016). Knudson and Ravelo (2015b), demonstrate that Site U1342, at ~800 m water depth in the southern Bering Sea, is affected by enhanced NPIW formation during extreme glacials (including MIS 2) of the Mid- to late Pleistocene, indicated by negative offset of the local glacial $\delta^{18}O_b$ compared to the global LR04 stack (Lisiecki and Raymo, 2005). $\delta^{18}O_b$ at Site U1343 during the LGM is characterised by two episodes of slightly decreased values compared to the LR04 stack (~0.2 ‰), at ~25 ka and centred around 17.5 ka (Figure 4.7). Whilst no BWT data is available at 25 ka, the second interval around 17.5 ka shows no pronounced increase in BWT, indicating that the decrease in $\delta^{18}O_b$ at this point in time likely results from changes in $\delta^{18}O_w$, suggesting the contribution of a low $\delta^{18}O_w$ water mass to Site U1343. Further Mg/Ca ratios of reductively cleaned *Uvigerina peregrina* samples from IODP Site U1342 in the southern Bering Sea at ~800 m water depth suggest LGM intermediate water temperatures (IWT) of -1.2 ± 0.2 °C (17-25 ka, s.e.) (Figure 4.7), calculated using the *Uvigerina* spp. Mg/Ca BWT calibration developed by Elderfield et al. (2010), adjusted to samples cleaned according to the Cd-cleaning protocol (Elderfield et al., 2010) (Table 2.1). Thus, colder than expected LGM BWT of -0.3 ± 0.75 °C (s.e.) at Site U1343 in combination with a smaller $\Delta\delta^{18}O_w$ of 0.89 ± 0.30 ‰ compared to the global mean, could potentially result from entrainment of NPIW in deep waters along the eastern Bering Sea slope.

Cook et al. (2016) suggest that the divide between well-ventilated NPIW and poorly ventilated NPDW during the LGM in the Bering Sea was around ~1000 m water depth, based on $\delta^{18}O_b$ and $\delta^{13}C$ from IODP Sites U1339 and U1345 from the Umnak Plateau

and the eastern Bering Sea slope. However, BWT and $\delta^{18}\text{O}_b$ evidence from Site U1343 at ~2000 m water depth, potentially supports intermittent admixture of NPIW to the deep Bering Sea during the LGM and across the early deglaciation, even though NPDW likely is the main contributing water mass to Site U1343. This is in line with a much smaller reconstructed LGM-Holocene $\Delta\delta^{18}\text{O}_w$ change at Site U1342 of 0.23 ‰ (Knudson and Ravelo, 2015b), compared to Site U1343 (0.89 ± 0.30 ‰, s.e.), suggesting less contribution of NPIW to the deeper Site.

In addition to enhanced NPIW formation, the LGM in the Bering Sea was characterised by a widespread decrease in primary productivity, also noted in the Sea of Okhotsk and the western subarctic North Pacific (Jaccard et al., 2005, Brunelle et al., 2007, Brunelle et al., 2010, Kohfeld and Chase, 2011, Kim et al., 2014). The observed regional-wide decrease in primary productivity did not result from increased sea ice extent and decreased light availability alone as this was likely variable between regions (Méheust et al., 2016, Matul, 2017, Méheust et al., 2018). Instead, increased stratification of the subpolar water column has been proposed as a mechanism to explain the large-scale changes in productivity (Jaccard et al., 2005, Brunelle et al., 2007, Brunelle et al., 2010, Knudson and Ravelo, 2015a). As seawater approaches the point of maximum density (equal to the freezing point of seawater at atmospheric temperatures for salinities >24.7 psu (Talley et al., 2011)), the effect of temperature on density is reduced (Winton, 1997, Sigman et al., 2004, de Boer et al., 2007). Therefore, at homogenous low water column temperatures, surface cooling, typically initiating overturning by densification of low salinity surface waters in high latitudes, is not as effective (de Boer et al., 2007), indicating the importance of BWT for subpolar ocean stratification. Colder LGM SSTs in the Bering Sea and North Pacific (Max et al., 2012, Meyer et al., 2016) together with a BWT 2.03 ± 0.78 °C (s.e.) colder than during the Holocene is in support of homogenous water column cooling, supporting increased salinity stratification during glacial intervals in the North Pacific and its marginal seas. Decreased thermal stratification, may also be able to explain lower intermediate than deep water temperatures in the Bering Sea during MIS 2, as reconstructed from IODP Sites U1343 and U1342 (Figure 4.7).

Increased stratification would limit the nutrient supply to the surface ocean effectively decreasing primary productivity. Following this hypothesis the re-invigoration of overturning in the North Pacific and the Bering Sea would be driven by deep ocean

warming across Termination I (Brunelle et al., 2007), increasing the sensitivity of seawater density to temperature, promoting temperature driven overturning during wintertime in the polar and subpolar ocean (Sigman et al., 2004). Biogenic opal records indicate an increase in primary productivity between ~16 ka and 15 ka in the Bering Sea (Brunelle et al., 2007, Kohfeld and Chase, 2011, Riethdorf et al., 2013a, Riethdorf et al., 2013b, Kim et al., 2014), whereas nitrogen isotopes ($\delta^{15}\text{N}$) indicate decreased nutrient utilisation and thus increased nutrient supply to the surface ocean from 17.5 ka (Brunelle et al., 2007). Similar patterns of primary productivity and $\delta^{15}\text{N}$ are also observed in the subarctic North Pacific (Jaccard et al., 2005, Galbraith et al., 2007, Jaccard et al., 2009, Brunelle et al., 2010, Kohfeld and Chase, 2011). Even though the low resolution record of BWT does not allow to pinpoint the exact onset of warming, it clearly demonstrates that major warming did not commence until after 16.4 ka (Figure 4.7). Hence, if the early deglacial decrease in $\delta^{15}\text{N}$ reflects increased nutrient supply from below, the weakening of the subpolar water column stratification must have had a different cause than BWT warming. The mismatch in $\delta^{15}\text{N}$ and primary productivity, could potentially result from an early deglacial weakening of the stratification together with sea ice effectively limiting the light availability for phytoplankton until ~15 ka (Brunelle et al., 2010). This is supported by sea ice studies from the Bering Sea and the North Pacific, demonstrating a change from more extended to seasonal/ice free conditions around 15 ka (Caissie et al., 2010, Méheust et al., 2016, Méheust et al., 2018).

Overall, the BWT record at Site U1343 suggests an LGM-Holocene ΔBWT of 2.03 ± 0.78 °C with a reconstructed $\Delta\delta^{18}\text{O}_w$ of 0.89 ± 0.30 ‰, based on the interpolated $\delta^{18}\text{O}_b$ record (Asahi et al., 2016). The smaller $\Delta\delta^{18}\text{O}_w$ compared to the suggested mean ocean change of 1.05 ± 0.20 ‰ (Duplessy et al., 2002) across Termination I, either results from uncertainties in the BWT reconstructions or suggests intermittent admixture of glacial NPIW to Site U1343 during the LGM. Future studies should explore the role of NPIW for the North Pacific carbon cycle, as a deeper well-ventilated intermediate water mass, may reduce eddy-driven upwelling of CO_2 -rich deep waters (Kender et al., in review). Additionally, increased export of NPIW during glacials has been linked to increased primary productivity in the equatorial Pacific (Max et al., 2017), again suggesting fundamental changes in the North Pacific carbon cycle during glacial intervals. Moreover, the BWT record from Site U1343 in the eastern Bering Sea lends

support to the hypothesis that homogenous cooling of the water column in the subarctic Pacific during the LGM promoted salinity-driven stratification (Figure 4.7). A more stratified water column in the North Pacific during glacial times has important implications for the carbon cycle, with less overturning promoting deep ocean carbon storage, potentially aiding in the atmospheric drawdown of CO₂ during the LGM (Galbraith et al., 2007, Jaccard et al., 2009).

4.4.1.2 Mid-Pleistocene bottom water temperature in the eastern Bering Sea – implications for the Mid-Pleistocene climate transition

BWT at Site U1343 demonstrates distinct orbital variability across the Mid-Pleistocene together with pronounced long-term trends (Figure 4.6). Across the MPT spectral analysis of $\delta^{18}\text{O}_b$ at Site U1343 demonstrates a significant 100 ka cycle first emerging around 1200 ka, with dominant 100 ka frequency not until 700 ka (Asahi et al., 2016). Prior to 1200 ka the BWT record is sparse, however, pre and early MPT climate cycles (>1000 ka) are characterised by an average glacial and interglacial BWT of 1.05 ± 0.45 °C (s.e.) and 1.58 ± 0.61 °C (s.e.), respectively (Figure 4.6). Late and post MPT climate cycles (<850 ka), on the other hand, demonstrate an average glacial and interglacial BWT of 0.72 ± 0.66 °C (s.e.) and 1.31 ± 0.16 °C (s.e.) (Figure 4.6). Even though these estimates are within error of each other, this suggests that there may have been cooling during both glacials and interglacials in the eastern Bering Sea associated with the MPT.

The low resolution of BWT reconstructions, resulting from the influence of early diagenesis on foraminiferal geochemistry at Site U1343, however, make an in-depth analysis of BWT changes on G/IG timescales across the MPT challenging. Additionally, uncertainties associated with the $\Delta[\text{CO}_3^{2-}]$ effect and the composite nature of the Mg/Ca record hinder orbital-scale interpretations of the BWT reconstructions. Instead, the 3-point running mean, aimed at reducing the uncertainty associated with the BWT reconstructions, is used to determine long-term trends in Mid-Pleistocene Bering Sea BWT history. Beyond 1200 ka the age model at Site U1343 is less well constrained (Asahi et al., 2016). Further, the resolution of the BWT record decreases prior to MIS 34 (Figure 4.6), which is why the BWT data >1120 ka have been excluded from the discussion of long-term trends across the Mid-Pleistocene.

Table 4.2 Ages of important and frequently mentioned marine isotope stages (MIS) across the Mid-Pleistocene transition.

MIS	Glacial/Interglacial	Age (ka)
21	IG	814-866
22	G	866-900
23	IG	900-917
24	G	917-936
25	IG	936-959
26	G	959-970
27	IG	970-982
28	G	982-1014

Between 1120 ka and 450 ka BWT at Site U1343 actually demonstrates a subtle warming of 0.2 ± 0.4 °C. A BWT warming across the Pleistocene contradicts previously published records from DSDP Site 607 (Sosdian and Rosenthal, 2009, Ford et al., 2016), indicating long-term deep ocean cooling. However, Site U1343 is not the only Pacific Site where warming has been observed. An unpublished BWT record from ODP Site 1208 on Shatsky Rise (3346 m water depth) also demonstrates BWT warming between ~1000 ka and ~850 ka (Ford and Raymo, 2017), with similar absolute BWT values to Site U1343. A potential mechanism to explain BWT warming across the Mid-Pleistocene in the North Pacific could be pronounced changes in the thermohaline overturning circulation as observed from MIS 24 (Table 4.2) onwards (Hall et al., 2001, Venuti et al., 2007, Pena and Goldstein, 2014). A slowdown of the Atlantic meridional overturning circulation (AMOC) during glacials from MIS 24 (Table 4.2) (Pena and Goldstein, 2014) together with a more sluggish southern overturning cell following MIS 22 (Table 4.2) (Hall et al., 2001, Venuti et al., 2007) could result in slower circulation in the deep Pacific leading to older bottom waters that are more strongly influenced by the geothermal heat flux at the seafloor. Additionally, increased salinity stratification (see above) during glacials could have isolated North Pacific bottom waters even further (Sigman et al., 2004, Jaccard et al., 2005, Brunelle et al., 2007, Brunelle et al., 2010). If an increased geothermal heat flux, associated with a slowdown of the deep Pacific circulation observed after MIS 22 (Hall et al., 2001, Venuti et al., 2007), was the primary driver of BWT warming in the Bering Sea across the Mid-Pleistocene, the main increase in BWT would be expected following MIS 22 (Table 4.2). Instead, however, pronounced BWT warming is observed between MIS 34 and MIS 22 (0.63 ± 1.10 °C (s.e.)) (Figure 4.9), while MIS

22 to MIS 12 demonstrates BWT cooling of 1.21 ± 0.63 °C (s.e.) (Figure 4.9). MIS 22 is a critical stage across the MPT, part of the so-called ‘900-ka event’, characterised by the first long glaciation as seen from the LR04 stack (Lisiecki and Raymo, 2005, Clark et al., 2006) and potentially associated with an increase in continental ice volume (Elderfield et al., 2012, Rohling et al., 2014). Further, the 900-ka event stands out in many climate records, such as SSTs (McClymont et al., 2013), deep water $\delta^{13}\text{C}$ (Raymo et al., 1997, Hodell et al., 2003), and oceanic circulation (Pena and Goldstein, 2014), depicting pronounced changes in the global climate (Clark et al., 2006).

Splitting the $\delta^{18}\text{O}_b$ record (1200–450 ka) at Site U1343 (Asahi et al., 2016, Kender et al., in review) into a pre and post-MIS 22 interval, reveals an increase of 0.49 ± 0.18 ‰ (s.e.) prior to MIS 22 and a subtle decrease of -0.17 ± 0.14 ‰ (s.e.) post MIS 22 (Figure 4.9). A $\delta^{18}\text{O}_b$ increase prior to MIS 22 of 0.49 ± 0.18 ‰ (s.e.) with a $\delta^{18}\text{O}_b$ BWT sensitivity of 0.22 ± 0.03 ‰ °C⁻¹ (Marchitto et al., 2014) would require 2.23 ± 0.27 °C (s.e.) BWT cooling, if $\delta^{18}\text{O}_b$ was dominated by BWT changes. Instead, Mg/Ca BWTs at Site U1343 demonstrates warming of 0.63 ± 1.10 °C (s.e.). This suggests a $\delta^{18}\text{O}_w$ increase across this interval indicating either increased ice volume and/or hydrographic changes in the deep Bering Sea. NPIW formation in the Bering Sea during glacials is a low $\delta^{18}\text{O}_w$ water mass (Knudson and Ravelo, 2015b, Cook et al., 2016), thus hydrographic changes causing an increase in $\delta^{18}\text{O}_w$ would likely be related to changes in NPDW during glacials. On the other hand, increased $\delta^{18}\text{O}_w$ could result from a build-up of continental ice volume across this interval, however, the BWT record at Site U1343 does not allow to distinguish, whether this would be represented by a gradual increase until MIS 22 (Table 4.2) or an abrupt step-like change during MIS 22, as suggested by Elderfield et al. (2012).

Considering the post-MIS 22 interval, if the subtle decrease in $\delta^{18}\text{O}_b$ of -0.17 ± 0.14 ‰ (s.e.) was dominated by BWT changes, an increase in the Bering Sea BWT of 0.77 ± 0.59 °C (s.e.) would be expected. Mg/Ca BWT, however, demonstrates a cooling of 1.21 ± 0.63 °C (s.e.) between 900 ka and 450 ka, indicative of either continental ice volume decrease or hydrographic changes across the Mid-Pleistocene resulting in lower $\delta^{18}\text{O}_w$ in the deep Bering Sea. An overall decrease in continental ice volume across the Mid- to late Pleistocene seems unlikely. Even though the long-term $\delta^{18}\text{O}_w$ histories reconstructed from the North Atlantic and the southwestern Pacific differ, both demonstrate increased ice volume during post-MPT glacials (Sosdian and

Rosenthal, 2009, Elderfield et al., 2012, Ford et al., 2016), in line with sea level reconstructions (Rohling et al., 2014, Grant et al., 2014). On the other hand, a decrease in $\delta^{18}\text{O}_w$ across the late Pleistocene in the Bering Sea could result from contribution of glacial NPIW (Knudson and Ravelo, 2015b, Cook et al., 2016). NPIW forms via brine rejection, increasing the local salinity without fractionating oxygen isotopes (Brennan et al., 2013) and thus carries the low $\delta^{18}\text{O}_w$ signature of high-latitude surface waters to greater depth. Evidence of oxygen and carbon isotopes together with ϵ_{ND} suggests that NPIW formed, at least partly, in the Bering Sea during late Pleistocene glacials (Horikawa et al., 2010, Rella et al., 2012, Max et al., 2014, Knudson and Ravelo, 2015b, Max et al., 2017). Knudson and Ravelo (2015b) demonstrate that enhanced NPIW formation in the Bering Sea likely occurred during extreme glacials of the Mid- to late Pleistocene characterised by a closed Bering Strait. Based on the recently published sea level stack for the late Pleistocene between 0-800 ka (Spratt and Lisiecki, 2016) and the sea level estimates from DSDP Site 607 (Sosdian and Rosenthal, 2009) and ODP Site 1123 (Elderfield et al., 2012) between 800-1600 ka, Pleistocene glacials with a closed Bering Strait encompass MIS 52, MIS 50, MIS 38, MIS 34, and MIS 22 to MIS 2. Thus, contribution of glacial NPIW to bottom waters at Site U1343 following MIS 22 could lead to a long-term decrease in $\delta^{18}\text{O}_w$. This is additionally supported by a subtle decrease in the $\delta^{18}\text{O}_b$ of glacials between MIS 2 and MIS 22 ($-0.02 \pm 0.03 \text{ ‰}$ (s.e.)), whilst interglacials since MIS 21 show a minor increase in $\delta^{18}\text{O}_b$ of $0.22 \pm 0.03 \text{ ‰}$ (s.e.), suggesting that the decreasing trend in $\delta^{18}\text{O}_b$ between MIS 12 and MIS 22 (~450-900 ka) is dominated by glacial intervals, in line with enhanced contribution of glacial NPIW to Site U1343.

As a result of its sheer size, the deep Pacific Ocean is typically thought to represent mean deep ocean changes on orbital timescales. Hence, NPIW contribution to Site U1343 across the Mid-Pleistocene should be manifested by a negative offset of $\delta^{18}\text{O}_b$ from the LR04 stack (Knudson and Ravelo, 2015b, Cook et al., 2016). In general, the LR04 stack and $\delta^{18}\text{O}_b$ at Site U1343 co-vary both in shape and amplitude between 1200 ka to 450 ka (Figure 4.9). However, there are subtle differences, both prior to and post MIS 22 (Table 4.2).

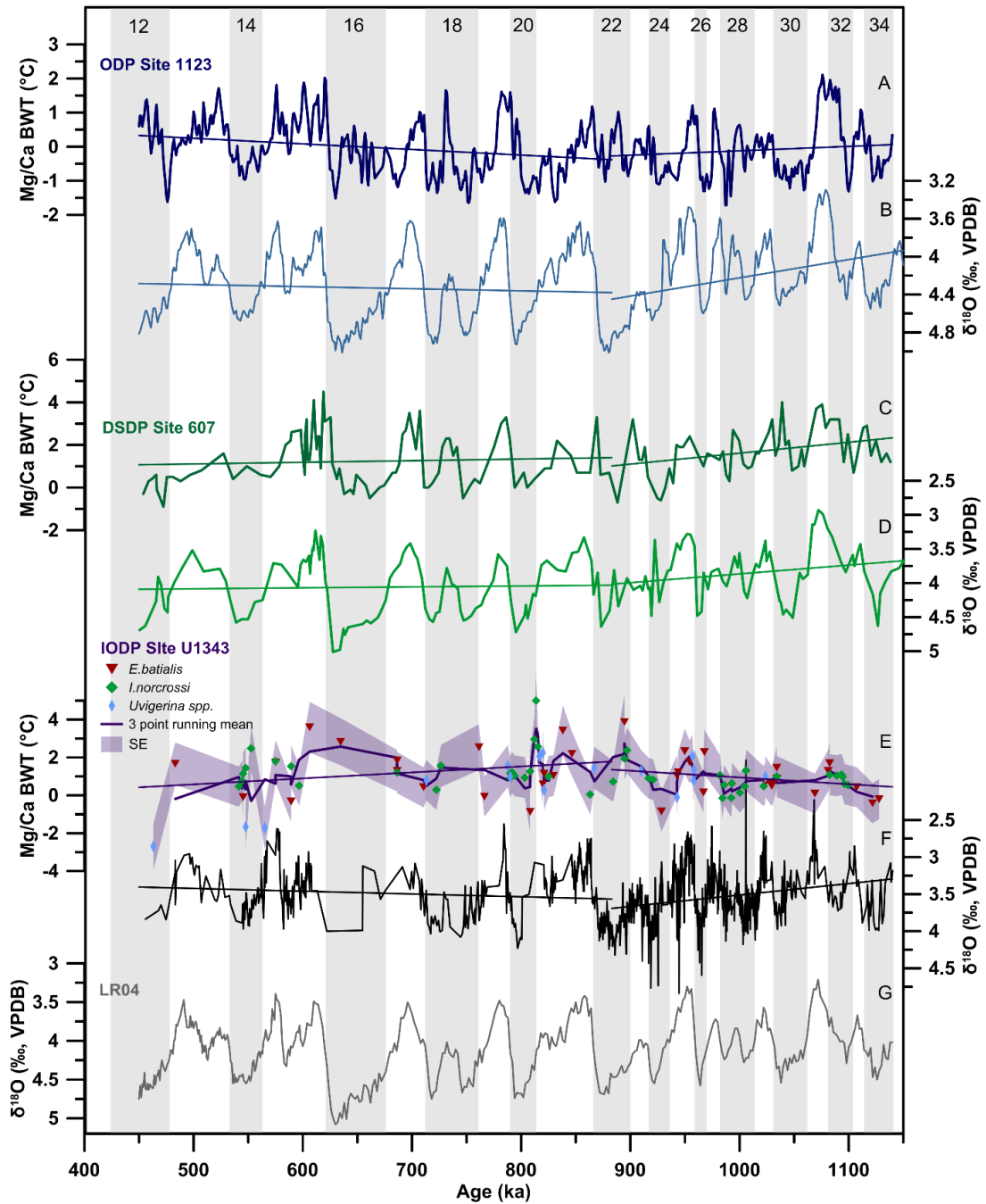


Figure 4.9 (A) BWT evolution at ODP Site 1123 (dark blue) in the southwestern Pacific across the Mid-Pleistocene (Elderfield et al., 2012). (B) $\delta^{18}\text{O}_b$ at Site 1123 (light blue) (Elderfield et al., 2012). (C) BWT at Site 607 in the North Atlantic (dark green) (Sosdian and Rosenthal, 2009, Ford et al., 2016) together with (D) the $\delta^{18}\text{O}_b$ record at Site 607 (light green) (Ruddiman et al., 1989, Sosdian and Rosenthal, 2009, Ford et al., 2016). (E) The 3-point running mean of BWT at Site U1343 (dark purple) based on a multi-species Mg/Ca composite (*E. batialis* (red triangles), *I. norcrossi* (green diamonds), *Uvigerina* spp. (blue diamonds)). (F) $\delta^{18}\text{O}_b$ at Site U1343 (black) (Asahi et al., 2016, Kender et al., in review) together with (G) the global LR04 stack (Lisiecki and Raymo, 2005). The horizontal lines demonstrate the long-term trends of both BWT and $\delta^{18}\text{O}_b$ prior to and after MIS 22 (Table 4.2). The grey vertical bars represent glacial intervals, numbers at the top correspond to marine isotope stages (MIS boundaries from (Lisiecki and Raymo, 2005)).

Some glacials, including the early MIS 22, MIS 28, and MIS 32 show periods of higher $\delta^{18}\text{O}_b$ at Site U1343 compared to the LR04 stack, whereas other intervals such as the late MIS 22 (Kender et al., in review) and late MIS 18 actually demonstrate a negative offset to the LR04 stack (Figure 4.10). This points towards contribution of glacial NPIW at Site U1343, however, higher resolution records of $\delta^{18}\text{O}_b$ and BWT are needed to test whether this is a consistent feature for all late Pleistocene glacials. Increased NPIW contribution to Site U1343 is in line with the long-term BWT cooling observed across the Mid- to late Pleistocene following MIS 22 (Table 4.2), as suggested from colder IWT (Knudson and Ravelo, 2015b) compared to BWT in the Bering Sea across the LGM (section 4.1.1) (Figure 4.7).

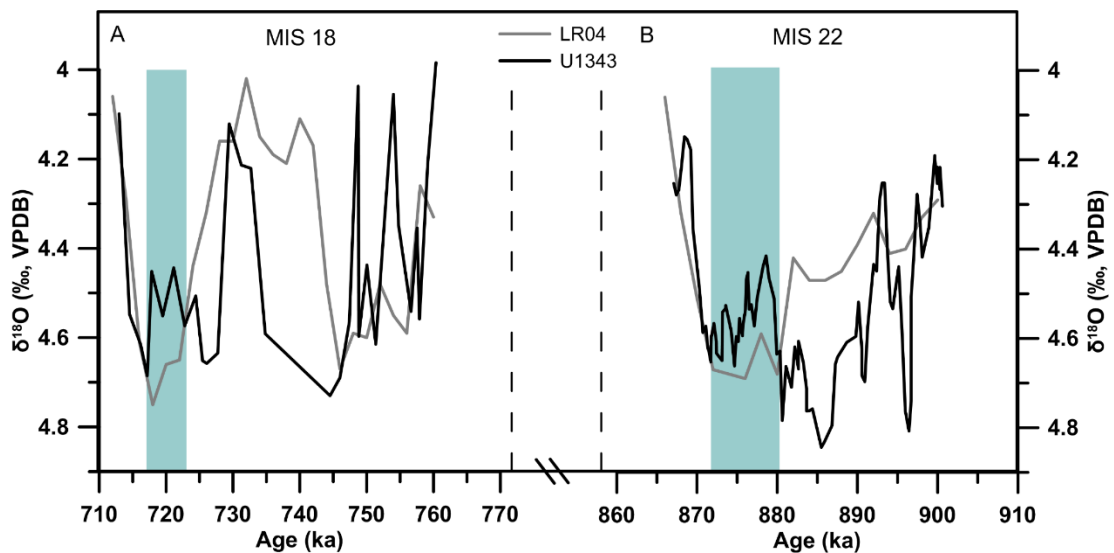


Figure 4.10 Records of $\delta^{18}\text{O}_b$ at Site U1343 (black) together with the LR04 stack (grey) across MIS 18 (A) and MIS 22 (3-pt running mean U1343 $\delta^{18}\text{O}_b$) (B) (Lisiecki and Raymo, 2005, Asahi et al., 2016, Kender et al., in review). The vertical blue bars indicate times when U1343 demonstrates a negative offset from the LR04 stack, potentially suggesting entrainment of low $\delta^{18}\text{O}_w$ NPIW at Site U1343.

Finally, the observed evolution in $\delta^{18}\text{O}_b$ and BWT across the Mid-Pleistocene could result from a hydrographic event centred on MIS 22 (Table 4.2), characterised by the contribution of a relatively warm, high $\delta^{18}\text{O}_w$ waters to the deep Bering Sea, with no long-term ice volume change across the MPT (Figure 4.9). As per Ford and Raymo (2017), Site 1208 shows a pronounced $\delta^{18}\text{O}_w$ excursion during MIS 22 that is, however, not indicative of a step-like change in $\delta^{18}\text{O}_w$ as suggested per Site 1123 (Elderfield et al., 2012), but is likely related to BWT warming across MIS 22, in

support of hydrographic changes in the deep Pacific Ocean across the 900-ka event. Paired $\delta^{18}\text{O}_b$ and BWT measurements at Site U1343 are not available, however interpolation of the published $\delta^{18}\text{O}_b$ (Asahi et al., 2016, Kender et al., in review) records provides a means to calculate $\delta^{18}\text{O}_w$ (Equation 2.4). Prior to interpolating $\delta^{18}\text{O}_b$, the high resolution interval between ~1000 ka and ~800 ka (Kender et al., in review) was smoothed using a 3-point running mean, to reduce the effect of outliers in the $\delta^{18}\text{O}_b$ record (Figure 4.11).

The 3-point running mean of $\delta^{18}\text{O}_w$ at Site U1343 demonstrates no long-term trend across the Mid-Pleistocene (450-1120 ka) (0.07 ± 0.13 ‰ (s.e.)), however a pronounced positive excursion is evident during MIS 22 (Figure 4.11), similar in absolute values to $\delta^{18}\text{O}_w$ at ODP Site 1123 across MIS 22 (Figure 4.11). To better compare the available records of $\delta^{18}\text{O}_w$ across the MPT (Sosdian and Rosenthal, 2009, Elderfield et al., 2012), I calculated the glacial and interglacial $\delta^{18}\text{O}_w$ averages (based on the MIS mean) as deviation from the respective record mean (Figure 4.12). This clearly demonstrates the step-like increase in glacial $\delta^{18}\text{O}_w$ at ODP Site 1123 during MIS 22, with large positive deviations from the mean since MIS 22 (Table 4.2), while all previous glacials are characterised by a small negative deviation from the mean (Figure 4.12). DSDP Site 607, on the other hand, shows more variable glacial $\delta^{18}\text{O}_w$ deviations from the mean (both positive and negative) prior to MIS 22 (Table 4.2), with exclusively positive glacial deviations since MIS 22, even though of variable amplitude and smaller compared to ODP Site 1123 (Figure 4.12). Glacial $\delta^{18}\text{O}_w$ at Site U1343 is characterised by both positive and negative deviations from the mean until MIS 24 (Table 4.2), similar to DSDP Site 607, while available late Pleistocene cycles again are exclusively characterised by a positive glacial $\delta^{18}\text{O}_w$ deviation from the mean within error of the deviations observed at both ODP Site 1123 and DSDP Site 607, with exception of MIS 20 and MIS 2, where ODP Site 1123 demonstrates more positive $\delta^{18}\text{O}_w$ (Figure 4.12). Prior to MIS 22, MIS 30 and MIS 26 (Table 4.2) stand out at Site U1343, demonstrating large amplitude positive deviations from the mean. Considering the two possible scenarios of ice volume evolution suggested from co-examining $\delta^{18}\text{O}_b$ and BWT at Site U1343, positive $\delta^{18}\text{O}_w$ excursions prior to MIS 22 together with consistently positive deviations from the mean following MIS 22 are in support of continental ice volume increase associated with the MPT and potential

entrainment of NPIW at Site U1343 during, at least some, late Pleistocene climate cycles indicated by lower $\delta^{18}\text{O}_w$.

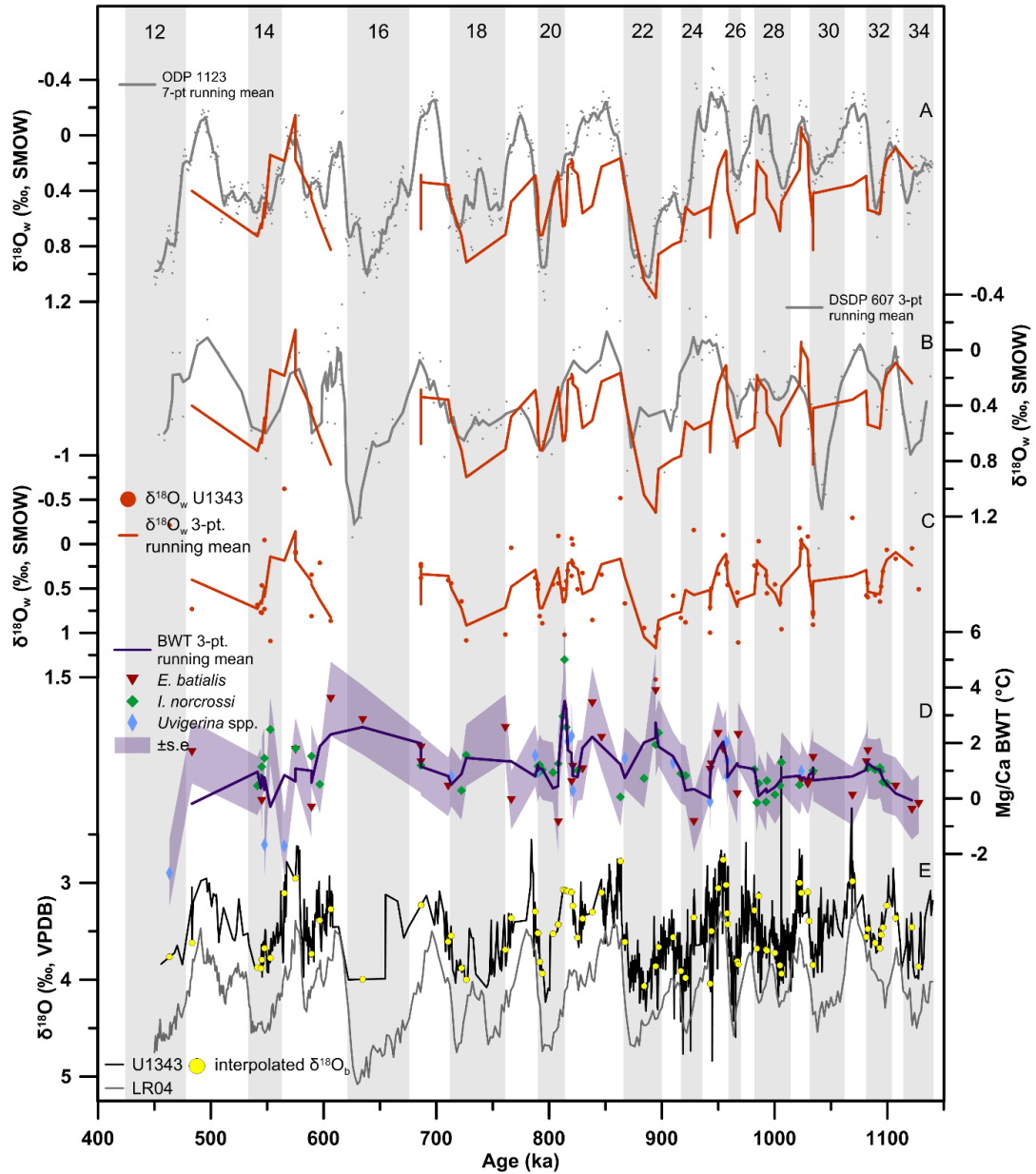


Figure 4.11 (A) The 7-point running mean of $\delta^{18}\text{O}_w$ at ODP Site 1123 (grey) (Elderfield et al., 2012) together with the 3-point running mean of $\delta^{18}\text{O}_w$ at Site U1343 (orange) across the Mid-Pleistocene. (B) The 3-point running mean of $\delta^{18}\text{O}_w$ at DSDP Site 607 (grey) (Sodrian and Rosenthal, 2009, Ford et al., 2016) and Site U1343 (orange). (C) $\delta^{18}\text{O}_w$ at Site U1343 (orange dots) together with the 3-point running mean (orange line). (D) 3-point running mean of BWT at Site U1343 (purple) across the Mid-Pleistocene based on *E. batialis* (red triangles), *I. norcrossi* (green diamonds), and *Uvigerina* spp. (blue diamonds) including the \pm s.e. envelope (light purple). (E) $\delta^{18}\text{O}_b$ at Site U1343 (black) (Asahi et al., 2016, Kender et al., in review) together with the interpolated values (yellow dots) used for $\delta^{18}\text{O}_w$ reconstructions and the LR04 stack (grey) (Lisiecki and Raymo, 2005). The grey vertical bars represent glacial intervals, numbers at the top represent marine isotope stages (MIS boundaries from (Lisiecki and Raymo, 2005)).

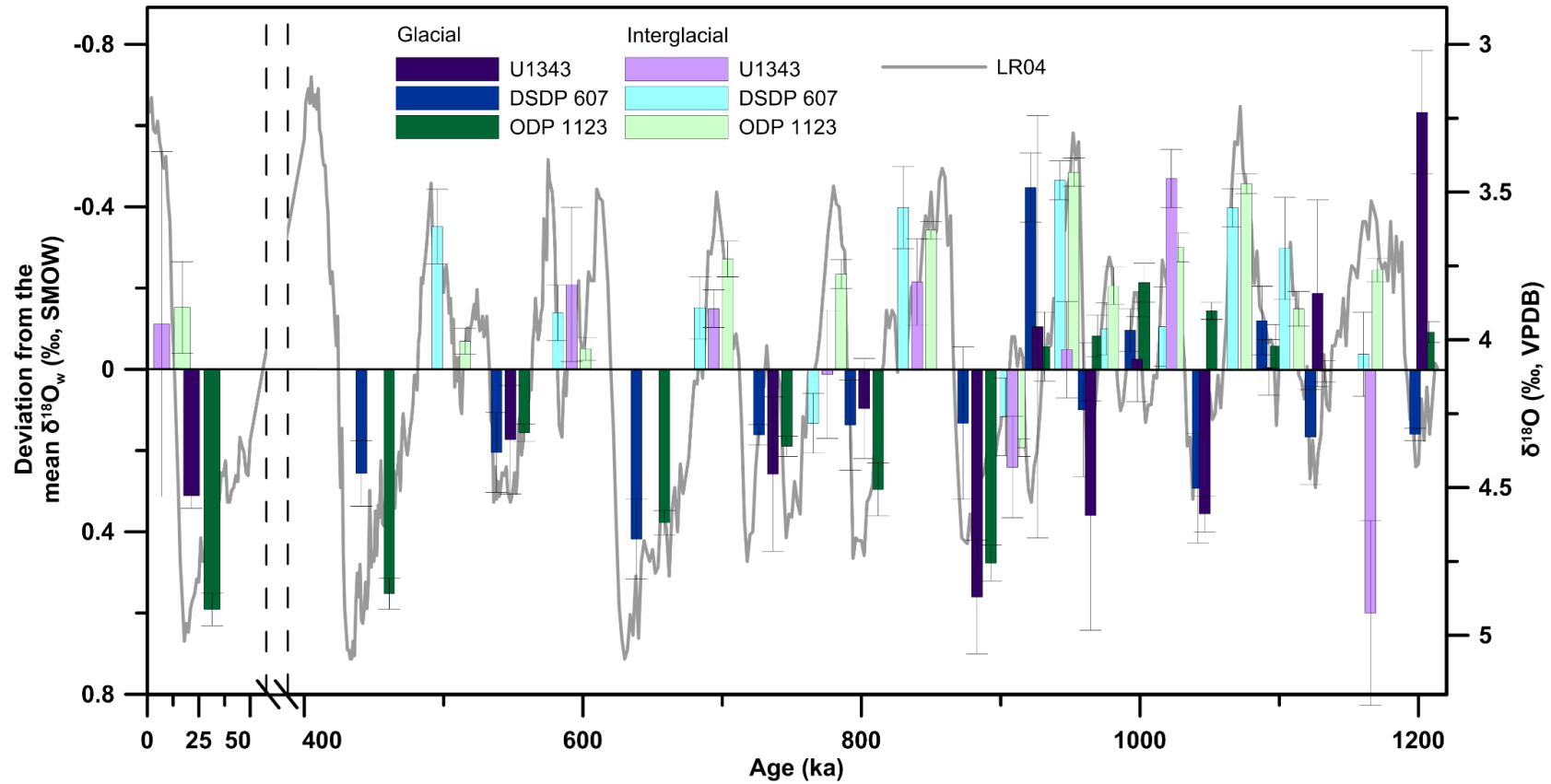


Figure 4.12 The deviation of the glacial and interglacial average of $\delta^{18}\text{O}_w$ from the respective mean at Site U1343 (dark blue, dark red), ODP Site 1123 (medium blue, orange) (Elderfield et al., 2012), and DSDP Site 607 (light blue, pink) (Sosdian and Rosenthal, 2009, Ford et al., 2016) across the Mid-Pleistocene, together with the LR04 stack (grey) (Lisiecki and Raymo, 2005). The error bars represent the standard error.

Even though large differences exist in the relative changes of glacial $\delta^{18}\text{O}_w$ at DSDP Site 607 (Sosdian and Rosenthal, 2009), ODP Site 1123 (Elderfield et al., 2012), and IODP Site U1343, likely resulting from regional effects, such as changes in the circulation or local evaporation/precipitation patterns (Shackleton, 1967, Schrag et al., 2002, LeGrande and Schmidt, 2006), the direction (positive/negative) of the glacial $\delta^{18}\text{O}_w$ deviation from the mean is consistent in all three cores from MIS 24 (Table 4.2) onwards (Figure 4.12). This highlights the 900-ka event as an important interval in continental ice volume evolution across the MPT, however, additional records from across the global oceans are needed to determine the nature of continental ice volume increase, particularly with respect to a gradual or abrupt change, and to decipher different regional influences on $\delta^{18}\text{O}_w$.

Interglacial $\delta^{18}\text{O}_w$ deviations from the mean are more consistent in their direction for all three cores with predominantly negative deviations (Figure 4.12). MIS 35 stands out at Site U1343, while MIS 19 shows a small positive deviation in both Site U1343 and Site 607. The only interglacial with all three cores demonstrating a positive deviation from their respective mean is MIS 23 (Table 4.2), again highlighting the 900-ka event as a crucial time period for continental ice volume across the MPT (Figure 4.12).

4.5 Conclusions

In this study I present records of BWT in the eastern Bering Sea from the LGM-Holocene and across the Mid-Pleistocene. The results reveal both important long-term and orbital scale changes in the Bering Sea hydrography across the Mid- and late Pleistocene.

Across Termination I the BWT record demonstrates an increase of 2.03 ± 0.78 °C (s.e.), from average LGM values of -0.31 ± 0.75 °C (s.e.) to an average Holocene BWT of 1.71 ± 0.81 °C (s.e.). Careful examination of BWT together with $\delta^{18}\text{O}_b$ (Asahi et al., 2016, Kender et al., in review) at Site U1343 indicates a smaller but within error $\delta^{18}\text{O}_w$ change (0.89 ± 0.30 ‰ (s.e.)) compared to the proposed mean ocean $\delta^{18}\text{O}_w$ change of 1.05 ± 0.20 ‰ (Duplessy et al., 2002) across Termination I. This suggests potential admixture of a low $\delta^{18}\text{O}_w$ water mass to Site U1343 across the LGM, supported by two episodes of decreased $\delta^{18}\text{O}_b$ compared to the LR04 stack around 25

ka and 17.5 ka. Whereas, no BWT data is available for 25 ka, the second interval around 17.5 ka shows no pronounced change in BWT, suggesting that the decrease in $\delta^{18}\text{O}_b$ results from changes in $\delta^{18}\text{O}_w$.

Long-term trends in Mid-Pleistocene BWT at Site U1343 in conjunction with $\delta^{18}\text{O}_b$ (Asahi et al., 2016, Kender et al., in review) suggest two possible scenarios of MPT climate change in the eastern Bering Sea. The first scenario depicts no long-term change in MPT ice volume with BWT warming and increased $\delta^{18}\text{O}_w$ across MIS 22 (Table 4.2) in the Bering Sea resulting from a onetime event. Similar changes in BWT and $\delta^{18}\text{O}_w$ evolution to Site U1343 are also observed at ODP Site 1208 on Shatsky Rise in the deep North Pacific (Ford and Raymo, 2017), potentially indicating a more widespread hydrographical event at this time. On the other hand, the observed BWT and $\delta^{18}\text{O}_b$ changes at Site U1343 can be explained by an increase in continental ice volume prior to or during MIS 22 (Table 4.2) and enhanced incursion of NPIW in the deep Bering Sea during post-MPT glacials, in line with the LGM-Holocene record. The latter scenario is additionally supported by $\delta^{18}\text{O}_w$ reconstructions at Site U1343 from interpolated $\delta^{18}\text{O}_b$ and BWT, indicating positive $\delta^{18}\text{O}_w$ deviations from the mean during and preceding MIS 22 (Figure 4.12).

$\delta^{18}\text{O}_w$ at Site U1343 in conjunction with $\delta^{18}\text{O}_w$ from Site 607 (Sosdian and Rosenthal, 2009) and Site 1123 (Elderfield et al., 2012), highlights the 900-ka event as an important interval for MPT continental ice volume evolution, marking the onset of a more 'in-phase' behaviour of all three records in the $\delta^{18}\text{O}_w$ deviation from the mean across both glacial and interglacial intervals (Figure 4.12). However, this study also emphasizes the importance of the regional hydrography on $\delta^{18}\text{O}_w$ as proposed by Ford et al. (2016) and highlights the need for additional high resolution records of $\delta^{18}\text{O}_w$ across the MPT to derive a globally averaged stack, less sensitive to regional climate signals.

Even though, the BWT record at Site U1343 was not able to reconcile the divergent ice volume histories for the MPT as reconstructed from the North Atlantic (Sosdian and Rosenthal, 2009, Ford et al., 2016) and the Southwest Pacific (Elderfield et al., 2012), it represents a valuable contribution to our understanding of North Pacific climate change, particularly with respect to the importance of NPIW in this region. Recent studies suggest that increased export of NPIW during the LGM may have

increased primary productivity in the equatorial Pacific (Max et al., 2017) and that a deeper penetration of NPIW during glacials of the Mid-Pleistocene could potentially aid in atmospheric CO₂ drawdown by reducing the eddy-driven upwelling of old and CO₂-rich deep waters in the Bering Sea (Kender et al., in review). Thus, additional records of $\delta^{18}\text{O}_b$ and $\delta^{18}\text{O}_w$ in conjunction with carbon cycle proxies are needed in areas of the North Pacific sensitive to changes in the local hydrography, in order to decipher the depth of NPIW during Pleistocene glacials and its role for the North Pacific carbon cycle.

5. Pleistocene variability in sedimentary redox chemistry in the eastern Bering Sea

5.1 Introduction

Today the Bering Sea is characterized by high primary productivity along the eastern shelf break, maintained by CO₂ and nutrient rich upwelled deep waters (Mizobata et al., 2002, Mizobata and Saitoh, 2004, Mizobata et al., 2008, Ladd et al., 2012), tidal mixing, transverse circulation (Springer et al., 1996, Mizobata et al., 2006, Hurst et al., 2010, Tanaka et al., 2012), and nutrient release during spring sea ice melting (Wang et al., 2014). As such, low oxygen concentrations are pervasive in mid-depth waters, forming a pronounced oxygen minimum zone (OMZ) (Whitledge and Luchin, 1999, Expedition 323 Scientists 2010) (Figure 1.5). Changes in the ventilation and export productivity in the past have been shown to impact this OMZ on orbital timescales. In particular the contribution of well-ventilated North Pacific Intermediate Water (NPIW) versus poorly ventilated North Pacific Deep Water (NPDW), changes in the ventilation of NPDW, and enhanced/reduced primary productivity during interglacials and glacials, respectively, fundamentally alter the oxygen concentrations ([O₂]) in intermediate to deep waters of the Bering Sea.

O₂ in the ocean interior is replenished by a process called ventilation, where O₂-rich waters equilibrated with the atmosphere are subducted via deep or intermediate water formation. No deep waters form in the North Pacific today, resulting from the low surface ocean salinities and the strong stratification of the water column with a pronounced halocline (Warren, 1983, Emile-Geay et al., 2003). However, intermediate waters form by mixing of brines produced during sea ice freezing in the Sea of Okhotsk with subsurface waters (Talley, 1993). Evidence of oxygen and carbon isotopes, suggest increased ventilation of intermediate waters in the Bering Sea during glacials of the last 1200 ka, accompanied by a deepening of the divide between well-ventilated intermediate waters and poorly ventilated deep water masses, at least for the last glacial maximum (LGM) (Duplessy et al., 1989, Matsumoto et al., 2002, Ahagon et al., 2003, Sagawa and Ikehara, 2008, Okazaki et al., 2012, Jaccard and

Galbraith, 2013, Rae et al., 2014, Max et al., 2014, Knudson and Ravelo, 2015b, Cook et al., 2016). Today NPIW, formed from atmospherically-equilibrated sea ice brines in the Sea of Okhotsk and mixing with nutrient-rich subsurface waters (Talley, 1993, Shcherbina et al., 2003), is found at 300-700 m water depth (Talley, 1993), while increased ventilation during glacials has been reported from 800 m water depth for the last 1200 ka (Knudson and Ravelo, 2015b) and even deeper between 1000 m to ~3500 m water depth during the LGM and across cold stadials of the last deglaciation in the Bering Sea and across the North Pacific (Duplessy et al., 1989, Ahagon et al., 2003, Sagawa and Ikehara, 2008, Okazaki et al., 2012, Rae et al., 2014, Max et al., 2014, Cook et al., 2016). Increased intermediate/deep water formation in the North Pacific during Heinrich stadial 1 (HS1) is also seen in climate models (Saenko et al., 2004, Okazaki et al., 2010), however, proxy evidence from > ~2400 m water depth in the north western and north eastern North Pacific does not show increased ventilation during HS1 (Lund et al., 2011, Jaccard and Galbraith, 2013), with the exception of one record in the Gulf of Alaska (Rae et al., 2014), contradicting the formation of a ‘true’ deep water mass in the North Pacific during the last deglaciation. Nevertheless, proxy records from across the North Pacific and its marginal seas during the last glacial/interglacial (G/IG) cycle, indicate increased penetration of well-ventilated intermediate waters to depths of up to ~2000 m (Duplessy et al., 1989, Ahagon et al., 2003, Sagawa and Ikehara, 2008, Okazaki et al., 2012, Rae et al., 2014, Max et al., 2014, Cook et al., 2016), underlain by NPDW characterised by decreased glacial [O₂] (Galbraith et al., 2007, Jaccard et al., 2009, Lund et al., 2011, Jaccard and Galbraith, 2013). Evidence of carbon and oxygen isotopes together with neodymium isotopes (ϵ_{Nd}), suggests that the Bering Sea may have been the primary location of glacial NPIW water formation during the late Pleistocene, with brine formation during sea ice freezing facilitating the subduction of atmospherically-equilibrated O₂-rich waters (Ohkushi et al., 2003, Horikawa et al., 2010, Rella et al., 2012, Knudson and Ravelo, 2015b). On the other hand, the Sea of Okhotsk might also have been important with respect to NPIW water formation during both glacials and interglacials (Talley, 1993, Watanabe and Wakatsuchi, 1998, Max et al., 2014, Okazaki et al., 2014), indicating that further research is needed to fully understand the source region dynamics of NPIW on G/IG timescales.

Compared to intermediate waters that are ventilated locally, deep waters in the North Pacific originate in the south and are ventilated primarily by deep water formation around Antarctica (Killworth, 1983, Broecker et al., 1998, Kawabe and Fujio, 2010). On orbital timescales large amounts of carbon were likely stored in the deep ocean during glacials and released across the deglaciation (Boyle, 1988, Galbraith et al., 2007, Jaccard et al., 2009, Yu et al., 2010a, Skinner et al., 2010, Burke and Robinson, 2012). Additionally, evidence from the North Atlantic suggest increased deep ocean carbon storage first observed between 800-1000 ka associated with the Mid-Pleistocene transition (MPT) (Lear et al., 2016, Sosdian et al., 2018). Sequestration of carbon in the deep ocean via changes in the air-sea gas exchange (Stephens and Keeling, 2000, Toggweiler et al., 2006, Schmittner and Galbraith, 2008, Anderson et al., 2009, Jaccard et al., 2013, Ferrari et al., 2014, Billups et al., 2018) and/or changes in the efficiency of the biological pump (Martin, 1990, Jaccard et al., 2009, Jaccard and Galbraith, 2012, Ziegler et al., 2013, Jaccard et al., 2013, Martínez-García et al., 2014, Gottschalk et al., 2016), has the potential to influence the bottom water [O₂] on orbital time scales. Whereas, reduced air-sea gas exchange, caused by increased sea ice and/or stratification in areas of deep water formation around Antarctica (Stephens and Keeling, 2000, Schmittner and Galbraith, 2008, Ferrari et al., 2014, Billups et al., 2018), would decrease bottom water oxygenation by reducing the invasion of atmospheric O₂ and the evasion of dissolved CO₂, changes in the biological pump, would affect deep water [O₂] by increasing the amount of respired carbon that accumulates in the deep ocean (Jaccard et al., 2009, Bradtmiller et al., 2010, Jaccard and Galbraith, 2012, Gottschalk et al., 2016). The deep North Pacific [O₂] has been shown to sensitively respond to changes in deep ocean carbon storage on G/IG timescales throughout the late Pleistocene. Decreased [O₂] of NPDW is observed in the equatorial Pacific during marine isotope stage (MIS) 2, 4, 6 and 8 (Jacobel et al., 2017) and in the North Pacific during glacial intervals of the last ~150 ka, associated with a change in the ratio of preformed to regenerated nutrients, facilitating deep ocean carbon storage (Galbraith et al., 2007, Jaccard et al., 2009).

In addition to changes in the water mass structure across G/IG cycles, Bering Sea bottom water [O₂] is influenced by regional processes, in particular primary productivity, causing an expansion or contraction of the mid-depth OMZ. Today, primary productivity in the Bering Sea 'Green Belt' is on the order of 175-275 g C m⁻²

$^2 \text{ yr}^{-1}$ (Springer et al., 1996) and causes high rates of remineralisation of organic matter settling through the water column accompanied by oxygen consumption and the formation of a mid-depth OMZ, with $[\text{O}_2]$ of 0.43-1.57 mg L^{-1} (Whitledge and Luchin, 1999) (Figure 1.5). Laminated sediments on the Bering Sea Ridges and along the continental margin are faithful recorders of OMZ dynamics, indicating an expansion of the OMZ during periods of increased primary productivity across the last deglaciation, such as the Bølling-Allerød (B/A, ~12.7 ka to 14.7 ka) and the early Holocene (Cook et al., 2005, Expedition 323 Scientists 2010, Caissie et al., 2010, Aiello and Ravelo, 2012, Kuehn et al., 2014, Pelto et al., 2018).

Multiple approaches exist to reconstruct past bottom water $[\text{O}_2]$, including bulk sedimentary redox sensitive trace metals (Morford and Emerson, 1999, Chase et al., 2001, Morford et al., 2007, Jaccard et al., 2009, Pattan and Pearce, 2009), benthic foraminiferal assemblages (Hayward et al., 2005, Jorissen et al., 2007, Ovsepyan et al., 2017), foraminiferal I/Ca (Lu et al., 2010, Glock et al., 2014) and Mn/Ca (Groeneveld and Filipsson, 2013, Koho et al., 2015, McKay et al., 2015), and authigenic foraminiferal U/Ca and U/Mn (Boiteau et al., 2012, Gottschalk et al., 2016, Chen et al., 2017), however each proxy comes with individual caveats. To date only very limited applications have been reported for reconstructing bottom water $[\text{O}_2]$ across the Mid-Pleistocene (Hayward et al., 2005).

I present records of authigenic U/Mn and U/Ca of benthic and planktonic foraminifera as a proxy for sedimentary redox chemistry linked to bottom water $[\text{O}_2]$ (Boiteau et al., 2012, Gottschalk et al., 2016, Chen et al., 2017), in combination with benthic foraminiferal assemblages, as an independent quantitative ecological parameter (Jorissen et al., 2007), from International Ocean Discover Program (IODP) Site U1343 in the eastern Bering Sea (~2000 m water depth) across the Mid-Pleistocene and the LGM-Holocene. Benthic foraminiferal assemblages, benthic/planktonic U/Mn, and planktonic U/Ca demonstrate prominent changes in the sedimentary redox chemistry on G/IG timescales, influenced by the range of processes described above. Even though the influence of primary productivity on bottom water $[\text{O}_2]$ cannot be ruled out, records of sedimentary redox chemistry and foraminiferal assemblages likely suggest a deepening of NPIW across the MPT, also seen during the LGM and HS1.

5.2 Materials and methods

5.2.1 U/Mn and U/Ca of authigenic foraminiferal coatings

U/Ca and Mn/Ca was measured on benthic and planktonic foraminifera across the last G/IG cycle and the Mid-Pleistocene at IODP Site U1343. Benthic U/Mn of *Elphidium batialis*, *Islandiella norcrossi*, and *Uvigerina* spp. (150-250 μm size fraction) was calculated from U/Ca and Mn/Ca ratios measured on the same sample material as Mg/Ca, cleaned according to the Cd-cleaning protocol (Boyle, 1983, Boyle and Keigwin, 1985). In total U/Mn was quantified on 55, 79, and 18 *E. batialis*, *I. norcrossi*, and *Uvigerina* spp. samples respectively. Additionally, 54 samples of *Neogloboquadrina pachyderma* from the 150-250 μm size fraction cleaned according to the Mg-cleaning protocol (Barker et al., 2003), were analysed for Mn/Ca and U/Ca to calculate the U/Mn ratios.

All samples were analysed on a Thermo Element XR High Resolution Inductively Coupled Plasma Mass Spectrometer (ICP-MS) at Cardiff University with matrix-matched standards for ratio calculations. The consistency standards contain 0.16 mmol mol^{-1} and 0.14 mmol mol^{-1} U/Mn, respectively with an external reproducibility of $\pm 3.11\%$ and $\pm 2.26\%$ (relative standard deviation (r.s.d.)) across the time period of this study. Based on the approach taken to calculate benthic and planktonic U/Mn ratios, the average propagated analytical uncertainty is very low for all species (below $\pm 0.06 \text{ mmol mol}^{-1}$, s.e.).

5.2.2 Low oxygen benthic foraminifera assemblage census counts

The assemblage in the mid-depth Bering Sea is typically dominated by calcareous infaunal foraminiferal species, controlled by the oxygen conditions and supply of organic matter to the seafloor (Setoyama and Kaminski, 2015). Dominant species are tolerant to depleted oxygen conditions, related to the pronounced mid-depth OMZ and large export of organic carbon to the sediments, particularly within the Green Belt along the eastern slope (Khusid et al., 2006, Setoyama and Kaminski, 2015).

The dominant benthic foraminiferal species at Site U1343 include *Elphidium batialis*, *Uvigerina* spp., *Islandiella norcrossi*, *Eubuliminella exilis*, *Cassidulinoides parkerianus*, *Nonionella labradorica*, and *Globobulimina* spp. (primarily *G. pacifica*

and *G. affinis*). Other commonly occurring species include *Valvulineria auracana*, *Nonionella digitata*, *Lagena* spp., and *Epistominella exigua*.

Table 5.1 Dysoxic foraminiferal assemblage in the Bering Sea

Dysoxic (0.1-0.3 ml L⁻¹ [O₂]) foraminiferal assemblage	
Species	Reference
<i>Bolivina</i> spp. <i>Globobulimina</i> spp. <i>Nonionella digitata</i> <i>Chilostomella fimbriata</i>	Ovsepyan et al. (2017)
<i>Eubuliminella exilis</i>	McKay et al. (2016), Caralp (1989), Jannink et al. (1998), Filipsson et al. (2011), Cauelle et al. (2014)

The dysoxic (0.1-0.3 ml L⁻¹) (Kaiho, 1994) foraminiferal assemblage is based on the criteria set out in Ovsepyan et al. (2017) (Table 5.1), with predominantly *Nonionella digitata*, and *Globobulimina* spp. occurring at Site U1343. Additionally, *Eubuliminella exilis* associated with high input of labile organic matter and tolerant to low-oxygen environments is considered for the dysoxic assemblage (Caralp, 1989, Jannink et al., 1998, Filipsson et al., 2011, Cauelle et al., 2014, McKay et al., 2016) (Table 5.1). In total 241 samples from the Mid-Pleistocene and 30 samples from the LGM-Holocene were processed for benthic foraminiferal assemblage counts. The census counts of the dysoxic benthic foraminiferal assemblage are presented in percentage of the total counts of foraminifera in the respective sample. All samples with >30 specimens are considered. When present, *E. exilis* occurs in large quantities, dominating the dysoxic assemblage at Site U1343.

5.3 Results

5.3.1 Down-core U/Mn and U/Ca of authigenic foraminiferal coatings at IODP Site U1343

U/Mn ratios of shallow infaunal benthic foraminifera at Site U1343 across the Mid-Pleistocene (1200 ka to 450 ka) vary between 0.3-11.3 mmol mol⁻¹, 0.7-23.5 mmol mol⁻¹, and 0.2-7.6 mmol mol⁻¹, for *E. batialis*, *I. norcrossi*, and *Uvigerina* spp.,

respectively, similar to the overall range in U/Mn of the planktonic species *N. pachyderma* (1.32-12.5 mmol mol⁻¹) (Figure 5.1).

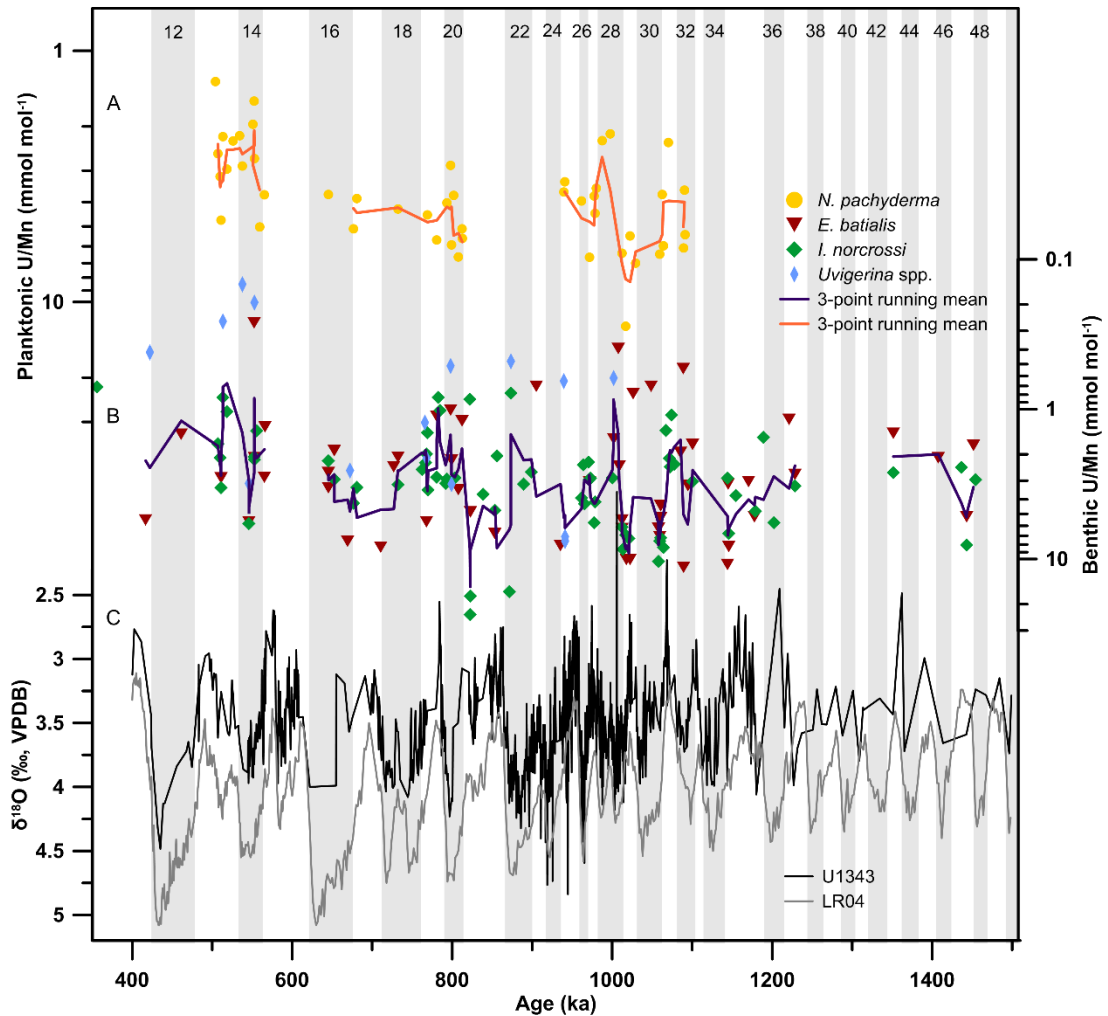


Figure 5.1 (A) Planktonic U/Mn of *N. pachyderma* (orange dots) including the 3-point running mean (thick orange line) across the Mid-Pleistocene from Site U1343, together with (B) the benthic U/Mn of *E. batialis* (red triangles), *I. norcrossi* (green diamonds), and *Uvigerina* spp. (blue diamonds) and the 3-point running mean (thick purple line). Note that the axes for U/Mn are on the logarithmic scale. (C) The $\delta^{18}\text{O}_b$ curve at IODP Site U1343 (Asahi et al., 2016, Kender et al., in review) (black) together with the LR04 stack (grey) (Lisiecki and Raymo, 2005). The grey vertical bars represent glacial intervals, numbers at the top correspond to marine isotope stages (MIS boundaries from (Lisiecki and Raymo, 2005)).

Across the LGM-Holocene interval U/Mn varies between 0.1-0.2 mmol mol⁻¹ and 0.5-1.2 mmol mol⁻¹ for *Uvigerina* spp. and *I. norcrossi*, respectively (Figure 5.2). However, interpretation of benthic U/Mn across this interval is hindered by a faunal change associated with the deglaciation, with *I. norcrossi* exclusively occurring during

the LGM and *Uvigerina* spp. only during the Holocene (Figure 5.2). As these samples are from above the Sulphate-Methane Transition Zone (SMTZ), less authigenic carbonate formation is expected, such that chemical cleaning may be more effective in removing the authigenic phases.

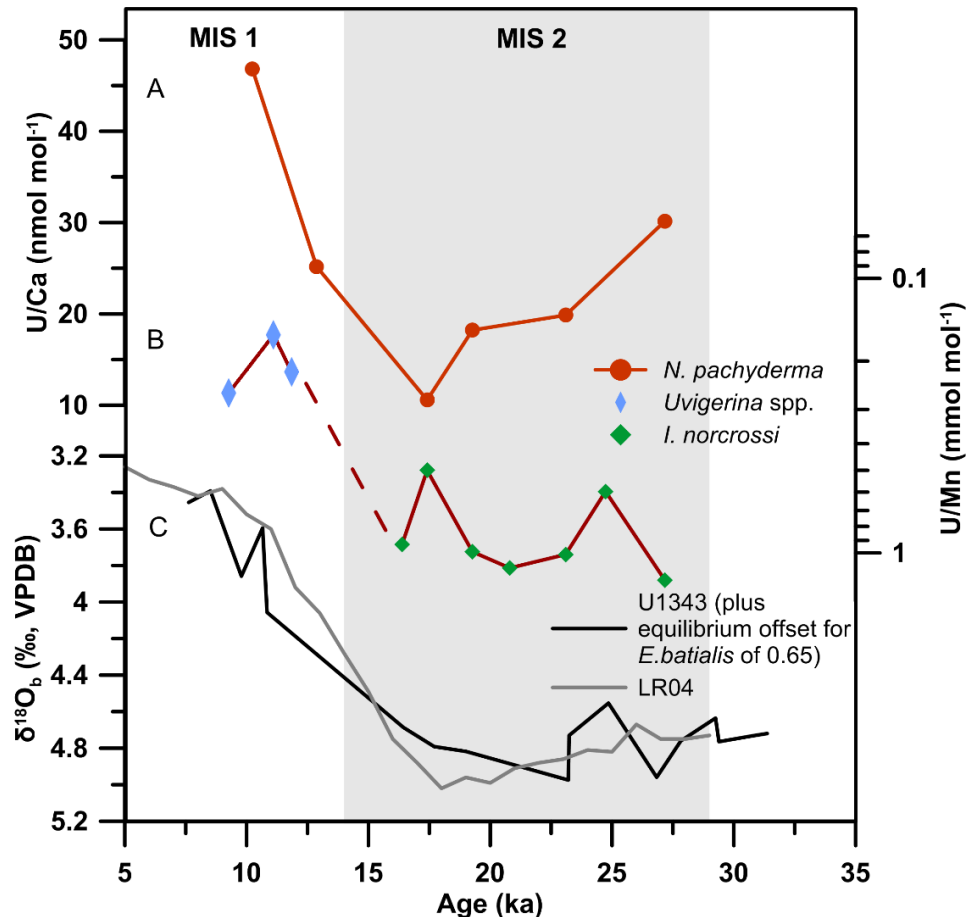


Figure 5.2 (A) U/Ca of planktonic foraminiferal species *N. pachyderma* (orange) across Termination I. (B) U/Mn of *I. norcrossi* (green diamonds) and *Uvigerina* spp. (blue diamonds) across the LGM-Holocene, the deglaciation is associated with a faunal change (dashed line). Note that the axis for U/Mn is on the logarithmic scale. (C) $\delta^{18}\text{O}_6$ record at IODP Site U1343 (adjusted for the offset between *E. batialis* and equilibrium) (black) (Asahi et al., 2016) and the LR04 stack (grey) (Lisiecki and Raymo, 2005). The grey vertical bar represents the last glacial interval, numbers at the top correspond to marine isotope stages (MIS boundaries from (Lisiecki and Raymo, 2005)).

This is in line with U/Ca and Mn/Ca ratios of benthic foraminifera across the LGM-Holocene, cleaned according to the Cd-cleaning protocol, being within the expected range of primary foraminiferal calcite of $<23 \text{ nmol mol}^{-1}$ and $<100 \text{ } \mu\text{mol mol}^{-1}$ for U/Ca and Mn/Ca, respectively (Barker et al., 2003, Chen et al., 2017). Thus, the

primary foraminiferal trace metal ratios may have a larger influence on the measured U/Mn signal, compared to samples from below the SMTZ. Mn/Ca ratios of primary foraminiferal calcite, for example have been proposed to increase together with the average living depth of the organism (Koho et al., 2017). However, Koho et al. (2017) also note a large interspecific difference likely reflecting changes in the Mn partitioning, also observed for U partitioning into primary foraminiferal calcite (Raitzsch et al., 2011). Consistently higher U/Mn ratios in *Uvigerina* spp. compared to *I. norcrossi* across this interval, are thus either related to changes in the redox chemistry between the LGM and the Holocene, or reflect species-specific differences in the partition coefficient of Mn (Koho et al., 2017) or U into foraminiferal calcite (Raitzsch et al., 2011).

Samples of *N. pachyderma* across the LGM-Holocene were too small to quantify the Mn/Ca ratio with certainty (signal-to-noise ratio <5). Instead, U/Ca varying between 10.6 nmol mol⁻¹ and 46.8 nmol mol⁻¹ are examined across the LGM-Holocene transition (Termination I). U/Ca ratios of authigenic foraminiferal coatings are also proposed to reflect changes in the ocean's redox chemistry, similar to U/Mn (Boiteau et al., 2012). Compared to U/Mn, however, U/Ca may be affected by differences in the surface-to-mass ratio of foraminiferal tests, influenced by the shell size and wall thickness (Gottschalk et al., 2016). Thus, U/Ca ratios may exhibit bias with respect to size fraction and species. Since records of planktonic U/Ca are from a single species and a relatively narrow size fraction (150-250 µm), the effect of the surface-to-mass ratio on authigenic carbonate accumulation is likely small.

5.3.2 The effect of different cleaning techniques on foraminiferal authigenic U/Mn

Unlike benthic foraminiferal U/Mn ratios that were acquired on the same sample material as Mg/Ca ratios, cleaned using the Cd-protocol (Boyle, 1983, Boyle and Keigwin, 1985), *N. pachyderma* samples were cleaned using the Mg-cleaning protocol (Chapter 2 section 2.3.7) (Barker et al., 2003). Boiteau et al. (2012) demonstrate that authigenic U/Ca ratios of planktonic foraminifera are highly sensitive to the applied chemical cleaning techniques, with a reduction in U/Ca of ~30 % during the reductive cleaning, likely as a result of dissolution of the U-enriched contamination phase (Boiteau et al., 2012). Similar reduction in U/Ca, related to the reductive cleaning, has

also been observed for core top benthic foraminiferal U/Ca ratios (Chen et al., 2017), while U/Mn ratios of the same samples seemed to be less sensitive to the cleaning method (Chen et al., 2017).

Oxidatively cleaned planktonic and reductively cleaned benthic foraminifera from Site U1343 demonstrate very similar trends in U/Mn across the Mid-Pleistocene, highlighted by a significant positive correlation ($R^2 = 0.51$ [0.29; 0.68], $n = 25$) (Figure 5.3). Thus, even though reductive cleaning likely removes a larger fraction of the contamination phase (Pena et al., 2005, Hasenfratz et al., 2017a), the measured U/Mn of reductively cleaned foraminiferal samples at Site U1343 still varies in conjunction with changes in the U/Mn of authigenic carbonates. Scanning electron microscope (SEM) images and Electron probe microanalyser (EPMA) chemical mapping of individual foraminifera fragments, demonstrates that authigenic carbonates can form as a crust on the inside and/or outside of the foraminiferal tests, or as recrystallization within the test walls (Figure 3.8). Hence, a complete removal of authigenic carbonates by reductive cleaning is unlikely, indicating that both planktonic and benthic foraminiferal U/Mn ratios reflect changes in the authigenic carbonate composition, at least below the SMTZ.

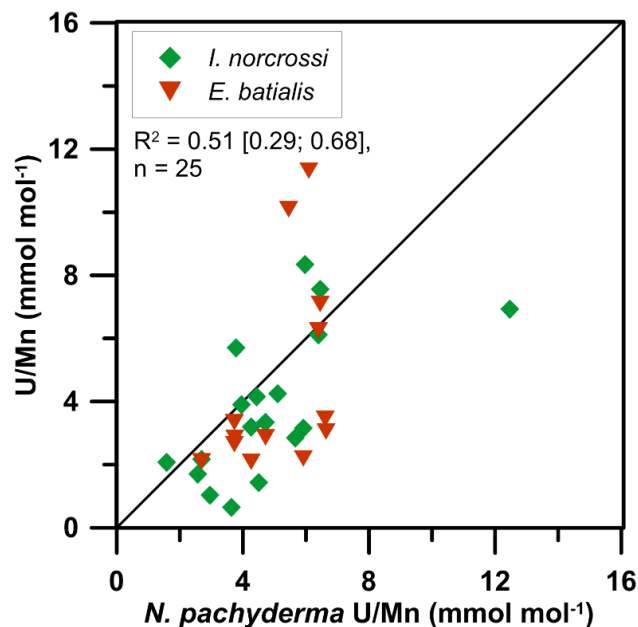


Figure 5.3 Cross plot of U/Mn of benthic foraminifera (*I. norcrossi* (green diamonds) and *E. batialis* (red triangles)) cleaned using the Cd-protocol (Boyle and Keigwin, 1985, Boyle and Keigwin, 1987) and U/Mn of planktonic foraminiferal species *N. pachyderma* cleaned using the Mg-protocol (Barker et al., 2003). There is a significant positive correlation ($R^2 = 0.51$ [0.29; 0.68], $n = 25$).

5.3.3 Inter- and intra-species variability of U/Mn

To assess the natural variability in U/Mn, two replicates of two *E. batialis* and one *Uvigerina* spp. sample were picked, cleaned, and measured separately. The variability is on the order of 5-16 % (relative standard deviation (r.s.d.)). The inter-species variability between *E. batialis*, *I. norcrossi*, and *Uvigerina* spp. at Site U1343 in samples from below the SMTZ varies between 1.5 % (r.s.d.) and 82 % (r.s.d.), however, the offsets between species are inconsistent (Figure 5.4). I therefore conclude, that the intra-species variability cannot solemnly result from offsets in the primary foraminiferal U/Ca and Mn/Ca ratios as a result of microhabitat differences of the individual species. Gottschalk et al. (2016) propose, that normalising foraminifera-bound authigenic U to Mn, rather than Ca, reduces the species-specific effects, associated with the surface to mass ratio of the tests, as both U and Mn are primarily associated with the authigenic phases. The observed intra-species variability thus likely reflects spatial variability in the sedimentary redox chemistry and the formation of microenvironments within the sediment/foraminifera tests, fostering authigenic carbonate precipitation. This is also supported by the large inter and intra species variability in diagenetic alteration within one sample as seen under the reflective light microscope (Chapter 3).

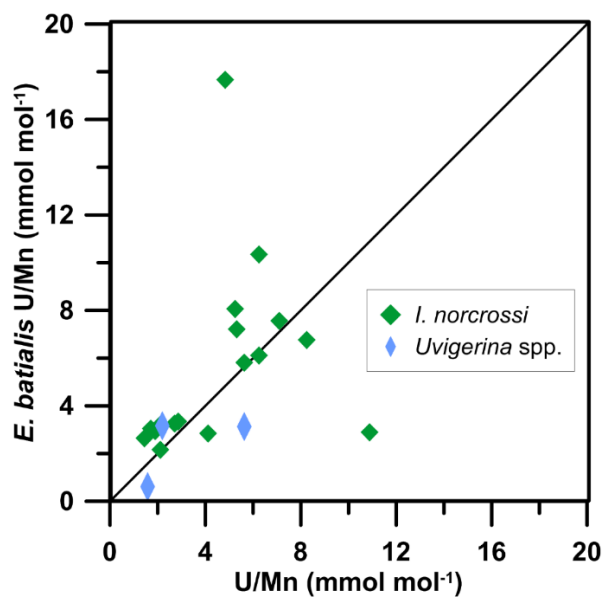


Figure 5.4 Cross plot of U/Mn of *E. batialis* versus U/Mn of *I. norcrossi* (green diamonds) and *Uvigerina* spp. (blue diamonds) from the same sample. The species-specific offsets are not consistent as seen from the scatter in the data both above and below the 1:1 line (black line).

5.3.4 Low oxygen benthic foraminiferal assemblages

The abundance of low oxygen tolerant foraminifera at IODP Site U1343 varies between 3 % and 93 % across the LGM-Holocene and between 0 % and 87 % across the Mid-Pleistocene (Figure 5.5). The abundance demonstrates distinct variability on G/IG timescales. MIS 2 is marked by an average abundance of 32 ± 5 % (standard error (s.e.)), whereas the deglaciation shows up to 93 % low oxygen benthic foraminifera, indicating prominent changes in either bottom water [O₂] and/or the supply of labile organic matter on these timescales. Across the Mid-Pleistocene glacial intervals are characterised by an average of 15 ± 7 % (s.e.), whereas interglacials show an average abundance of 18 ± 6 % (s.e.). In general the dysoxic benthic foraminiferal assemblage demonstrates low abundance prior to MIS 26 (Table 4.2). Following MIS 26 peaks in the dysoxic foraminiferal assemblage occur predominantly during late glacial/early deglaciations (Figure 5.5).

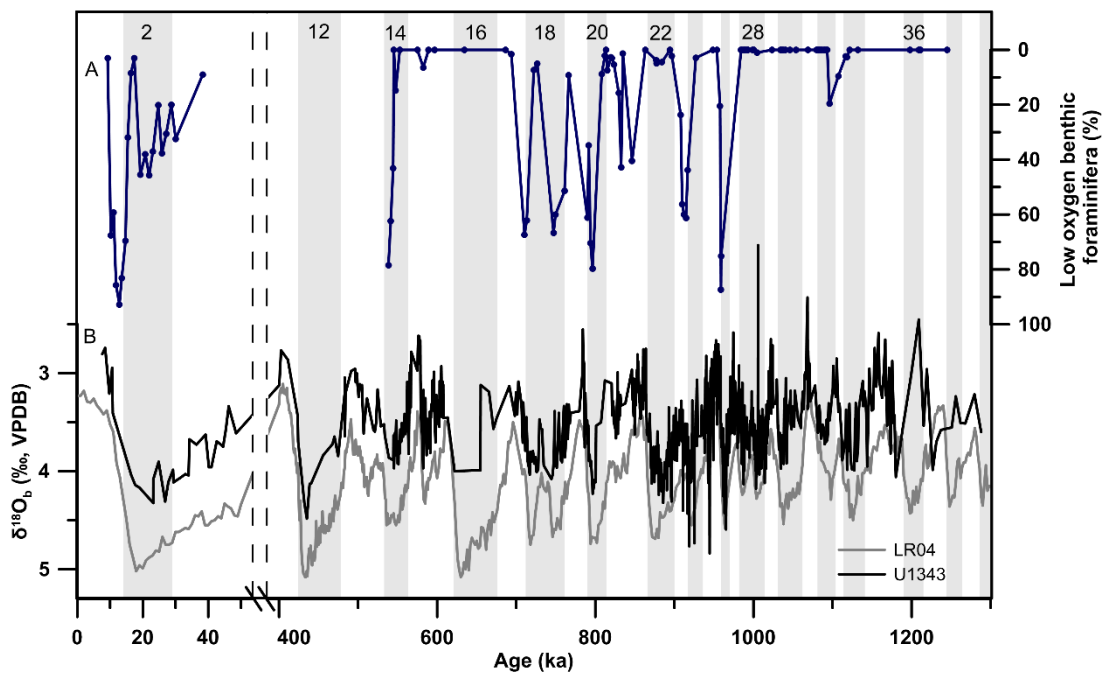


Figure 5.5 (A) The abundance of dysoxic benthic foraminiferal species at Site U1343 (dark blue) across the LGM-Holocene and the Mid-Pleistocene in percent. (B) $\delta^{18}\text{O}_b$ at IODP Site U1343 (black) (Asahi et al., 2016) together with the LR04 stack (grey) (Lisiecki and Raymo, 2005). The grey vertical bars represent glacial intervals, numbers at the top correspond to marine isotope stages (MIS boundaries from (Lisiecki and Raymo, 2005)).

5.4 Discussion

5.4.1 Authigenic foraminiferal U/Mn as a proxy for sedimentary redox conditions above and below the SMTZ

As demonstrated in Chapter 3 foraminiferal-bound U and Mn are significantly influenced by early diagenesis at Site U1343. Laser ablation inductively coupled plasma mass spectrometry (LA-ICP-MS) U/Ca ratios of foraminifera from above the modern SMTZ suggest precipitation of minor amounts of authigenic low-Mg calcite, as a result of organoclastic sulphate reduction. This could indicate that instead of representing changes in the redox chemistry, authigenic carbonates on foraminiferal tests accumulate continuously as they get buried in the sediments. Even though dissolved U concentrations in pore waters vary with the redox chemistry, continuous accumulation would likely be characterised by increased authigenic U/Ca ratios of foraminifera with increasing depth. U/Ca ratios of planktonic foraminiferal species *N. pachyderma*, however, decrease with increasing sediment depth (Figure 5.2), suggesting that foraminiferal trace metal ratios of authigenic carbonates from above the SMTZ track early diagenetic processes, related to changes in the redox chemistry in support of previous studies (Gottschalk et al., 2016, Chen et al., 2017).

Within the SMTZ anaerobic oxidation of methane (AOM) drives authigenic carbonate precipitation (Pierre et al., 2016), significantly influencing the U/Ca and Mn/Ca ratio of foraminiferal authigenic coatings at Site U1343 (Chapter 3). LA-ICP-MS data and SEM imaging of foraminifera (Chapter 3) show that major diagenetic alterations of foraminiferal tests, likely indicating more intense rates of AOM and authigenic carbonate formation, are accompanied by increased Mn/Ca and U/Ca ratios (Figure 3.11). However, the U/Ca versus Mn/Ca ratios do not fall on a 1:1 line, instead the U/Ca increase associated with a higher degree of diagenetic alterations of foraminiferal tests is proportionally larger compared to the related Mn/Ca increase (Figure 3.13). This suggests an increase in the U/Mn ratio with diagenetic alteration, in line with more reducing conditions leading to stronger rates of AOM and authigenic carbonate formation. Thus, the U/Mn ratios of foraminifera from below the SMTZ likely vary according to changes in the sedimentary redox state, however, the vertical movement of the SMTZ could have caused build-up of authigenic carbonates in sedimentary horizons. Consequently, U/Mn ratios of foraminifera from below the

SMTZ either reflect changes in the sedimentary redox chemistry and/or residence time of foraminifera tests within the SMTZ associated with vertical migration of this redox-horizon. The former implies an age offset between the SMTZ precipitation and the redox state it reflects, determined by the depth of the SMTZ, which is driven by the balance of the downward flux of sulphate and the upward flux of methane in the pore waters (Wehrmann et al., 2011).

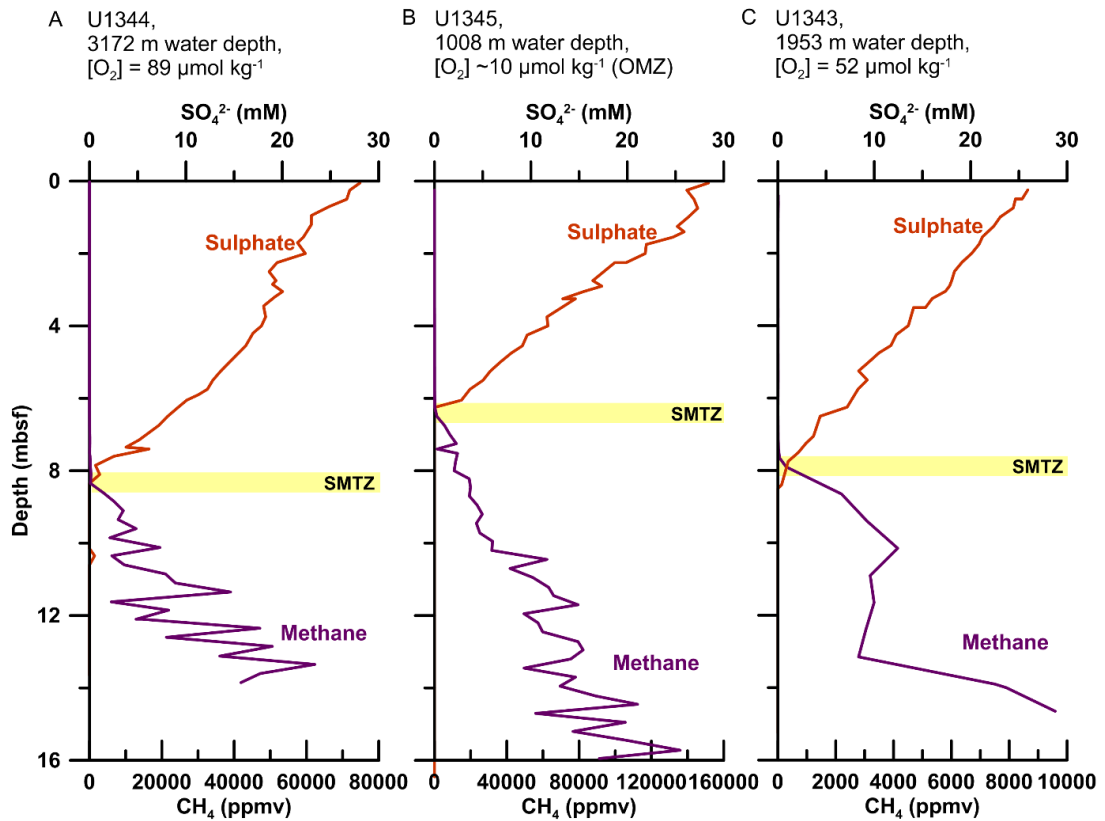


Figure 5.6 The depth of the Sulphate-Methane Transition Zone (SMTZ) at 3 different Sites (A) U1344, (B) U1345, and (C) U1343 along the eastern Bering Sea slope, cored during IODP Leg 323 (Expedition 323 Scientists 2010). The pore water sulphate and methane profiles demonstrate clear gradients with no/little overlap, characteristic of the SMTZ. The depth of the SMTZ along the eastern Bering Sea slope is governed by the bottom water $[O_2]$ (Wehrmann et al., 2011). Dissolved sulphate and methane concentrations from LIMS Version 17.3 (<http://web.iodp.tamu.edu/LORE/>), bottom water $[O_2]$ from Olsen et al. (2016) and Garcia et al. (2006a).

Sulphate in pore waters originates from diffusion of seawater with constant sulphate concentrations (~ 29 mM (Millero, 2013)), thus changes in the sulphate flux into the SMTZ are primarily related to rates of organoclastic sulphate reduction above the SMTZ (Wehrmann et al., 2011). Changes in the methane flux, on the other hand, are

controlled by the supply of methane from either a thermogenic origin or, in the case of the eastern Bering Sea continental margin, microbial methanogenesis in deeper sediments (Wehrmann et al., 2011). The modern depth of the SMTZ along the eastern Bering Sea slope is governed by the [O₂] of the bottom waters, with a shallower SMTZ depth for sediments within the OMZ, related to the increased availability of labile organic matter for methanogenesis in deeper sediments due to an early shift from aerobic to anaerobic remineralisation pathways (Wehrmann et al., 2011) (Figure 5.6). This indicates that the SMTZ depth at Site U1343 may have changed in the past in relation to changes in the bottom water [O₂], as a result of either local OMZ expansion or changes in the [O₂] of water masses contributing to the deep Bering Sea. Laminated intervals from across the Bering Sea (Expedition 323 Scientists 2010, Aiello and Ravelo, 2012, Kuehn et al., 2014, Pelto et al., 2018) and at Site U1343 (Expedition 323 Scientists 2010), correlating with the B/A and the early Holocene (Expedition 323 Scientists 2010), demonstrate OMZ expansion during times of increased primary productivity and increased organic carbon remineralization in the water column (Aiello and Ravelo, 2012, Kuehn et al., 2014) (Figure 5.7). Additionally, studies from the North Pacific and the Bering Sea indicate prominent changes in bottom and intermediate water [O₂] on G/IG timescales in relation to increased deep ocean carbon storage during glacial intervals and local NPIW formation (Galbraith et al., 2007, Jaccard et al., 2009, Knudson and Ravelo, 2015b, Cook et al., 2016, Max et al., 2017).

The rate and magnitude of vertical SMTZ migration in relation to environmental changes, however, is still poorly understood. In the modern day Bering Sea, the SMTZ depth along the eastern Bering Sea margin between 1000-3000 m water depth varies by ~2 m in conjunction with differences in the bottom water [O₂] (Wehrmann et al., 2011) (Figure 5.6). Foraminiferal Mg/Ca and U/Ca LA-ICP-MS data from IODP Site U1343, support potential SMTZ migration on a meter-scale. Considering the LGM-Holocene climate change, the lowest bottom water [O₂] in the eastern Bering Sea is expected during the B/A and the early Holocene, characterised by laminated sediments at Site U1343 and throughout the Bering Sea (Cook et al., 2005, Expedition 323 Scientists 2010, Caissie et al., 2010, Aiello and Ravelo, 2012, Kuehn et al., 2014, Pelto et al., 2018), indicating bottom water [O₂] below <0.1 ml L⁻¹ (Moffitt et al., 2015).

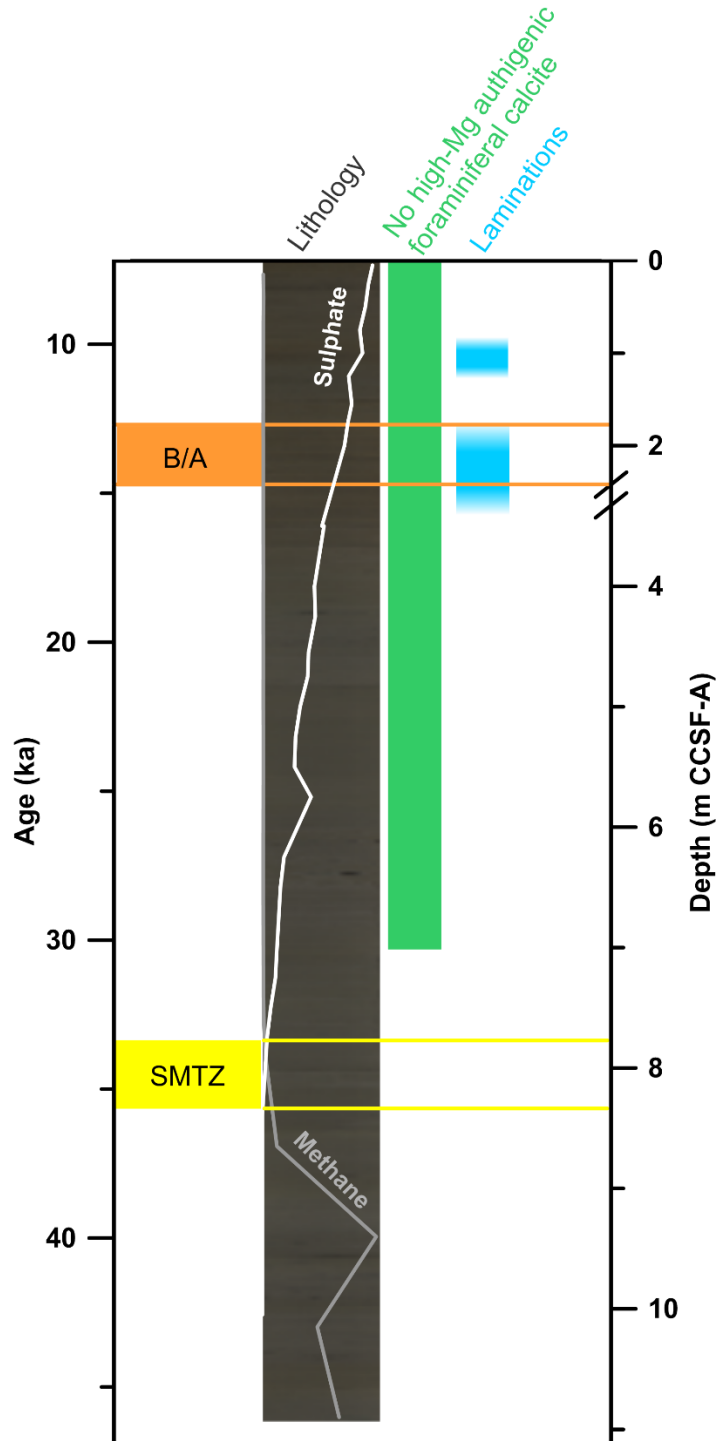


Figure 5.7 Schematic view of the lithology and stratigraphy of the core composite at IODP Site U1343. The age model is based on oxygen isotope stratigraphy (Asahi et al., 2016), the depth of the modern Sulphate-Methane Transition Zone (SMTZ) is at ~8 mbsf (Wehrmann et al., 2011) (yellow horizontal bar). There is no evidence of SMTZ-related high-Mg authigenic calcite on foraminiferal shells above ~7 m CCSF-A (green vertical bar), indicating that during the B/A (orange horizontal bar) the SMTZ could not have been above ~4.6 mbsf. Laminations are indicated in blue (Expedition 323 Scientists 2010). Core images and dissolved sulphate (white) and methane (light grey) concentrations from LIMS (<http://web.iodp.tamu.edu/LORE/>).

Since the B/A, ~2.4 m of sediments have accumulated at Site U1343, indicating a minimum possible SMTZ depth of ~4.6 mbsf during this time, as there is no evidence for SMTZ-related authigenic high-Mg precipitation on foraminifera above ~7 m core composite depth below seafloor (CCSF-A) today (Figure 5.7). Other studies from the western Svalbard margin also demonstrate SMTZ-related authigenic carbonate precipitation within ~1 m of the present day SMTZ in support of vertical migration on a meter-scale (Panieri et al., 2017). Assuming SMTZ migration on the order of ± 4 m would imply an age uncertainty of 24 ± 11 ka associated with authigenic carbonates precipitated within the SMTZ, considering sedimentation rates of 34 ± 11 cm ka⁻¹ at Site U1343 (Asahi et al., 2016).

This uncertainty accounts for roughly half a G/IG cycle prior to the MPT and a quarter of a climate cycle post-MPT. I thus argue that even though the precise timing of changes in the U/Mn related to bottom water [O₂] of samples from below the SMTZ may not be definable, average glacial and interglacial U/Mn values may still provide valuable information with respect to environmental changes on orbital timescales, especially during the late Pleistocene, marked by 100-ka climate cyclicity. To calculate the age offset (Δka) between the authigenic carbonate formation within the SMTZ and the changes in the sedimentary redox-chemistry it reflects, I used the linear sedimentation rates (LSR) at Site U1343 in combination with the modern depth of the SMTZ (~ 8 mbsf (Wehrmann et al., 2011)) assuming a constant depth of the SMTZ through time (Equation 5.1).

$$\Delta ka = \frac{Depth_{SMTZ} (cm)}{LSR (cm ka^{-1})} \quad (\text{Equation 5.1})$$

Subsequently, glacial and interglacial averages of both planktonic and benthic U/Mn were calculated to reduce the bias associated with the SMTZ migration and the inter-species U/Mn differences.

5.4.2 Sedimentary redox chemistry across the last glacial maximum to the Holocene

Authigenic U/Mn and U/Ca of benthic and planktonic foraminifera at Site U1343 across the LGM to Holocene demonstrate prominent changes in the sedimentary redox regime. Here I explore changes in the bottom water [O₂] and primary productivity as

drivers of sedimentary redox conditions, to infer changes in the Bering Sea ventilation across MIS 2 and MIS 1 at ~2000 m water depth.

Modern bottom water oxygen concentrations at Site U1343, bathed in NPDW, are 52 $\mu\text{mol kg}^{-1}$ (Olsen et al., 2016) underlying the prominent mid-depth OMZ in the Bering Sea (Figure 1.5). Glacial NPDW in the North Pacific is characterised by decreased bottom water $[\text{O}_2]$ on the order of 20 [5; 50] $\mu\text{mol kg}^{-1}$ (Jaccard et al., 2009) across the LGM, suggesting decreased bottom water $[\text{O}_2]$ at Site U1343 during glacials if it was consistently bathed in NPDW. On the other hand, atmospherically-equilibrated O_2 -rich NPIW has been proposed to form locally in the Bering Sea during glacials, carrying well ventilated waters to greater depth (Horikawa et al., 2010, Rella et al., 2012, Knudson and Ravelo, 2015b, Cook et al., 2016), thus episodes of NPIW entrainment at Site U1343 should be characterised by increased bottom water $[\text{O}_2]$ compared to the modern concentration. Laminated sediments along the eastern Bering slope, however, demonstrate that OMZ expansion may also have played a fundamental role for oxygenation of mid-depth waters, primarily across intervals of enhanced primary productivity across the last deglaciation, namely the B/A and the early Holocene (Expedition 323 Scientists Cook et al., 2005, 2010, Aiello and Ravelo, 2012, Kuehn et al., 2014, Ovsepyan et al., 2017, Pelto et al., 2018), characterised by bottom water $[\text{O}_2]$ of $<5 \mu\text{mol kg}^{-1}$ (Moffitt et al., 2015).

During MIS 2 benthic foraminiferal U/Mn measured on *I. norcrossi* is $0.92 \pm 0.12 \text{ mmol mol}^{-1}$ standard error (s.e.) on average, with two episodes of slightly decreased values ($0.55 \pm 0.05 \text{ mmol mol}^{-1}$ (s.e.)) around ~25 ka and ~17.5 ka, coinciding with HS1 (~14.7-18 ka), indicative of either decreased export productivity or increased $[\text{O}_2]$ of bottom waters at Site U1343 (Figure 5.8). This is also supported by the dysoxic benthic foraminiferal assemblage, demonstrating a decrease at 25 ka, but even more prominently at 17.5 ka (Figure 5.8). Whilst the decrease in benthic U/Mn at ~25 ka is marked by an interval barren in planktonic foraminifera, a coeval decrease in benthic U/Mn and planktonic U/Ca at ~17.5 ka reinforces the sedimentary redox changes observed across this period (Figure 5.8). The mass accumulation rate of biogenic opal (MAR_{opal}) at Site U1343 (Kim et al., 2014), indicative of first order changes in primary productivity, is consistently low across the LGM with no pronounced changes at 25 ka and 17.5 ka (Figure 5.8), suggesting that decreased benthic U/Mn and planktonic U/Ca likely reflect increased bottom water $[\text{O}_2]$ of the Bering Sea at ~2000 m during

these times rather than decreased remineralisation of organic matter. Increased bottom water [O₂] could either result from increased ventilation of waters at 2000 m in the Bering Sea or the release of respired carbon from the deep ocean, of which the latter would result in an increase in atmospheric CO₂. There is no increase in atmospheric CO₂ at 25 ka (Figure 5.8) (Bereiter et al., 2015), however, the second interval of increased bottom water [O₂] at Site U1343 during HS1 is coeval with an increase in atmospheric CO₂ of ~40 ppmv (Figure 5.8) (Bereiter et al., 2015). A study from the Gulf of Alaska suggests a breakdown of North Pacific stratification during HS1 resulting in release of deeply sequestered carbon, which could have resulted in an atmospheric CO₂ rise of ~30 ppm (Rae et al., 2014). This is accompanied by local deep water formation transporting well ventilated waters to depth of up to ~3500 m (Rae et al., 2014). Other shallower records from the western and eastern North Pacific, however, do not agree with a release of carbon from the deep ocean during HS1, instead an increase in ventilation is not observed until the B/A interstadial (Galbraith et al., 2007, Jaccard et al., 2009, Lund et al., 2011, Jaccard and Galbraith, 2012). Thus, if a release of deeply stored carbon was the main driver of increased [O₂] in the Bering Sea at ~2000 m water depth at 17.5 ka a more local mechanism must have been responsible, instead of a North Pacific wide breakdown in stratification. One such mechanism could be a strengthening of the eddy kinetic energy along the eastern Bering Sea slope. Stronger, deeper reaching eddies could tap into the carbon reservoir of the deep ocean, causing upwelling of CO₂-rich, high-nutrient deep waters to the surface ocean along the eastern Bering slope, potentially contributing to the observed atmospheric CO₂ rise of ~40 ppmv during HS1 (Figure 5.8) (Bereiter et al., 2015). Eddy kinetic energy of the Bering Slope Current is related to its flow speed, which in turn changes with the inflow of Alaskan Stream waters through the Aleutian Arc, sensitive to sea level changes (Mizobata and Saitoh, 2004). Hence, a slightly higher sea level during HS1 of -101.2 ± 5.8 m (s.e.) compared to the LGM (-122.9 ± 1.7 m (s.e.)) (Spratt and Lisiecki, 2016) could have increased the inflow of Alaskan Stream waters into the southern Bering Sea. *Neodenticula seminae*, a diatom species associated with the Alaskan Stream (Sancetta, 1983), however, does not increase until 15 ka in the western Bering Sea (Max et al., 2012) and 11 ka at the Umnak Plateau (Caissie et al., 2010). This suggests that locally enhanced eddy kinetic energy along the eastern Bering Sea slope is likely not the driving mechanism of increased bottom water [O₂] along the eastern Bering slope during HS1.

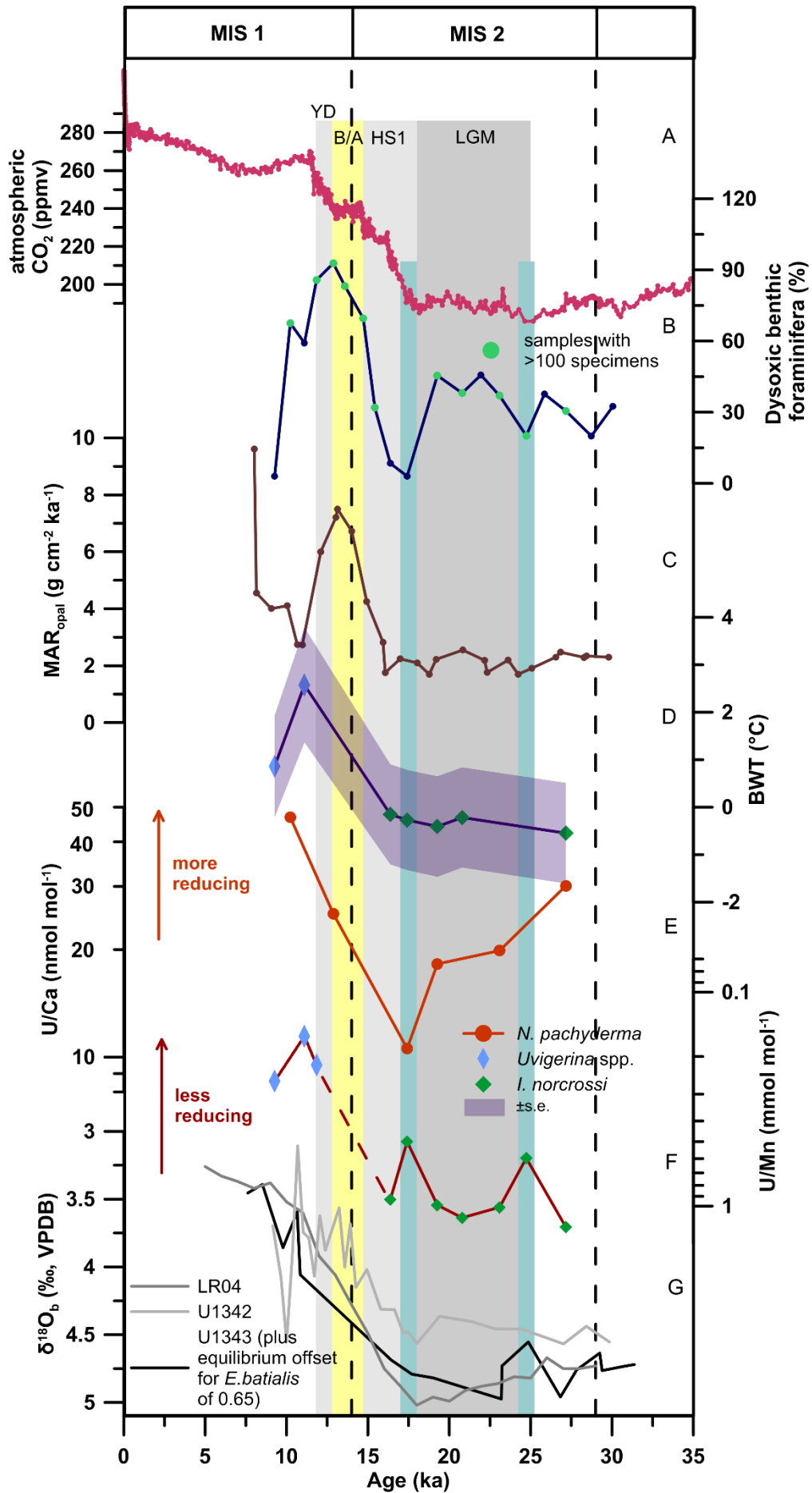


Figure 5.8 (A) Atmospheric CO₂ record from the Antarctic ice core composite (pink) across the LGM-Holocene transition (Bereiter et al., 2015). (B) The abundance of dysoxic benthic foraminiferal species (dark blue) at Site U1343 in percent. The green dots represent samples with >100 specimens. (C) The MAR_{opal} at Site U1343 (brown) indicative of first order changes in primary productivity (Kim et al., 2014). (D) BWT at Site U1343 (purple) across Termination I based on *I. norcrossi* (green diamonds) and *Uvigerina* spp. (blue diamonds) including the \pm s.e. envelope (light purple). (E) U/Ca of *N. pachyderma* (orange) at Site U1343, higher values suggest more reducing conditions in the sediments. Note that the axis for U/Ca is on the logarithmic scale. (F) U/Mn of *I. norcrossi* (green diamonds) and *Uvigerina* spp. (blue diamonds) across the LGM-Holocene, the deglaciation is associated with a faunal change (dashed line). Note that the axis for U/Mn is on the logarithmic scale. (G) $\delta^{18}\text{O}_b$ records from U1343 adjusted for the *E. batialis* equilibrium offset (+0.65 ‰) (black) (Asahi et al., 2016) and U1342 (light grey) (Knudson and Ravelo, 2015b) together with the LR04 stack (middle grey) (Lisiecki and Raymo, 2005). The dark grey bar represents the LGM (18-25 ka), the light grey vertical bars represent the Heinrich stadial 1 (~14.7-18 ka) and the Younger Dryas (~12.9-11.7 ka), while the yellow vertical bar represents the Bølling-Allerød (~12.7 ka to 14.7 ka). The dashed vertical lines represent the MIS boundaries and numbers at the top correspond to the respective MIS (MIS boundaries from (Lisiecki and Raymo, 2005)). The blue vertical bars indicate intervals across MIS 2 where NPIW incursion likely occurred at ~2000 m water depth in the eastern Bering Sea.

Instead, increased bottom water [O₂] at 25 ka and 17.5 ka at ~2000 m water depth in the eastern Bering Sea is likely driven by increased ventilation and deepening of glacial NPIW. HS1, characterised by cooling in the northern hemisphere, is marked by a widespread increase in the intermediate water ventilation in the Bering Sea and the North Pacific (Duplessy et al., 1989, Ahagon et al., 2003, Sagawa and Ikehara, 2008, Okazaki et al., 2012, Rae et al., 2014, Max et al., 2014, Cook et al., 2016). The depth of well-ventilated waters is still a subject of debate, however, the divide between well-ventilated intermediate and poorly ventilated deep waters was likely close to ~2000 m in the North Pacific (Matsumoto et al., 2002, Jaccard and Galbraith, 2013). NPIW on G/IG timescales forms via brine rejection during sea ice freezing in the Sea of Okhotsk (Watanabe and Wakatsuchi, 1998, Max et al., 2014, Okazaki et al., 2014) or the Bering Sea (Horikawa et al., 2010, Rella et al., 2012, Knudson and Ravelo, 2015b), carrying O₂-rich, oxygen isotope depleted waters to greater depth (Knudson and Ravelo, 2015b, Cook et al., 2016). Across HS1 Méheust et al. (2016) and Méheust et al. (2018) demonstrate increased sea ice extent in the western Bering Sea and the North Pacific, in line with simultaneous ice rafted debris (IRD) peaks in the North Pacific (Gebhardt et al., 2008) and sea ice expansion in the Sea of Okhotsk (Seki et al., 2005, Sakamoto et al., 2005, Lo et al., 2018). Thus, even though the resolution of the U1343 foraminiferal U/Mn and U/Ca records does not allow the reconstruction of millennial scale climate events, increased bottom water ventilation at Site U1343

around 17.5 ka, likely resulted from regional cooling, associated with the HS1 and increased formation of NPIW. Additionally, the benthic foraminiferal oxygen isotope ($\delta^{18}\text{O}_b$) record at Site U1343 (Asahi et al., 2016) demonstrates a negative offset from the LR04 stack during times of decreased U/Mn and U/Ca across MIS 2 (Figure 5.8), in line with ^{16}O -rich NPIW entrainment at 25 ka and 17.5 ka (Knudson and Ravelo, 2015b, Cook et al., 2016).

Following HS1 the B/A and the early Holocene, periods of northern hemisphere warming, are marked by laminated sediments in mid-depth waters across the Bering Sea (Cook et al., 2005, Aiello and Ravelo, 2012, Kuehn et al., 2014, Pelto et al., 2018) and at Site U1343 (Expedition 323 Scientists 2010), suggesting bottom water $[\text{O}_2]$ concentrations $<5 \mu\text{mol kg}^{-1}$ (Moffitt et al., 2015) (Figure 5.7). Whereas U/Mn of shallow infaunal benthic foraminifera decreases across Termination I, U/Ca of planktonic foraminifera increases across the B/A and the early Holocene (Figure 5.8). As aforementioned, benthic U/Mn across the deglaciation is associated with a faunal change from *I. norcrossi* to *Uvigerina* spp. (Figure 5.8). Opposite changes of benthic U/Mn compared to planktonic U/Ca, thus likely suggest species-specific differences in the partition coefficient of U and/or Mn into primary foraminiferal calcite (Raitzsch et al., 2011, Koho et al., 2017), altering the benthic U/Mn ratios across this interval. Hence, the decrease in benthic U/Mn across Termination I likely reflects species-specific effects, rather than changes in the sedimentary redox state. U/Ca of planktonic foraminiferal species *N. pachyderma*, on the other hand, shows a pronounced increase across the B/A and early Holocene, in line with reduced bottom water $[\text{O}_2]$, as suggested from laminated sediments at Site U1343 (Expedition 323 Scientists 2010). The B/A and early Holocene coincide with a pronounced peak in the MAR_{opal} at Site U1343 (Kim et al., 2014) (Figure 5.8), suggesting increased primary productivity at these times, also seen across the North Pacific (Okazaki et al., 2005, Cook et al., 2005, Brunelle et al., 2007, Kohfeld and Chase, 2011, Max et al., 2012, Lam et al., 2013). Laminated sediments, together with decreased bottom water $[\text{O}_2]$ and enhanced rates of primary productivity and remineralisation of organic carbon in the water column during the B/A and early Holocene, suggest expansion of the mid-depth OMZ (Cook et al., 2005, Expedition 323 Scientists 2010, Aiello and Ravelo, 2012, Kuehn et al., 2014, Pelto et al., 2018). An expansion of the OMZ is also supported by a broad peak in the dysoxic benthic foraminiferal assemblage at Site U1343 around ~ 12.5 ka (Figure

5.8). Across this interval the dysoxic assemblage is dominated by *E. exilis*, associated with low oxygen environments (Ovsepyan et al., 2017), but also occurring in relation to sustained flux of labile organic matter (Corliss, 1985, Caralp, 1989). Hence, the peak in dysoxic benthic foraminifera between 15-10 ka (Figure 5.8) is related to the co-occurring peak in MAR_{opal} (Kim et al., 2014) and OMZ expansion across the B/A and early Holocene (Cook et al., 2005, Expedition 323 Scientists 2010, Aiello and Ravelo, 2012, Kuehn et al., 2014, Pelto et al., 2018).

The sedimentary redox state along the eastern Bering slope across the LGM-Holocene, is therefore controlled by both changes in bottom water [O₂] and primary productivity. During intervals of low productivity, characterised by a contracted OMZ, such as MIS 2, sedimentary redox conditions seem to be more sensitive to changes in the water mass [O₂], as indicated by the influence of well-ventilated NPIW on authigenic U/Mn and U/Ca of benthic and planktonic foraminifera at ~25 ka and ~17.5 ka. Intervals of high primary productivity such as the B/A and the early Holocene, on the other hand, seem to be dominated by the influence of organic carbon export and remineralisation in the water column, leading to OMZ expansion and decreased [O₂] in bottom waters at Site U1343.

5.4.3 Sedimentary redox changes in the deep eastern Bering Sea across the Mid-Pleistocene

In this section I explore the glacial and interglacial averages of planktonic and benthic U/Mn across the Mid-Pleistocene together with glacial and interglacial averages of the dysoxic benthic foraminiferal assemblage. Averages have been determined based on the respective MIS, in order to reduce the age uncertainty associated with authigenic U/Mn below the SMTZ at Site U1343.

Across the Mid-Pleistocene glacial planktonic U/Mn averages vary between 2.7 mmol mol⁻¹ and 6.5 mmol mol⁻¹ and interglacial planktonic U/Mn averages vary between 2.7 mmol mol⁻¹ and 8.3 mmol mol⁻¹ (Figure 5.9). Both glacial and interglacial planktonic U/Mn averages demonstrate a long-term decrease across the Mid-Pleistocene (Figure 5.9). Similarly, benthic U/Mn averages vary between 0.7 mmol mol⁻¹ and 8.1 mmol mol⁻¹ during glacials and 0.7 mmol mol⁻¹ and 8.0 mmol mol⁻¹ during interglacials, also with a long-term decrease observed during both glacials and interglacials (Figure 5.9). A long-term decrease in both planktonic and benthic U/Mn glacial and interglacial

averages across the Mid-Pleistocene suggests a decrease in the reducing conditions of sediments along the eastern Bering Sea slope, which I infer to represent increased bottom water [O₂], in line with previous studies (Gottschalk et al., 2016, Chen et al., 2017). Bottom water [O₂] in the eastern Bering Sea on orbital timescales is driven by changes in the biogeochemical cycling, in particular primary productivity and remineralisation of organic matter in the water column, with higher primary productivity likely causing more reducing conditions by either OMZ expansion and/or increased remineralisation of organic matter in the sediments. Additionally, Bering Sea bottom water [O₂] is controlled by the contribution and ventilation of NPIW and NPDW. Below I explore the variability and long-term trends in planktonic and benthic U/Mn across interglacials and glacials, separately.

5.4.3.1 Interglacial evolution of sedimentary redox conditions across the Mid-Pleistocene

As previously mentioned, average interglacial U/Mn values of both benthic and planktonic foraminifera show a decreasing trend across the Mid-Pleistocene (Figure 5.9). Benthic U/Mn during MIS 23 (Table 4.2) stands out, marked by relatively low U/Mn (Figure 5.9). However, MIS 23 is only characterised by one data point, indicating that this might not represent the true variability in sedimentary redox chemistry across this MIS. Nonetheless, a long-term decrease suggests an increase in interglacial bottom water [O₂] across the Mid-Pleistocene in the eastern Bering Sea, resulting from either changes in the ventilation and/or local primary productivity. Well-ventilated NPIW likely plays a less prominent role during interglacial intervals, as it is formed locally from brine rejection during sea ice freezing (Talley, 1993, Yasuda, 1997), with reduced ventilation observed during warm phases of the last 1200 ka (Knudson and Ravelo, 2015b). Thus, increased ventilation could result from changes in NPDW. Studies of the flow speed of the Deep Western Boundary Current (DWBC), a precursor of NPDW, suggest a more sluggish inflow into the deep South Pacific following MIS 22 (Table 4.2), observed during both glacials and interglacials (Hall et al., 2001, Venuti et al., 2007), contradicting enhanced ventilation of the deep Pacific Ocean across the Mid-Pleistocene. On the other hand, a long-term interglacial increase in [O₂] of NPDW across the Pleistocene could result from a decrease in the accumulation of respired carbon. Inferring changes in the respired carbon content of

NPDW, however, is challenging, as this depends on the evolution of primary productivity and the efficiency of the biological pump downstream.

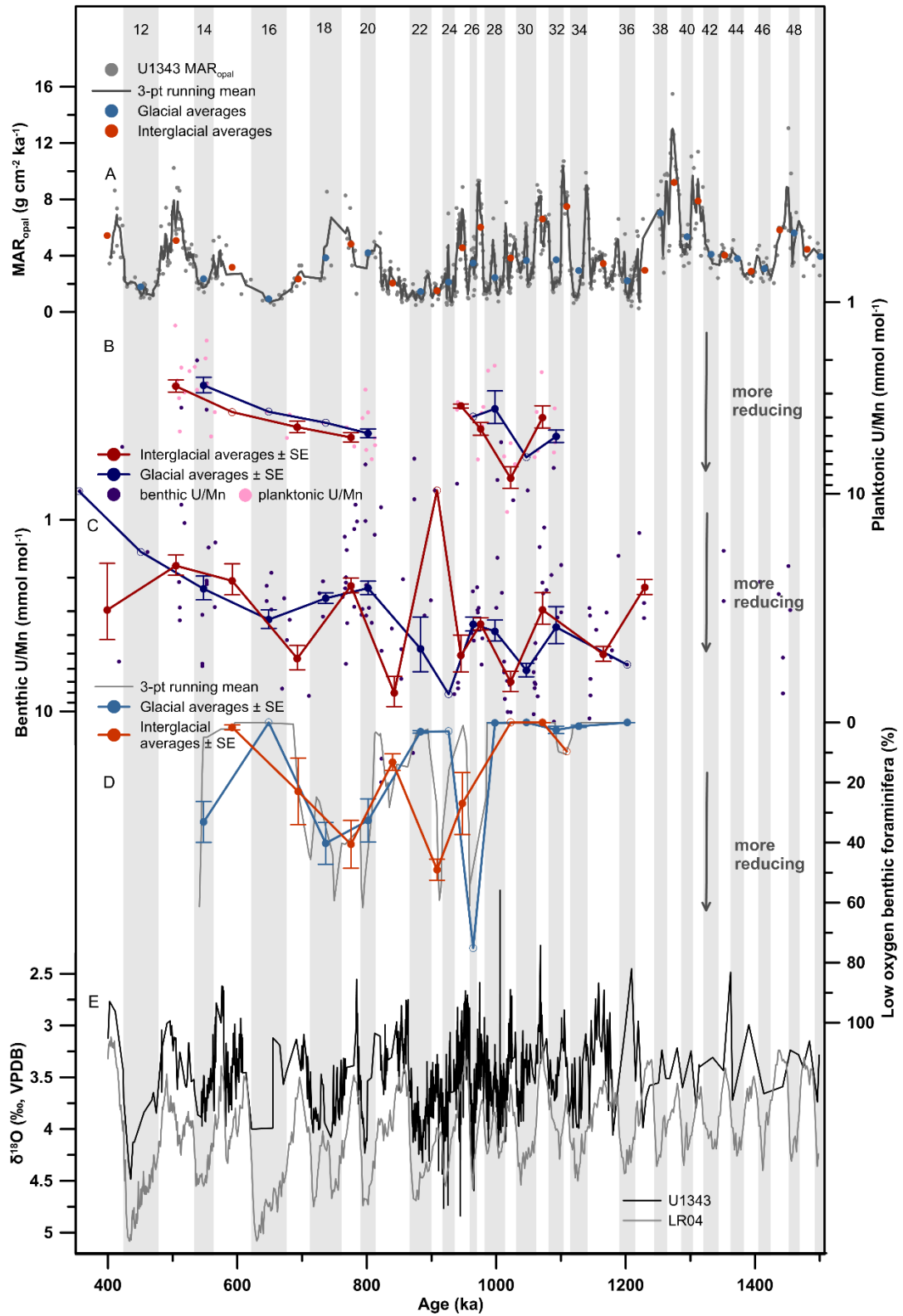


Figure 5.9 (A) MAR_{opal} (grey dots) together with the 3-point running mean (grey line) at Site U1343 (Kim et al., 2014) including the glacial (blue dots) and interglacial (orange dots) averages. (B) Planktonic U/Mn data (pink dots) across the Mid-Pleistocene together with the glacial (blue dots) and interglacial (red dots) averages. Error bars represent the standard error, open symbols indicate intervals with only one data point. (C) Benthic U/Mn data (purple dots) across the Mid-Pleistocene together with the glacial (blue dots) and interglacial (red dots) averages. Error bars represent the standard error, open symbols indicate MISs with only one data point. Note that the axes for U/Mn are on the logarithmic scale. (D) The 3-point running mean of the abundance of dysoxic foraminiferal species (grey line) at Site U1343 together with the glacial (blue dots) and interglacial (orange dots) averages. Error bars represent the standard error, intervals with no error bars are only represented by one data point. (E) $\delta^{18}O_b$ at Site U1343 (black) (Asahi et al., 2016, Kender et al., in review) together with the LR04 stack (grey) (Lisiecki and Raymo, 2005). The grey vertical bars represent glacial intervals, numbers at the top correspond to marine isotope stages (MIS boundaries from (Lisiecki and Raymo, 2005)).

Recent studies of primary productivity from across the Pacific indicate variable patterns of both decreased and increased productivity following the MPT (Diester-Haass et al., 2018). Nevertheless Ocean Drilling Program (ODP) Site 1123 and ODP Site 806 in the southwestern and western equatorial Pacific, respectively, demonstrate decreased interglacial productivity compared to glacial intervals following the MPT, in line with potentially decreased accumulation of respired carbon in the deep North Pacific during interglacials (Diester-Haass et al., 2018).

In addition to changes in the respired carbon content of NPDW, local primary productivity might also have played an important role in driving interglacial bottom water $[O_2]$ across the Mid-Pleistocene. The MAR_{opal} at Site U1343 (Kim et al., 2014) demonstrates increased productivity during interglacials compared to glacial intervals (Figure 5.9), in line with the generally higher interglacial than glacial U/Mn averages, in particular seen in planktonic foraminifera (Figure 5.9). Additionally, superimposed on the G/IG variability of MAR_{opal} there is a long-term decrease the interglacial productivity at Site U1343 across the Mid-Pleistocene, in line with an increase in bottom water $[O_2]$ (Figure 5.9). However, average interglacial MAR_{opal} and interglacial U/Mn of both planktonic and benthic foraminifera demonstrate a significant negative correlation ($R^2 = -0.5$ [-0.8; -0.1], $n = 17$) (Figure 5.10). This suggests that primary productivity in the Bering Sea likely did not exert the predominant control on interglacial bottom water $[O_2]$ across this time interval and records of NPDW nutrient content and $[O_2]$ are needed to decipher the influence of ventilation and respired carbon content on the $[O_2]$ of the deep Bering Sea.

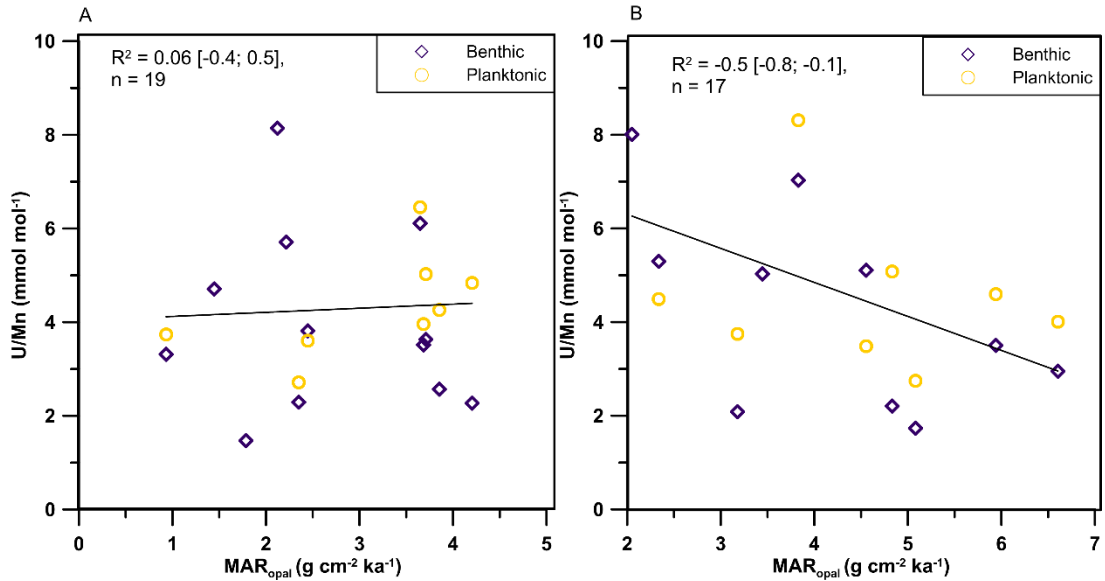


Figure 5.10 Cross plots of (A) glacial and (B) interglacial U/Mn (both benthic and planktonic) versus the average glacial and interglacial MAR_{opal} (Kim et al., 2014) at Site U1343 across the Mid-Pleistocene. Glacial U/Mn does not show a significant correlation with MAR_{opal}, whereas interglacial U/Mn demonstrates a significant negative correlation with MAR_{opal}.

5.4.3.2 Glacial variability and long-term trends of sedimentary redox conditions across the Mid-Pleistocene

Similar to interglacial U/Mn, average glacial U/Mn values of both benthic and planktonic foraminifera show a decreasing trend across the Mid-Pleistocene (Figure 5.9), with the first pronounced decrease in glacial U/Mn in both benthic and planktonic observed during MIS 28 (Table 4.2) (Figure 5.9). Preceding MIS 28, MIS 32 is also marked by relatively low U/Mn, however, this is primarily observed in benthic foraminifera and less pronounced in planktonic U/Mn (Figure 5.9). Higher glacial benthic and planktonic U/Mn values during MIS 36 and 30 (Figure 5.9), suggest more reducing conditions with lower bottom water [O₂] during early Mid-Pleistocene compared to late Mid-Pleistocene glacials.

A simultaneous decrease in glacial benthic and planktonic U/Mn is first observed during MIS 28 (Table 4.2), followed by consistently low benthic U/Mn values during MIS 26 (Table 4.2), and between MIS 10 to MIS 20 (~2 mmol mol⁻¹) together with a decreasing trend in planktonic U/Mn where data is available (Figure 5.9). Lower U/Mn in both planktonic and benthic foraminifera likely indicates increased glacial bottom water [O₂], following MIS 28, in line with a long-term decrease in the average glacial

MAR_{opal} at Site U1343 (Kim et al., 2014) (Figure 5.9). However, even though a decrease in the glacial primary productivity is observed coinciding with MIS 28 (Kim et al., 2014) (Figure 5.9), this is not a consistent feature throughout the following glacials also characterised by decreased benthic and planktonic U/Mn (MIS 26, MIS 10-20) (Figure 5.9). Additionally, no significant correlation was found between average glacial benthic and planktonic U/Mn and average MAR_{opal} at Site U1343 (Kim et al., 2014) ($R^2 = 0.06$ [-0.4; 0.5], $n = 19$). Hence, increased Bering Sea bottom water [O₂] during glacial intervals of the Mid-Pleistocene was most likely driven by changes in the ventilation and/or contribution of NPIW and NPDW.

The MPT was accompanied by an increase in the glacial deep ocean carbon storage, recorded in the North Atlantic around ~900 ka (Lear et al., 2016, Sosdian et al., 2018) in conjunction with prominent changes in the thermohaline overturning circulation (Pena and Goldstein, 2014). Furthermore, decreased glacial CaCO₃ accumulation is observed in the deep North Pacific throughout the entire Pleistocene (Haug et al., 1995, Jaccard et al., 2005, Burls et al., 2017) indicating more corrosive glacial than interglacial bottom waters. Together with the more sluggish deep Pacific inflow following MIS 22 (Table 4.2) (Hall et al., 2001, Venuti et al., 2007) this suggests that decreased [O₂] content of NPDW, as observed for the last 150 ka (Jaccard et al., 2009), could have been a consistent feature of Pleistocene glacials, even though absolute [O₂] likely varied in response to deep ocean carbon storage and changes in the thermohaline circulation. On the other hand, Knudson and Ravelo (2015b) demonstrate increased ventilation of NPIW during glacials of the last 1200 ka at 800 m water depth in the Bering Sea, however, there are no constraints on the maximum depth of glacial NPIW on these timescales. Thus, increased bottom water [O₂] at Site U1343, observed from MIS 28 (Table 4.2), is most likely derived from enhanced incursion of well-ventilated NPIW.

NPIW carries the low oxygen isotope composition of seawater ($\delta^{18}\text{O}_w$) of subpolar surface waters, as it is produced from brine rejection during sea ice freezing with little fractionation of oxygen isotopes (Knudson and Ravelo, 2015b, Cook et al., 2016). Hence, if NPIW was the predominant contributing water mass to Site U1343 across MIS 28, MIS 26 (Table 4.2), and MIS 10-20 the $\delta^{18}\text{O}_b$ record would be expected to show a negative offset from the LR04 stack, as observed for other shallower sites in the Bering Sea (Knudson and Ravelo, 2015b, Cook et al., 2016). $\delta^{18}\text{O}_b$ at Site U1343

across MIS 28 (Asahi et al., 2016, Kender et al., in review) compares well with the LR04 stack (Figure 5.9), indicating that NPDW likely was the main water mass at Site U1343 with only little entrainment of NPIW as suggested from the planktonic and benthic U/Mn. Some of the following glacials, however, show intervals with a negative offset from the LR04 stack, such as MIS 18 (Figure 4.10), in line with enhanced NPIW contribution to Site U1343.

MIS 22 and MIS 24 (Table 4.2) stand out from the trend of decreased glacial benthic U/Mn, with higher U/Mn ratios compared to MIS 28 and MIS 26 (Table 4.2), suggestive of decreased bottom water [O₂] (Figure 5.9). MIS 24, however, consists of only one data point close to the boundary of MIS 24/25 (Figure 5.9), which may not capture the true bottom water [O₂] variability across this interval. MIS 22, on the other hand, is characterised by six data points with a relatively large spread in the data (Figure 5.9). The MAR_{opal} (Kim et al., 2014) is consistently low across MIS 23, MIS 22, and early MIS 21 (Table 4.2), indicating that primary productivity driven OMZ expansion likely did not cause a decrease in the bottom water [O₂] across this interval (Figure 5.9). Thus, decreased bottom water [O₂] suggests less contribution of NPIW to Site U1343 and/or decreased [O₂] of NPDW during MIS 22. MIS 22 coincides with the onset of increased carbon storage in the deep North Atlantic (Lear et al., 2016, Sosdian et al., 2018) and, as part of the 900-ka event, with pronounced changes in the thermohaline overturning circulation (Pena and Goldstein, 2014). Additionally, MIS 22 stands out in records of BWT and $\delta^{18}\text{O}_w$ at Site U3143, with BWT warming during MIS 22 also observed at ODP Site 1208 on Shatsky Rise (Ford and Raymo, 2017), indicating that there may have been North Pacific wide hydrographical changes at this time. Kender et al. (in review) suggest increased NPIW contribution to Site U1343 during late MIS 22, supported by a positive U1343 $\delta^{18}\text{O}_b$ offset from the LR04 stack during late MIS 22 (Figure 5.11). Examining the non-averaged benthic U/Mn record across MIS 22 demonstrates that the proposed interval of NPIW entrainment at Site U1343 is indeed characterised by low U/Mn, indicating higher bottom water [O₂], whereas both the early and late MIS 22 show decreased bottom water [O₂], however one needs to consider that the U/Mn data is associated with an age uncertainty of 24 ± 11 ka (Figure 5.11).

As previously mentioned, the dysoxic tolerant benthic foraminiferal assemblage at Site U1343 is dominated by *E. exilis*, which occurs in low oxygen environments

(Ovsepyan et al., 2017), but also in relation to sustained flux of labile organic matter (Corliss, 1985, Caralp, 1989). I suggest that at higher glacial bottom water [O₂], as inferred from benthic and planktonic U/Mn from MIS 28 onwards, the dysoxic foraminiferal assemblage may be more sensitive to changes in the supply of labile organic matter, also indicated by the TROX (Trophic OXYgen) model (Jorissen et al., 1995) (Figure 2.7). Hence, the foraminiferal assemblage may be more sensitive to changes in the primary productivity, compared to U/Mn.

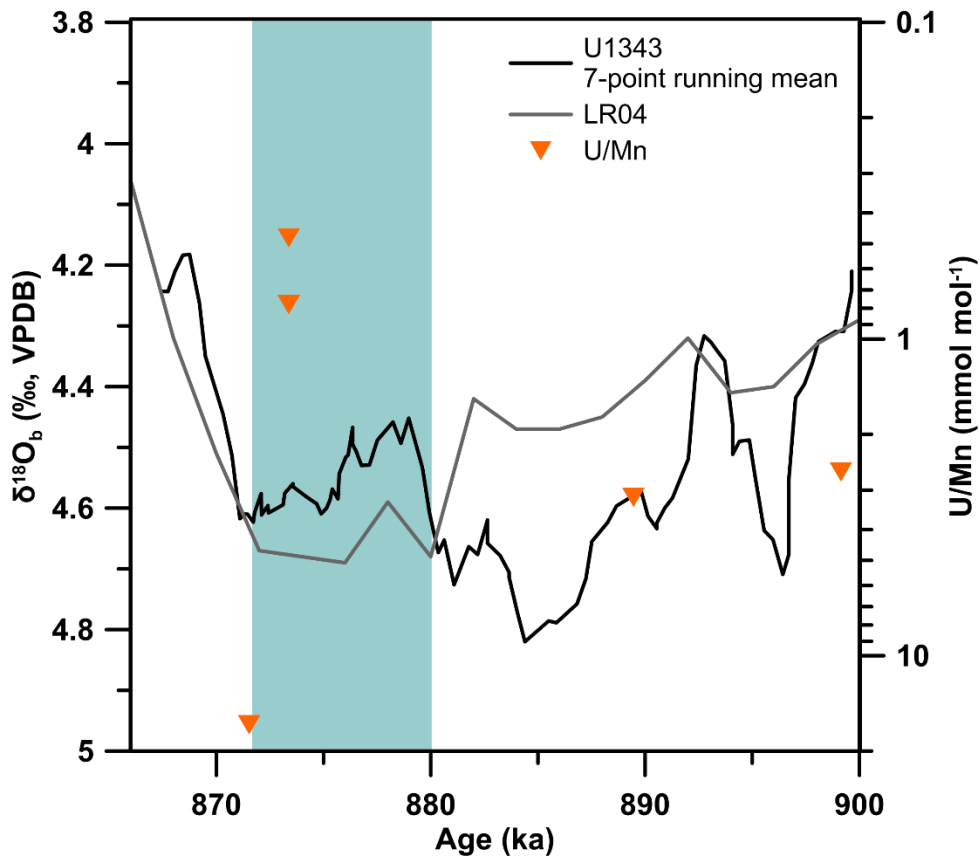


Figure 5.11 The 7-point running mean of $\delta^{18}\text{O}_b$ at Site U1343 adjusted for the *E. batialis* equilibrium offset (+0.65 ‰) (Asahi et al., 2016) (black) (Kender et al., in review) together with the LR04 stack (grey) (Lisiecki and Raymo, 2005) and U/Mn (orange) across MIS 22. Note that the axis for U/Mn is on the logarithmic scale. The blue vertical bar represents the interval characterised by a negative U1343 $\delta^{18}\text{O}_b$ offset from the LR04 stack, in line with NPIW contribution and high bottom water [O₂], as suggested from U/Mn. However, U/Mn data are associated with an age uncertainty of 24 ± 11 ka.

The increase in bottom water [O₂], first observed during MIS 28 (Table 4.2), coincides with a prominent change in the sea ice regime in the eastern Bering Sea from MIS 28 onwards (Detlef et al., 2018) (Chapter 6). Enhanced sea ice formation during glacial

intervals since MIS 28, suggests increased brine formation in the Bering Sea, potentially contributing to the increased ventilation and deepening of NPIW across this time period. The significant correlation of eastern Bering Sea sea ice across the MPT with records of intermediate water ventilation from the Bowers Ridge (Knudson and Ravelo, 2015b), further supports a link between sea ice formation in the Bering Sea and increased NPIW ventilation (Detlef et al., 2018). However, it is unclear whether glacial NPIW was exclusively formed in the Bering Sea or if the Sea of Okhotsk also played a fundamental role for driving NPIW ventilation, as no sea ice records or intermediate depth ventilation records exist across the MPT from the Sea of Okhotsk to decipher the influence of these two regions.

Lastly, Mid-Pleistocene glacial average benthic U/Mn values (0.7-8.3 mmol mol⁻¹) suggest more reducing conditions in the sediments along the eastern Bering Sea slope, compared to the LGM, characterised by benthic U/Mn of 0.5 mmol mol⁻¹ to 1.3 mmol mol⁻¹ (Figure 5.8, Figure 5.9). This is in line with the long-term decrease in glacial benthic U/Mn observed across the Mid-Pleistocene and NPIW contribution to Site U1343 during the LGM and HS1 as seen from benthic U/Mn and planktonic U/Ca in conjunction with a negative $\delta^{18}\text{O}_b$ offset from the LR04 stack (Figure 5.8). Hence, enhanced ventilation and deepening of NPIW may be consistent across glacial intervals following the MPT, in line with sea ice diatom assemblages in the Bering Sea (Teraishi et al., 2016, Stroynowski et al., 2017), suggesting enhanced sea ice extent during the late Pleistocene and biomarker sea ice reconstructions at Site U1343 (Detlef et al., 2018) (Chapter 6).

5.5 Conclusions

Here I present records of benthic and planktonic foraminiferal authigenic U/Mn and U/Ca together with dysoxic foraminiferal assemblage counts, suggesting prominent changes in the bottom water [O₂] in the eastern Bering Sea resulting from the contribution of different water masses and changes in the local primary productivity. LGM-Holocene benthic authigenic U/Mn and planktonic authigenic U/Ca indicate intermittent admixture of NPIW to Site U1343 during the LGM and HS1 (Figure 5.8). Increased bottom water [O₂] during HS1 at 2000 m water depth agrees well with records from across the Bering Sea and the North Pacific suggesting enhanced intermediate overturning at this time, ventilating the North Pacific to depth of ~2000

m (Duplessy et al., 1989, Ahagon et al., 2003, Sagawa and Ikehara, 2008, Okazaki et al., 2012, Rae et al., 2014, Max et al., 2014, Cook et al., 2016) (Figure 5.8). Across deglacial warm phases, such as the B/A and the early Holocene, planktonic authigenic U/Ca and dysoxic foraminiferal assemblages indicate decreased bottom water [O₂] at the eastern Bering slope. This is corroborated by abundant laminated sediments across the Bering Sea during the B/A and early Holocene (Cook et al., 2005, Expedition 323 Scientists 2010, Caissie et al., 2010, Aiello and Ravelo, 2012, Kuehn et al., 2014, Pelto et al., 2018), suggesting OMZ expansion to ~2000 m water depth at times of enhanced primary productivity (Figure 5.8).

Across the Mid-Pleistocene U/Mn reveals a long-term decrease during both glacial and interglacial intervals (Figure 5.9). While no Holocene analogue exists for benthic foraminiferal U/Mn, LGM values indicate that the decrease in U/Mn might have continued throughout late Pleistocene glacials (Figure 5.8). A long-term decrease in U/Mn suggests a decrease in reducing conditions in sediments at Site U1343, indicative of an increase in bottom water [O₂] across the Pleistocene. Whereas the mechanisms for increased interglacial bottom water [O₂] across the Mid-Pleistocene are unclear, glacial U/Mn in conjunction with regional and global climate records, suggests deepening and enhanced ventilation of NPIW during glacials, leading to entrainment of atmospherically-equilibrated O₂ enriched waters at Site U1343. Even though higher resolution records from different water depth across the Bering Sea are needed, deepening of NPIW likely occurred together with a prominent change in the Bering Sea sea ice dynamics (Detlef et al., 2018), suggesting that the Bering Sea may have played a prominent role in NPIW ventilation during glacial intervals since the MPT. However, the $\delta^{18}\text{O}_b$ record (Asahi et al., 2016, Kender et al., in review), indicates that even though NPIW entrainment might have occurred, NPDW remained the primary water mass at Site U1343 throughout glacial intervals of the late Pleistocene.

Increased formation and deepening of NPIW together with decreased eddy strength during late Pleistocene glacials, as suggested from decreased inflow of the Alaskan Stream into the southern Bering Sea (Teraishi et al., 2016), could have provided a mechanism for glacial atmospheric CO₂ drawdown, by reducing the outgassing of CO₂-rich bottom waters along the eastern Bering slope (Kender et al., in review). Thus,

future studies should focus on constraining the depth of NPIW throughout the MPT and its role for the North Pacific carbon cycle.

6. Sea ice dynamics in the Bering Sea across the Mid- to late Pleistocene

6.1 Introduction

Sea ice plays a key role in both long-term (Tziperman and Gildor, 2003, Sayag et al., 2004) and abrupt millennial-scale (Hoff et al., 2016) climate change as a result of its far-reaching climate feedbacks, including the ice albedo effect, ocean-atmosphere gas/moisture exchange and ocean circulation patterns. In recent decades sea ice has undergone a dramatic reduction in the Arctic and subarctic realm, with fundamental consequences for the ecosystem (Hunt Jr et al., 2002, Grebmeier et al., 2006, Serreze et al., 2007, Wassmann et al., 2011, Stroeve et al., 2012). Our ability to predict future sea ice extent hinges, in part, on a greater understanding of the sensitivity of sea ice to climate change. However, it is only through the identification of long-term sea ice dynamics that our understanding of the role of sea ice for climate change can improve and hence our ability to predict future sea ice extent. This study focuses on Pleistocene sea ice dynamics in the eastern Bering Sea, with emphasis on the Mid-Pleistocene transition (MPT, ~0.7-1.2 Ma) and the last glacial maximum (LGM) to Holocene, to determine the role of sea ice in changing climates.

The deglacial climate evolution in the Bering Sea and the North Pacific realm across the LGM-Holocene transition (Termination I) has experienced recurrent attention in the past decade, as modelling and proxy studies disagree concerning the North Pacific response to millennial-scale climate change in the North Atlantic. Across Termination I two cold events, the Heinrich stadial 1 (HS1, ~14.7-18 ka) and the Younger Dryas (YD, ~12.9-11.7 ka), most prominently seen in Greenland ice core and North Atlantic sea surface temperature (SST) records (Heinrich, 1988, Dansgaard et al., 1993, Bond et al., 1993), are linked to freshwater perturbations and a slowdown of the Atlantic meridional overturning circulation (AMOC) (Heinrich, 1988, McManus et al., 2004), associated with a decrease in the northward heat transport. Whilst some studies indicate warming in the North Pacific in response to North Atlantic cooling (Sarnthein et al., 2004, Kiefer and Kienast, 2005, Sarnthein et al., 2006, Okazaki et al., 2010), for

example as a result of the onset of a Pacific Meridional Overturning Circulation (PMOC) and increased heat transport (Saenko et al., 2004, Okazaki et al., 2010), other studies suggest in-phase climate change of the North Atlantic and North Pacific as a result of atmospheric or oceanic teleconnections (Kienast and McKay, 2001, Pisias et al., 2001, Okumura et al., 2009, Caissie et al., 2010, Max et al., 2012, Chikamoto et al., 2012, Meyer et al., 2016). Across the LGM-Holocene detailed studies of sea ice related biomarker abundances across the Bering Sea and the North Pacific reveal a seasonally extended sea ice cover in the eastern and western North Pacific for the LGM, together with pronounced millennial-scale sea ice variability across Termination I (Méheust et al., 2016, Méheust et al., 2018). Enhanced LGM sea ice cover in the Bering Sea is also seen in records of sea ice diatoms, suggesting seasonal or perennial sea ice cover across the Bering Sea (Katsuki et al., 2003, Katsuki and Takahashi, 2005, Cook et al., 2005, Caissie et al., 2010).

Sea ice in the Sea of Okhotsk and the Bering Sea plays a fundamental role for North Pacific Intermediate Water (NPIW) formation on glacial/interglacial (G/IG) timescales. Whereas at modern times brine rejection in the Sea of Okhotsk is important for NPIW formation, evidence of neodymium isotopes (ϵ_{Nd}), microfossil assemblages, and foraminiferal oxygen and carbon isotopes suggest that glacial NPIW was at least partly formed in the Bering Sea (Ohkushi et al., 2003, Horikawa et al., 2010, Rella et al., 2012, Knudson and Ravelo, 2015b). Increased ventilation and extent of glacial NPIW (Keigwin, 1998, Ohkushi et al., 2003, Rae et al., 2014, Knudson and Ravelo, 2015b, Cook et al., 2016, Max et al., 2017) together with a markedly increased sea ice cover in the Bering Sea during the LGM and cold phases of Termination I (Katsuki et al., 2003, Cook et al., 2005, Katsuki and Takahashi, 2005, Caissie et al., 2010, Méheust et al., 2016, Méheust et al., 2018), thus demonstrates the potential importance of the Bering Sea for glacial oceanic circulation patterns in the North Pacific realm and beyond (Keigwin, 1998, Max et al., 2017).

Investigating the interactions of sea ice dynamics with ocean circulation and productivity patterns and identifying the role of sea ice for major climate transitions is thus critical for our understanding of Arctic and sub-Arctic climate change. One such climate transition during the Quaternary period is the MPT. The shift in G/IG frequency across the MPT (Ruddiman et al., 1989, Mudelsee and Schulz, 1997, Lisiecki and Raymo, 2005, Clark et al., 2006) without attributable changes in orbital

forcing, indicates a shift in the response of the climate system to external forcing, likely caused by internal climate mechanisms. Conceptual modelling (coupled meridional box model) has identified potential key feedback mechanisms involving sea ice, such as the so-called ‘sea ice-switch’ hypothesis (SIS) (Gildor and Tziperman, 2001, Tziperman and Gildor, 2003, Sayag et al., 2004), which suggests that sea ice can modify the climate state, switching it between a growing and a retreating land glacier mode, via a temperature-precipitation feedback. This hypothesis makes two critical predictions. First, the SIS invokes a gradual deep ocean cooling and a change in the vertical ocean mixing as the underlying cause for increased high-latitude sea ice extent across the MPT (Gildor and Tziperman, 2001, Tziperman and Gildor, 2003, Sayag et al., 2004). Second, the SIS proposes a land versus sea ice hysteresis, with large sea ice extent across early deglaciations (Sayag et al., 2004). Recent modelling studies also suggest that the periodicity of G/IG cycles is linked to changes in the interhemispheric pattern of sea ice growth (Lee et al., 2017). However, while modelling studies clearly suggest the importance of sea ice for controlling climate change across the MPT (Gildor and Tziperman, 2001, Tziperman and Gildor, 2003, Sayag et al., 2004, Lee et al., 2017), complementary high-resolution proxy-based reconstructions of sea ice dynamics are yet to be reported.

Recent advances in the development of source-specific biomarkers for paleoenvironmental reconstructions, including IP₂₅ (Belt et al., 2007), a proxy for seasonal Arctic sea ice, together with those indicative of open water conditions (Belt et al., 2015) and in combination with proxies for primary productivity (Méheust et al., 2016), such as the mass accumulation rate of opal (MAR_{opal}), enable high-resolution reconstructions of past sea ice dynamics. To date, IP₂₅ has been readily identified in sediments dating back to the Plio-Pleistocene boundary (Knies et al., 2014) and has even been detected in sediments of Miocene age (Stein et al., 2016), albeit from different locations. Sedimentary IP₂₅ abundance has been found to reliably reflect variations in seasonal spring sea ice extent, while absent/low IP₂₅ is normally considered to reflect ice free or extended sea ice cover regimes (Müller et al., 2009, Xiao et al., 2013, Méheust et al., 2013, Müller and Stein, 2014, Xiao et al., 2015, Smik et al., 2016, Berben et al., 2017). Consistent with these interpretations, IP₂₅ is present in surface sediments from sites in the sub-polar North Pacific that experience seasonal sea ice cover during modern times, but is absent from year-round ice free locations

(Méheust et al., 2013). Further, elevated concentrations of a tri-unsaturated highly branched isoprenoid biomarker (HBI III), shown recently to be produced by certain diatoms in polar environments (Belt et al., 2017), reflect the spring ice-edge bloom within the open waters of the marginal ice zone (MIZ), at least within the Barents Sea (Belt et al., 2015), which has a similar annual sea ice cycle to the Bering Sea. In contrast, lower abundances of HBI III (Belt et al., 2015) and variable abundances of other phytoplankton biomarkers, including brassicasterol (Navarro-Rodriguez et al., 2013), are found in year-round ice free settings of the Barents Sea and Norwegian Sea. However, lower abundances of phytoplankton biomarkers also generally occur under perennial sea ice conditions, similar to IP₂₅. Measurements of MAR_{opal} provide an alternative means of distinguishing these two extremes in sea ice cover, especially as siliceous phytoplankton are the most important primary producers in the Bering Sea today (Tsunogai et al., 1979). In the subarctic North Pacific, MAR_{opal} represents first order changes in primary productivity (Kim et al., 2014) such that extended sea ice cover leads to decreased productivity in the region (Kim et al., 2014). Previously, Méheust et al. (2016) used the sedimentary biogenic opal content in the western Bering Sea across Termination I, in order to distinguish between different sea ice states.

Additionally, beyond looking at the absolute biomarker concentrations, the nature of the correlation between IP₂₅ and HBI III can also provide insight into seasonal sea ice dynamics, although these relationships are not yet fully understood. Nevertheless, observational surface sediment calibration studies (Belt et al., 2015, Smik et al., 2016) and downcore records from the Barents and Norwegian Sea (Belt et al., 2015, Berben et al., 2017) have shown that a weak or inverse relationship between IP₂₅ and HBI III is associated with a strong seasonal sea ice cycle, whereas a positive in-phase relationship likely reflects a fluctuating sea ice margin, with reduced seasonality, and smaller changes in the position of the winter and summer sea ice edge (Cabedo-Sanz and Belt, 2016, Smik and Belt, 2017). Other biomarkers, including brassicasterol, are also indicative of open water settings (Müller et al., 2009), although the complication of other potential sources (e.g. riverine input and potentially sea ice algae (Belt et al., 2013)), somewhat limits their use beyond a qualitative indication of general phytoplankton production. However, the relationship between IP₂₅ and brassicasterol may provide context with respect to phytoplankton production in the high-productivity region of the eastern Bering Sea slope (Springer et al., 1996).

Two records of sea ice development based on the abundance of sea ice diatoms exist across the MPT in the Bering Sea (Teraishi et al., 2016, Stroynowski et al., 2017). Both reconstructions from International Ocean Discovery Program (IODP) Site U1344 and U1343 indicate sea ice advancement in conjunction with MPT climate change. However, their low temporal resolutions, preclude a robust evaluation of sea ice dynamics on G/IG timescales. Additionally, even though detailed reconstructions of deglacial sea ice dynamics exist for Termination I in the Bering Sea, LGM records of biomarker-based sea ice variability have not yet been reported.

Here, I address this gap by presenting a high-resolution sea ice reconstruction for the MPT, between 1220-800 ka, from IODP Site U1343 located close to the present day winter sea ice margin. Further the MPT findings are examined by comparisons with data obtained from the same core (Site U1343) corresponding to the pre-MPT 41-ka (~1530-1360 ka), the post-MPT 100-ka (~500-340 ka) G/IG cycles, and the LGM-Holocene (~40-10 ka) to test previous hypotheses of a strong causal link between sea ice and the changing nature of G/IG cycles.

The sea ice reconstruction is based on IP₂₅ from Site U1343, together with HBI III and MAR_{opal} (Kim et al., 2014). Building on the approach of Méheust et al. (2016), MAR_{opal} is utilised together with threshold concentrations of IP₂₅ and HBI III in order to provide a classification of the sea ice states recorded at Site U1343.

Together the proxy records from Site U1343 provide the first high-resolution reconstruction of sea ice dynamics in the eastern Bering Sea spanning four time intervals across the Pleistocene. Most notably, a substantial increase of sea ice in the Bering Sea is seen together with the appearance of transient late-glacial/deglacial sea ice maxima across the MPT, in support of land glacier retreat via a temperature-precipitation feedback mechanism as proposed by the SIS model. Further, I examine the LGM-Holocene record in light of regional sea ice records and proposed forcing mechanisms of deglacial sea ice dynamics. Together with existing regional and global climate records, I propose that sea ice extent in the eastern Bering Sea plays an important role for glacial NPIW formation since the MPT and potentially North Pacific carbon storage.

6.2 Materials and methods

6.2.1 Biomarker extraction and analysis

In total, IP₂₅ and HBI III were measured in 157 samples for this study. Brassicasterol, on the other hand, was measured in 142 samples only, as the sterol content in the Holocene-LGM samples has not yet been determined.

HBI lipids were extracted from 3 g of freeze dried homogenized sediments as described in Belt et al. (2012). Additionally removal of elemental sulphur was performed (Cabedo-Sanz and Belt, 2015) and sterol fractions were collected. In addition to sediment samples a blank and two samples of standard sediments with known biomarker concentrations were added to each extraction batch. Standard sediments are from the Canadian Arctic Archipelago and 0.5 g of sediment were weighed in per sample. 10 µl of 0.01 mg mL⁻¹ 9-octylheptadec-8-ene (9-OHD) and 5 α-androstan-3βol solution were added to each sediment vial and procedural blank as internal standards for HBI and sterol quantification, respectively. The samples were extracted three times using a mixture of Dichloromethane (high performance liquid chromatography (HPLC) grade) and Methanol (MeOH, HPLC grade) 2:1 (v/v). Gas chromatography of the first extraction batch showed high concentrations of elemental sulphur in Site U1343 sediment samples that interfere with IP₂₅ analysis. Therefore sulphur removal (Cabedo-Sanz and Belt, 2015) using tetrabutylammonium sulphite reagent (TBA) was performed for all samples prior to silica column chromatographic purification of the total organic extracts (TOE) (Belt et al., 2012). During silica chromatography non-polar components (HBIs, including IP₂₅) were eluted with hexane and collected in new pre-labelled 7 mL glass vials (TOE-2), whereas more polar hydrocarbon fractions (sterols) were eluted using hexane methyl acetate (1:4, v/v) and collected in separate pre-labelled 7 mL glass vials (TOE-3). TOE-2 was dried under N₂ flow at 25°C and re-dissolved in 150 µL hexane before being transferred to 300 µL Gas chromatography (GC) glass vials, concentrated to 20 µL under N₂ flow at 25°C, and capped with aluminium crimp-top caps with Teflon septa (Chromacol Ltd., UK). Due to low abundance of HBI lipids and high concentrations of n-alkanes HBI fractions from the oldest time interval (1530-1360 ka) were additionally purified using silver-ion chromatography (5:95 AgNO₃:SiO₂) to remove n-alkanes. TOE-3 was dried under N₂ flow at 25°C and derivatised using N,O-Bis(trimethylsilyl)-

trifluoroacetamide (50 μ L, 70°C; 1h). All samples were measured on the gas chromatography mass spectrometer (Agilent 7890A GC coupled to a 5975 series mass selective detector fitted with an Agilent HP-5ms column) at Plymouth University using the operating conditions specified in Belt et al. (2012) (Table 6.1). The identification of individual lipids was based on their characteristic retention time and mass spectra and quantification was achieved by integrating the peak area of selected ions (m/z 350 (IP₂₅); 346 (HBI III); 470 (brassicasterol)) in comparison to the peak area of the internal standards added to each sample (Belt et al., 2012). Quantification of individual lipids also considers an instrumental response factor obtained from known concentrations of biomarker lipids in the standard sediments (Belt et al., 2012).

Table 6.1 GC-MS operating conditions

Sample injection	Auto-splitless mode 1 μ l sample injected Injector temperature: 300 °C Constant flow of helium carrier gas (1 mL min ⁻¹)
Oven temperature profile	40-300 °C at 10 °C min ⁻¹ 300 °C for 10 minutes
Data collection and quantification software	Agilent Chemstation

6.3 Results

6.3.1 Sea ice biomarker variability across the LGM-Holocene and the Mid-Pleistocene in the eastern Bering Sea

Across the LGM-Holocene Biomarker concentrations were measured at an average resolution of ~2 ka between 10-40 ka (early MIS 1 to late MIS 3), with IP₂₅ varying between 0-5.6 ng g⁻¹ dry sediment (sed) (Figure 6.1). IP₂₅ concentrations are relatively constant throughout late marine isotope stage (MIS) 3 and MIS 2, with maximum concentrations during early MIS 2 (Figure 6.1). Minimum IP₂₅ concentrations are

encountered during early MIS 1 with two samples characterised by absent IP₂₅ (Figure 6.1).

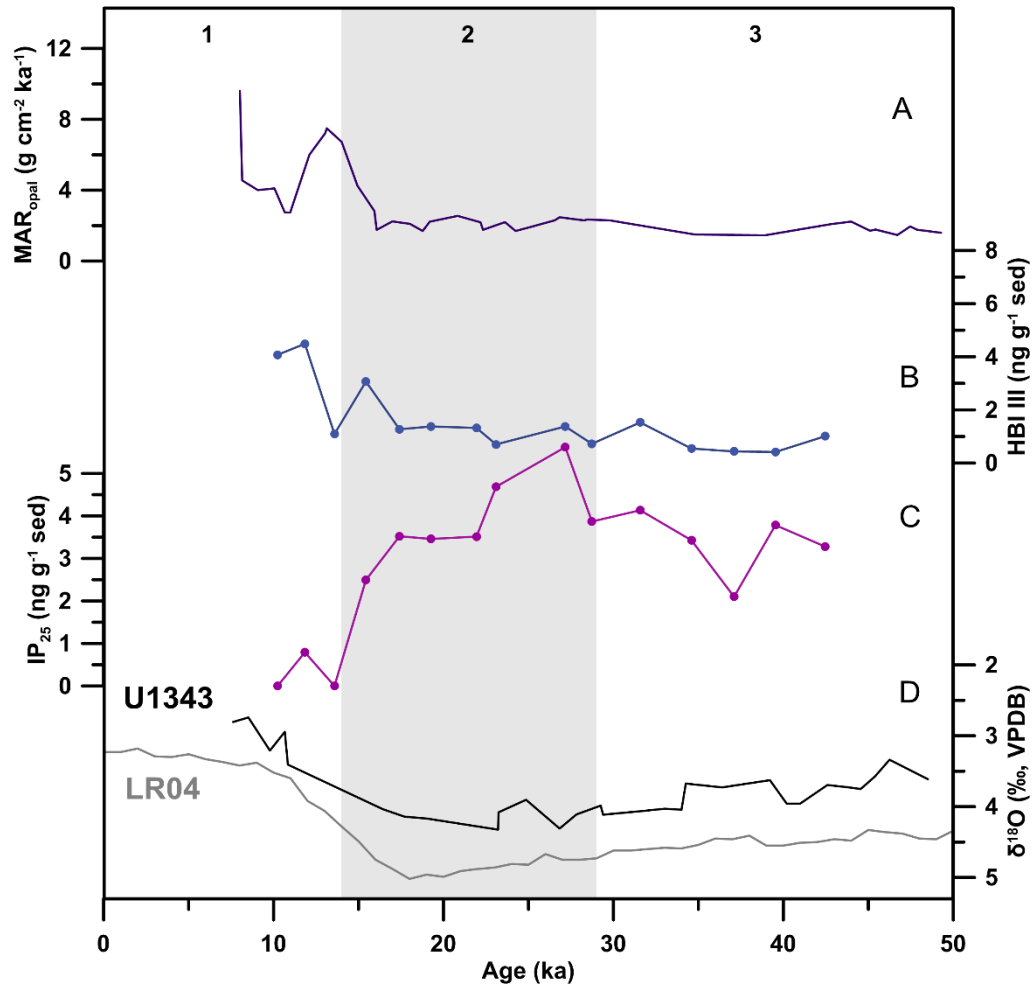


Figure 6.1 (A) Sedimentary mass accumulation rate of biogenic opal (MAR_{opal}) at Site U1343 (purple) (Kim et al., 2014). (B) HBI III (blue) and (C) IP₂₅ (violet) at Site U1343 expressed in $ng\ g^{-1}$ dry sediment (sed) across MIS 1-3 (~10-40 ka). (D) The benthic foraminiferal oxygen isotope record of Site U1343 (black) (Asahi et al., 2016) together with the LR04 stack (grey) (Lisiecki and Raymo, 2005). The light grey vertical bar indicates the last glacial interval and the white bars mark interglacial intervals (numbers at the top correspond to marine isotope stages (MIS), MIS boundaries from Lisiecki and Raymo (2005)).

Across the Mid-Pleistocene IP₂₅ demonstrates pronounced orbital variability with an average resolution of ~5.1 ka between 1365 ka to 1520 ka and 343 ka to 503 ka and ~5.4 ka on average between 808 ka and 1220 ka. MIS 10 to MIS 13 (340-500 ka) are characterised by IP₂₅ concentrations between 0-4.9 $ng\ g^{-1}$ sed, with highest IP₂₅ during early glacial intervals (Figure 6.2). A prolonged period of absent IP₂₅, indicating either perennial and/or ice free sea ice conditions, is observed during early MIS 11 to late

MIS 12 (Figure 6.2). The interval between MIS 20 to MIS 36 (800-1220 ka) spans the onset and the majority of the MPT (700-1200 ka). IP₂₅ was identified in 71 out of the 78 samples analysed varying between 0-4.3 ng g⁻¹ sed (Figure 6.3), demonstrating the presence of seasonal sea ice in the eastern Bering Sea throughout most of the MPT, in line with the late Pleistocene interval. Between MIS 44 and MIS 51 (1362 ka to 1510 ka) IP₂₅ varies on the order of 0-1.69 ng g⁻¹ sed, demonstrating the presence of seasonal sea ice in the eastern Bering Sea prior to the MPT. Glacial intervals across this period are generally characterised by increased IP₂₅ concentrations (Figure 6.4), however, the age model resolution at Site U1343 decreases beyond 1200 ka (Asahi et al., 2016), making orbital inferences more challenging.

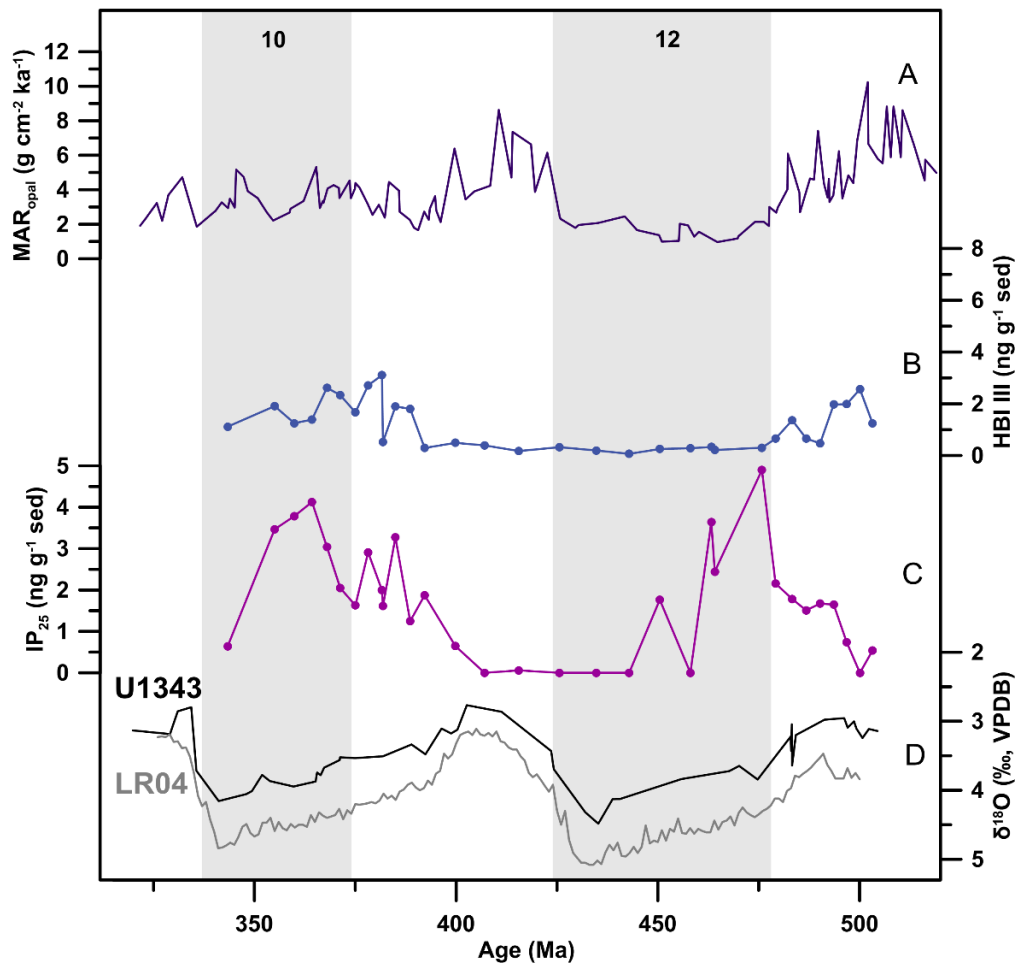


Figure 6.2 (A) Sedimentary mass accumulation rate of biogenic opal (MAR_{opal}) at Site U1343 (purple) (Kim et al., 2014). (B) HBI III (blue) and (C) IP₂₅ (violet) at Site U1343 expressed in ng g⁻¹ dry sediment (sed) across MIS 10-13 (~340-500 ka). (D) The benthic foraminiferal oxygen isotope record of Site U1343 (black) (Asahi et al., 2016) together with the LR04 stack (grey) (Lisiecki and Raymo, 2005). The light grey vertical bars indicate glacial intervals and the white bars mark interglacial intervals (numbers at the top correspond to marine isotope stages (MIS), MIS boundaries from Lisiecki and Raymo (2005)).

In general there is an increasing trend in IP₂₅ concentrations across all four intervals, with the highest concentrations observed during MIS 2. This is consistent with studies of sea ice diatoms in the Bering Sea, indicating a progressive expansion of sea ice across the Pleistocene (Teraishi et al., 2016, Stroynowski et al., 2017).

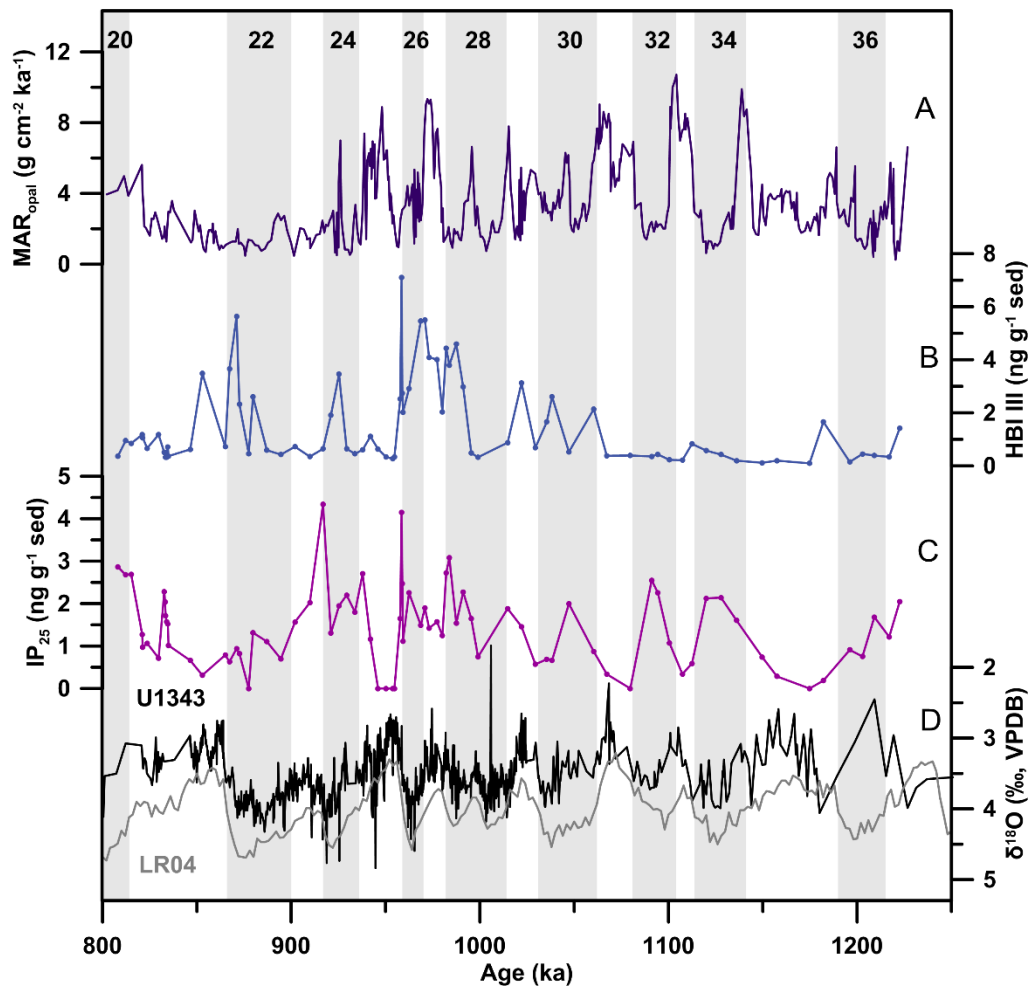


Figure 6.3 (A) Sedimentary mass accumulation rate of biogenic opal (MAR_{opal}) at Site U1343 (purple) (Kim et al., 2014). (B) HBI III (blue) and (C) IP₂₅ (violet) at Site U1343 expressed in $ng\ g^{-1}$ dry sediment (sed) across MIS 20-36 (~800-1200 ka). (D) The benthic foraminiferal oxygen isotope record of Site U1343 (black) (Asahi et al., 2016) together with the LR04 stack (grey) (Lisiecki and Raymo, 2005). The light grey vertical bars indicate glacial intervals and the white bars mark interglacial intervals (numbers at the top correspond to marine isotope stages (MIS), MIS boundaries from Lisiecki and Raymo (2005)).

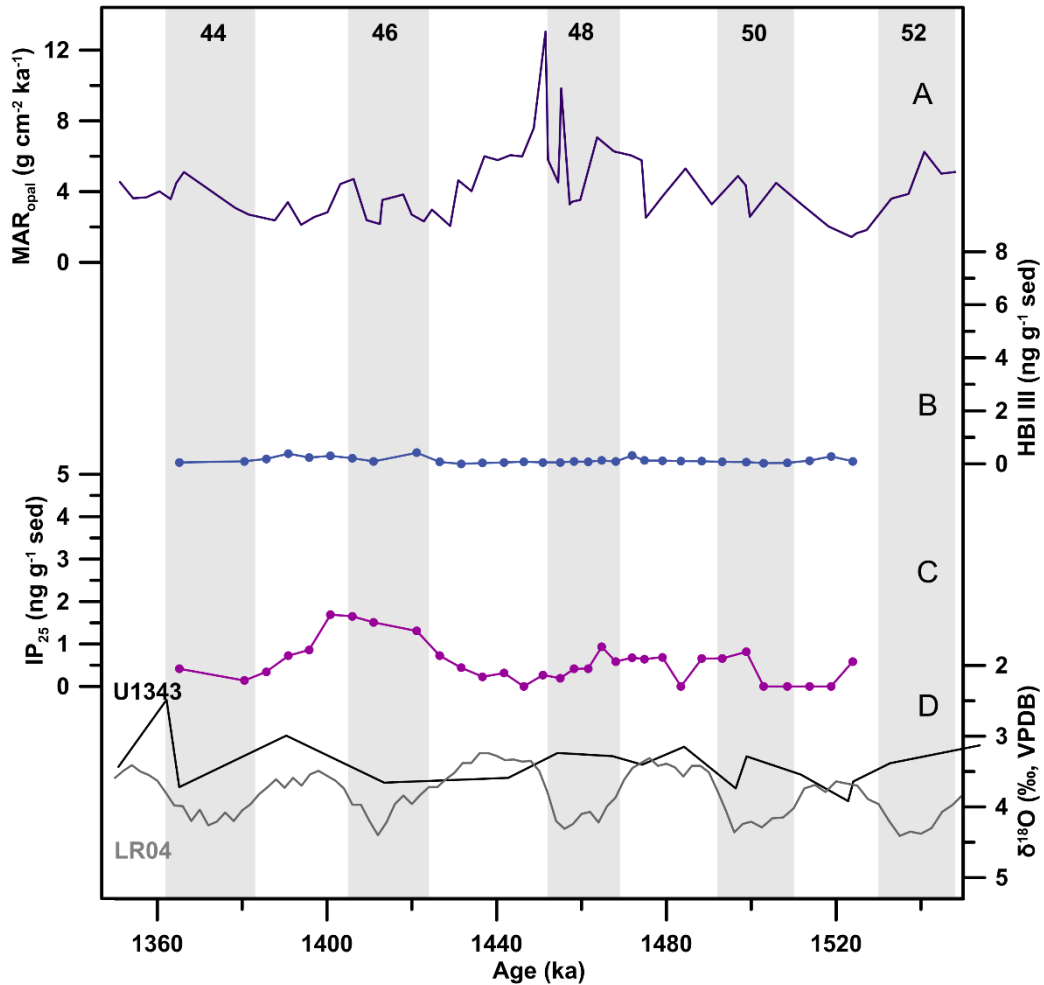


Figure 6.4 (A) Sedimentary mass accumulation rate of biogenic opal (MAR_{opal}) at Site U1343 (purple) (Kim et al., 2014). (B) HBI III (blue) and (C) IP_{25} (violet) at Site U1343 expressed in $ng\ g^{-1}$ dry sediment (sed) across MIS 44-51 (~1350-1500 ka). (D) The benthic foraminiferal oxygen isotope record of Site U1343 (black) (Asahi et al., 2016) together with the LR04 stack (grey) (Lisiecki and Raymo, 2005). The light grey vertical bars indicate glacial intervals and the white bars mark interglacial intervals (numbers at the top correspond to marine isotope stages (MIS), MIS boundaries from Lisiecki and Raymo (2005)).

6.3.2 Phytoplankton biomarkers in the eastern Bering Sea

6.3.2.1 HBI III across the LGM-Holocene and the Mid-Pleistocene

HBI III, indicative of the MIZ, varies between $0.4\ ng\ g^{-1}\ sed$ and $4.5\ ng\ g^{-1}\ sed$ across MIS 1 to MIS 3 (Figure 6.1). The concentration of HBI III is low throughout MIS 3 and most of MIS 2 (~ $1\ ng\ g^{-1}\ sed$) before it increases towards a local maximum during late MIS 2 and early MIS 1 (Figure 6.1).

The Mid-Pleistocene is characterised by HBI III concentrations of 0-0.4 5 ng g⁻¹ sed, 0.1-7.1 ng g⁻¹ sed, and 0.1-3.1 ng g⁻¹ sed between MIS 10 to MIS 13, MIS 20 to MIS 36, and MIS 44 to MIS 51, respectively (Figure 6.2, Figure 6.3, Figure 6.4). In general HBI III concentrations tend to be highest during transitional periods from interglacials to glacials or vice versa (Figure 6.2, Figure 6.3, Figure 6.4), however prominent peaks can also be observed during some glacial intervals, such as MIS 22 to MIS 30 (Figure 6.3).

Compared to IP₂₅ concentrations, that seem to increase consistently across the four measured intervals, HBI III concentrations are highest during the MPT interval across MIS 26 to MIS 28 (Table 4.2) (Figure 6.3). This coincides with a pronounced increase in IP₂₅ concentrations (Figure 6.3).

6.3.2.2 Brassicasterol across the Mid-Pleistocene

Brassicasterol, a general phytoplankton biomarker of primarily marine origin (Goad and Withers, 1982, Gladu et al., 1990, Volkman, 2006) with potential additional sources such as riverine input and sea ice algae (Belt et al., 2013), has concentrations an order of magnitude higher than IP₂₅ and HBI III. It varies between 74.2 ng g⁻¹ sed and 733.4 ng g⁻¹ sed, 41.1 ng g⁻¹ sed and 1049.3 ng g⁻¹ sed, and 0.2 ng g⁻¹ sed and 638.0 ng g⁻¹ sed, for MIS 10 to MIS 13, MIS 20 to MIS 36, and MIS 44 to MIS 51, respectively (Figure 6.5). MIS 44 to MIS 55 are characterised by highest brassicasterol concentrations during interglacials (Figure 6.5), whereas the remaining two intervals (MIS 10-13 and MIS 20-36) show increased brassicasterol during glacial intervals (Figure 6.5).

In general, brassicasterol concentrations vary between 0 ng g⁻¹ sed and 800 ng g⁻¹ sed between MIS 44 to MIS 51 and MIS 20 to MIS 36, with a slight increase observed towards the end of the latter interval (Figure 6.5). MIS 10 to MIS 13, however, is characterised by a pronounced decrease in the brassicasterol concentrations compared to the previous intervals (Figure 6.5).

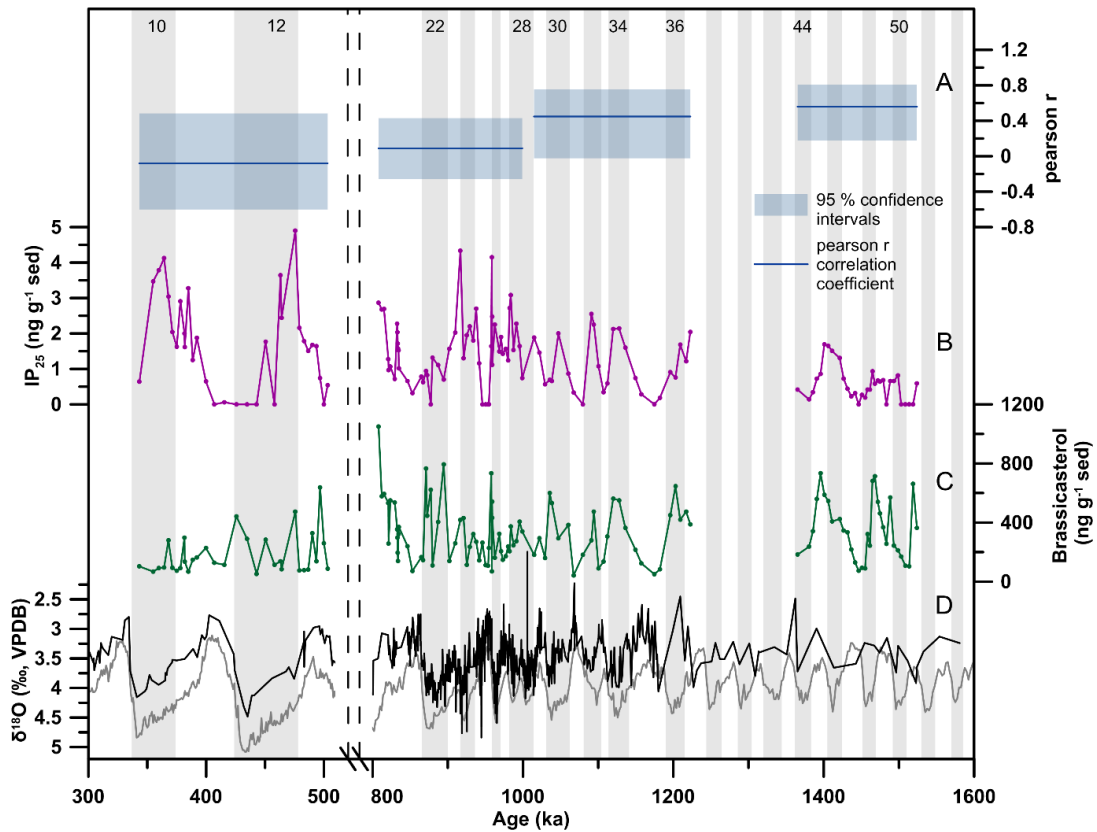


Figure 6.5 (A) The Pearson r correlation coefficient of brassicasterol and IP_{25} at IODP Site U1343 (blue), including the 95% confidence interval (blue shaded area) (B) IP_{25} at Site U1343 expressed in $ng\ g^{-1}$ dry sediment (sed) (violet) across all three Mid-Pleistocene intervals (350–500 ka, 800–1200 ka, 1350–1500 ka). (C) Brassicasterol in $ng\ g^{-1}$ sed (green) across all three Mid-Pleistocene intervals (350–500 ka, 800–1200 ka, 1350–1500 ka). (D) The benthic foraminiferal oxygen isotope record of Site U1343 (black) (Asahi et al., 2016) together with the LR04 stack (grey) (Lisiecki and Raymo, 2005). The light grey vertical bars indicate glacial intervals and the white bars mark interglacial intervals (numbers at the top correspond to marine isotope stages (MIS), MIS boundaries from Lisiecki and Raymo (2005)).

6.4 Discussion

6.4.1 Defining sea ice boundary conditions

In recent years a mathematical approach of IP_{25} in combination with phytoplankton biomarkers (PIP_{25}), such as HBI III, brassicasterol, or dinosterol has provided important advances with regard to semi-quantitative sea ice reconstructions, the ambiguity of absent IP_{25} , and the comparison of sea ice reconstructions from different regions (Müller et al., 2011, Smik et al., 2016). However, difficulties exist with calculating the PIP_{25} index, as it includes a balance term (c-factor) to account for differences in the abundance of IP_{25} and phytoplankton biomarkers (Müller et al.,

2011) (Equation 2.1). The c-factor can be calculated from the downcore data, or from a regional surface sediment calibration. The latter, however, does not yet exist for the Bering Sea. Calculating the c-factor based on mean sedimentary abundances of IP₂₅ and the respective phytoplankton biomarker potentially introduces bias to the balance term based on the core sections studied (Belt and Müller, 2013). This study is based on four distinct core sections of IODP Site U1343 across the Pleistocene, characterised by variable c-factors (MIS 3-1: 1.9, MIS 13-MIS 10: 1.5, MIS 37-20: 0.94, MIS 51-44: 4.2). Potentially a result of the prominent changes in the eastern Bering Sea sea ice regime across this interval, as suggested from diatom assemblages (Teraishi et al., 2016, Stroynowski et al., 2017), or a result of the difference in resolution of data points per G/IG cycle. Using an average c-factor for all four studied intervals, on the other hand, might also introduce bias, based on the fact that the record is non-continuous with variable resolution across the studied intervals.

Table 6.2 Threshold values for identification of sea ice scenarios

Sea ice state	IP ₂₅ (ng g ⁻¹ sed)	HBI III (ng g ⁻¹ sed)	MAR _{opal} (g cm ⁻² ka ⁻¹)
Ice free	< 0.56	< 0.7	> 4
Extended sea ice	< 0.56	< 0.7	< 4
Seasonal sea ice (within the MIZ)	> 0.56	> 0.7	variable
Seasonal sea ice (outside the MIZ)	> 0.56	< 0.7	variable

Thus, in order to reconstruct different sea ice states, a combinatory approach of IP₂₅ (indication of seasonal sea ice), HBI III (most prominent in the MIZ), and the MAR_{opal} (first order changes in export productivity) (Kim et al., 2014) is used, building on the method outlined in Méheust et al. (2016). Méheust et al. (2016) used threshold values for IP₂₅ and sedimentary biogenic opal content in the western Bering Sea to identify sea ice regime shifts over the past 20 ka. Site U1343, is located on a topographic high off the eastern Bering slope, which reduces the influence of downslope transport. However, to avoid potential siliciclastic dilution effects, the MAR_{opal} (Kim et al.,

2014) was used, rather than the sedimentary biogenic opal content. IP_{25} and MAR_{opal} at Site U1343 are significantly anti-correlated (IP_{25} - MAR_{opal} : $R^2 = -0.30$ [-0.48; -0.11], $n = 157$), consistent with the interpretation, that an increased sea ice cover leads to decreased primary productivity as a result of light limitation in the surface ocean.

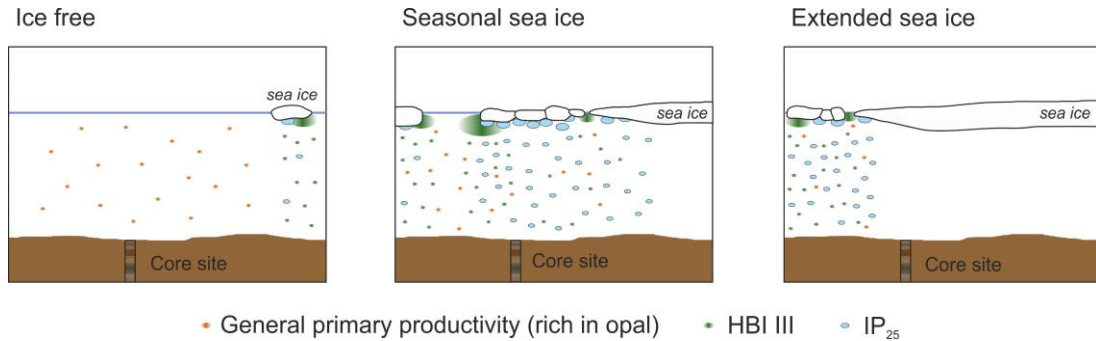


Figure 6.6 Schematic overview of the IP_{25} (light blue), HBI III (green), and MAR_{opal} (orange) dynamics under ice free, seasonal sea ice, and extended sea ice conditions. Seasonal sea ice at IODP Site U1343 is characterised by variable MAR_{opal} conditions and can be further subdivided based on the concentration of HBI III, with higher HBI III concentrations indicating predominantly marginal ice zone conditions.

A multi-proxy classification was developed, where threshold values of IP_{25} , HBI III, and the MAR_{opal} are used to identify four different sea ice states (Table 6.2) (Figure 6.6, Figure 6.7). The threshold values of IP_{25} and HBI III represent 10% of the total range of the respective biomarker (total range of IP_{25} : 0-5.6 ng g⁻¹ sed, total range of HBI III: 0-7 ng g⁻¹ sed), while the corresponding threshold value of the MAR_{opal} is based on the past 20 ka. Sea ice reconstructions using IP_{25} and sea ice diatoms from the western Bering Sea (Méheust et al., 2016, Méheust et al., 2018) and the Umnak Plateau (Caissie et al., 2010), respectively, indicate a change from a more extended sea ice cover to seasonal sea ice/ice free conditions around 15 ka across Termination I (Figure 6.8). This is in line with LGM-Holocene IP_{25} and HBI III records from Site U1343 (Figure 6.1), demonstrating a decrease in IP_{25} abundance from ~15.4 ka, together with a marked increase in HBI III, suggestive of more MIZ conditions and decreased seasonal sea ice cover along the eastern Bering Sea slope. This suggests a contemporaneous change in Bering Sea sea ice dynamics around 15 ka towards reduced seasonal sea ice extent. The MAR_{opal} value at Site U1343 at 15 ka is 4 g cm⁻² ka⁻¹ (Figure 6.8), which is used as the threshold value to distinguish between an

extended sea ice cover and more seasonal sea ice/ice free conditions (Table 6.2) (Figure 6.6). In contrast to the western Bering Sea (Méheust et al., 2016), seasonal sea ice conditions in the eastern Bering Sea (as indicated by increased IP_{25}) are characterised by variable MAR_{opal} values. This could be a result of the dynamic high productivity region overlying the core Site of U1343, indicating that sea ice concentration, even though of major importance, is not the sole driver of primary productivity along the eastern Bering slope.

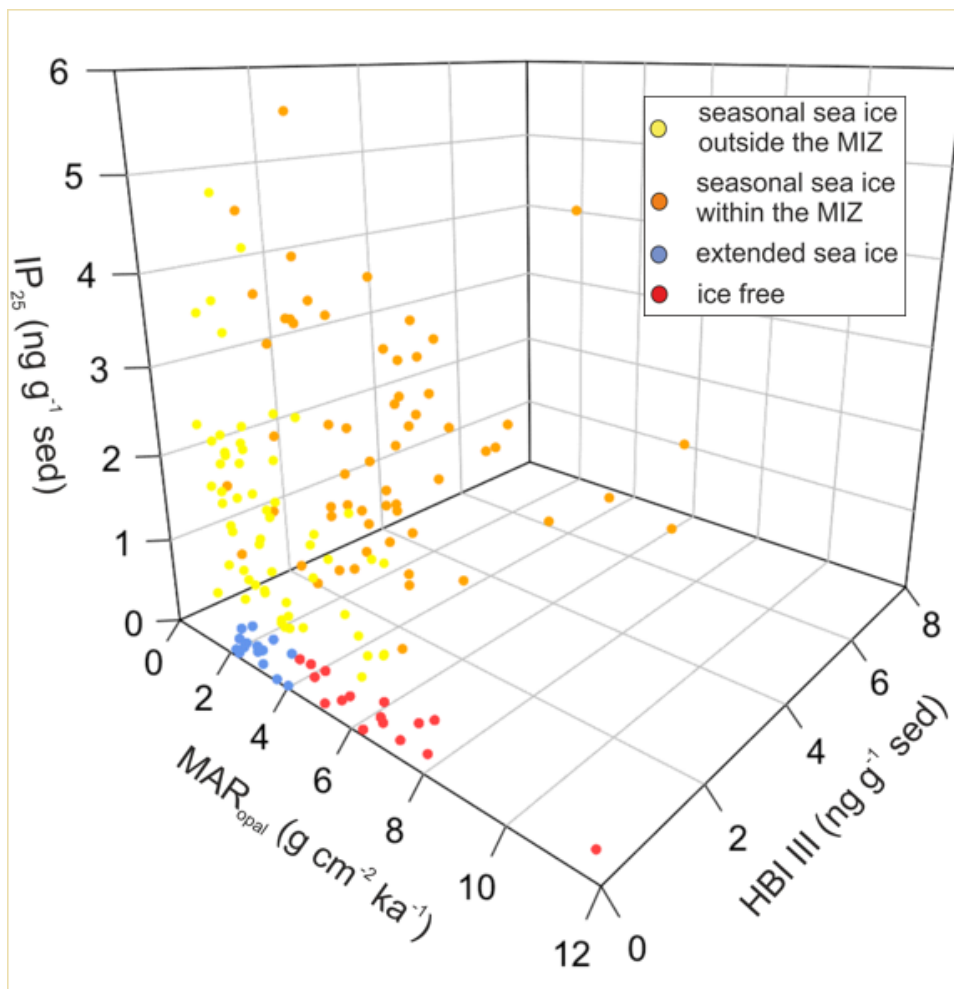


Figure 6.7 All biomarker samples are clustered according to their predominant sea ice state (for biomarker and MAR_{opal} boundaries see Table 6.2). Blue data points represent extended sea ice cover, red ice free conditions, orange seasonal sea ice within the MIZ, and yellow seasonal sea ice outside the MIZ. The ice free and extended ice cover scenarios are separated by MAR_{opal} of $4 \text{ g cm}^{-2} \text{ ka}^{-1}$, determined from sea ice studies (Méheust et al., 2016) and MAR_{opal} at Site U1343 across Termination I (Figure 6.8, Figure 6.1).

Five data points do not fit with the proposed sea ice state classification (Table 6.3), as a result of low IP_{25} , but HBI III values above the threshold value for the extended/ice free states. The reasons for this are unclear, but potentially indicate predominantly ice free/perennial sea ice conditions with occasional MIZ sedimentation. For these data points, the MAR_{opal} and were available other records of Bering Sea sea ice dynamics can be used to distinguish between ice free and extended ice cover scenarios (Table 6.3).

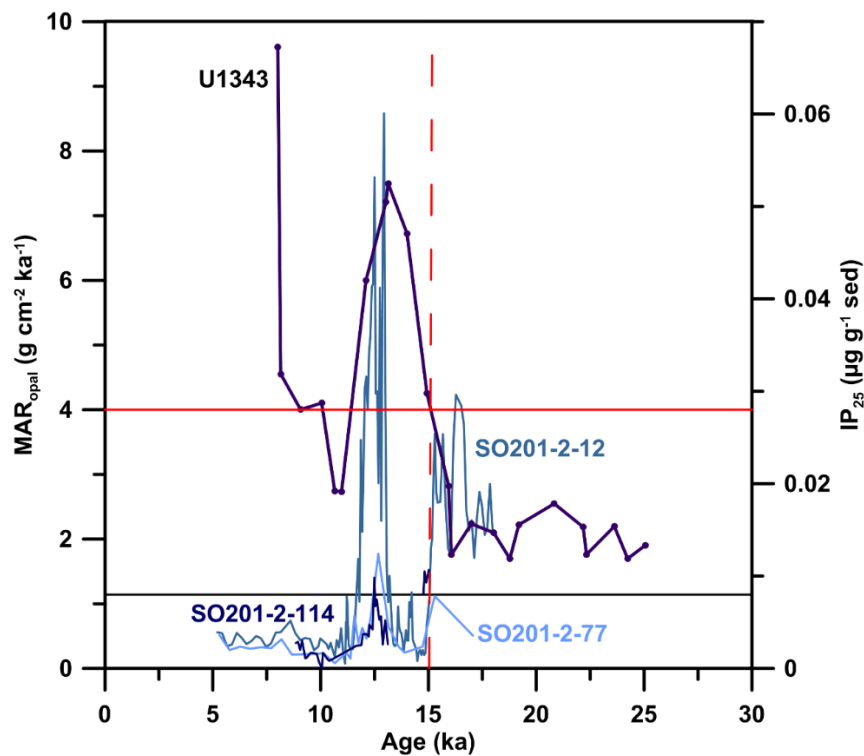


Figure 6.8 Termination I sea ice studies based on IP_{25} from three sediment cores in the western Bering Sea (SO201-2-114 (navy blue), SO201-2-77 (light blue)) and the northwest Pacific (SO201-2-12 (medium blue)) (Méheust et al., 2016) and the mass accumulation rate of biogenic opal (MAR_{opal}) at Site U1343 (Kim et al., 2014) (purple). The black horizontal line represents IP_{25} values of $0.008 \mu\text{g g}^{-1} \text{sed}$, the boundary between seasonal and ice free/extended sea ice conditions in the western Bering Sea, as identified by Méheust et al. (2016). Seasonal/ice free conditions are observed from 15 ka onwards (red dashed vertical line) in the western Bering Sea. At 15 ka MAR_{opal} at Site U1343 is $4 \text{ g cm}^{-2} \text{ ka}^{-1}$ (red horizontal line), taken as the boundary to identify ice free versus extended sea ice conditions at Site U1343.

Table 6.3 Data points that do not fit the sea ice scenario classification

Age (ka)	IP ₂₅ (ng g ⁻¹ sed)	HBI III (ng g ⁻¹ sed)	MAR _{opal} (g cm ⁻² ka ⁻¹)
10.2	0	4.07	3.69
13.6	0	1.09	7.10
500.0	0	2.56	7.74
846.7	0.31	3.48	1.26
1182.1	0.19	1.66	3.17

6.4.2 Sea ice variability in the eastern Bering Sea across the Mid- to late Pleistocene

6.4.2.1 Marine isotope stages 1 to 3

Co-examining IP₂₅, HBI III, and MAR_{opal} at Site U1343 across MIS 1 to MIS 3 suggests primarily seasonal sea ice of variable duration with a pronounced MIZ bloom along the eastern Bering slope (Figure 6.9). Early MIS 2 is characterised by the highest IP₂₅ concentrations across this interval, in conjunction with low but >0.7 ng g⁻¹ sed HBI III concentrations, suggesting enhanced seasonal sea ice across the early MIS 2 and the LGM (~25-18 ka) with a pronounced ice edge bloom in the vicinity of the core Site (Figure 6.9). Late MIS 2, on the other hand, is characterised by a decrease in IP₂₅ coinciding with an increase in the HBI III concentration. This suggests a slight reduction in the seasonal sea ice extent in the eastern Bering Sea and predominantly MIZ sedimentation (Figure 6.9). Contrasting MIS 2, early MIS 1 is marked by absent or reduced IP₂₅ together with an increase in HBI III (Figure 6.1). Both data points with absent IP₂₅ across the early MIS 1 do not fit with the proposed thresholds values for the different sea ice scenarios (Table 6.3) in the eastern Bering Sea, as a result of increased HBI III > 0.7 ng g⁻¹ sed. Considering the contemporaneous MAR_{opal} at Site U1343 and other records of sea ice variability in the Bering Sea and across the subarctic North Pacific (Méheust et al., 2016, Méheust et al., 2018) for the same time interval both data points are characterised as representing predominantly ice free conditions (Figure 6.9). IP₂₅ and HBI III demonstrate no significant correlation ($R^2 = -0.58 [-0.97; 0.65]$, $n = 15$) across MIS 1 to MIS 3. The lack of correlation suggests a

strong seasonal sea ice cycle in the eastern Bering Sea across this time interval (Figure 6.10), in line with modern sea ice dynamics (Méheust et al., 2013).

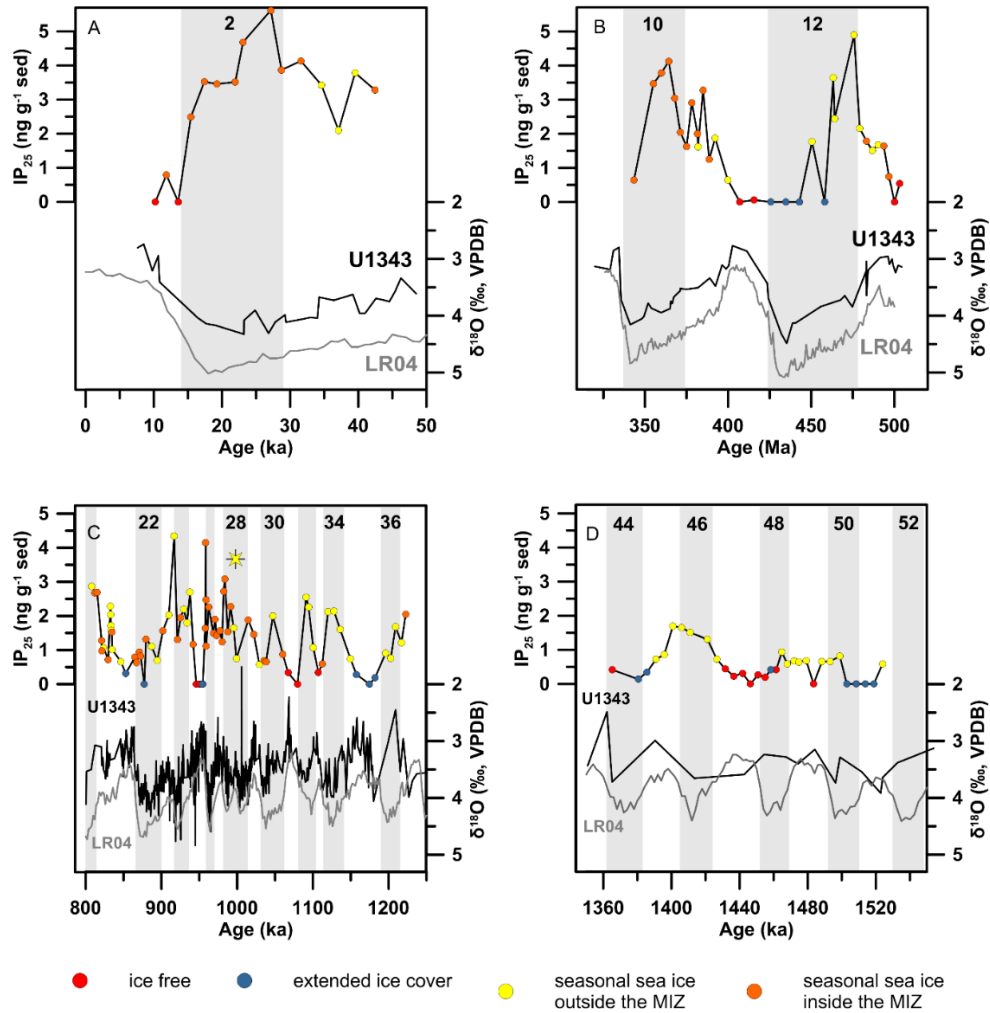


Figure 6.9 Overview of eastern Bering Sea sea ice dynamics across (A) MIS 1 to MIS 3 (10-40 ka), (B) MIS 10 to MIS 13 (350-500 ka), (C) MIS 20 to MIS 36 (800-1200 ka), and (D) MIS 44 to MIS 51 (1350-1500 ka). Different sea ice scenarios have been colour coded with red representing ice free conditions, blue extended sea ice, yellow seasonal sea ice outside of the MIZ, and orange seasonal sea ice within the MIZ (see Table 6.2 for threshold values of sea ice conditions). This is in comparison to the benthic foraminiferal oxygen isotope record of Site U1343 (black) (Asahi et al., 2016) together with the LR04 stack (grey) (Lisiecki and Raymo, 2005). The light grey vertical bars indicate glacial intervals and the white bars mark interglacial intervals (numbers at the top correspond to marine isotope stages (MIS), MIS boundaries from Lisiecki and Raymo (2005)).

6.4.2.2 Marine isotope stages 10 to 13

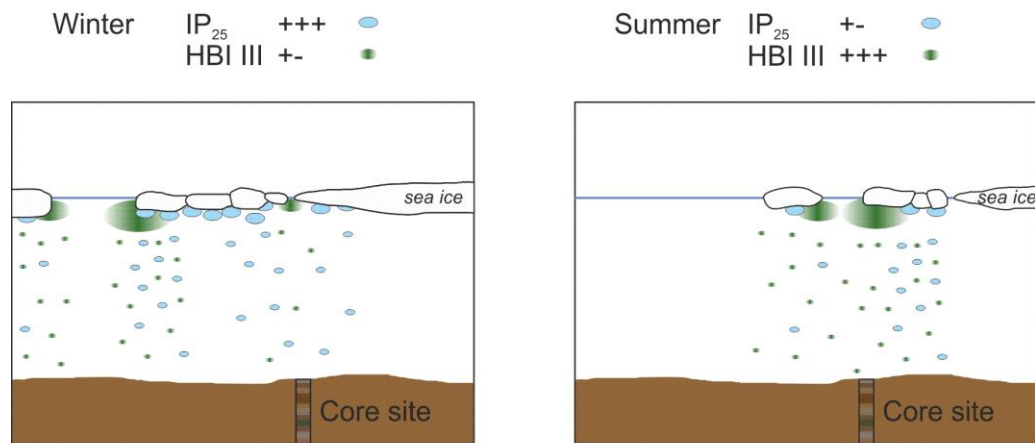
MIS 10 to MIS 13 (500-340 ka) represents two G/IG cycles during the post-MPT quasi-100-ka climate variability. A broad gradual increase of IP₂₅ and HBI III,

accompanied by a high MAR_{opal} , occurs during cooling phases of the interglacial intervals, indicative of seasonal sea ice of increasing duration, with predominantly MIZ conditions (Figure 6.9). Biomarker data at 500 ka (MIS 13) do not conform to the suggested sea ice state classification (Table 6.3) as a result of relatively high HBI III concentrations ($>0.7 \text{ ng g}^{-1} \text{ sed}$), yet low IP_{25} content. However, a high MAR_{opal} is indicative of ice free conditions (Table 6.3, Figure 6.9). Absent or very low IP_{25} across the MIS 12/11 transition is accompanied by low HBI III concentrations, and low/high MAR_{opal} values, indicating extended sea ice cover across the late-glacial/deglacial, and ice free conditions during the interglacial MIS 11 from ~425 ka (Figure 6.9). This is in line with sea ice variability at IODP Site U1345 across this time interval, reconstructed from diatom assemblages, indicating increased sea ice extent during late MIS 12 and late MIS 11, compared to the early MIS 11 (Caissie et al., 2016). There is no change observed in HBI III associated with the transition from extended sea ice to ice free conditions across the MIS 12/11 transition, potentially resulting from a very rapid shift in sea ice dynamics (Figure 6.2). The relationship of IP_{25} and HBI III shows no correlation across G/IG cycles ($R^2 = 0.24 [-0.53; 0.79]$, $n = 32$), suggesting a strong seasonal sea ice cycle (Figure 6.10) similar to sea ice dynamics across MIS 1 to MIS 3.

6.4.2.3 Marine isotope stages 20 to 36

MIS 20 to MIS 36 covers large parts of the MPT, associated with a pronounced shift in the frequency of the benthic foraminiferal oxygen isotope composition ($\delta^{18}O_b$) at Site U1343 from 41-ka to 100-ka first apparent around ~1200 ka and dominant from 700 ka onwards (Asahi et al., 2016). IP_{25} concentrations exhibits distinct variability on G/IG timescales, with generally higher values throughout glacial intervals (Figure 6.9), indicative of regionally enhanced sea ice cover. Low IP_{25} , HBI III, and MAR_{opal} values during MIS 35, 26/25 (Table 4.2), and 22 (Table 4.2), collectively suggest extended sea ice cover at the eastern Bering slope at these times (Figure 6.9). In contrast, low IP_{25} and HBI III concentrations, together with a relatively high MAR_{opal} during MIS 31 and 33, suggest ice free conditions (Figure 6.9). The biomarker values at 850 ka (MIS 21) and 1180 ka (early MIS 35) (Table 6.3) do not convincingly fall within the proposed sea ice state classifications (Table 6.2), largely as a result of relatively high HBI III content ($>0.7 \text{ ng g}^{-1} \text{ sed}$). The reasons for this are unclear, but potentially indicate the influence of occasional MIZ sedimentation.

Pronounced seasonal sea ice cycle



Fluctuating sea ice margin

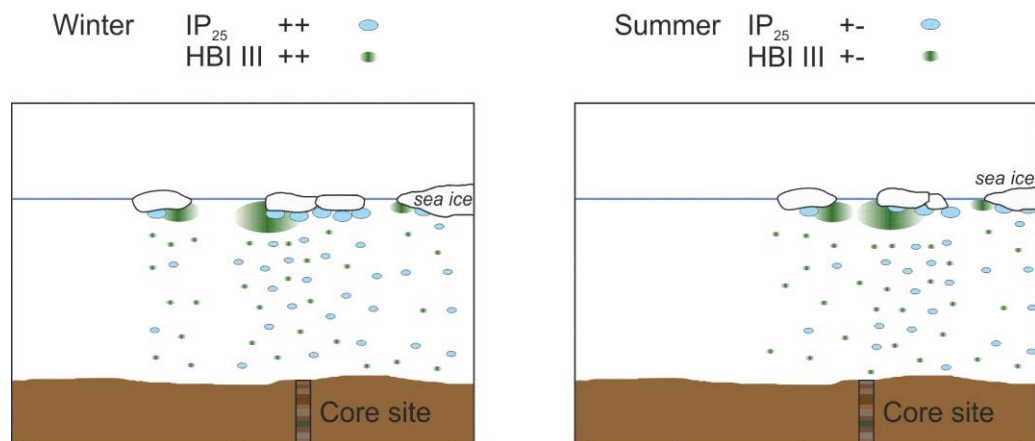


Figure 6.10 Schematic cartoon of the correlation of IP₂₅ and HBI III in the sediments underlying the seasonal sea ice/ice marginal zone depending on the seasonal sea ice cycle at the core site. A pronounced seasonal cycle leads to a negative or no correlation between IP₂₅ and HBI III, whereas a more fluctuating sea ice margin typically leads to a positive correlation of IP₂₅ and HBI III.

A pronounced increase in peak glacial IP₂₅ values is observed consistently across all glacial intervals following MIS 28 (~1000 ka) concomitant with a shift in the timing of the glacial IP₂₅ maximum from the mid-glacial to the late-glacial/deglacial (Figure 6.9), with exception of MIS 22 (Table 4.2). Furthermore, the correlation of IP₂₅ and HBI III changes to one that is in-phase between 1000-950 ka (Figure 6.11) ($R^2 = 0.67$ [0.15; 0.90], $n = 17$), indicating a more fluctuating sea ice margin with predominantly MIZ conditions (Figure 6.10). This is framed by intervals of no apparent correlation between these two biomarkers from 1220-1000 ka, MIS 36 to 29 ($R^2 = -0.02$ [-0.30;

0.27], $n = 26$) and 950-800 ka, MIS 24-20 ($R^2 = -0.17$ [-0.44; 0.12], $n = 35$) (Figure 6.11) more consistent with a stronger seasonal cycle and a pronounced advance and retreat of the sea ice margin (Figure 6.10), as seen in the modern setting and for most other Arctic marginal seas (Deser and Teng, 2008, Méheust et al., 2013).

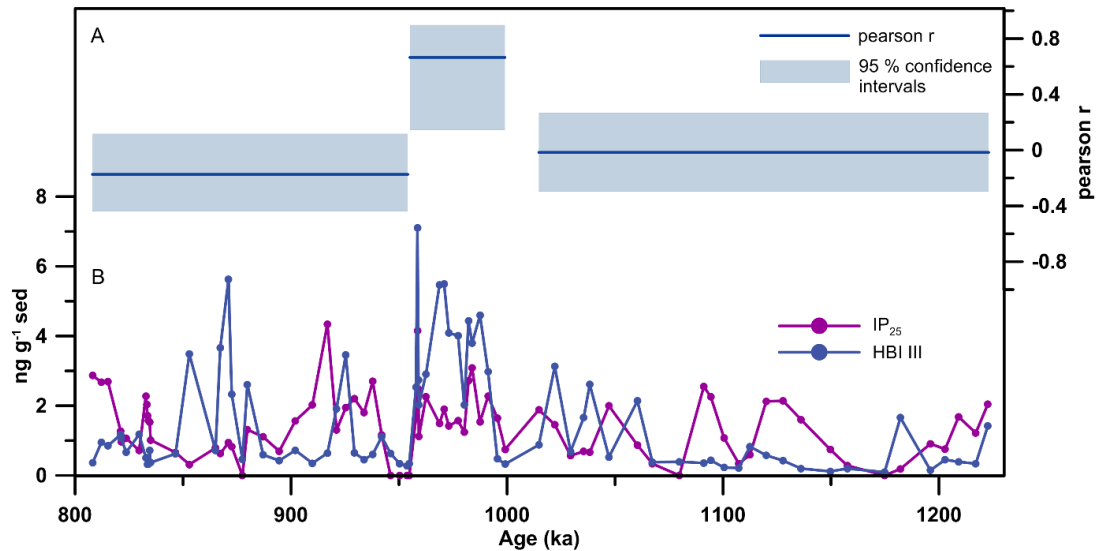


Figure 6.11 (A) Pearson r correlation coefficient for IP₂₅ and HBI III between 800-1220 ka (blue), including the 95% confidence interval (shaded blue area), calculated using Pearson T3 (Mudelsee, 2003). The interval has been divided into three subsections based on the correlation of both biomarkers, the absolute concentration, and the profile of sea ice increase across glacial periods. (B) IP₂₅ (violet) and HBI III (blue) concentrations between 800 ka and 1220 ka expressed in ng g⁻¹ dry sediment (sed).

6.4.2.4 Marine isotope stages 44 to 51

MIS 44 to MIS 51 precedes the onset of the MPT and is characterised by 41-ka G/IG frequency, as seen from the $\delta^{18}\text{O}_b$ record at Site U1343, demonstrating significant 41-ka periodicity from 1500 ka (Asahi et al., 2016) in accordance with the global LR04 stack (Lisiecki and Raymo, 2005). Although the relative timing of sea ice changes in comparison to G/IG cycles is uncertain, resulting from the low resolution of the U1343 $\delta^{18}\text{O}_b$ record prior to 1200 ka (Figure 6.9), it is nonetheless clear that this interval is within the late Pleistocene as indicated by biostratigraphy, magnetostratigraphy, and tuning of long-term U1343 $\delta^{18}\text{O}_b$ (Asahi et al., 2016) to the LR04 stack (Lisiecki and Raymo, 2005).

Across this interval periods of absent IP₂₅ are accompanied by variable MAR_{opal} values indicative of both ice free (high MAR_{opal}) and perennial sea ice (low MAR_{opal}) conditions (Figure 6.9). Concentrations of HBI III were generally low, indicating that a spring ice edge bloom associated with the retreating MIZ most likely did not occur in the vicinity of Site U1343 during this interval. Further, a weak positive relationship between IP₂₅ and HBI III (IP₂₅-HBI III: $R^2 = 0.47$ [0.18; 0.69], $n = 32$) suggests a fluctuating sea ice margin (Figure 6.10), with smaller changes in the position of the summer and winter sea ice edge.

6.4.3 Sea ice dynamics in the eastern Bering Sea across the last glacial cycle

Sea ice variability as reconstructed from IP₂₅ and HBI III in the eastern Bering Sea across MIS 3 to MIS 1 exerts distinct G/IG variability (Figure 6.12), in line with other Pleistocene intervals studied at Site U1343. Late MIS 3 is marked by conditions predominantly outside the MIZ, indicating the presence of seasonal sea ice in the eastern Bering Sea, but no spring sea ice edge bloom in the vicinity of the core Site (Figure 6.12). Seasonal sea ice expansion is supported by increased content of ice rafted debris (IRD) in sediments of the southern Bering Sea across MIS 3 and MIS 2 (Gorbarenko et al., 2010) and radiolarian assemblages, indicating a low-temperature, low-salinity surface layer during MIS 3, favourable for sea ice formation (Tanaka and Takahashi, 2005). Following MIS 3, early MIS 2 is characterised by the highest IP₂₅ concentrations throughout all four intervals studied at Site U1343 (Figure 6.9), in line with the proposed increase in sea ice extent across the Pleistocene based on diatom assemblages (Teraishi et al., 2016, Stroynowski et al., 2017) and increased IP₂₅ in the western and eastern North Pacific (Méheust et al., 2018). HBI III concentrations across this interval, indicate a prominent spring sea ice edge bloom at Site U1343 (Figure 6.12) and the relationship of HBI III and IP₂₅ is in favour of a pronounced seasonal advance and retreat of the sea ice margin. Compared to MIS 3 (-84 ± 3 m (standard error (s.e.)) (Spratt and Lisiecki, 2016)), MIS 2 is characterised by a lower sea level (-123 ± 2 m (s.e.) (Spratt and Lisiecki, 2016)) in conjunction with increased continental ice volume. Thus, even though both MIS 3 and MIS 2 were marked by a closed Bering Strait (~ 50 m water depth), the shoreline of Beringia was closer to Site U1343 during MIS 2, in line with a reduced geographical retreat of the spring sea ice edge and an associated phytoplankton bloom in the vicinity of the eastern Bering Sea slope.

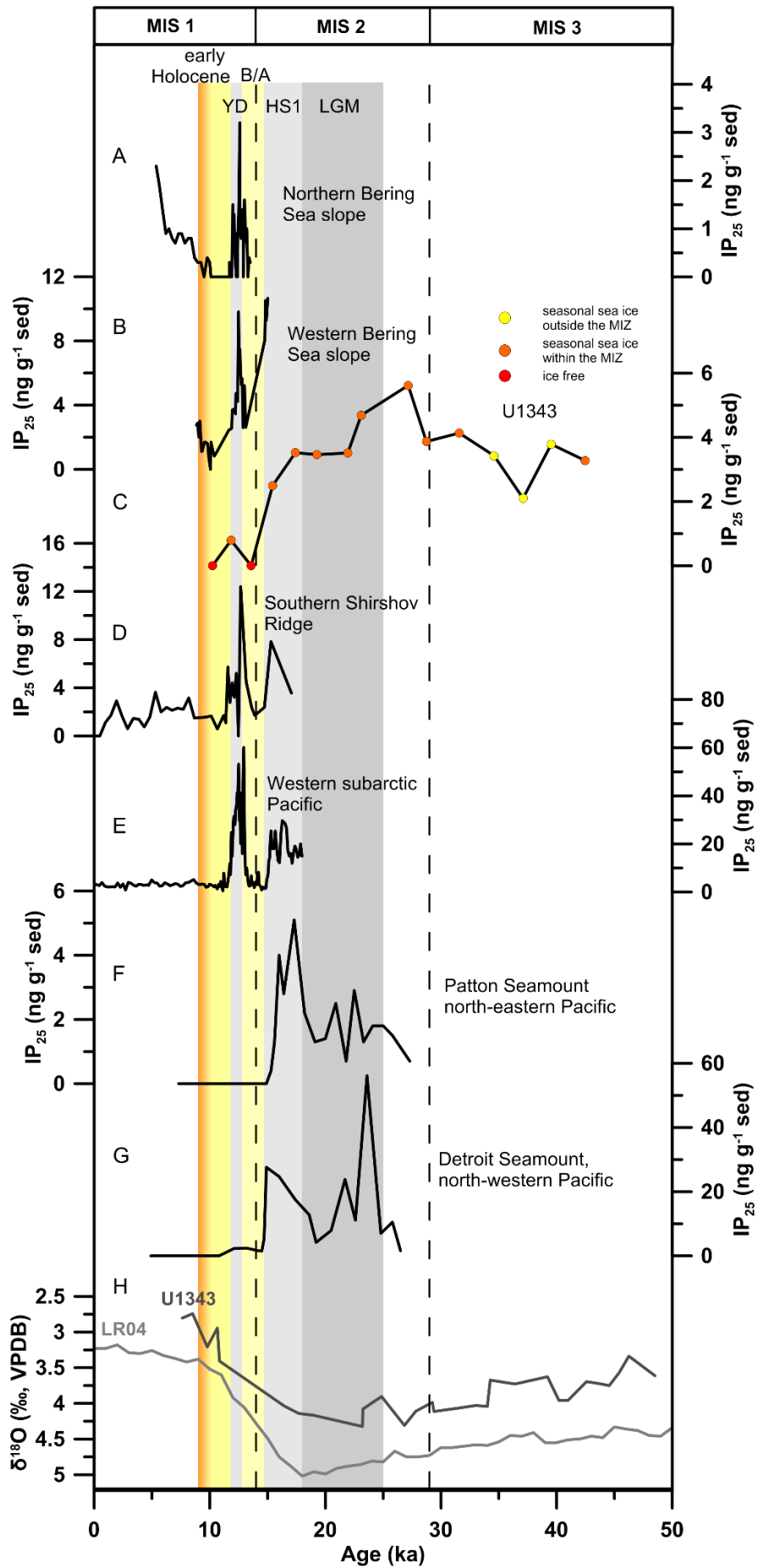


Figure 6.12 All biomarker-based sea ice studies from the Bering Sea and the North Pacific in geographical order from the north to the south. (A) IP₂₅ at site SO202-18-6 on the northern Bering Sea slope (Méheust et al., 2018), (B) SO201-2-114 on the western Bering Sea slope (Méheust et al., 2016), (C) Site U1343 (this study) with data points coloured according to the predominant sea ice state (orange: seasonal sea ice within the MIZ, yellow: seasonal sea ice outside the MIZ, red: ice free), (D) SO201-2-77 on the southern Shirshov Ridge (Méheust et al., 2016), (E) SO201-2-12 in the western subarctic Pacific (Méheust et al., 2016), (F) SO202-27-6 on Patton Seamount in the north-eastern Pacific (Méheust et al., 2018), and (G) SO202-07-6 on Detroit Seamount in the north-western Pacific (Méheust et al., 2018), together with (H) $\delta^{18}\text{O}_b$ at Site U1343 (black) (Asahi et al., 2016) and the global LR04 stack (grey) (Lisiecki and Raymo, 2005). The dark grey vertical bar indicates the last glacial maximum (LGM, ~25-18 ka), the light grey bars represent deglacial cold events, the Heinrich stadial 1 (HS1, ~14.7-18 ka) and the Younger Dryas (YD, ~12.9-11.7 ka), the yellow bar marks the Bølling-Allerød (B/A, 12.7 ka to 14.7 ka), and the yellow/orange bar indicates the early Holocene including the Holocene Thermal Maximum (9-11.5 ka). The dashed vertical lines represent the marine isotope stage (MIS) boundaries as indicated by numbers at the top, MIS boundaries from Lisiecki and Raymo (2005).

Across the LGM (~18-25 ka) a small decrease in IP₂₅ is observed, however, consistently high concentrations are in line with enhanced seasonal sea ice in the eastern Bering Sea similar to the early MIS 2 (Figure 6.12). This is in agreement with both biomarker and diatom assemblage records of sea ice variability in the Bering Sea and the North Pacific, suggesting variable sea ice extent in western North Pacific and extended sea ice cover in the eastern North Pacific (Méheust et al., 2018), together with perennial or extended seasonal sea ice at the Umnak Plateau, the Shirshov Ridge, and in the western subarctic Pacific (Katsuki et al., 2003, Cook et al., 2005, Katsuki and Takahashi, 2005, Caissie et al., 2010, Max et al., 2012) (Figure 6.12).

MIS 3 and MIS 2 are characterised by relatively well-ventilated intermediate waters at IODP Site U1342 (~800 m water depth) in the southern Bering Sea (Knudson and Ravelo, 2015b), however controversy exists, whether NPIW was formed in the Bering Sea or the Sea of Okhotsk. Based on the distribution of radiolarian assemblages Tanaka and Takahashi (2005) conclude that NPIW was formed in both the Bering Sea and the Sea of Okhotsk during MIS 3, whereas the Bering Sea was likely the primary location of NPIW formation during MIS 2. Neodymium isotope evidence indicates more radiogenic ϵ_{Nd} during MIS 2 compared to MIS 3, suggesting enhanced intermediate water formation in the Bering Sea across the LGM (Horikawa et al., 2010). Rella et al. (2012) also suggest increased Bering Sea intermediate water formation during stadial events of MIS 3 and across Termination I, whilst other studies indicate that the Sea of Okhotsk remained the primary location for NPIW formation

during millennial-scale cold events (Max et al., 2014, Okazaki et al., 2014). Increased sea ice extent in the Bering Sea, together with a pronounced seasonal sea ice cycle, as suggested from the relationship of HBI III and IP₂₅ ($R^2 = -0.58 [-0.97;0.65]$, $n = 15$), across MIS 3 and MIS 2 is in support of increased brine rejection in the Bering Sea, potentially indicating increased NPIW formation. Further, records of nitrogen isotopes and biological productivity in the Bering Sea and the North Pacific, suggest increased stratification and decreased primary productivity during MIS 3 and MIS 2 as a result of enhanced salinity stratification and reduced nutrient supply to the surface ocean (Jaccard et al., 2005, Brunelle et al., 2007, Brunelle et al., 2010, Ovsepyan et al., 2017), in agreement with the MAR_{opal} at Site U1343 (Kim et al., 2014) (Figure 6.1). Increased seasonal sea ice cover could aid in enabling decreased primary productivity by reducing the light availability and facilitating stratification by strengthening the halocline during winter and freshwater input during summer.

6.4.3.1 Sea ice evolution in the eastern Bering Sea across Termination I

The resolution of IP₂₅ across Termination I at Site U1343 is relatively low with an average temporal resolution of ~1.8 ka, hampering an in-depth discussion of millennial-scale climate events (Figure 6.12). Nevertheless, I will be examining the deglacial sea ice history at Site U1343 in light of additional sea ice records from across the Bering Sea and the North Pacific, providing a comprehensive picture of sea ice variability across Termination I.

Across HS1 two samples were measured for sea ice reconstructions at Site U1343 (Figure 6.12), with the early HS1 (17.4 ka) characterised by similar sea ice conditions to the LGM and the late HS1 (15.4 ka) indicating a decrease in the seasonal sea ice extent, as suggested from decreased IP₂₅ and increased HBI III concentrations (Figure 6.1, Figure 6.12). This is in agreement with biomarker-based sea ice reconstructions from the western Bering Sea, the Shirshov Ridge, and the western and eastern North Pacific all demonstrating increased seasonal sea ice extent during HS1 (Méheust et al., 2016, Méheust et al., 2018) (Figure 6.12). Further, a simultaneous decrease in sea ice extent around ~15 ka can be observed across the Bering Sea and the western subarctic Pacific (Caissie et al., 2010, Méheust et al., 2016, Méheust et al., 2018) (Figure 6.12), in line with a coeval increase in the regional primary productivity (Brunelle et al., 2007, Kim et al., 2014, Méheust et al., 2018, Pelto et al., 2018) and SST warming

(Meyer et al., 2016). However, due to the lower resolution the sea ice record at Site U1343 likely does not capture the true dynamic nature of the HS1 sea ice evolution as seen in other biomarker records from across the Bering Sea (Méheust et al., 2016, Méheust et al., 2018) (Figure 6.12). A pronounced increase in the mid-depth ventilation of the Bering Sea (Rella et al., 2012, Max et al., 2014, Knudson and Ravelo, 2015b) and a deepening of NPIW penetration (Gebhardt et al., 2008, Max et al., 2014, Rae et al., 2014) (Chapter 5), point towards increased formation of intermediate waters via brine rejection during sea ice freezing across HS1. Enhanced seasonal sea ice formation in the Bering Sea during HS1 is in support of strengthened brine rejection, likely promoting intermediate water ventilation. However, further research is needed to determine, whether the Bering Sea and/or the Sea of Okhotsk were the primary sources of intermediate water formation during HS1 (Rella et al., 2012, Okazaki et al., 2014, Max et al., 2014).

The Bølling-Allerød (B/A, ~12.7 ka to 14.7 ka) warm period following HS1 is marked by absent IP₂₅ at Site U1343 suggesting ice free conditions, in line with ice free conditions in the subarctic North Pacific and reduced sea ice extent in the western and south eastern Bering Sea (Caissie et al., 2010, Méheust et al., 2016, Méheust et al., 2018) (Figure 6.12). Decreased sea ice extent is accompanied by an increase in the SST in the western Bering Sea (Max et al., 2012, Meyer et al., 2016) and increased primary productivity (Brunelle et al., 2007, Caissie et al., 2010, Kim et al., 2014, Méheust et al., 2016, Méheust et al., 2018). Warming and enhanced remineralisation of organic matter in the water column led to a pronounced expansion of the mid-depth oxygen minimum zone (OMZ) across the B/A, as seen from widespread laminated sediments (up to ~2000 m water depth) (Expedition 323 Scientists 2010, Aiello and Ravelo, 2012, Kuehn et al., 2014, Ovsepyan et al., 2017, Pelto et al., 2018) and from benthic foraminiferal assemblages and elemental proxies along the eastern Bering slope (Chapter 5).

Following the B/A the YD cold event (~12.9-11.7 ka) is characterised by the re-emergence of increased seasonal sea ice extent in the Bering Sea (Méheust et al., 2016, Méheust et al., 2018), also seen at Site U1343 (Figure 6.12). However, again the temporal resolution of the sea ice record with only one sample at the YD/Holocene boundary (Figure 6.12), suggests that the true sea ice variability may not be represented at Site U1343, likely explaining the dampened increase in IP₂₅ compared

to other Bering Sea sites across the YD (Figure 6.12). Markedly increased HBI III concentrations in this sample are in favour of pronounced MIZ conditions along the eastern Bering Sea slope around 11.8 ka (Figure 6.12).

Holocene sea ice variability at Site U1343 is represented by one data point at 10.2 ka that falls within the Holocene Thermal Maximum (9-11.5 ka), a warm period within the last interglacial driven by peak northern hemisphere summer insolation (12-10 ka) (Kaufman et al., 2004). It is characterised by absent IP₂₅ concentrations, increased HBI III $\sim 4 \text{ ng g}^{-1} \text{ sed}$, and MAR_{opal} ($3.7 \text{ g cm}^{-2} \text{ ka}^{-1}$) close to the threshold of seasonal sea ice versus ice free/extended sea ice conditions. Thus, although it does not fall convincingly within the proposed boundary conditions for eastern Bering Sea sea ice scenarios (Table 6.2), co-examination with other biomarker-based sea ice reconstructions from across the Bering Sea and the subarctic North Pacific (Méheust et al., 2016, Méheust et al., 2018), suggest ice free conditions prevailed along the eastern Bering Sea slope (Figure 6.12). This is further supported by SST warming in the Bering Sea across the early Holocene (Caissie et al., 2010, Max et al., 2012, Meyer et al., 2016) and increased warm Alaskan Stream inflow into the south eastern Bering Sea from around 11 ka as seen from the assemblage of the diatom species *Neodenticula seminae* at the Umnak Plateau (Katsuki and Takahashi, 2005, Caissie et al., 2010).

Thus, biomarker-based sea ice records at Site U1343 across MIS 3 to MIS 1 support previously reconstructed G/IG and millennial-scale changes in Bering Sea sea ice extent, demonstrating variability closely linked to deglacial North Atlantic millennial-scale climate events via oceanic or atmospheric teleconnections (Caissie et al., 2010, Max et al., 2012, Méheust et al., 2016, Méheust et al., 2018). Potential oceanic teleconnections of North Atlantic climate change and Bering Sea sea ice variability include changes in the sea level, driving warm and salty Alaskan Stream inflow into the southern Bering Sea (Méheust et al., 2016, Méheust et al., 2018), influencing the sea ice extent. Abundances of *N. seminae*, a diatom species indicative of Alaskan Stream waters (Sancetta, 1983), increases in the subarctic western Pacific during the B/A and at the onset of the Holocene (Max et al., 2012), in line with sea ice development at this site (Méheust et al., 2016). In the southeastern Bering Sea, however, *N. seminae* does not increase until ~ 11 ka at the Umnak Plateau (Katsuki and Takahashi, 2005, Caissie et al., 2010), suggesting decreased influence of the

Alaskan Stream during deglacial warm phases prior to 11 ka. Meyer et al. (2016) suggest that the subarctic western Pacific may be more sensitive to changes in the surface ocean circulation related to reduced Alaskan Stream flow through the Aleutian Arc during sea level lowstands, such as the LGM and early deglaciation, whilst the surface ocean conditions in the Bering Sea are more sensitive to atmospheric teleconnections. Possible atmospheric teleconnections include increased advection of cold air masses from the North Atlantic via increased zonal wind velocities during deglacial cold events (Manabe and Stouffer, 1988). Moreover, Okumura et al. (2009) suggest an influence of tropical SST anomalies on North Pacific atmospheric circulation in conjunction with AMOC slowdown during deglacial stadials. Decreased northward heat transport in the Atlantic, thus causes a deeper and stronger Aleutian Low over the North Pacific, increasing the surface heat fluxes and the southward Ekman transport, promoting hemisphere-wide cooling during HS1 and the YD (Okumura et al., 2009).

Across the LGM-Holocene biomarker-based sea ice reconstructions from IODP Site U1343, thus agree well with previous studies from across the Bering Sea and the North Pacific (Méheust et al., 2016, Méheust et al., 2018), suggesting millennial-scale sea ice changes in-phase with North Atlantic climate change across Termination I (Figure 6.12). Additionally, the record of sea ice variability at Site U1343 is the first biomarker-based record in the Bering Sea extending into the LGM and even as far back as MIS 3, indicating extended seasonal sea ice throughout late MIS 3 and MIS 2 (Figure 6.12), corroborated by findings of diatom assemblage studies (Katsuki et al., 2003, Katsuki and Takahashi, 2005, Caissie et al., 2010, Max et al., 2012).

6.4.4 Mid-Pleistocene sea ice dynamics in the eastern Bering Sea

Variations in sea ice and phytoplankton biomarkers, together with previously reported MAR_{opal} from Site U1343, demonstrate major changes in sea ice dynamics in the eastern Bering Sea during the past 1500 ka, especially across the interval covering the MPT (Figure 6.13). Three broad intervals of sea ice change are identified corresponding to the early-mid Pleistocene (1220-1000 ka), an interim state (1000-950 ka), and the mid-to-late Pleistocene (950-800 ka and 500-340 ka).

During the early-mid Pleistocene (1220-1000 ka) IP₂₅ and HBI III concentrations are de-coupled (Figure 6.11), indicating a pronounced seasonal advance and retreat of the

sea ice margin, as per modern conditions. This contrasts the preceding interval (MIS 51 to 43) where IP₂₅ and HBI III concentrations exhibit a weak positive correlation indicative of a fluctuating sea ice margin (Cabedo-Sanz and Belt, 2016) and relatively small changes in the position of the winter and summer sea ice edge during 41-ka climate cycles, potentially as a result of less extreme climate variability (Figure 6.13).

At ~1000 ka, an increase in IP₂₅ and HBI III, together with a shift to a statistically significant in-phase relationship between these two biomarkers (Figure 6.11), indicates a return to a more fluctuating sea ice margin (Cabedo-Sanz and Belt, 2016), and the onset of an interim state in sea ice dynamics. This is accompanied by a pronounced increase in the mean abundance of sea ice related diatoms at Site U1343 (Figure 6.13) (Teraishi et al., 2016), in line with the increase in IP₂₅ indicating a larger sea ice extent. Highest HBI III concentrations within the entire record (Figure 6.13) indicate that MIZ conditions likely prevailed close to Site U1343. Additionally, the temporal profile of sea ice increase across glacial periods changes during the interim state, such that sea ice reaches its maximum during the late-glacial/deglacial, compared to the mid-glacial IP₂₅ peaks of the early-MPT interval (1220-1000 ka) (Figure 6.13). The gradual early glacial increase in sea ice during the interim state is followed by a pronounced maximum in IP₂₅ concentration, first observed during MIS 28 (Table 4.2) (Figure 6.13). Determination of the exact duration of late-glacial/deglacial sea ice maxima is limited by variable sample resolution, although the best resolved maxima during late MIS 26/early MIS 25 (Table 4.2) has a duration of ~4.8 ka. These transient late-glacial/deglacial sea ice maxima, even though of variable resolution (one to four data points), are observed during MIS 28, 26, 24 (Table 4.2), and 12. Compared to the sea ice maxima observed across the MPT interval, however, the sea ice maximum during late MIS 12 is characterised by a prolonged period (~33 ka) of extended sea ice cover, as shown by the low MAR_{opal} values (Figure 6.13). This potentially points towards an intensification of late-glacial/deglacial sea ice maxima between the MPT G/IG cycles and the quasi-100 ka cycles of the late Pleistocene, though a continuous sea ice record, spanning at least the last 1500 ka, is needed, to confirm this suggestion. Nevertheless, in support of this interpretation, it has been reported previously that perennial sea ice dominated the western Bering Sea (Méheust et al., 2016) the Umnak Plateau (Caissie et al., 2010), and the subarctic North Pacific (Méheust et al., 2018) (Figure 6.12) until ~15 ka across Termination I, with ice free

conditions not reached until ~11 ka (Figure 6.12). This is additionally corroborated by the sea ice record at Site U1343 suggesting increased sea ice extent until ~15.4 ka in the eastern Bering Sea. Studies from other marginal seas, such as the Barents Sea, the Fram Strait, and the Nordic Seas, also confirm the presence of an extensive sea ice cover during Termination I (Aagaard-Sørensen et al., 2010, Müller and Stein, 2014, Hoff et al., 2016), suggesting that this could be a common feature of late Pleistocene climate cycles.

In addition to IP₂₅ and HBI III a third biomarker, brassicasterol (24-methylcholesta-5,22E-dien-3 β -ol), was measured, which has a variety of sources, including marine and lacustrine phytoplankton (Goad and Withers, 1982, Gladu et al., 1990, Volkman, 2006, Belt et al., 2013) and potentially even sea ice algae (Belt et al., 2013). As such, brassicasterol is used to investigate the importance of sea ice for phytoplankton growth in the eastern Bering Sea and, indeed, a weak positive relationship ($R^2 = 0.56$ [0.16; 0.81], $n = 32$) is found between IP₂₅ and brassicasterol (Figure 6.5) from 1530-1360 ka. This likely reflects production of brassicasterol by sea ice algae or phytoplankton stimulated by nutrient release during spring sea ice melting (Wang et al., 2014). From at least ~1000 ka onwards, however, brassicasterol and IP₂₅ are de-coupled (~1000-800 ka: $R^2 = 0.09$ [-0.26; 0.43], $n = 52$; ~500-340 ka: $R^2 = -0.08$ [-0.60; 0.48], $n = 32$) (Figure 6.5), which is suggestive of additional sources for brassicasterol (e.g. possibly from non-biogenic entrainment in sea ice) and/or other mechanisms potentially becoming more important for nutrient supply to the surface ocean at the eastern Bering Sea slope. Possible mechanisms include changes in the ocean stratification/vertical mixing and/or changes in the inflow of nutrient-rich Pacific waters, specifically the Alaskan Stream (Mordy et al., 2005). The abundance of the diatom species *N. seminae* (Teraishi et al., 2016), shows a pronounced decrease in the mean percentage in Site U1343 at the end of the interim state 950 ka (Figure 6.13). This suggests that mid-to-late Pleistocene glacial periods (at least) are characterised by decreased influence of North Pacific waters at the core Site as a result of glacial sea level lowstands (Teraishi et al., 2016). With respect to nutrient transport to the surface ocean along the Bering Sea slope, this indicates that upwelling of nutrient-rich waters via deep-reaching eddies (Mizobata and Saitoh, 2004) potentially played the most important role for nutrient supply and phytoplankton growth from at least 950 ka onwards.

The continued inflow of North Pacific waters (as indicated by *N. seminae* (Figure 6.13)) into the southern Bering Sea during the interim state (1000-950 ka) is consistent with the in-phase relationship between IP₂₅ and HBI III (Figure 6.11), suggesting smaller variations in the position of the summer and winter sea ice margin. Even though regional climate cooling in the North Pacific from ~1150 ka (see below) promoted an increase in the eastern Bering Sea seasonal sea ice cover, as seen by increased IP₂₅ concentrations, the continued inflow of North Pacific waters could have counteracted an extensive seasonal expansion of sea ice and resulted in the observed fluctuating sea ice margin at Site U1343 across the interim state. Concomitant with the decrease in Alaskan Stream inflow at 950 ka, as suggested by the abundance of *N. seminae* in U1343 (Figure 6.13), the correlation of HBI III and IP₂₅ shifts (Figure 6.11) to one that is more indicative of a pronounced seasonal cycle in the position of the winter and summer sea ice margin.

The onset of the mid-to-late Pleistocene interval (950-800 ka, 500-340 ka), beginning at MIS 25 (Table 4.2), is characterised by an ice free eastern Bering Sea (Figure 6.13), as shown by absent IP₂₅, low HBI III, and high MAR_{opal}. Temporal IP₂₅ variability across G/IG cycles is similar to that of the interim state with higher IP₂₅ concentration indicative of increased sea ice cover during the late-glacial/deglacial. Exceptionally, MIS 22 (Table 4.2) is characterised by lower IP₂₅ values compared to the three preceding glacial periods, apart from one sample indicating extended sea ice cover along the eastern Bering slope (Figure 6.13). However, a consistently low MAR_{opal} between MIS 23 and late MIS 21 (Table 4.2) suggest a persistent seasonal/extended sea ice cover during this time interval, which may explain the relatively lower IP₂₅ content during MIS 22 (Table 4.2) (Figure 6.13).

Overall, the data suggest a twofold change in sea ice dynamics across the MPT with an increase in sea ice extent from ~1150 ka accompanied by a change in the timing of glacial sea ice increase at ~1000 ka. From 1220-1000 ka sea ice maxima are encountered during mid-glacials (Figure 6.13), whereas the studied glacial periods post ~1000 ka show distinct sea ice maxima during the late-glacial/deglacial (Figure 6.13), with the exception of MIS 22 (Table 4.2).

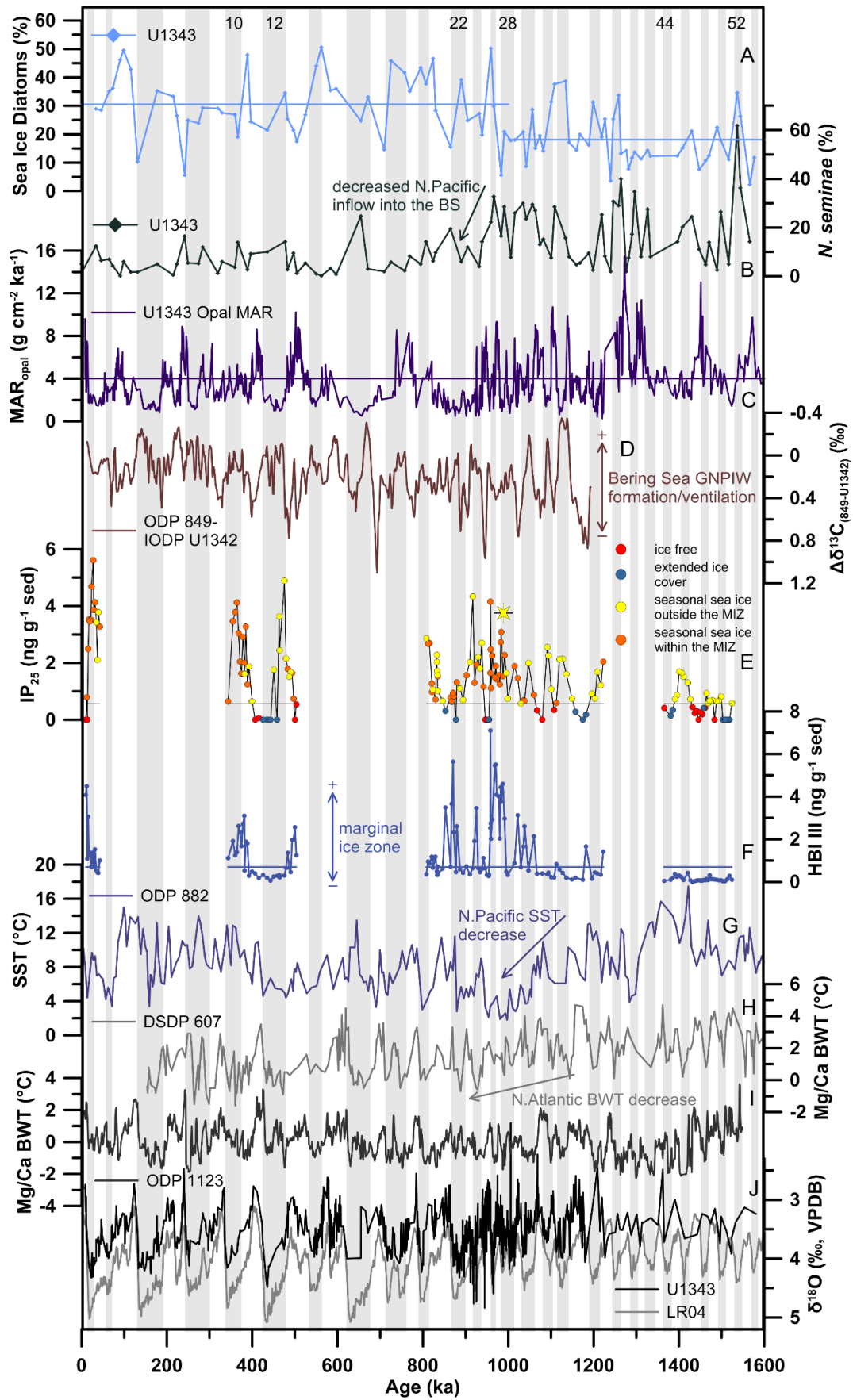


Figure 6.13 Overview of regional and global climate records across the Pleistocene. (A) Abundance of sea ice diatoms in Site U1343 (Teraishi et al., 2016) (light blue) together with the mean values pre and post 1000 ka. (B) Abundance of *N. seminae* in sediments of Site U1343 (Teraishi et al., 2016) (dark green). (C) Site U1343 mass accumulation rate of biogenic opal (Kim et al., 2014) (MAR_{opal}) (purple). (D) $\Delta\delta^{13}C_{(849-U1342)}$ (Knudson and Ravelo, 2015b) indicative of NPIW ventilation/formation (brown). (E) Site U1343 IP_{25} record (this study), colour-coded according to the predominant sea ice regime (red: ice free, blue: extended ice cover, orange: seasonal sea ice within the MIZ, yellow: seasonal sea ice outside the MIZ). The IP_{25} peak labelled with an asterisk denotes the first glacial interval (MIS 28) characterised by a late glacial/deglacial sea ice maximum. (F) Site U1343 HBI III (blue) record (this study). (G) Alkenone-based North Pacific SSTs ODP Site 882 (Martínez-García et al., 2010) (light purple). (H) BWT in DSDP Site 607 (Sosdian and Rosenthal, 2009) in the North Atlantic (light grey). (I) BWT in ODP Site 1123 (Elderfield et al., 2012) in the southwest Pacific (dark grey). (J) Site U1343 $\delta^{18}O_b$ record (Asahi et al., 2016) (black) together with the global $\delta^{18}O_b$ stack (grey) (LR04) (Lisiecki and Raymo, 2005). The horizontal lines in the MAR_{opal} , IP_{25} , and HBI III records indicate the threshold values for interpreting the sea ice scenarios (as indicated in Table 2). Grey bars indicate glacial intervals, white bars represent interglacials (numbers at the top correspond to MIS, MIS boundaries from Lisiecki and Raymo (2005)).

As previously shown by Gildor and Tziperman (2001), extensive sea ice cover during glacial terminations negatively impacts snow accumulation on continental glaciers via the temperature-precipitation feedback, limiting evaporation from the polar ocean, and via the diversion of the winter storm tracks. Model results suggest a sea ice versus land ice hysteresis with a deglacial sea ice spike of 5-10 ka (Sayag et al., 2004), which is of slightly longer duration than the best resolved sea ice maximum during the MIS 25/24 transition (Table 4.2) (~4.8 ka) recorded at Site U1343 (Figure 6.13, Figure 6.9). Where observed, the transient sea ice maxima are concomitant with deglaciations (Figure 6.13), as determined from $\delta^{18}O_b$, suggesting that sea ice likely aids in the initiation of major terminations. Furthermore, the overall increase in sea ice extent across the MPT is in accordance with outcomes from a recent modelling study (Lee et al., 2017), which indicates that a cooler climate results in larger sea ice extent and an asymmetric sea ice response between hemispheres, leading to 100-ka G/IG cycles (Lee et al., 2017). However, since there are, as yet, no Antarctic sea ice records available for the MPT, I cannot directly assess the interhemispheric relationship of sea ice growth. Nevertheless, proxy data across the MPT demonstrates a sea ice/land ice hysteresis as predicted by the SIS hypothesis (Gildor and Tziperman, 2001, Tziperman and Gildor, 2003, Sayag et al., 2004). Thus, despite its variable temporal resolution, the sea ice reconstruction from Site U1343 highlights the potential for MPT sea ice change to influence the timing and shape of late Pleistocene climate cycles. This is not only important with respect to understanding long-term sea ice and G/IG dynamics,

but also offers the opportunity for improving proxy-model comparisons aimed at assessing the role of sea ice on climate change. Still, further studies from different regions and of even higher resolution are needed, to confirm the presence and duration of sea ice maxima in the Arctic marginal seas across late-glacials/deglacials during late Pleistocene G/IG cycles.

6.4.4.1 Mechanisms for Mid-Pleistocene sea ice change

The SIS hypothesis invokes a long-term deep ocean cooling, associated with increased polar ocean stratification and changes in the surface ocean heat capacity as a possible cause for sea ice changes across the MPT (Tziperman and Gildor, 2003). To date, three orbitally-resolved bottom water temperature (BWT) records exist across the MPT; two from Deep Sea Drilling Project (DSDP) Site 607 in the North Atlantic (Sosdian and Rosenthal, 2009, Ford et al., 2016) and another from Ocean Drilling Program (ODP) Site 1123 in the South Pacific (Elderfield et al., 2012) (Figure 6.13). As discussed in Chapter 4 both records show divergent trends in the BWT history. North Atlantic DSDP Site 607 demonstrates a prominent decline in BWT between ~1150 ka and 850 ka (Sosdian and Rosenthal, 2009, Ford et al., 2016), in line with the SIS hypothesis. ODP Site 1123, on the other hand, shows no evidence for a long-term cooling across the MPT (Elderfield et al., 2012), indicating that there are pronounced regional differences in BWT history across the MPT unlikely to cause global changes in sea ice dynamics.

The low resolution BWT record at Site U1343 indicates warming across the early MPT (until MIS 22) and cooling throughout the late Pleistocene (Figure 4.9). However, there is no evidence for BWT cooling at MIS 28 (Table 4.2), the onset of the interim state in Bering Sea sea ice dynamics. Thus, enhanced polar ocean stratification driven by homogenous water column cooling and resulting increased salinity stratification (Sigman et al., 2004), likely did not cause the initial increase in the Bering Sea sea ice extent, even though it may have played a role for late Pleistocene climate cycles, where a long-term BWT cooling is observed (Figure 4.9) in conjunction with increased IP₂₅ concentrations (Figure 6.13). Another potential mechanism driving vertical water column mixing in the eastern Bering Sea today are mesoscale eddies, forming along the shelf break. Eddy formation is correlated to the strength of the Bering Slope Current (Mizobata and Saitoh, 2004), which in turn is related to Alaskan Stream inflow

into the Bering Sea. Decreased Alaskan Stream inflow during glacial intervals from 950 ka (Teraishi et al., 2016) (Figure 6.13), could have limited eddy formation, as a result of less vigorous surface ocean circulation, promoting a more stratified water column. Sea ice extent in the eastern Bering Sea, however, increases prior to 950 ka, indicating that circulation-driven changes in the vertical mixing are likely not the primary cause for changes in the MPT sea ice dynamics. This is further supported by a record of nitrogen isotopes at IODP Site U1342 suggesting enhanced stratification of the Bering Sea water column throughout all glacial intervals of the last 1200 ka, with no pronounced change observed at MIS 28 (Knudson and Ravelo, 2015a).

Instead, changes in sea ice dynamics in the Bering Sea across the MPT are accompanied by regional climate cooling as observed in North Pacific SST records (Martínez-García et al., 2010) and from regional glacier advances (Bintanja and van de Wal, 2008b). Bintanja and van de Wal (2008b) modelled ice volume in the northern hemisphere over the past 3000 ka. The model results show that the North American Ice Sheet started to advance at ~1000 ka during MIS 28 coeval with the onset of deglacial sea ice maxima, potentially as a result of strengthened Walker Circulation and increased moisture transport to high latitudes (McClymont and Rosell-Melé, 2005). During MIS 26 (Table 4.2) when the first severe deglacial sea ice spike is observed the Cordilleran and Laurentide ice sheet merged for the first time (Bintanja and van de Wal, 2008b) (Figure 6.13). Largest ice volume increase in their model, however, did not occur until 900 ka in consensus with reconstructions of the oxygen isotope composition of seawater ($\delta^{18}\text{O}_w$) (Elderfield et al., 2012). Further, the increase in sea ice extent in the Bering Sea is consistent with a long-term decrease of North Pacific SSTs (ODP Site 882 (Martínez-García et al., 2010, McClymont et al., 2013), Figure 6.13) as a result of the progressive expansion of North Pacific polar water masses from ~1150 ka (McClymont et al., 2008). Long-term North Pacific SST cooling intensified around 1100 ka with lowest SSTs coinciding with the sea ice interim state (1000-950 ka) (Figure 6.13). A subsequent increase in North Pacific SSTs between 950-850 ka has been attributed to a northward movement of the North Pacific Polar Front (McClymont et al., 2008). However, MIS 12, MIS 10, and MIS 2 show increased sea ice extent at Site U1343 (Figure 6.13) even though SSTs from Site 882 remain high from ~850 ka onwards and increase even further from ~500 ka (Figure 6.13) (Martínez-García et al., 2010). This indicates that the northward shift of the

North Pacific Polar Front did not propagate into the Bering Sea as sea ice duration and extent increase throughout the late Pleistocene interval. The increase in sea ice extent in the Bering Sea thus paralleled North Pacific SST decrease and regional glacier advances in association with changes in the atmospheric circulation pattern, suggesting a response to global climate change.

6.4.4.2 The influence of Bering Sea sea ice on intermediate water formation

Finally, the importance of Mid-Pleistocene sea ice extent in the eastern Bering Sea for glacial NPIW formation is examined. The difference between benthic foraminiferal carbon isotopes ($\delta^{13}\text{C}$) recorded at ODP Site 849 (Mix et al., 1995) ($0^{\circ}11.0'\text{N}$, $110^{\circ}31.1'\text{W}$; 3851 m) and IODP Site U1342, $\Delta\delta^{13}\text{C}_{(849-U1342)}$, is used as a proxy for Bering Sea glacial NPIW formation/ventilation as proposed by Knudson and Ravelo (2015b) (Figure 6.13). Specifically, since the Site 849 $\delta^{13}\text{C}$ is believed to approximate global oceanic dissolved inorganic carbon ($\delta^{13}\text{C}_{\text{DIC}}$) values (Mix et al., 1995), subtraction of site-specific $\delta^{13}\text{C}$ values enables local influences to be determined (Knudson and Ravelo, 2015b). Site U1342 is located in the southern Bering Sea on the Bowers Ridge and lies just below the modern depth of NPIW (300-800 m (Max et al., 2017)) at 818 m water depth. At modern times, Site U1342 is bathed in NPDW with very low $\delta^{13}\text{C}_{\text{DIC}}$ (Knudson and Ravelo, 2015b). During glacial periods, however, NPIW was, at least partly, formed in the Bering Sea and reached down to the seafloor (at U1342), transporting high $\delta^{13}\text{C}_{\text{DIC}}$ surface waters to greater depth (Knudson and Ravelo, 2015b). Thus high (low) $\Delta\delta^{13}\text{C}_{(849-U1342)}$ represents reduced (enhanced) NPIW influence at Site U1342 (Figure 6.13). U1343 IP_{25} and $\Delta\delta^{13}\text{C}_{(849-U1342)}$ are inversely correlated ($R^2 = -0.29$ [-0.46; -0.10], $n = 118$) (Figure 6.14), supporting a role of sea ice extent in the eastern Bering Sea for NPIW formation via brine rejection, which is consistent with previous studies, indicating intermediate water formation in the Bering Sea (Horikawa et al., 2010, Rella et al., 2012, Max et al., 2017). Additionally, U/Mn of authigenic foraminiferal coatings at Site U1343 suggest better ventilated deep waters (~ 2000 m) from MIS 28 (Table 4.2) and throughout most MPT glacial intervals (Figure 5.9).

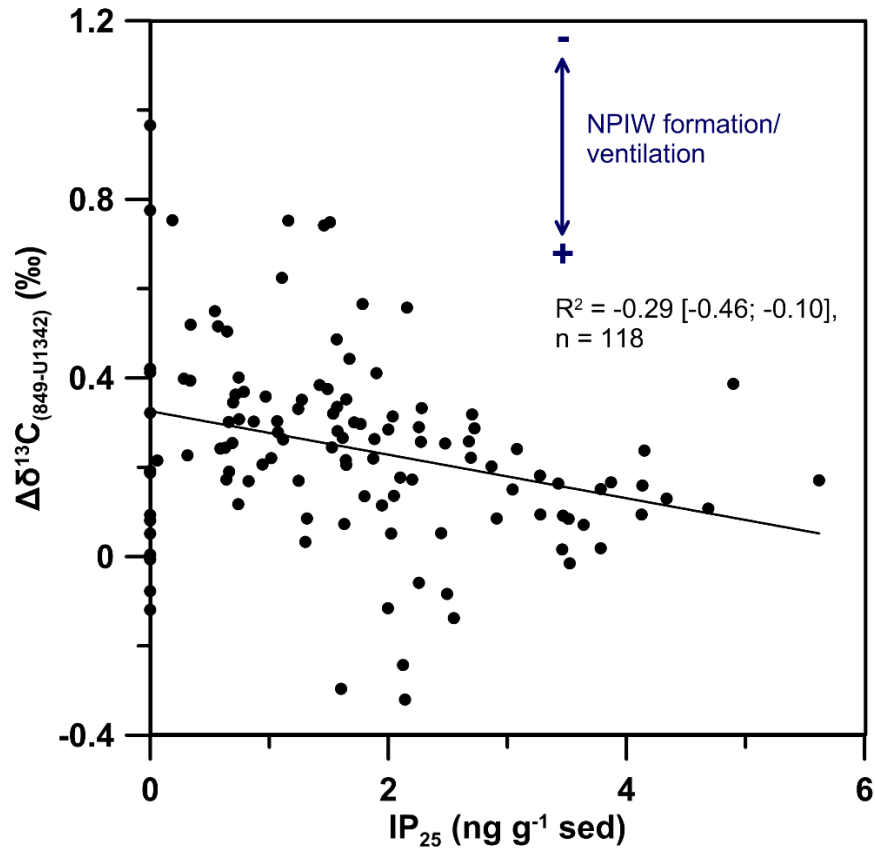


Figure 6.14 Cross plot of IP₂₅ from Site U1343 versus Δδ¹³C_(849-U1342) (Knudson and Ravelo, 2015b) a proxy for intermediate water ventilation at Site U1342 (~800 m water depth), including the Pearson r correlation coefficient and the linear regression (grey). Δδ¹³C_(849-U1342) has been re-sampled at the same age points as the U1343 IP₂₅ record, using AnalySeries 2.0.8 (Paillard et al., 1996).

MIS 28 represents the onset of the interim state in sea ice dynamics and is marked by the first prominent deglacial sea ice spike (Figure 6.13), suggesting that enhanced sea ice formation caused a greater penetration of well-ventilated intermediate waters in the Bering Sea since the MPT. Increased sea ice cover during glacials and greater penetration of intermediate waters potentially has important implications for the ocean/atmosphere gas exchange. Presently, deep reaching eddies bring high-CO₂ NPDW to the surface ocean along the eastern Bering slope (Mizobata and Saitoh, 2004), resulting in occasional CO₂ outgassing (Kelley et al., 1971). It is possible that increased sea ice extent in the Bering Sea during late and post-MPT glacial periods aided glacial atmospheric CO₂ drawdown via two mechanisms. First, by carbon sequestration during the formation of NPIW and by reducing the amount of upwelled NPDW through greater penetration of NPIW (Kender et al., in review), and second, by reducing CO₂ outgassing by acting as a physical barrier. Increased sea ice extent in

the Bering Sea across the mid Pleistocene thus has the potential to aid in increased glacial abyssal North Pacific carbon storage, as proposed by studies from Site 882 during the late Pleistocene (Jaccard et al., 2005, Galbraith et al., 2007, Jaccard et al., 2009). Future work should focus on reconstructing the depth of glacial NPIW throughout the North Pacific realm across the late Pleistocene and its ability for carbon sequestration, as this would likely have been influenced by the amount of brine formation and thus sea ice dynamics.

6.5 Conclusions

In summary, the sea ice reconstructions across four intervals covering the Mid- to late Pleistocene at IODP Site U1343 in the Bering Sea show pronounced G/IG variability during both 41-ka and 100-ka climate cycles. Furthermore, fundamental changes in sea ice dynamics are observed associated with the MPT.

The LGM-Holocene, in conjunction with additional high-resolution studies of sea ice dynamics from across the Bering Sea and the North Pacific (Katsuki et al., 2003, Katsuki and Takahashi, 2005, Cook et al., 2005, Caissie et al., 2010, Max et al., 2012, Méheust et al., 2016, Méheust et al., 2018), suggests extended seasonal sea ice cover across the late MIS 3 and MIS 2, together with pronounced millennial-scale sea ice variability across Termination I. North Atlantic cold stadials, such as HS1 and the YD, together with the LGM are characterised by increased sea ice extent in the Bering Sea (Figure 6.15), whereas warm intervals, like the B/A and early Holocene are marked by ice free conditions (Figure 6.15). This suggests in-phase deglacial climate change in the Bering Sea with North Atlantic millennial-scale events, likely resulting from atmospheric teleconnections (Manabe and Stouffer, 1988, Okumura et al., 2009).

Furthermore, a twofold change in sea ice dynamics is observed across the MPT (Figure 6.13, Figure 6.15). The early-mid Pleistocene (1220-1000 ka) is characterised by a fluctuating sea ice margin around the eastern Bering slope during glacial intervals and predominantly ice free conditions during interglacials (Figure 6.15). Around 1000 ka there is a prominent increase in the IP₂₅ and HBI III concentrations at Site U1343, indicating a prolonged seasonal sea ice extent during both glacial and interglacials and a fluctuating sea ice margin until ~950 ka (Figure 6.15), likely influenced by the inflow of relatively warm and salty Alaskan Stream waters into the southern Bering Sea

(Figure 6.13). Since ~950 ka the Bering Sea has been dominated by a pronounced seasonal advance and retreat of the sea ice margin (Figure 6.15) and restricted Alaskan Stream inflow, at least during glacial intervals (Figure 6.13). This sea ice evolution is supported by studies of diatom assemblages (Teraishi et al., 2016, Stroynowski et al., 2017) in the eastern Bering Sea (Figure 6.13).

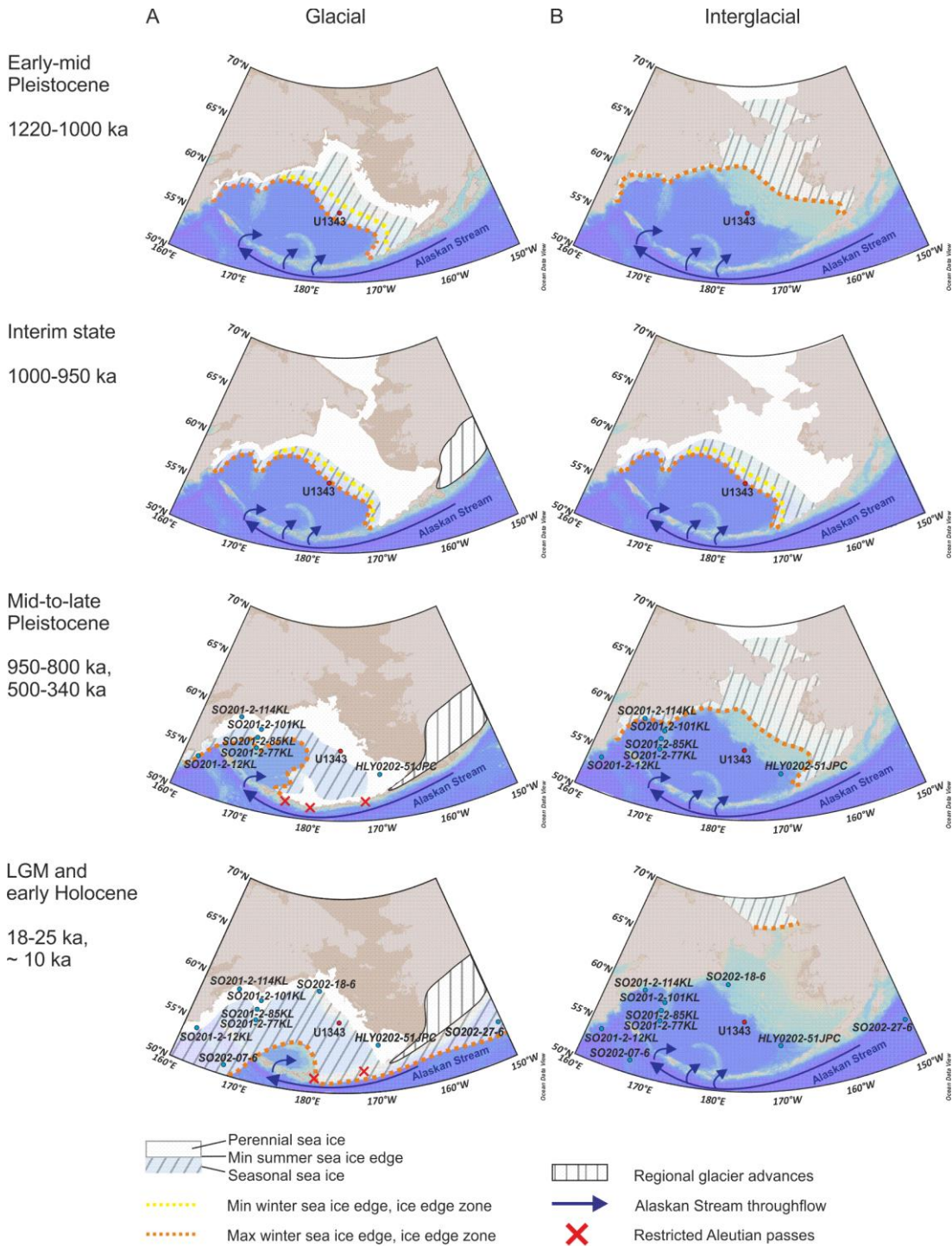


Figure 6.15 Simplified schematic overview of sea ice change in the Bering Sea across the mid-to-late Pleistocene showing the sea ice dynamics across the four intervals identified as the early-mid Pleistocene (1220-1000 ka), an interim state (1000-950 ka), the mid-to-late Pleistocene (950-800 ka and 500-300 ka), and the LGM (25-18 ka) and the early Holocene (~10 ka). (A) Sea ice dynamics across glacial intervals of the respective time period. (B) Sea ice dynamics across interglacial intervals of the respective time period. Maps were created using Ocean Data View (Schlitzer, 2011). Glacial sea level is based on $\delta^{18}\text{O}_w$ from DSDP Site 607 (Sosdian and Rosenthal, 2009), ODP Site 1123 (Elderfield et al., 2012), and the late Pleistocene sea level stack (Spratt and Lisiecki, 2016) with the coastline representing the average minimum sea level across all glacial intervals of that period. The mid-to-late Pleistocene glacial and LGM/Holocene sea ice schematics are additionally supported by studies from the Umnak Plateau (Caissie et al., 2010), the eastern Bering Sea and across the North Pacific (Max et al., 2012, Méheust et al., 2016, Méheust et al., 2018) across Termination I (blue dots). Continental glacier advances are simplified schematics based on maximum Pleistocene glacier extent in Alaska (Kaufman and Manley, 2004).

The increase in sea ice extent around ~1000 ka is accompanied by the appearance of a consistent late-glacial/deglacial sea ice maximum in all but one studied glacial periods post ~1000 ka (Figure 6.13), as predicted by the SIS hypothesis (Gildor and Tziperman, 2001, Tziperman and Gildor, 2003, Sayag et al., 2004). On the contrary, regional and global climate records across the MPT indicate that long-term deep ocean cooling, as suggested by the SIS hypothesis (Tziperman and Gildor, 2003), was likely not the primary driver of changes in Bering Sea sea ice dynamics. Instead sea ice likely responded to regional and global climate cooling, as seen from coeval expansion of polar water masses with lower SSTs in the North Pacific (Martínez-García et al., 2010, McClymont et al., 2013), increased extent of the North American Ice Sheet (Bintanja and van de Wal, 2008a), and changes in the atmospheric circulation (McClymont and Rosell-Melé, 2005). Nonetheless, I propose that the MPT is accompanied by fundamental changes in Bering Sea sea ice dynamics, which might have played a crucial role in the timing and shape of late Pleistocene climate cycles by reducing the moisture supply to continental glaciers across the onset of deglaciations.

This study is an important step forward in understanding the role of sea ice for the MPT, but will need to be supplemented by further high-resolution (and continuous) orbitally-resolved sea ice records over the past 1500 ka to determine, the exact timing of sea ice build-up across G/IG cycles. Additionally, sea ice records from other Arctic marginal seas across the MPT should help confirm the occurrence of deglacial sea ice maxima in late-to-post MPT glacial periods and to further understand their implications. Finally, additional studies of Bering Sea surface ocean chemistry are

needed to determine the role of sea ice for CO₂ sequestration and ultimately deep ocean carbon storage via glacial NPIW formation.

7. Synthesis and outlook

7.1 Diagenetic alterations of foraminifera underlying the high-productivity region of the Green Belt in the eastern Bering Sea – challenges and opportunities

The primary goal of Chapter 3 was to explore the trace metal composition and spatial variability of foraminiferal authigenic carbonates in continental margin sediments underlying the high productivity area of the eastern Bering Sea slope and to examine the potential of carbonate proxies for paleoclimate reconstructions. Continental margins are often characterised by very high sedimentation rates, representing ideal climate archives to study past climate change at an orbital to sub-orbital resolution. Over the last decades the trace metal and isotopic composition of calcareous foraminifera have become one of the most important means to reconstruct a large variety of different environmental conditions, such as temperature, continental ice volume, water mass changes, and carbonate system parameters. However, application in continental margin settings is limited due to abundant microbial activity in the sediments, resulting from enhanced primary productivity in the surface ocean and sedimentary carbon burial, impacting the preservation of calcareous foraminifera. Thus, a comprehensive understanding and characterisation of the influence of post-depositional processes on the foraminiferal geochemistry, has never been more important.

The eastern Bering Sea continental margin is characterised by abundant methane of biogenic origin with a modern Sulphate-Methane Transition Zone (SMTZ) at ~8 meters below seafloor (mbsf) at International Ocean Discovery Program (IODP) Site U1343 (Wehrmann et al., 2011). Above the SMTZ organoclastic sulphate reduction takes place (Wehrmann et al., 2011), with both anaerobic oxidation of methane (AOM) within the SMTZ and organoclastic sulphate reduction raising the pore water alkalinity by producing HCO_3^- (Boetius et al., 2000, Hinrichs and Boetius, 2003, Treude et al., 2005, Wehrmann et al., 2011). Increased pore water alkalinity can lead to the formation of authigenic carbonates, with foraminiferal tests acting as a template for authigenic carbonate precipitation.

Detailed single specimen imaging and chemical analyses revealed that authigenic carbonates can form crusts on the inside and/or outside of foraminiferal tests. Further, complete and partial recrystallization of foraminiferal test walls can be observed. Recrystallization is likely initiated along lines of weakness within the foraminiferal tests, where pore waters may enter, as seen from foraminiferal cross sections with authigenic carbonate banding associated with the primary foraminiferal carbonate layers.

Geochemical analyses demonstrate that high-Mg calcite (HMC) and low-Mg calcite (LMC) are the main contamination phases in foraminifera at IODP Site U1343, in line with studies of authigenic carbonate crystals demonstrating the presence of HMC, LMC, dolomite and Fe-carbonates (Pierre et al., 2016). Dolomite and Fe-carbonate crystals, however, form in a deeper zone of carbonate diagenesis at ~260 mbsf (Pierre et al., 2016) with no pronounced change in foraminiferal geochemistry observed across this zone. Trace metal ratios of diagenetically altered foraminifera from above and below the modern SMTZ suggest that LMC precipitates on foraminifera above the SMTZ, likely as a result of the inhibiting effect of dissolved sulphate on Mg incorporation into carbonates (Walter, 1986), whilst HMC with varying amounts of Mg represents the main contamination phase in foraminifera below the SMTZ. Additionally, the geochemical analyses demonstrate that authigenic carbonates are enriched in Sr, Fe, U, and Mn.

To date two main approaches exist to correct for foraminiferal contamination in paleoceanographic studies, in particular Mg/Ca for temperature reconstructions. The first one relies on constant Mg/metal ratios (Hasenfratz et al., 2017a), whilst the second one utilises the molar ratio of Mg/Ca and a trace metal primarily associated with the contamination phase to subtract the Mg stemming from the contaminant (Lea et al., 2005). Out of the trace metals enriched in foraminiferal authigenic carbonates, U is the most suitable to correct for authigenic carbonates in paleoceanographic studies, such as foraminiferal Mg/Ca for temperature reconstructions. Compared to Mn and Fe, U is only marginally influenced by other potential contamination phases, such as Mn-Fe-oxides and pyrite and is much more enriched in authigenic carbonates compared to Sr. However, as a result of the dynamic nature of the redox regime along the eastern Bering Sea slope, Mg/U ratios of diagenetically altered foraminifera are highly variable, indicating that the first approach is not feasible at IODP Site U1343.

The second approach uses the molar ratio of Mg/Ca to U/Ca derived from the slope of the regression to correct for Mg/Ca associated with the contamination phase (Lea et al., 2005). The regression of U/Ca versus Mg/Ca of diagenetically altered foraminifera at Site U1343 is best described by an exponential function, however, samples with high Mg/Ca and U/Ca seem to be less well represented by this regression, resulting in unrealistically high corrected Mg/Ca ratios. This indicates that this correction could be utilised for foraminifera with moderate but not major diagenetic alteration.

Thus, paleoceanographic studies utilising primary foraminiferal trace metal ratios from continental margin settings underlying high primary productivity zones and those characterised by abundant microbial activity related to methane cycling in the pore waters, should establish thresholds of trace metals primarily associated with the authigenic carbonates. At IODP Site U1343 a threshold of U/Ca represents the best approach to minimise the influence of authigenic carbonates on measured foraminiferal metal/Ca ratios. However, the threshold is likely to vary based on the study region, including different redox chemical settings, the analytical instruments, and the sample preparation techniques used.

Nevertheless, authigenic carbonates also offer unique opportunities to study environmental change through time using new approaches. Authigenic foraminiferal U/Mn has been proposed to record changes in the sedimentary redox chemistry, linked to bottom water oxygenation and sedimentary carbon burial (Gottschalk et al., 2016, Chen et al., 2017). A proportionally larger incorporation of U compared to Mn in authigenic carbonate at IODP Site U1343 with a higher degree of diagenetic alteration, suggests an increase in the U/Mn ratio associated with stronger microbial activity and more reducing conditions in the sediment. Application of this proxy offers qualitative tool to reconstruct past changes in sedimentary redox chemistry. Together with proxies of primary productivity this allows to make inferences regarding deep ocean carbon storage, water mass changes, and/or oxygen minimum zone (OMZ) dynamics depending on the study area.

7.2 Last glacial maximum to Holocene climate change in the eastern Bering Sea – records of bottom water temperature, oxygenation, and sea ice

The last glacial maximum (LGM) to Holocene transition is marked by pronounced changes in the Bering Sea oceanography. Records of bottom water temperature (BWT) at IODP Site U1343 demonstrate a LGM-Holocene Δ BWT of 2.03 ± 0.78 °C (standard error (s.e.)) (Figure 7.1), similar to other records from across the Pacific between 800-3500 m water depth suggesting a Δ BWT of 1-3°C (Shackleton, 2000, Waelbroeck et al., 2002, Gorbarenko et al., 2002, Martin et al., 2002, Elderfield et al., 2010, Woodard et al., 2014, Knudson and Ravelo, 2015b, McClymont et al., 2016). In conjunction with the published benthic foraminiferal oxygen isotope ($\delta^{18}\text{O}_b$) record at Site U1343 (Asahi et al., 2016) BWT reconstructions suggest an LGM-Holocene difference in seawater $\delta^{18}\text{O}$ ($\Delta\delta^{18}\text{O}_w$) of 0.89 ± 0.30 ‰ (s.e.), slightly smaller but within error of the proposed mean ocean $\Delta\delta^{18}\text{O}_w$ of 1.05 ± 0.2 ‰ (Duplessy et al., 2002). Taken at face value, the smaller than mean ocean $\Delta\delta^{18}\text{O}_w$ supports entrainment of North Pacific Intermediate Water (NPIW) at Site U1343. NPIW forms locally from brine rejection during sea ice freezing with minimal oxygen isotope fractionation (Knudson and Ravelo, 2015b, Cook et al., 2016). Thus, NPIW is expected to carry the low $\delta^{18}\text{O}_w$ signature of subarctic surface waters to greater depth (Knudson and Ravelo, 2015b, Cook et al., 2016). Enhanced contribution of NPIW during glacial intervals of the last 1.2 Ma is observed at IODP Site U1342 in the southern Bering Sea at 800 m water depth, manifested by a negative offset of the $\delta^{18}\text{O}_b$ record from the global LR04 stack (~ 0.5 ‰ for the LGM) (Lisiecki and Raymo, 2005, Knudson and Ravelo, 2015b). Two episodes of decreased $\delta^{18}\text{O}_b$ compared to the LR04 stack (~ 0.2 ‰) are observed at IODP Site U1343 at ~ 25 ka and ~ 17.5 ka, coinciding with the LGM and Heinrich stadial 1 (HS1, ~ 18 ka to 15 ka), respectively (Figure 7.1). Whilst no BWT data is available at 25 ka, constant BWTs around 17.5 ka (Figure 7.1) support a decrease in the local $\delta^{18}\text{O}_w$, likely driven by NPIW entrainment.

This is further supported by records of sedimentary redox chemistry at Site U1343. As aforementioned, NPIW forms locally from brine rejection causing the subduction of atmospherically-equilibrated O_2 -rich waters, in line with decreased authigenic foraminiferal U/Mn ratios at 25 ka and ~ 17.5 ka, indicating less reducing conditions in the sediments. As there is no concurrent change in the primary productivity and

benthic foraminiferal assemblage data also demonstrates a decrease in the abundance of dysoxic species, increased bottom water oxygen concentrations ($[O_2]$) is inferred for 25 ka and ~17.5 ka (Figure 7.1). Hence, reconstructions of $\Delta\delta^{18}O_w$ and bottom water oxygenation in the Bering Sea across the LGM to Holocene suggest periodic entrainment of NPIW at water depth of ~2000 m, which is deeper than the previously suggested divide of well and poorly ventilated LGM water masses in the Bering Sea of ~1000 m water depth (Cook et al., 2016).

Increased formation and deepening of NPIW during the LGM and HS1 is in agreement with extended seasonal sea ice in the Bering Sea (Figure 7.1) (Katsuki and Takahashi, 2005, Caissie et al., 2010, Méheust et al., 2016, Méheust et al., 2018). Whilst the sea ice record at Site U1343 is of too low resolution to make millennial-scale inferences (Figure 7.1), comparison with other records of sea ice variability from across the Bering Sea demonstrates distinct millennial changes across the last deglaciation, with a larger sea ice extent observed during the LGM, HS1 and the Younger Dryas (YD, ~12.9-11.7 ka) (Méheust et al., 2016, Méheust et al., 2018) (Figure 7.1). Studies of Neodymium isotopes, suggest that the Bering Sea may have been the primary location of NPIW formation during the LGM and HS1 (Horikawa et al., 2010), while other studies indicate that the Sea of Okhotsk remained the primary source (Max et al., 2014, Okazaki et al., 2014). A larger sea ice extent in conjunction with enhanced ventilation at ~2000 m water depth during the LGM and HS1 supports, at least partial, NPIW formation in the Bering Sea (Figure 7.1).

Across HS1 increased ventilation of the North Pacific has been commonly reported from water depth of up to ~2000 m water depth (Duplessy et al., 1989, Ahagon et al., 2003, Sagawa and Ikehara, 2008, Okazaki et al., 2012, Rae et al., 2014, Max et al., 2014, Cook et al., 2016) with one record from the Gulf of Alaska even demonstrating decreased ventilation ages at ~3500 m water depth (Rae et al., 2014). Thus, enhanced ventilation and deepening of NPIW in the Bering Sea during HS1 is in agreement with records from across the North Pacific, suggesting increased intermediate overturning. Modelling studies propose that a slowdown in the Atlantic meridional overturning circulation (AMOC) during cold events of the last deglaciation, such as HS1 and YD (McManus et al., 2004), resulted in increased North Pacific overturning leading to a larger northward heat transport in the Pacific (Saenko et al., 2004, Okazaki et al., 2010). Even though records of $\delta^{18}O_w$ and bottom water oxygenation at IODP Site

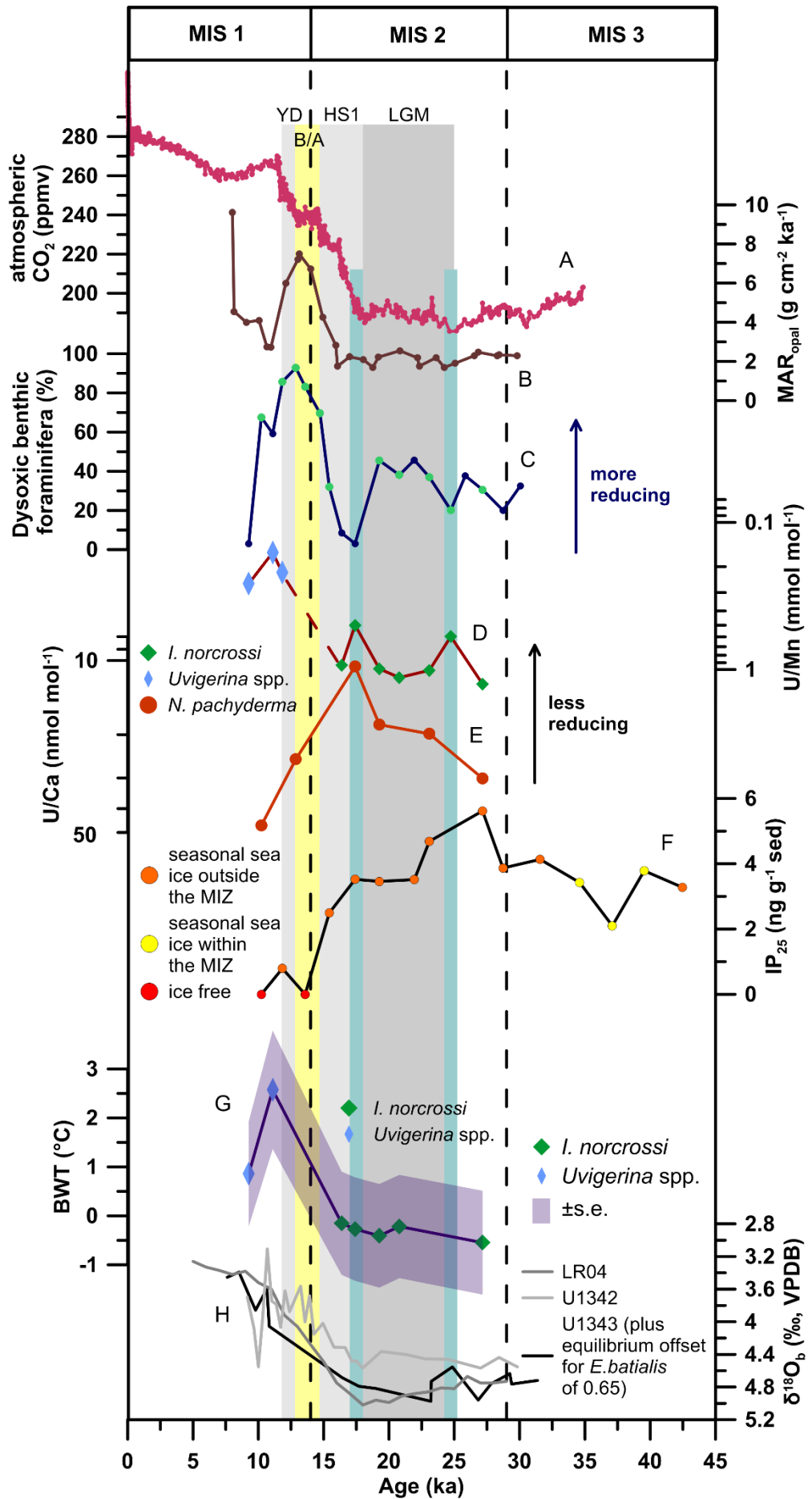


Figure 7.1 (A) Atmospheric CO₂ record from the Antarctic ice core composite (pink) across the LGM-Holocene transition (Bereiter et al., 2015). (B) The MAR_{opal} at Site U1343 (brown) indicative of first order changes in primary productivity (Kim et al., 2014). (C) The abundance of dysoxic benthic foraminiferal species (dark blue) at Site U1343 in percent. The green dots represent samples with >100 specimens picked. (D) U/Mn of *I. norcrossi* (green diamonds) and *Uvigerina* spp. (blue diamonds) across the LGM-Holocene, the deglaciation is associated with a faunal change (dashed line). Note that the axis for U/Mn is on the logarithmic scale. (E) U/Ca of *N. pachyderma* (orange) at Site U1343, higher values suggest more reducing conditions in the sediments. Note that the axis for U/Ca is on the logarithmic scale. (F) Site U1343 sea ice dynamics with data points coloured according to the predominant sea ice state (orange: seasonal sea ice within the MIZ, yellow: seasonal sea ice outside the MIZ, red: ice free). (G) BWT at IODP Site U1343 (purple) across Termination I based on *I. norcrossi* (green diamonds) and *Uvigerina* spp. (blue diamonds) Mg/Ca ratios including the \pm s.e. envelope (light purple). (H) $\delta^{18}\text{O}_b$ records from U1343 adjusted for the *E. batialis* equilibrium offset (+0.65 ‰) (black) (Asahi et al., 2016) and U1342 (light grey) (Knudson and Ravelo, 2015b) together with the LR04 stack (middle grey) (Lisiecki and Raymo, 2005). The dark grey bar represents the LGM (18-25 ka), the light grey vertical bars represent the Heinrich stadial 1 (~14.7-18 ka) and the Younger Dryas (~12.9-11.7 ka), while the yellow vertical bar represents the Bølling-Allerød (~12.7 ka to 14.7 ka). The dashed vertical lines represent the MIS boundaries and numbers at the top correspond to the respective MIS (MIS boundaries from (Lisiecki and Raymo, 2005)). The blue vertical bars indicate intervals across MIS 2 where NPIW incursion likely occurred at ~2000 m water depth in the eastern Bering Sea.

U1343 support increased intermediate water formation during HS1, the large extent of sea ice across HS1 and the YD observed in records from around the Bering Sea and the North Pacific (Caissie et al., 2010, Méheust et al., 2016, Méheust et al., 2018) contradicts enhanced Pacific northward heat transport.

Additionally, a greater sea ice extent together with enhanced vertical mixing during HS1 in the Bering Sea and the North Pacific (Méheust et al., 2016, Méheust et al., 2018) may be able to explain the mismatch between decreased nutrient utilisation first observed in records of nitrogen isotopes ($\delta^{15}\text{N}$) around 17.5 ka (Brunelle et al., 2007, Brunelle et al., 2010, Pelto et al., 2018) and increased primary productivity, not observed until ~15-16 ka (Jaccard et al., 2005, Brunelle et al., 2007, Galbraith et al., 2007, Jaccard et al., 2009, Brunelle et al., 2010, Kohfeld and Chase, 2011, Max et al., 2012, Pelto et al., 2018). Greater nutrient utilisation during the LGM in the Bering Sea and the North Pacific likely results from stronger stratification of the subpolar water column due to homogenous cooling, supported by BWTs at Site U1343 (Figure 7.1). BWTs, however, do not increase until after ~16.4 ka, proposing that BWT warming was likely not the main driver of increased vertical mixing and nutrient supply to the surface ocean during HS1. Instead, increased NPIW formation could have resulted in a weakening of stratification and improved vertical mixing. Stronger vertical mixing

could have enhanced the supply of nutrients to the surface ocean, as indicated by decreased nutrient utilisation (Brunelle et al., 2007, Brunelle et al., 2010), while the large sea ice extent in the Bering Sea and the eastern and western North Pacific observed until ~15 ka (Caissie et al., 2010, Méheust et al., 2016, Méheust et al., 2018) (Figure 7.1) effectively limited the regional primary productivity due to reduced light availability. However, other possible explanations for the mismatch in $\delta^{15}\text{N}$ and primary productivity across the LGM-Holocene transition include an early deglacial decrease in the iron-to-nitrate ratio of the surface ocean, limiting the drawdown of nitrate (Brunelle et al., 2010).

Compared to the LGM and HS1, deglacial warm phases, such as the Bølling-Allerød (B/A, ~12.7 ka to 14.7 ka) and the early Holocene are marked by a decrease in the bottom water oxygenation at Site U1343, as seen from planktonic foraminiferal U/Ca ratios and the abundance of dysoxic foraminifera (Figure 7.1). Decreased bottom water $[\text{O}_2]$ is in accordance with laminated sediments observed at intermediate-depth across the Bering Sea, including Site U1343, during the B/A and the early Holocene, suggesting OMZ expansion in conjunction with increased primary productivity (Figure 7.1) (Cook et al., 2005, Expedition 323 Scientists 2010, Caissie et al., 2010, Aiello and Ravelo, 2012, Kuehn et al., 2014, Pelto et al., 2018). Greater surface ocean productivity and warming across these intervals is in line with ice free conditions, as recorded at Site U1343 (Figure 7.1) and in the North Pacific (Méheust et al., 2018) and reduced seasonal sea ice seen in the western Bering Sea (Méheust et al., 2016, Méheust et al., 2018).

Consequently, the Bering Sea demonstrates in-phase deglacial climate oscillations with the North Atlantic, with cooling during HS1 and the YD, when the AMOC is reduced (McManus et al., 2004), and warming during the B/A and the early Holocene, supporting atmospheric teleconnections causing hemisphere-wide climate change at these times (Manabe and Stouffer, 1988, Okumura et al., 2009). Additionally, records of BWT, $\delta^{18}\text{O}_w$, and sedimentary redox chemistry at Site U1343 suggest deeper than previously reported NPIW entrainment in the Bering Sea to depth of ~2000 m coinciding with the LGM and HS1.

7.3 The Mid-Pleistocene transition from a Bering Sea perspective

The Mid-Pleistocene transition (MPT, 0.7-1.2 Ma) marks the last great transition in Quaternary climate, likely driven by changes internal to the climate system. Hence, it is ideal to study the influence of a changing climate on Earth's long-term climate dynamics, and represents a unique opportunity to investigate climate forcing mechanisms and interactions.

Our understanding of the North Pacific and its marginal seas across this crucial interval is relatively limited. Studies suggest sea surface temperature (SST) cooling associated with the early phase of the MPT (McClymont et al., 2008, Martínez-García et al., 2010), together with step-wise expansion of sea ice in the Bering Sea as seen from low-resolution records of diatom assemblages (Teraishi et al., 2016, Ikenoue et al., 2016, Stroynowski et al., 2017), indicating polar water mass expansion. Further Pleistocene glacials in the Bering Sea are characterised by enhanced ventilation of mid-depth waters and strengthened stratification of the subpolar water column (Knudson and Ravelo, 2015b, Knudson and Ravelo, 2015a). This suggests, a highly dynamic system on orbital timescales with pronounced changes observed across the Pleistocene. Records of BWT, bottom water [O₂], and sea ice dynamics at IODP Site U1343 across the MPT provide valuable insights into Bering Sea climate dynamics with important implications for the regional and potentially global climate during the Mid-Pleistocene.

Reconstructions of BWT at IODP Site U1343 demonstrate a long-term deep ocean warming between marine isotope stage (MIS) 34 and MIS 22 (866 ka to 1141 ka) (0.63 ± 1.10 °C), followed by long-term cooling between MIS 12 and MIS 22 (424 ka to 900 ka) (1.21 ± 0.63 °C) (Figure 7.2). Together with published records of $\delta^{18}\text{O}_b$ at Site U1343 (Asahi et al., 2016, Kender et al., in review) two possible scenarios for MPT continental ice volume arise.

The first scenario depicts no long-term change in continental ice volume, with a distinct hydrographical event centred on MIS 22 (Table 4.2). MIS 22 is marked by pronounced BWT warming at Site U1343, also observed on Shatsky Rise in the North Pacific (Ford and Raymo, 2017), together with a positive excursion in $\delta^{18}\text{O}_w$ (Figure 7.2). Considering, the different water masses contributing to the Bering Sea on orbital

timescales, with NPIW representing a well-ventilated, low $\delta^{18}\text{O}_w$ water mass, the observed changes across MIS 22 would likely be driven by North Pacific Deep Water (NPDW). This is in line with similar BWT warming observed at 3346 m water depth on Shatsky Rise, bathed in NPDW (Ford and Raymo, 2017). However, it is unclear what could have caused the observed fluctuations across MIS 22 (Table 4.2). BWT warming suggests a potential slowdown of the deep Pacific circulation, with a greater influence of the geothermal heat flux at the seafloor. Records of the flow speed of the Deep Western Boundary Current (DWBC) a precursor of NPDW, however, do not indicate a slowdown until after MIS 22 (Hall et al., 2001, Venuti et al., 2007). The large positive excursion in $\delta^{18}\text{O}_w$ observed during MIS 22 at both IODP Site U1343 and ODP Site 1208 on Shatsky Rise (Ford and Raymo, 2017) is also challenging to explain. Considering the different water masses that contribute to the deep Pacific today, North Atlantic Deep Water (NADW) has a higher $\delta^{18}\text{O}_w$ compared to southern sourced deep waters (LeGrande and Schmidt, 2006). However, records of Neodymium isotopes demonstrate a pronounced decrease in NADW export associated with the MPT, primarily observed across MIS 22 (Table 4.2) (Pena and Goldstein, 2014).

On the other hand, increased $\delta^{18}\text{O}_w$ could result from a pronounced increase in continental ice volume during MIS 22 as suggested by Elderfield et al. (2012). Thus, the second scenario to explain the trends in BWT and $\delta^{18}\text{O}_b$ across the MPT as seen from IODP Site U1343 infers continental ice volume increase prior to/during MIS 22 with enhanced NPIW contribution to Site U1343 during the following glacials of the late Pleistocene. This is additionally supported by some glacial intervals demonstrating a negative $\delta^{18}\text{O}_b$ offset at Site U1343 from the LR04 stack, as seen for the LGM-Holocene, suggesting NPIW entrainment.

Even though, records of BWT and $\delta^{18}\text{O}_w$ at IODP Site U1343 were unable to reconcile the different proposed continental ice volume histories across the MPT, comparison of all available records of $\delta^{18}\text{O}_w$ (Deep Sea Drilling Project (DSDP) Site 607 (Sostdian and Rosenthal, 2009, Ford et al., 2016), Ocean Drilling Program (ODP) Site 1123 (Elderfield et al., 2012), IODP Site U1343) by means of the deviation from the respective record average, highlights the 900-ka event (MIS 24 to MIS 22, 866-936 ka) as an important interval for MPT continental ice volume evolution (Figure 7.2). Starting during MIS 22 (Table 4.2) all records demonstrate consistent positive deviations from their respective average during glacials, in line with increased

continental ice volume during late Pleistocene climate cycles. Furthermore, this study emphasises the

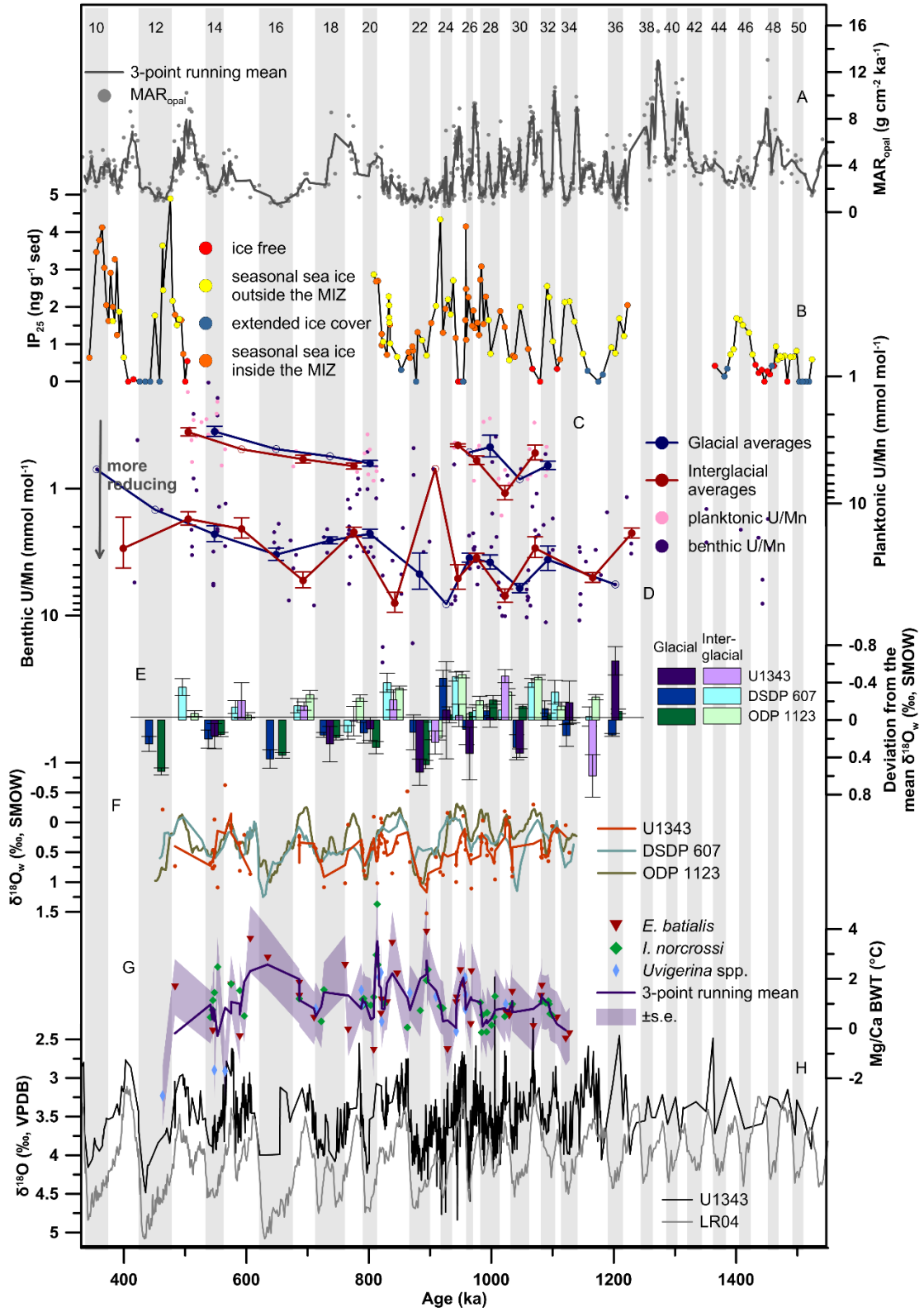


Figure 7.2 (A) MAR_{opal} (grey dots) together with the 3-point running mean (grey line) at Site U1343 (Kim et al., 2014). (B) Site U1343 IP_{25} record across the Mid-Pleistocene, colour-coded according to the predominant sea ice regime (red: ice free, blue: extended ice cover, orange: seasonal sea ice within the MIZ, yellow: seasonal sea ice outside the MIZ). (C) Planktonic U/Mn data (pink dots) across the Mid-Pleistocene together with the glacial (blue dots) and interglacial (red dots) averages. (D) Benthic U/Mn data (purple dots) across the Mid-Pleistocene together with the glacial (blue dots) and interglacial (red dots) averages. Error bars represent the s.e., open symbols indicate intervals with only one data point in both panels C and D. Note that the axes for planktonic and benthic U/Mn are on the logarithmic scale. (E) The deviation of the glacial and interglacial average of $\delta^{18}O_w$ from the respective mean at Site U1343 (dark blue, dark red), ODP Site 1123 (medium blue, orange) (Elderfield et al., 2012), and DSDP Site 607 (light blue, pink) (Sosdian and Rosenthal, 2009, Ford et al., 2016) across the Mid-Pleistocene. The error bars represent the s.e. (F) $\delta^{18}O_w$ at Site U1343 (orange dots) together with the 3-point running mean (orange line) and $\delta^{18}O_w$ at ODP Site 1123 (green) (Elderfield et al., 2012) and DSDP Site 607 (blue) (Sosdian and Rosenthal, 2009, Ford et al., 2016). (G) 3-point running mean of BWT at Site U1343 (purple) across the Mid-Pleistocene based on *E. batialis* (red triangles), *I. norcrossi* (green diamonds), and *Uvigerina* spp. (blue diamonds) including the \pm s.e. envelope (light purple). (H) $\delta^{18}O_b$ at Site U1343 (black) (Asahi et al., 2016, Kender et al., in review) together with the LR04 stack (grey) (Lisiecki and Raymo, 2005). The grey vertical bars represent glacial intervals, numbers at the top represent marine isotope stages (MIS). MIS boundaries from (Lisiecki and Raymo, 2005).

importance of regional hydrography on the $\delta^{18}O_w$ as proposed by Ford et al. (2016) and highlights the need to consider the relative changes in water mass contribution when studying $\delta^{18}O_w$ on these timescales. This calls upon additional records of $\delta^{18}O_w$ from different ocean regions across the MPT to derive a globally averaged stack, less sensitive to regional variability.

In addition to BWT, I used authigenic foraminiferal U/Mn glacial/interglacial (G/IG) averages across the MPT to explore changes in the sedimentary redox chemistry over time, linked to variability in primary productivity and bottom water $[O_2]$. Both glacials and interglacials are marked by a long-term decrease in benthic and planktonic U/Mn across the Mid-Pleistocene, suggesting progressively less reducing conditions in sediments along the eastern Bering Sea slope. While the mechanisms for less reducing conditions across interglacials are less clear and may involve changes in the accumulation of respired carbon in NPDW and/or change in the local primary productivity, the decrease in glacial benthic and planktonic U/Mn is most likely driven by enhanced contribution of NPIW to Site U1343, first observed in both planktonic and benthic foraminiferal U/Mn during MIS 28 (Table 4.2) (Figure 7.2). NPIW forms locally from atmospherically-equilibrated sea ice brines ventilating the North Pacific

at intermediate depth. Reconstructions of sea ice dynamics in the eastern Bering Sea suggest an increase in sea ice extent during MIS 28, coinciding with improved ventilation of Bering Sea deep waters, indicating that sea ice in the Bering Sea may have played a fundamental role for NPIW formation during the Mid-Pleistocene (Figure 7.2).

Thus, both sedimentary redox chemistry and sea ice extent suggest dynamic changes in the water mass contribution at Site U1343 during MIS 28, while records of BWT and $\delta^{18}\text{O}_b$ indicate potential NPIW contribution to Site U1343 following MIS 22 (Table 4.2) (Figure 7.2). However, as I am only exploring the long-term trends in BWT and $\delta^{18}\text{O}_b$ at Site U1343 prior to and following MIS 22 orbital-scale features, such as increased NPIW contribution from MIS 28 may be subdued. Strikingly, MIS 22 stands out in all records generated as part of this study. While BWTs demonstrate pronounced warming together with a positive excursion in $\delta^{18}\text{O}_w$, benthic foraminiferal authigenic U/Mn ratios during MIS 22 deviate from the long-term decrease, suggesting more reducing conditions (Figure 7.2). Additionally, MIS 22 stands out in the reconstructed sea ice dynamics by lower IP_{25} concentrations and the lack of late glacial/deglacial sea ice maximum, observed consistently from MIS 28 onwards (Figure 7.2). Thus, instead of the two proposed scenarios, it is likely that a combination of the two is needed to fully explain the paleoclimate records, highlighting the need for additional studies across this fundamental time period of Quaternary climate change to fully disentangle the influence of regional versus global climate change on BWT, sedimentary redox chemistry, and sea ice dynamics in the Bering Sea.

7.3.1 The role of sea ice for the Mid-Pleistocene transition

Modelling studies have shown that sea ice might have played a fundamental role for changes in the frequency of G/IG cycles across the MPT (Gildor and Tziperman, 2001, Tziperman and Gildor, 2003, Ashkenazy and Tziperman, 2004, Lee et al., 2017). In particular two predictions were made that can be tested using proxy methods. The first being a pronounced increase in the sea ice extent associated with the MPT and the second one is land ice sea ice hysteresis during late Pleistocene climate cycles with a large sea ice extent across deglaciations (Gildor and Tziperman, 2001, Tziperman and Gildor, 2003, Ashkenazy and Tziperman, 2004).

The results presented in this thesis support an increase in the sea ice extent in the Bering Sea across the MPT, starting during MIS 28 (Table 4.2) (Figure 7.2). This is associated with a shift in the glacial IP₂₅ maximum from mid-glacials during the early MPT towards the late glacial/early deglaciation observed during MIS 28, 26, 24 (Table 4.2), and 12 (Figure 7.2). Furthermore, IP₂₅ at Site U1343 together with additional records from across the Bering Sea suggests a deglacial sea ice peak across the LGM-Holocene transition, also observed in the Barents Sea, the Fram Strait, and the Nordic Seas (Aagaard-Sørensen et al., 2010, Müller and Stein, 2014, Hoff et al., 2016). Thus, biomarker-based reconstructions of sea ice dynamics in the Bering Sea support a fundamental role of sea ice for late Pleistocene deglaciations, likely limiting the evaporation from the surface ocean and consequently the moisture supply to continental glaciers.

In comparison to the sea ice switch (SIS) hypothesis, however, sea ice increase in the Bering Sea did not result from a long-term decrease in BWT, as the early MPT is marked by a BWT increase in the deep eastern Bering Sea (Figure 7.2). Instead, sea ice increase paralleled regional climate cooling, seen from progressive SST cooling and regional glacier advances (McClymont et al., 2008, Bintanja and van de Wal, 2008a, Martínez-García et al., 2010). Nevertheless, BWT cooling during the late Pleistocene (Figure 7.2) may have played a role in observed long-term increase in sea ice extent suggested from the increase in IP₂₅ concentrations across all four studied intervals.

Additionally, the sea ice record at Site U1343 correlates significantly with intermediate water ventilation in the southern Bering Sea at 800 m water depth (Knudson and Ravelo, 2015b). This suggests that sea ice in the Bering Sea might have played a fundamental role for intermediate water formation in the North Pacific throughout glacials of the Mid-to late Pleistocene, further highlighting the importance of sea ice dynamics in the North Pacific for MPT climate change. Kender et al. (in review) suggest that enhanced formation and deepening of NPIW in the Bering Sea during the Mid-Pleistocene may have provided a positive feedback for atmospheric CO₂ drawdown by reducing the upwelling of CO₂-rich deep waters in eddies along the eastern Bering Sea slope. This points towards an effect of sea ice for the North Pacific carbon cycle.

In conclusion, sea ice reconstructions in the Bering Sea reveal essential dynamics with respect to the MPT, advancing our understanding of the role of sea ice for climate change. Furthermore, this study emphasises the importance of sea ice for the regional climate dynamics, in particular NPIW formation in the North Pacific.

7.4 Future work

This study is a significant step forward in our understanding of North Pacific climate change across the Mid- to late Pleistocene. In particular it highlights the importance of dynamic changes in sea ice extent and NPIW formation on long-term and orbital timescales across the MPT and the LGM-Holocene. Changes in the water mass contribution to the deep Bering Sea have pivotal consequences for the $\delta^{18}\text{O}_w$, the ventilation, and potentially even bottom water temperature, emphasising the need to determine the role of NPIW for paleoclimate reconstructions. Further, this work has provided a more comprehensive understanding of the trace metal composition of authigenic carbonates resulting from AOM and organoclastic sulphate reduction. It has shown both the limits and the application of traditional paleoclimate proxies, such as Mg/Ca, in areas of intense microbially-induced authigenic carbonate formation, but also demonstrated the associated opportunities, such as authigenic U/Mn for reconstructions of sedimentary redox conditions.

Hence, future work should focus on exploring the spatial variability of NPIW across the Mid-Pleistocene to test a potential deepening of this water mass associated with the MPT, as suggested by inferences of $\delta^{18}\text{O}_w$, sedimentary redox conditions, and sea ice dynamics in the eastern Bering Sea. NPIW is characterised as a well-ventilated, low $\delta^{18}\text{O}_w$ water mass. Thus, multi-proxy reconstructions of bottom water ventilation and $\delta^{18}\text{O}_w$ from different depths across the Bering Sea, the Sea of Okhotsk, and the North Pacific could aid in deciphering both the primary source region and spatial variability of NPIW. This study uses authigenic foraminiferal U/Mn and dysoxic foraminiferal assemblages as a qualitative tool to reconstruct sedimentary redox conditions driven by bottom water $[\text{O}_2]$ and changes in the supply of organic carbon. Other, more established proxies include the analysis of bulk sedimentary redox sensitive elements (Morford and Emerson, 1999, Chase et al., 2001, Morford et al., 2007, Jaccard et al., 2009, Pattan and Pearce, 2009) and the carbon isotope gradient ($\Delta\delta^{13}\text{C}$) between epi- and infaunal benthic foraminiferal species (Hoogakker et al.,

2015, Gottschalk et al., 2016), which would allow a more quantitative reconstruction of bottom water oxygenation when combined with proxies for primary productivity. When studying $\Delta\delta^{13}\text{C}$, however, it is important to avoid areas with methane-related authigenic carbonate formation, as these are characterised by depleted $\delta^{13}\text{C}$ (Schneider et al., 2017, Panieri et al., 2017), resulting from the incorporation of methane-derived carbon, overprinting the primary foraminiferal $\delta^{13}\text{C}$ signature. This work could additionally benefit from studying G/IG cycles in carbonate preservation using an XRF core scanner (Gottschalk et al., 2018), a comparably quick analytical technique. The deep North Pacific demonstrates distinct carbonate preservation cycles with decreased CaCO_3 accumulation during glacials, likely linked to enhanced deep ocean carbon storage with more corrosive bottom waters (Haug et al., 1995, Jaccard et al., 2005, Burls et al., 2017). Thus, if a site, sensitive to changes in the water mass contribution was primarily bathed by NPDW during interglacials, but NPIW during glacials, this could potentially be reflected in a ‘reversed’ CaCO_3 accumulation pattern, with increased preservation during glacial intervals as a result of the presence of better ventilated NPIW.

Additionally, further work should focus on exploring the influence of different states of NPIW formation on the North Pacific carbon cycle. Recent work suggests that enhanced export of NPIW during Heinrich stadial 1 may have increased primary productivity in the equatorial Pacific (Max et al., 2014). Moreover, Kender et al. (in review) propose that NPIW deepening during MIS 22 (Table 4.2) could have decreased eddy-induced CO_2 outgassing along the eastern Bering Sea slope. Hence, both studies indicate a negative feedback of increased NPIW formation on atmospheric CO_2 concentrations. Consequently, it is important to study the nutrient content of NPIW on G/IG timescales and its ability to promote primary productivity. Further, examining carbon cycle parameters, such as pH, may provide insights into CO_2 dynamics. Traditionally, reconstructions of oceanic pH are based on boron isotopes ($\delta^{11}\text{B}$) of benthic or planktonic foraminifera (Sanyal et al., 1995, Hönisch and Hemming, 2005, Yu et al., 2010b). However, the methodology requires a large amount of sample material, which is challenging in the North Pacific due to the low CaCO_3 preservation potential. Yet, newly established approaches use the $\delta^{11}\text{B}$ of aragonitic deep sea corals (*Scleractinia*) to infer changes in the oceanic carbonate chemistry at intermediate depth (Burke et al., 2017). Abundant deep sea corals have been reported

from the upper continental slope in the Bering Sea, potentially offering a chance to explore the pH of mid-depth waters across the last G/IG cycle, although the abundance of the coral order *Scleractinia* is relatively low (Stone and Shotwell, 2007, Miller et al., 2012), indicating the need for detailed site surveys.

Moreover, future research should aim to reconstruct a continuous ~1.5 Ma record of sea ice dynamics in the Bering Sea, to examine the full Pleistocene orbital-scale variability and to provide further insights into the role of sea ice for the MPT. A continuous record offers the opportunity to study the leads and lags of sea ice dynamics versus $\delta^{18}\text{O}_b$, to determine the role of sea ice for the deglacial continental ice sheet retreat. In addition, biomarker-based records of MPT sea ice evolution from other regions across the northern hemisphere and eventually the Southern Ocean are needed to confirm the observed changes of MPT sea ice dynamics in the Bering Sea and to determine the role of interhemispheric sea ice patterns for climate change (Lee et al., 2017).

Furthermore, it is important for our understanding of high latitude regions to promote studies exploring Mg/Ca temperature calibrations of high-latitude specific foraminiferal species and/or the Mg/Ca dynamics of global species towards the ‘cold end’ of the established calibrations. Especially in relation to future climate change, understanding the sensitivity of different climate parameters in high latitude regions is of relevance. Additionally, examining the effect of CaCO_3 saturation on infaunal foraminiferal species is fundamental, in particular with regard to the deep Pacific, where old carbon-rich bottom waters prevail.

Lastly, high resolution records of $\delta^{18}\text{O}_w$ across the MPT are needed from around the world’s ocean. Together with results presented in Ford et al. (2016) this study demonstrates the importance of regional hydrography for the $\delta^{18}\text{O}_w$. Thus, a global stack is needed, similar to the LR04 stack (Lisiecki and Raymo, 2005) to derive an averaged record of continental ice volume evolution across this pivotal climate transition. Together with future endeavours to drill Antarctic ice cores reaching as far back as the early MPT, allowing the reconstruction of atmospheric CO_2 (Parrenin et al., 2017), this will provide critical momentum in understanding internal climate mechanism driving Mid-Pleistocene climate change.

References

- AAGAARD-SØRENSEN, S., HUSUM, K., HALD, M. & KNIES, J. 2010. Paleooceanographic development in the SW Barents Sea during the Late Weichselian–Early Holocene transition. *Quaternary Science Reviews*, 29, 3442-3456.
- ADCROFT, A., SCOTT, J. R. & MAROTZKE, J. 2001. Impact of geothermal heating on the global ocean circulation. *Geophysical Research Letters*, 28, 1735-1738.
- ADKINS, J. F., MCINTYRE, K. & SCHRAG, D. P. 2002. The Salinity, Temperature, and $\delta^{18}\text{O}$ of the Glacial Deep Ocean. *Science*, 298, 1769-1773.
- AGUILAR-ISLAS, A. M., HURST, M. P., BUCK, K. N., SOHST, B., SMITH, G. J., LOHAN, M. C. & BRULAND, K. W. 2007. Micro- and macronutrients in the southeastern Bering Sea: Insight into iron-replete and iron-depleted regimes. *Progress in Oceanography*, 73, 99-126.
- AHAGON, N., OHKUSHI, K. I., UCHIDA, M. & MISHIMA, T. 2003. Mid-depth circulation in the northwest Pacific during the last deglaciation: Evidence from foraminiferal radiocarbon ages. *Geophysical Research Letters*, 30, 2097.
- AIELLO, I. W. & RAVELO, A. C. 2012. Evolution of marine sedimentation in the Bering Sea since the Pliocene. *Geosphere*, 8, 1231-1253.
- ALOISI, G., BOULOUBASSI, I., HEIJS, S. K., PANCOST, R. D., PIERRE, C., SINNINGHE DAMSTÉ, J. S., GOTTSCHAL, J. C., FORNEY, L. J. & ROUCHY, J.-M. 2002. CH_4 -consuming microorganisms and the formation of carbonate crusts at cold seeps. *Earth and Planetary Science Letters*, 203, 195-203.
- ALOISI, G., PIERRE, C., ROUCHY, J.-M., FOUCHER, J.-P. & WOODSIDE, J. 2000. Methane-related authigenic carbonates of eastern Mediterranean Sea mud volcanoes and their possible relation to gas hydrate destabilisation. *Earth and Planetary Science Letters*, 184, 321-338.
- ANDERSON, R. F., ALI, S., BRADTMILLER, L. I., NIELSEN, S. H. H., FLEISHER, M. Q., ANDERSON, B. E. & BURCKLE, L. H. 2009. Wind-Driven Upwelling in the Southern Ocean and the Deglacial Rise in Atmospheric CO_2 . *Science*, 323, 1443-1448.
- ANTONOV, J. I., LOCARNINI, R. A., BOYER, T. P., MISHONOV, A. V. & GARCIA, H. E. 2006. World Ocean Atlas 2005, Volume 2: Salinity. In: LEVITUS, S. (ed.) *NOAA Atlas NESDIS 62*. Washington, D.C.: U.S. Government Printing Office.
- ARMSTRONG, J. 1988. Quantitative analysis of silicate and oxide materials: comparison of Monte Carlo, ZAF and $\phi(\rho z)$ procedures. *Microbeam Analysis* 239-246.
- ASAHI, H., KENDER, S., IKEHARA, M., SAKAMOTO, T., TAKAHASHI, K., RAVELO, A. C., ALVAREZ ZARIKIAN, C. A., KHIM, B. K. & LENG, M. J. 2016. Orbital-scale benthic foraminiferal oxygen isotope stratigraphy at the northern Bering Sea Slope Site U1343 (IODP Expedition 323) and its Pleistocene paleoceanographic significance. *Deep Sea Research Part II: Topical Studies in Oceanography*, 125–126, 66-83.
- ASHKENAZY, Y. 2006. The role of phase locking in a simple model for glacial dynamics. *Climate Dynamics*, 27, 421-431.

- ASHKENAZY, Y. & TZIPERMAN, E. 2004. Are the 41 kyr glacial oscillations a linear response to Milankovitch forcing? *Quaternary Science Reviews*, 23, 1879-1890.
- BAHR, A., KABOTH, S., HODELL, D., ZEEDEN, C., FIEBIG, J. & FRIEDRICH, O. 2018. Oceanic heat pulses fueling moisture transport towards continental Europe across the mid-Pleistocene transition. *Quaternary Science Reviews*, 179, 48-58.
- BARKER, S., GREAVES, M. & ELDERFIELD, H. 2003. A study of cleaning procedures used for foraminiferal Mg/Ca paleothermometry. *Geochemistry, Geophysics, Geosystems*, 4, 8407.
- BARRIENTOS, N., LEAR, C. H., JAKOBSSON, M., STRANNE, C., O'REGAN, M., CRONIN, T. M., GUKOV, A. Y. & COXALL, H. K. 2018. Arctic Ocean benthic foraminifera Mg/Ca ratios and global Mg/Ca-temperature calibrations: New constraints at low temperatures. *Geochimica et Cosmochimica Acta*, in press.
- BAYON, G., LONCKE, L., DUPRÉ, S., CAPRAIS, J.-C., DUCASSOU, E., DUPERRON, S., ETOUBLEAU, J., FOUCHER, J.-P., FOUQUET, Y. & GONTHARET, S. 2009. Multi-disciplinary investigation of fluid seepage on an unstable margin: the case of the Central Nile deep sea fan. *Marine Geology*, 261, 92-104.
- BAYON, G., PIERRE, C., ETOUBLEAU, J., VOISSET, M., CAUQUIL, E., MARSSET, T., SULTAN, N., LE DREZEN, E. & FOUQUET, Y. 2007. Sr/Ca and Mg/Ca ratios in Niger Delta sediments: Implications for authigenic carbonate genesis in cold seep environments. *Marine Geology*, 241, 93-109.
- BELL, D. B., JUNG, S. J. A. & KROON, D. 2015. The Plio-Pleistocene development of Atlantic deep-water circulation and its influence on climate trends. *Quaternary Science Reviews*, 123, 265-282.
- BELT, S. T., BROWN, T. A., RINGROSE, A. E., CABEDO-SANZ, P., MUNDY, C. J., GOSSELIN, M. & POULIN, M. 2013. Quantitative measurement of the sea ice diatom biomarker IP₂₅ and sterols in Arctic sea ice and underlying sediments: Further considerations for palaeo sea ice reconstruction. *Organic Geochemistry*, 62, 33-45.
- BELT, S. T., BROWN, T. A., RODRIGUEZ, A. N., SANZ, P. C., TONKIN, A. & INGLE, R. 2012. A reproducible method for the extraction, identification and quantification of the Arctic sea ice proxy IP₂₅ from marine sediments. *Analytical Methods*, 4, 705-713.
- BELT, S. T., BROWN, T. A., SMIK, L., TATAREK, A., WIKTOR, J., STOWASSER, G., ASSMY, P., ALLEN, C. S. & HUSUM, K. 2017. Identification of C₂₅ highly branched isoprenoid (HBI) alkenes in diatoms of the genus *Rhizosolenia* in polar and sub-polar marine phytoplankton. *Organic Geochemistry*, 110, 65-72.
- BELT, S. T., CABEDO-SANZ, P., SMIK, L., NAVARRO-RODRIGUEZ, A., BERBEN, S. M. P., KNIES, J. & HUSUM, K. 2015. Identification of paleo Arctic winter sea ice limits and the marginal ice zone: Optimised biomarker-based reconstructions of late Quaternary Arctic sea ice. *Earth and Planetary Science Letters*, 431, 127-139.
- BELT, S. T., MASSÉ, G., ROWLAND, S. J., POULIN, M., MICHEL, C. & LEBLANC, B. 2007. A novel chemical fossil of palaeo sea ice: IP₂₅. *Organic Geochemistry*, 38, 16-27.

- BELT, S. T. & MÜLLER, J. 2013. The Arctic sea ice biomarker IP₂₅: a review of current understanding, recommendations for future research and applications in palaeo sea ice reconstructions. *Quaternary Science Reviews*, 79, 9-25.
- BERBEN, S. M. P., HUSUM, K., NAVARRO-RODRIGUEZ, A., BELT, S. T. & AAGAARD-SØRENSEN, S. 2017. Semi-quantitative reconstruction of early to late Holocene spring and summer sea ice conditions in the northern Barents Sea. *Journal of Quaternary Science*, 32, 587–603.
- BEREITER, B., EGGLESTON, S., SCHMITT, J., NEHRBASS-AHLES, C., STOCKER, T. F., FISCHER, H., KIPFSTUHL, S. & CHAPPELLAZ, J. 2015. Revision of the EPICA Dome C CO₂ record from 800 to 600 kyr before present. *Geophysical Research Letters*, 42, 542–549.
- BERGER, A., LI, X. S. & LOUTRE, M. F. 1999. Modelling northern hemisphere ice volume over the last 3 Ma. *Quaternary Science Reviews*, 18, 1-11.
- BERNER, R. A. 1980. *Early diagenesis: a theoretical approach*, Princeton University Press.
- BERNER, R. A. 1984. Sedimentary pyrite formation: An update. *Geochimica et Cosmochimica Acta*, 48, 605-615.
- BILLUPS, K. & SCHRAG, D. P. 2002. Paleotemperatures and ice volume of the past 27 Myr revisited with paired Mg/Ca and ¹⁸O/¹⁶O measurements on benthic foraminifera. *Paleoceanography*, 17, 3-1-3-11.
- BILLUPS, K., YORK, K. & BRADTMILLER, L. I. 2018. Water Column Stratification in the Antarctic Zone of the Southern Ocean During the Mid-Pleistocene Climate Transition. *Paleoceanography and Paleoclimatology*, 33, 432-442.
- BINTANJA, R. & VAN DE WAL, R. S. W. 2008a. North American ice-sheet dynamics and the onset of 100,000-year glacial cycles. *Nature*, 454, 869-872.
- BINTANJA, R. & VAN DE WAL, R. S. W. 2008b. North American ice-sheet dynamics and the onset of 100,000-year glacial cycles. *Nature*, 454, 869-872.
- BOETIUS, A., RAVENSCHLAG, K., SCHUBERT, C. J., RICKERT, D., WIDDEL, F., GIESEKE, A., AMANN, R., JØRGENSEN, B. B., WITTE, U. & PFANNKUCHE, O. 2000. A marine microbial consortium apparently mediating anaerobic oxidation of methane. *Nature*, 407, 623.
- BOITEAU, R., GREAVES, M. & ELDERFIELD, H. 2012. Authigenic uranium in foraminiferal coatings: A proxy for ocean redox chemistry. *Paleoceanography*, 27, PA3227.
- BOND, G., BROECKER, W., JOHNSEN, S., MCMANUS, J., LABEYRIE, L., JOUZEL, J. & BONANI, G. 1993. Correlations between climate records from North Atlantic sediments and Greenland ice. *Nature*, 365, 143.
- BOUDREAU, B. P. & JØRGENSEN, B. P. 2001. *The Benthic Boundary Layer*, Oxford University Press.
- BOYLE, E. A. 1983. Manganese carbonate overgrowths on foraminifera tests. *Geochimica et Cosmochimica Acta*, 47, 1815-1819.
- BOYLE, E. A. 1988. Vertical oceanic nutrient fractionation and glacial/interglacial CO₂ cycles. *Nature*, 331, 55.
- BOYLE, E. A. & KEIGWIN, L. 1987. North Atlantic thermohaline circulation during the past 20,000 years linked to high-latitude surface temperature. *Nature*, 330, 35.
- BOYLE, E. A. & KEIGWIN, L. D. 1985. Comparison of Atlantic and Pacific paleochemical records for the last 215,000 years: changes in deep ocean

- circulation and chemical inventories. *Earth and Planetary Science Letters*, 76, 135-150.
- BRADTMILLER, L. I., ANDERSON, R. F., SACHS, J. P. & FLEISHER, M. Q. 2010. A deeper respired carbon pool in the glacial equatorial Pacific Ocean. *Earth and Planetary Science Letters*, 299, 417-425.
- BRENNAN, C. E., MEISSNER, K. J., EBY, M., HILLAIRE-MARCEL, C. & WEAVER, A. J. 2013. Impact of sea ice variability on the oxygen isotope content of seawater under glacial and interglacial conditions. *Paleoceanography*, 28, 388-400.
- BROECKER, W. S. 1982. Ocean chemistry during glacial time. *Geochimica et Cosmochimica Acta*, 46, 1689-1705.
- BROECKER, W. S., PEACOCK, S. L., WALKER, S., WEISS, R., FAHRBACH, E., SCHROEDER, M., MIKOLAJEWICZ, U., HEINZE, C., KEY, R., PENG, T.-H. & RUBIN, S. 1998. How much deep water is formed in the Southern Ocean? *Journal of Geophysical Research: Oceans*, 103, 15833-15843.
- BROWN, S. J. & ELDERFIELD, H. 1996. Variations in Mg/Ca and Sr/Ca ratios of planktonic foraminifera caused by postdepositional dissolution: Evidence of shallow Mg-dependent dissolution. *Paleoceanography*, 11, 543-551.
- BROWN, T. A., BELT, S. T., PHILIPPE, B., MUNDY, C. J., MASSÉ, G., POULIN, M. & GOSSELIN, M. 2011a. Temporal and vertical variations of lipid biomarkers during a bottom ice diatom bloom in the Canadian Beaufort Sea: further evidence for the use of the IP₂₅ biomarker as a proxy for spring Arctic sea ice. *Polar Biology*, 34, 1857-1868.
- BROWN, T. A., BELT, S. T., TATAREK, A. & MUNDY, C. J. 2014. Source identification of the Arctic sea ice proxy IP₂₅. *Nat Commun*, 5, 4197.
- BROWN, Z. W. & ARRIGO, K. R. 2013. Sea ice impacts on spring bloom dynamics and net primary production in the Eastern Bering Sea. *Journal of Geophysical Research: Oceans*, 118, 43-62.
- BROWN, Z. W., VAN DIJKEN, G. L. & ARRIGO, K. R. 2011b. A reassessment of primary production and environmental change in the Bering Sea. *Journal of Geophysical Research: Oceans*, 116, C08014.
- BRUNELLE, B. G., SIGMAN, D. M., COOK, M. S., KEIGWIN, L. D., HAUG, G. H., PLESSSEN, B., SCHETTLER, G. & JACCARD, S. L. 2007. Evidence from diatom-bound nitrogen isotoped for subarctic Pacific stratification during the last ice age and a link to North Pacific denitrification changes. *Paleoceanography*, 22, PA1215.
- BRUNELLE, B. G., SIGMAN, D. M., JACCARD, S. L., KEIGWIN, L. D., PLESSSEN, B., SCHETTLER, G., COOK, M. S. & HAUG, G. H. 2010. Glacial/interglacial changes in nutrient supply and stratification in the western subarctic North Pacific since the penultimate glacial maximum. *Quaternary Science Reviews*, 29, 2579-2590.
- BUBENSHCHIKOVA, N., NÜRNBERG, D., LEMBKE-JENE, L. & PAVLOVA, G. 2008. Living benthic foraminifera of the Okhotsk Sea: Faunal composition, standing stocks and microhabitats. *Marine Micropaleontology*, 69, 314-333.
- BUBENSHCHIKOVA, N. V., NÜRNBERG, D., GORBARENKO, S. A. & LEMBKE-JENE, L. 2010. Variations of the oxygen minimum zone of the Okhotsk Sea during the last 50 ka as indicated by benthic foraminiferal and biogeochemical data. *Oceanology*, 50, 93-106.
- BURKE, A., RAE, J. W. B., STEWART, J., ROBINSON, L. F., ADKINS, J. F., CHEN, T., COLE, C. S., GREENOP, R., TAYLOR, B. & LI, T. Deep-sea

- coral evidence for millennial and centennial scale changes in Southern Ocean carbon chemistry. AGU Fall Meeting Abstracts, 2017.
- BURKE, A. & ROBINSON, L. F. 2012. The Southern Ocean's Role in Carbon Exchange During the Last Deglaciation. *Science*, 335, 557-561.
- BURLS, N. J., FEDOROV, A. V., SIGMAN, D. M., JACCARD, S. L., TIEDEMANN, R. & HAUG, G. H. 2017. Active Pacific meridional overturning circulation (PMOC) during the warm Pliocene. *Science Advances*, 3, e1700156.
- BURTON, E. A. 1993. Controls on marine carbonate cement mineralogy: review and reassessment. *Chemical Geology*, 105, 163-179.
- CABEDO-SANZ, P. & BELT, S. T. 2015. Identification and characterisation of a novel mono-unsaturated highly branched isoprenoid (HBI) alkene in ancient Arctic sediments. *Organic Geochemistry*, 81, 34-39.
- CABEDO-SANZ, P. & BELT, S. T. 2016. Seasonal sea ice variability in eastern Fram Strait over the last 2000 years. *arktos*, 2, 1-12.
- CAISSIE, B. E., BRIGHAM-GRETTE, J., COOK, M. S. & COLMENERO-HIDALGO, E. 2016. Bering Sea surface water conditions during Marine Isotope Stages 12 to 10 at Navarin Canyon (IODP Site U1345). *Clim. Past*, 12, 1739-1763.
- CAISSIE, B. E., BRIGHAM-GRETTE, J., LAWRENCE, K. T., HERBERT, T. D. & COOK, M. S. 2010. Last Glacial Maximum to Holocene sea surface conditions at Umnak Plateau, Bering Sea, as inferred from diatom, alkenone, and stable isotope records. *Paleoceanography*, 25, PA1206.
- CALVERT, S. E. & PEDERSEN, T. F. 1993. Geochemistry of Recent oxic and anoxic marine sediments: Implications for the geological record. *Marine Geology*, 113, 67-88.
- CARALP, M. H. 1989. Abundance of *Bulimina exilis* and *Melonis barleeanum*: Relationship to the quality of marine organic matter. *Geo-Marine Letters*, 9, 37-43.
- CAUELLE, C., KOHO, K. A., MOJTAHID, M., REICHART, G. J. & JORISSEN, F. J. 2014. Live (Rose Bengal stained) foraminiferal faunas from the northern Arabian Sea: faunal succession within and below the OMZ. *Biogeosciences*, 11, 1155-1175.
- CAVALIERI, D. J. & MARTIN, S. 1994. The contribution of Alaskan, Siberian, and Canadian coastal polynyas to the cold halocline layer of the Arctic Ocean. *Journal of Geophysical Research: Oceans*, 99, 18343-18362.
- CHALK, T. B., HAIN, M. P., FOSTER, G. L., ROHLING, E. J., SEXTON, P. F., BADGER, M. P. S., CHERRY, S. G., HASENFRATZ, A. P., HAUG, G. H., JACCARD, S. L., MARTÍNEZ-GARCÍA, A., PÄLIKE, H., PANCOST, R. D. & WILSON, P. A. 2017. Causes of ice age intensification across the Mid-Pleistocene Transition. *Proceedings of the National Academy of Sciences*, 114, 13114-13119.
- CHASE, Z., ANDERSON, R. F. & FLEISHER, M. Q. 2001. Evidence from authigenic uranium for increased productivity of the glacial subantarctic ocean. *Paleoceanography*, 16, 468-478.
- CHEN, P., YU, J. & JIN, Z. 2017. An evaluation of benthic foraminiferal U/Ca and U/Mn proxies for deep ocean carbonate chemistry and redox conditions. *Geochemistry, Geophysics, Geosystems*, 18, 617-630.
- CHIKAMOTO, M. O., MENVIEL, L., ABE-OUCHI, A., OHGAI, R., TIMMERMANN, A., OKAZAKI, Y., HARADA, N., OKA, A. &

- MOUCHET, A. 2012. Variability in North Pacific intermediate and deep water ventilation during Heinrich events in two coupled climate models. *Deep Sea Research Part II: Topical Studies in Oceanography*, 61-64, 114-126.
- CLARK, P. U., ARCHER, D., POLLARD, D., BLUM, J. D., RIAL, J. A., BROVKIN, V., MIX, A. C., PISIAS, N. G. & ROY, M. 2006. The middle Pleistocene transition: characteristics, mechanisms, and implications for long-term changes in atmospheric pCO₂. *Quaternary Science Reviews*, 25, 3150-3184.
- CLARK, P. U. & POLLARD, D. 1998. Origin of the Middle Pleistocene Transition by ice sheet erosion of regolith. *Paleoceanography*, 13, 1-9.
- COACHMAN, L. K. 1993. On the flow field in the Chirikov Basin. *Continental Shelf Research*, 13, 481-508.
- COACHMAN, L. K., WHITLEDGE, T. E. & GOERING, J. J. 1999. Silica in Bering Sea Deep and Bottom Water edited by T.R. Loughlin and K. Othani. *Dynamics of the Bering Sea, North Pacific Science Organization (PICES), published by University of Alaska Sea Grant, Fairbanks, Alaska*.
- COOK, M. S., KEIGWIN, L. D., BIRGEL, D. & HINRICHS, K.-U. 2011. Repeated pulses of vertical methane flux recorded in glacial sediments from the southeast Bering Sea. *Paleoceanography*, 26, PA2210.
- COOK, M. S., KEIGWIN, L. D. & SANCETTA, C. A. 2005. The deglacial history of surface and intermediate water of the Bering Sea. *Deep Sea Research Part II: Topical Studies in Oceanography*, 52, 2163-2173.
- COOK, M. S., RAVELO, A. C., MIX, A., NESBITT, I. M. & MILLER, N. V. 2016. Tracing subarctic Pacific water masses with benthic foraminiferal stable isotopes during the LGM and late Pleistocene. *Deep Sea Research Part II: Topical Studies in Oceanography*, 125-126, 84-95.
- CORLISS, B. H. 1985. Microhabitats of benthic foraminifera within deep-sea sediments. *Nature*, 314, 435.
- CRÉMIÈRE, A., PIERRE, C., BLANC-VALLERON, M.-M., ZITTER, T., ÇAĞATAY, M. N. & HENRY, P. 2012. Methane-derived authigenic carbonates along the North Anatolian fault system in the Sea of Marmara (Turkey). *Deep Sea Research Part I: Oceanographic Research Papers*, 66, 114-130.
- CRUNDWELL, M., SCOTT, G., NAISH, T. & CARTER, L. 2008. Glacial–interglacial ocean climate variability from planktonic foraminifera during the Mid-Pleistocene transition in the temperate Southwest Pacific, ODP Site 1123. *Palaeogeography, Palaeoclimatology, Palaeoecology*, 260, 202-229.
- CRUSIUS, J. & THOMSON, J. 2000. Comparative behavior of authigenic Re, U, and Mo during reoxidation and subsequent long-term burial in marine sediments. *Geochimica et Cosmochimica Acta*, 64, 2233-2242.
- CURRY, W. B. & MARCHITTO, T. M. 2008. A secondary ionization mass spectrometry calibration of *Cibicides pachyderma* Mg/Ca with temperature. *Geochemistry, Geophysics, Geosystems*, 9, Q04009.
- CURRY, W. B. & OPPO, D. W. 2005. Glacial water mass geometry and the distribution of $\delta^{13}\text{C}$ of ΣCO_2 in the western Atlantic Ocean. *Paleoceanography*, 20, PA1017.
- D'HONDT, S., RUTHERFORD, S. & SPIVACK, A. J. 2002. Metabolic Activity of Subsurface Life in Deep-Sea Sediments. *Science*, 295, 2067-2070.
- DANSGAARD, W., JOHNSEN, S. J., CLAUSEN, H. B., DAHL-JENSEN, D., GUNDESTRUP, N. S., HAMMER, C. U., HVIDBERG, C. S., STEFFENSEN, J. P., SVEINBJÖRNSDÓTTIR, A. E., JOUZEL, J. & BOND,

- G. 1993. Evidence for general instability of past climate from a 250-kyr ice-core record. *Nature*, 364, 218.
- DAVIES, L. & GATHER, U. 1993. The Identification of Multiple Outliers. *Journal of the American Statistical Association*, 88, 782-792.
- DE BOER, A. M., SIGMAN, D. M., TOGGWEILER, J. R. & RUSSELL, J. L. 2007. Effect of global ocean temperature change on deep ocean ventilation. *Paleoceanography*, 22.
- DE GARIDEL-THORON, T., ROSENTHAL, Y., BASSINOT, F. & BEAUFORT, L. 2005. Stable sea surface temperatures in the western Pacific warm pool over the past 1.75 million years. *Nature*, 433, 294.
- DE LANGE, G., VAN OS, B. & POORTER, R. 1992. Geochemical composition and inferred accretion rates of sediments and manganese nodules from a submarine hill in the Madeira Abyssal Plain, eastern North Atlantic. *Marine geology*, 109, 171-194.
- DECONTO, R. M. & POLLARD, D. 2003. Rapid Cenozoic glaciation of Antarctica induced by declining atmospheric CO₂. *Nature*, 421, 245-249.
- DELANEY, M. L., BE, A. W. H. & BOYLE, E. A. 1985. Li, Sr, Mg, Na in foraminiferal calcite shells from laboratory culture, sediment traps, and sediment cores. *Geochimica et Cosmochimica Acta*, 49, 1327-1341.
- DENINNO, L. H., CRONIN, T. M., RODRIGUEZ-LAZARO, J. & BRENNER, A. 2015. An early to mid-Pleistocene deep Arctic Ocean ostracode fauna with North Atlantic affinities. *Palaeogeography, Palaeoclimatology, Palaeoecology*, 419, 90-99.
- DESER, C. & TENG, H. 2008. Evolution of Arctic sea ice concentration trends and the role of atmospheric circulation forcing, 1979–2007. *Geophysical Research Letters*, 35, L02504.
- DETLEF, H., BELT, S. T., SOSDIAN, S. M., SMIK, L., LEAR, C. H., HALL, I. R., CABEDO-SANZ, P., HUSUM, K. & KENDER, S. 2018. Sea ice dynamics across the Mid-Pleistocene transition in the Bering Sea. *Nature Communications*, 9, 941.
- DICKSON, A. G. & MILLERO, F. J. 1987. A comparison of the equilibrium constants for the dissociation of carbonic acid in seawater media. *Deep Sea Research Part A. Oceanographic Research Papers*, 34, 1733-1743.
- DIESTER-HAASS, L., BILLUPS, K. & LEAR, C. 2018. Productivity changes across the mid-Pleistocene climate transition. *Earth-Science Reviews*, 179, 372-391.
- DISSARD, D., NEHRKE, G., REICHAERT, G. J. & BIJMA, J. 2010. The impact of salinity on the Mg/Ca and Sr/Ca ratio in the benthic foraminifera *Ammonia tepida*: Results from culture experiments. *Geochimica et Cosmochimica Acta*, 74, 928-940.
- DOUGLAS, D. C. 2010. Arctic sea ice decline: Projected changes in timing and extent of sea ice in the Bering and Chukchi Seas. *Open-File Report U. S. Geological Survey*.
- DUPLESSY, J.-C., ARNOLD, M., BARD, E., JUILLET-LECLERC, A., KALLEL, N. & LABEYRIE, L. 1989. AMS 14C Study of Transient Events and of the Ventilation Rate of the Pacific Intermediate Water During the Last Deglaciation. *Radiocarbon*, 31, 493-502.
- DUPLESSY, J.-C., LABEYRIE, L. & WAELBROECK, C. 2002. Constraints on the ocean oxygen isotopic enrichment between the Last Glacial Maximum and the Holocene: Paleoceanographic implications. *Quaternary Science Reviews*, 21, 315-330.

- DYEZ, K. A. & RAVELO, A. C. 2014. Dynamical changes in the tropical Pacific warm pool and zonal SST gradient during the Pleistocene. *Geophysical Research Letters*, 41, 7626-7633.
- EDGAR, K. M., ANAGNOSTOU, E., PEARSON, P. N. & FOSTER, G. L. 2015. Assessing the impact of diagenesis on $\delta^{11}\text{B}$, $\delta^{13}\text{C}$, $\delta^{18}\text{O}$, Sr/Ca and B/Ca values in fossil planktic foraminiferal calcite. *Geochimica et Cosmochimica Acta*, 166, 189-209.
- EDGAR, K. M., PÄLIKE, H. & WILSON, P. A. 2013. Testing the impact of diagenesis on the $\delta^{18}\text{O}$ and $\delta^{13}\text{C}$ of benthic foraminiferal calcite from a sediment burial depth transect in the equatorial Pacific. *Paleoceanography*, 28, 468-480.
- ELDERFIELD, H., FERRETTI, P., GREAVES, M., CROWHURST, S., MCCAVE, I. N., HODELL, D. & PIOTROWSKI, A. M. 2012. Evolution of Ocean Temperature and Ice Volume Through the Mid-Pleistocene Climate Transition. *Science*, 337, 704-709.
- ELDERFIELD, H., GREAVES, M., BARKER, S., HALL, I. R., TRIPATI, A., FERRETTI, P., CROWHURST, S., BOOTH, L. & DAUNT, C. 2010. A record of bottom water temperature and seawater $\delta^{18}\text{O}$ for the Southern Ocean over the past 440 kyr based on Mg/Ca of benthic foraminiferal *Uvigerina* spp. *Quaternary Science Reviews*, 29, 160-169.
- ELDERFIELD, H., YU, J., ANAND, P., KIEFER, T. & NYLAND, B. 2006. Calibrations for benthic foraminiferal Mg/Ca paleothermometry and the carbonate ion hypothesis. *Earth and Planetary Science Letters*, 250, 633-649.
- ELIAS, S. A., SHORT, S. K., NELSON, C. H. & BIRKS, H. H. 1996. Life and times of the Bering land bridge. *Nature*, 382, 60-63.
- EMILE-GEAY, J., CANE, M. A., NAIK, N., SEAGER, R., CLEMENT, A. C. & GEEN, A. V. 2003. Warren revisited: Atmospheric freshwater fluxes and "Why is no deep water formed in the North Pacific". *Journal of Geophysical Research: Oceans*, 108, 3178.
- EREZ, J. 2003. The Source of Ions for Biomineralization in Foraminifera and Their Implications for Paleoceanographic Proxies. *Reviews in Mineralogy and Geochemistry, Biomineralization*, 54, 115-150.
- EVANS, D. & MÜLLER, W. 2012. Deep time foraminifera Mg/Ca paleothermometry: Nonlinear correction for secular change in seawater Mg/Ca. *Paleoceanography*, 27, PA4205.
- EVANS, D. & MÜLLER, W. 2018. Automated Extraction of a Five-Year LA-ICP-MS Trace Element Data Set of Ten Common Glass and Carbonate Reference Materials: Long-Term Data Quality, Optimisation and Laser Cell Homogeneity. *Geostandards and Geoanalytical Research*, 42, 159-188.
- EXPEDITION, 323 & SCIENTISTS 2010. Bering Sea paleoceanography: Pliocene-Pleistocene paleoceanography and climate history of the Bering Sea. *IODP Prl. Report*, 323.
- FANTLE, M. S. & DEPAOLO, D. J. 2005. Variations in the marine Ca cycle over the past 20 million years. *Earth and Planetary Science Letters*, 237, 102-117.
- FANTLE, M. S. & DEPAOLO, D. J. 2006. Sr isotopes and pore fluid chemistry in carbonate sediment of the Ontong Java Plateau: Calcite recrystallization rates and evidence for a rapid rise in seawater Mg over the last 10 million years. *Geochimica et Cosmochimica Acta*, 70, 3883-3904.
- FENG, F. & BAILER-JONES, C. A. L. 2015. Obliquity and precession as pacemakers of Pleistocene deglaciations. *Quaternary Science Reviews*, 122, 166-179.

- FERRARI, R., JANSEN, M. F., ADKINS, J. F., BURKE, A., STEWART, A. L. & THOMPSON, A. F. 2014. Antarctic sea ice control on ocean circulation in present and glacial climates. *Proceedings of the National Academy of Sciences*, 111, 8753-8758.
- FILIPSSON, H. L., ROMERO, O. E., STUUT, J.-B. W. & DONNER, B. 2011. Relationships between primary productivity and bottom-water oxygenation off northwest Africa during the last deglaciation. *Journal of Quaternary Science*, 26, 448-456.
- FORD, H. L. & RAYMO, M. E. 2017. Detangling regional and global signals in seawater $\delta^{18}\text{O}$ records across the Mid-Pleistocene Transition. *PAGES-OSM: 02181*, 06. Zaragoza, Spain.
- FORD, H. L., SOSDIAN, S. M., ROSENTHAL, Y. & RAYMO, M. E. 2016. Gradual and abrupt changes during the Mid-Pleistocene Transition. *Quaternary Science Reviews*, 148, 222-233.
- FROELICH, P. N., KLINKHAMMER, G. P., BENDER, M. L., LUEDTKE, N. A., HEATH, G. R., CULLEN, D., DAUPHIN, P., HAMMOND, D., HARTMAN, B. & MAYNARD, V. 1979. Early oxidation of organic matter in pelagic sediments of the eastern equatorial Atlantic: suboxic diagenesis. *Geochimica et Cosmochimica Acta*, 43, 1075-1090.
- GALBRAITH, E. D., JACCARD, S. L., PEDERSEN, T. F., SIGMAN, D. M., HAUG, G. H., COOK, M. S., SOUTHON, J. R. & FRANCOIS, R. 2007. Carbon dioxide release from the North Pacific abyss during the last deglaciation. *Nature*, 449, 890-893.
- GALEOTTI, S., DECONTO, R., NAISH, T., STOCCHI, P., FLORINDO, F., PAGANI, M., BARRETT, P., BOHATY, S. M., LANCI, L., POLLARD, D., SANDRONI, S., TALARICO, F. M. & ZACHOS, J. C. 2016. Antarctic Ice Sheet variability across the Eocene-Oligocene boundary climate transition. *Science*, 352, 76-80.
- GARCIA, H. E., LOCARNINI, R. A., BOYER, T. P. & ANTONOV, J. I. 2006a. World Ocean Atlas 2005, Volume 3: Dissolved Oxygen, Apparent Oxygen Utilization, and Oxygen Saturation. In: LEVITUS, S. (ed.) *NOAA Atlas NESDIS 63*. Washington, D.C.: U.S. Government Printing Office.
- GARCIA, H. E., LOCARNINI, R. A., BOYER, T. P. & ANTONOV, J. I. 2006b. World Ocean Atlas 2005, Volume 4: Nutrients (phosphate, nitrate, silicate). In: LEVITUS, S. (ed.) *NOAA Atlas NESDIS 64*. Washington, D.C.: U.S. Government Printing Office.
- GAURAV, B., G., C. W., R., D. G., BRANDON, D. & J., H. G. 2008. Sulfate-methane transition as a proxy for average methane hydrate saturation in marine sediments. *Geophysical Research Letters*, 35, L03611.
- GEBHARDT, H., SARNTHEIN, M., GROOTES, P. M., KIEFER, T., KUEHN, H., SCHMIEDER, F. & RÖHL, U. 2008. Paleonutrient and productivity records from the subarctic North Pacific for Pleistocene glacial terminations I to V. *Paleoceanography*, 23, PA4212.
- GEERKEN, E., DE NOOIJER, L. J., VAN DIJK, I. & REICHART, G. J. 2018. Impact of salinity on element incorporation in two benthic foraminiferal species with contrasting magnesium contents. *Biogeosciences*, 15, 2205-2218.
- GILDOR, H. & TZIPERMAN, E. 2001. A sea ice climate switch mechanism for the 100-kyr glacial cycles. *Journal of Geophysical Research*, 106, 9117-9113.
- GLADU, P. K., PATTERSON, G. W., WIKFORS, G. H., CHITWOOD, D. J. & LUSBY, W. R. 1990. The occurrence of brassicasterol and epibrassicasterol in

- the chromophycota. *Comparative Biochemistry and Physiology Part B: Comparative Biochemistry*, 97, 491-494.
- GLOCK, N., LIEBETRAU, V. & EISENHAUER, A. 2014. I/Ca ratios in benthic foraminifera from the Peruvian oxygen minimum zone: analytical methodology and evaluation as proxy for redox conditions. *Biogeosciences Discussions*, 11, 7077-7095.
- GOAD, L. J. & WITHERS, N. 1982. Identification of 27-nor-(24R)-24-methylcholesta-5,22-dien-3 β -ol and brassicasterol as the major sterols of the marine dinoflagellate *Gymnodinium simplex*. *Lipids*, 17, 853-858.
- GOES, J. I., GOMES, H. D. R., HAUGEN, E. M., MCKEE, K. T., D'SA, E. J., CHEKALYUK, A. M., STOECKER, D. K., STABENO, P. J., SAITOH, S.-I. & SAMBROTTO, R. N. 2014. Fluorescence, pigment and microscopic characterization of Bering Sea phytoplankton community structure and photosynthetic competency in the presence of a Cold Pool during summer. *Deep Sea Research Part II: Topical Studies in Oceanography*, 109, 84-99.
- GOODAY, A. J. & RATHBURN, A. E. 1999. Temporal variability in living deep-sea benthic foraminifera: a review. *Earth-Science Reviews*, 46, 187-212.
- GORBARENKO, S. A., KHUSID, T. A., BASOV, I. A., OBA, T., SOUTHON, J. R. & KOIZUMI, I. 2002. Glacial Holocene environment of the southeastern Okhotsk Sea: evidence from geochemical and palaeontological data. *Palaeogeography, Palaeoclimatology, Palaeoecology*, 177, 237-263.
- GORBARENKO, S. A., PSHENEVA, O. Y., ARTEMOVA, A. V., MATUL', A. G., TIEDEMANN, R. & NÜRNBERG, D. 2010. Paleoenvironment changes in the NW Okhotsk Sea for the last 18kyr determined with micropaleontological, geochemical, and lithological data. *Deep Sea Research Part I: Oceanographic Research Papers*, 57, 797-811.
- GOTTSCHALK, J., HODELL, D. A., SKINNER, L. C., CROWHURST, S. J., JACCARD, S. L. & CHARLES, C. 2018. Past Carbonate Preservation Events in the Deep Southeast Atlantic Ocean (Cape Basin) and Their Implications for Atlantic Overturning Dynamics and Marine Carbon Cycling. *Paleoceanography and Paleoclimatology*, 0.
- GOTTSCHALK, J., SKINNER, L. C., LIPPOLD, J., VOGEL, H., FRANK, N., JACCARD, S. L. & WAELEBROECK, C. 2016. Biological and physical controls in the Southern Ocean on past millennial-scale atmospheric CO₂ changes. *Nature Communications*, 7, 11539.
- GRANT, K. M., ROHLING, E. J., RAMSEY, C. B., CHENG, H., EDWARDS, R. L., FLORINDO, F., HESLOP, D., MARRA, F., ROBERTS, A. P., TAMISIEA, M. E. & WILLIAMS, F. 2014. Sea-level variability over five glacial cycles. *Nature Communications*, 5, 5076.
- GREBMEIER, J. M., OVERLAND, J. E., MOORE, S. E., FARLEY, E. V., CARMACK, E. C., COOPER, L. W., FREY, K. E., HELLE, J. H., MCLAUGHLIN, F. A. & MCNUTT, S. L. 2006. A Major Ecosystem Shift in the Northern Bering Sea. *Science*, 311, 1461-1464.
- GROENEVELD, J. & FILIPSSON, H. L. 2013. Mg/Ca and Mn/Ca ratios in benthic foraminifera: the potential to reconstruct past variations in temperature and hypoxia in shelf regions *Biogeosciences*, 10, 5125-5138.
- GROUP, P. B. W. 1999. Paleoenvironmental atlas of Beringia presented in electronic form. *Quaternary Research*, 52, 270-271.

- GUSSONE, N., FILIPSSON, H. L. & KUHNERT, H. 2016. Mg/Ca, Sr/Ca and Ca isotope ratios in benthonic foraminifers related to test structure, mineralogy and environmental controls. *Geochimica et Cosmochimica Acta*, 173, 142-159.
- HAGUE, A. M., THOMAS, D. J., HUBER, M., KORTY, R., WOODARD, S. C. & JONES, L. B. 2012. Convection of North Pacific deep water during the early Cenozoic. *Geology*, 40, 527-530.
- HALL, I. R., MCCAIVE, I. N., SHACKLETON, N. J., WEEDON, G. P. & HARRIS, S. E. 2001. Intensified deep Pacific inflow and ventilation in Pleistocene glacial times. *Nature*, 412, 809-812.
- HASENFRATZ, A. P., MARTÍNEZ-GARCÍA, A., JACCARD, S. L., VANCE, D., WÄLLE, M., GREAVES, M. & HAUG, G. H. 2017a. Determination of the Mg/Mn ratio in foraminiferal coatings: An approach to correct Mg/Ca temperatures for Mn-rich contaminant phases. *Earth and Planetary Science Letters*, 457, 335-347.
- HASENFRATZ, A. P., SCHIEBEL, R., THORNALLEY, D. J. R., SCHÖNFELD, J., JACCARD, S. L., MARTÍNEZ-GARCÍA, A., HOLBOURN, A., JENNINGS, A. E., KUHN, W., LEAR, C. H., MARCHITTO, T. M., QUILLMANN, U., ROSENTHAL, Y., YU, J. & HAUG, G. H. 2017b. Mg/Ca-temperature calibration for the benthic foraminifera *Melonis barleeanum* and *Melonis pompilioides*. *Geochimica et Cosmochimica Acta*, 217, 365-383.
- HASIUK, F. J. & LOHMANN, K. C. 2010. Application of calcite Mg partitioning functions to the reconstruction of paleocean Mg/Ca. *Geochimica et Cosmochimica Acta*, 74, 6751-6763.
- HAUG, G. H., GANOPOLSKI, A., SIGMAN, D. M., ROSELL-MELE, A., SWANN, G. E. A., TIEDEMANN, R., JACCARD, S. L., BOLLMANN, J., MASLIN, M. A., LENG, M. J. & EGLINTON, G. 2005. North Pacific seasonality and the glaciation of North America 2.7 million years ago. *Nature*, 433, 821.
- HAUG, G. H., MASLIN, M., SARNTHEIN, M., STAX, R. & TIEDEMANN, R. 1995. Evolution of Northwest Pacific Sedimentation Patterns since 6 Ma (Site 882). *Proceedings of the Ocean Drilling Program, Scientific Results*, 145, 293-314.
- HAUG, G. H., SIGMAN, D. M., TIEDEMANN, R., PEDERSEN, T. F. & SARNTHEIN, M. 1999. Onset of permanent stratification in the subarctic Pacific Ocean. *Nature*, 401, 799-782.
- HAUG, G. H. & TIEDEMANN, R. 1998. Effect of the formation of the Isthmus of Panama on Atlantic Ocean thermohaline circulation. *Nature*, 393, 673-676.
- HAYS, J. D., IMBRIE, J. & SHACKLETON, N. J. 1976. Variations in the Earth's Orbit: Pacemaker of the Ice Ages. *Science*, 194, 1121-1132.
- HAYWARD, B. W., GRENFELL, H. R., SABAA, A. T. & SIKES, E. 2005. Deep-sea benthic foraminiferal record of the mid-Pleistocene transition in the SW Pacific. In: HEAD, M. J. & GIBBARD, P. L. (eds.) *Early–Middle Pleistocene Transitions: The Land–Ocean Evidence*. Geological Society of London.
- HEINRICH, H. 1988. Origin and consequences of cyclic ice rafting in the Northeast Atlantic Ocean during the past 130,000 years. *Quaternary Research*, 29, 142-152.
- HIGGINS, J. A., KURBATOV, A. V., SPAULDING, N. E., BROOK, E., INTRONE, D. S., CHIMIAK, L. M., YAN, Y., MAYEWSKI, P. A. & BENDER, M. L. 2015. Atmospheric composition 1 million years ago from blue ice in the Allan Hills, Antarctica. *Proceedings of the National Academy of Sciences*, 112, 6887-6891.

- HILL, D. J., HAYWOOD, A. M., VALDES, P. J., FRANCIS, J. E., LUNT, D. J., WADE, B. S. & BOWMAN, V. C. 2013. Paleogeographic controls on the onset of the Antarctic circumpolar current. *Geophysical Research Letters*, 40, 5199-5204.
- HILL, T. M., KENNETT, J. P. & SPERO, H. J. 2003. Foraminifera as indicators of methane-rich environments: A study of modern methane seeps in Santa Barbara Channel, California. *Marine Micropaleontology*, 49, 123-138.
- HILL, T. M., KENNETT, J. P. & VALENTINE, D. L. 2004. Isotopic evidence for the incorporation of methane-derived carbon into foraminifera from modern methane seeps, Hydrate Ridge, Northeast Pacific. *Geochimica et Cosmochimica Acta*, 68, 4619-4627.
- HINRICHS, K.-U. & BOETIUS, A. 2003. The Anaerobic Oxidation of Methane: New Insights in Microbial Ecology and Biogeochemistry. In: WEFER, G., BILLET, D., HEBBELN, D., JØRGENSEN, B. B., SCHLÜTER, M. & WEERING, T. C. E. (eds.) *Ocean Margin Systems*. Berlin, Heidelberg: Springer Berlin Heidelberg.
- HODELL, D. A., VENZ, K. A., CHARLES, C. D. & NINNEMANN, U. S. 2003. Pleistocene vertical carbon isotope and carbonate gradients in the South Atlantic sector of the Southern Ocean. *Geochemistry, Geophysics, Geosystems*, 4, 1-19.
- HOFF, U., RASMUSSEN, T. L., STEIN, R., EZAT, M. M. & FAHL, K. 2016. Sea ice and millennial-scale climate variability in the Nordic seas 90 kyr ago to present. *Nature Communications*, 7, 12247.
- HONG, W.-L., TORRES, M. E., KIM, J.-H., CHOI, J. & BAHK, J.-J. 2013. Carbon cycling within the sulfate-methane-transition-zone in marine sediments from the Ulleung Basin. *Biogeochemistry*, 115, 129-148.
- HÖNISCH, B. & HEMMING, N. G. 2005. Surface ocean pH response to variations in pCO₂ through two full glacial cycles. *Earth and Planetary Science Letters*, 236, 305-314.
- HÖNISCH, B., HEMMING, N. G., ARCHER, D., SIDDALL, M. & MCMANUS, J. F. 2009. Atmospheric Carbon Dioxide Concentration Across the Mid-Pleistocene Transition. *Science*, 324, 1551-1554.
- HOOGAKKER, B. A. A., ELDERFIELD, H., SCHMIEDL, G., MCCAVE, I. N. & RICKABY, R. E. M. 2015. Glacial-interglacial changes in bottom-water oxygen content on the Portuguese margin. *Nature Geosci*, 8, 40-43.
- HORIKAWA, K., ASAHARA, Y., YAMAMOTO, K. & OKAZAKI, Y. 2010. Intermediate water formation in the Bering Sea during glacial periods: Evidence from neodymium isotope ratios. *Geology*, 38, 435-438.
- HORITA, J., ZIMMERMANN, H. & HOLLAND, H. D. 2002. Chemical evolution of seawater during the Phanerozoic: Implications from the record of marine evaporites. *Geochimica et Cosmochimica Acta*, 66, 3733-3756.
- HOWE, J. N. W., PIOTROWSKI, A. M., NOBLE, T. L., MULITZA, S., CHIESSI, C. M. & BAYON, G. 2016. North Atlantic Deep Water Production during the Last Glacial Maximum. *Nature Communications*, 7, 11765.
- HUNT, A. S. & CORLISS, B. H. 1993. Distribution and microhabitats of living (stained) benthic foraminifera from the Canadian Arctic Archipelago. *Marine Micropaleontology*, 20, 321-345.
- HUNT JR, G. L., STABENO, P., WALTERS, G., SINCLAIR, E., BRODEUR, R. D., NAPP, J. M. & BOND, N. A. 2002. Climate change and control of the

- southeastern Bering Sea pelagic ecosystem. *Deep Sea Research Part II: Topical Studies in Oceanography*, 49, 5821-5853.
- HURST, M. P., AGUILAR-ISLAS, A. M. & BRULAND, K. W. 2010. Iron in the southeastern Bering Sea: Elevated leachable particulate Fe in shelf bottom waters as an important source for surface waters. *Continental Shelf Research*, 30, 467-480.
- HUYBERS, P. 2006. Early Pleistocene Glacial Cycles and the Integrated Summer Insolation Forcing. *Science*, 313, 508-511.
- HUYBERS, P. 2011. Combined obliquity and precession pacing of late Pleistocene deglaciations. *Nature*, 480, 229.
- HUYBERS, P. & TZIPERMAN, E. 2008. Integrated summer insolation forcing and 40,000 year glacial cycles: the perspective from an ice-sheet/energy-balance model. *Paleoceanography*, 23, PA1208.
- HUYBERS, P. & WUNSCH, C. 2005. Obliquity pacing of the late Pleistocene glacial terminations. *Nature*, 434, 491-494.
- IKENOUE, T., OKAZAKI, Y., TAKAHASHI, K. & SAKAMOTO, T. 2016. Bering Sea radiolarian biostratigraphy and paleoceanography at IODP Site U1341 during the last four million years. *Deep Sea Research Part II: Topical Studies in Oceanography*, 125, 38-55.
- IMBRIE, J., BERGER, A., BOYLE, E. A., CLEMENS, S. C., DUFFY, A., HOWARD, W. R., KUKLA, G., KUTZBACH, J., MARTINSON, D. G., MCINTYRE, A., MIX, A. C., MOLFINO, B., MORLEY, J. J., PETERSON, L. C., PISIAS, N. G., PRELL, W. L., RAYMO, M. E., SHACKLETON, N. J. & TOGGWEILER, J. R. 1993. On the structure and origin of major glacial cycles 2. The 100,000-year cycle. *Paleoceanography*, 8, 699-735.
- ISHIMURA, T., TSUNOGAI, U., HASEGAWA, S., NAKAGAWA, F., OI, T., KITAZATO, H., SUGA, H. & TOYOFUKU, T. 2012. Variation in stable carbon and oxygen isotopes of individual benthic foraminifera: tracers for quantifying the magnitude of isotopic disequilibrium. *Biogeosciences*, 9, 4353-4367.
- IVANOVA, E. V., OVSEPYAN, E. A., RISEBROBAKKEN, B. & VETROV, A. A. 2008. DOWNCORE DISTRIBUTION OF LIVING CALCAREOUS FORAMINIFERA AND STABLE ISOTOPES IN THE WESTERN BARENTS SEA. *Journal of Foraminiferal Research*, 38, 337-356.
- IWASAKI, S., TAKAHASHI, K., KANEMATSU, Y., ASAHI, H., ONODERA, J. & RAVELO, A. C. 2016. Paleoproductivity and paleoceanography of the last 4.3Myrs at IODP Expedition 323 Site U1341 in the Bering Sea based on biogenic opal content. *Deep Sea Research Part II: Topical Studies in Oceanography*, 125-126, 145-154.
- JACCARD, S. L. & GALBRAITH, E. D. 2012. Large climate-driven changes of oceanic oxygen concentrations during the last deglaciation. *Nature Geoscience*, 5, 151-156.
- JACCARD, S. L. & GALBRAITH, E. D. 2013. Direct ventilation of the North Pacific did not reach the deep ocean during the last deglaciation. *Geophysical Research Letters*, 40, 199-203.
- JACCARD, S. L., GALBRAITH, E. D., SIGMAN, D. M., HAUG, G. H., FRANCOIS, R., PEDERSEN, T. F., DULSKI, P. & THIERSTEIN, H. R. 2009. Subarctic Pacific evidence for a glacial deepening of the oceanic respired carbon pool. *Earth and Planetary Science Letters*, 277, 156-165.

- JACCARD, S. L., HAUG, G. H., SIGMAN, D. M., PEDERSEN, T. F., THIERSTEIN, H. R. & RÖHL, U. 2005. Glacial/Interglacial Changes in Subarctic North Pacific Stratification. *Science*, 308, 1003-1006.
- JACCARD, S. L., HAYES, C. T., MARTÍNEZ-GARCÍA, A., HODELL, D. A., ANDERSON, R. F., SIGMAN, D. M. & HAUG, G. H. 2013. Two Modes of Change in Southern Ocean Productivity Over the Past Million Years. *Science*, 339, 1419-1423.
- JACKSON, C. S. & BROCCOLI, A. J. 2003. Orbital forcing of Arctic climate: mechanisms of climate response and implications for continental glaciation. *Climate Dynamics*, 21, 539-557.
- JACOBEL, A. W., MCMANUS, J. F., ANDERSON, R. F. & WINCKLER, G. 2017. Repeated storage of respired carbon in the equatorial Pacific Ocean over the last three glacial cycles. *Nature Communications*, 8, 1727.
- JANNINK, N. T., ZACHARIASSE, W. J. & VAN DER ZWAAN, G. J. 1998. Living (Rose Bengal stained) benthic foraminifera from the Pakistan continental margin (northern Arabian Sea). *Deep Sea Research Part I: Oceanographic Research Papers*, 45, 1483-1513.
- JOCHUM, K. P., WEIS, U., STOLL, B., KUZMIN, D., YANG, Q., RACZEK, I., JACOB, D. E., STRACKE, A., BIRBAUM, K., FRICK, D. A., GÜNTHER, D. & ENZWEILER, J. 2011. Determination of Reference Values for NIST SRM 610–617 Glasses Following ISO Guidelines. *Geostandards and Geoanalytical Research*, 35, 397-429.
- JONKERS, L., BUSE, B., BRUMMER, G.-J. A. & HALL, I. R. 2016. Chamber formation leads to Mg/Ca banding in the planktonic foraminifer *Neogloboquadrina pachyderma*. *Earth and Planetary Science Letters*, 451, 177-184.
- JORISSEN, F. J. 1999. *Benthic foraminiferal microhabitats below the sediment-water interface*. In: *Modern Foraminifera*, Dordrecht, Springer.
- JORISSEN, F. J., DE STIGTER, H. C. & WIDMARK, J. G. V. 1995. A conceptual model explaining benthic foraminiferal microhabitats. *Marine Micropaleontology*, 26, 3-15.
- JORISSEN, F. J., FONTANIER, C. & THOMAS, E. 2007. Chapter Seven Paleooceanographical Proxies Based on Deep-Sea Benthic Foraminiferal Assemblage Characteristics. In: HILLAIRE-MARCEL, C. & DE VERNAL, A. (eds.) *Developments in Marine Geology*. Elsevier.
- JUDD, A. G., HOVLAND, M., DIMITROV, L. I., GIL, S. G. & JUKES, V. 2002. The geological methane budget at Continental Margins and its influence on climate change. *Geofluids*, 2, 109-126.
- KAIHO, K. 1994. Benthic foraminiferal dissolved-oxygen index and dissolved-oxygen levels in the modern ocean. *Geology*, 22, 719-722.
- KATSUKI, K. & TAKAHASHI, K. 2005. Diatoms as paleoenvironmental proxies for seasonal productivity, sea-ice and surface circulation in the Bering Sea during the late Quaternary. *Deep Sea Research Part II: Topical Studies in Oceanography*, 52, 2110-2130.
- KATSUKI, K., TAKAHASHI, K. & OKADA, M. 2003. Diatom Assemblage and Productivity Changes during the Last 340,000 Years in the Subarctic Pacific. *Journal of Oceanography*, 59, 695-707.
- KATZ, A. 1973. The interaction of magnesium with calcite during crystal growth at 25–90°C and one atmosphere. *Geochimica et Cosmochimica Acta*, 37, 1563-1586.

- KAUFMAN, D. S., AGER, T. A., ANDERSON, N. J., ANDERSON, P. M., ANDREWS, J. T., BARTLEIN, P. J., BRUBAKER, L. B., COATS, L. L., Cwynar, L. C., DUVALL, M. L., DYKE, A. S., EDWARDS, M. E., EISNER, W. R., GAJEWSKI, K., GEIRSDÓTTIR, A., HU, F. S., JENNINGS, A. E., KAPLAN, M. R., KERWIN, M. W., LOZHKIN, A. V., MACDONALD, G. M., MILLER, G. H., MOCK, C. J., OSWALD, W. W., OTTO-BLIESNER, B. L., PORINCHU, D. F., RÜHLAND, K., SMOL, J. P., STEIG, E. J. & WOLFE, B. B. 2004. Holocene thermal maximum in the western Arctic (0–180°W). *Quaternary Science Reviews*, 23, 529-560.
- KAUFMAN, D. S. & MANLEY, W. F. 2004. *Pleistocene Maximum and Late Wisconsinan glacier extents across Alaska, U.S.A.*, Elsevier.
- KAWABE, M. & FUJIO, S. 2010. Pacific ocean circulation based on observation. *Journal of Oceanography*, 66, 389-403.
- KEARNS, S., BUSE, B. & WADE, J. 2014. Mitigating thermal beam damage with metallic coats in low voltage FEG-EPMA of geological materials. *Microscopy and Microanalysis*, 20, 740-741.
- KEIGWIN, L. D. 1998. Glacial-age hydrography of the far northwest Pacific Ocean. *Paleoceanography*, 13, 323-339.
- KELLEY, J. J., LONGERICH, L. L. & HOOD, D. W. 1971. Effect of upwelling, mixing, and high primary productivity on CO₂ concentrations in surface waters of the Bering Sea. *Journal of Geophysical Research*, 76, 86787-8693.
- KEMP, A. E. S., GRIGOROV, I., PEARCE, R. B. & NAVEIRA GARABATO, A. C. 2010. Migration of the Antarctic Polar Front through the mid-Pleistocene transition: evidence and climatic implications. *Quaternary Science Reviews*, 29, 1993-2009.
- KENDER, S., RAVELO, A. C., LENG, M. J., ASAHI, H., BECKER, J., DETLEF, H., WORNE, S., SWANN, G. E. A., RADI, T., AIELLO, I. W., ANDREASEN, D. H. & HALL, I. R. in review. Closure of the Bering Strait and glacial lengthening at the Mid-Pleistocene Transition.
- KHUSID, T. A., BASOV, I. A., GORBARENKO, S. A. & CHEKHOVSKAYA, M. P. 2006. Benthic Foraminifers in Upper Quaternary Sediments of the Southern Bering Sea: Distribution and Paleooceanographic Interpretations. *Stratigraphy and Geological Correlation*, 14, 538-548.
- KIEFER, T. & KIENAST, M. 2005. Patterns of deglacial warming in the Pacific Ocean: a review with emphasis on the time interval of Heinrich event 1. *Quaternary Science Reviews*, 24, 1063-1081.
- KIENAST, S. S. & MCKAY, J. L. 2001. Sea surface temperatures in the subarctic northeast Pacific reflect millennial-scale climate oscillations during the last 16 kyrs. *Geophysical Research Letters*, 28, 1563-1566.
- KILLWORTH, P. 1983. Deep convection in the World Ocean. *Reviews of Geophysics*, 21, 1-26.
- KIM, S., TAKAHASHI, K., KHIM, B.-K., KANEMATSU, Y., ASAHI, H. & RAVELO, A. C. 2014. Biogenic opal production changes during the Mid-Pleistocene Transition in the Bering Sea (IODP Expedition 323 Site U1343). *Quaternary Research*, 81, 151-157.
- KLINKHAMMER, G. P. & PALMER, M. R. 1991. Uranium in the oceans: Where it goes and why. *Geochimica et Cosmochimica Acta*, 55, 1799-1806.
- KNIES, J., CABEDO-SANZ, P., BELT, S. T., BARANWAL, S., FIETZ, S. & ROSELL-MELÉ, A. 2014. The emergence of modern sea ice cover in the Arctic Ocean. *Nature Communications*, 5, 5608.

- KNUDSON, K. P. & RAVELO, A. C. 2015a. Enhanced subarctic Pacific stratification and nutrient utilization during glacials over the last 1.2 Myr. *Geophysical Research Letters*, 42, 9870-9879.
- KNUDSON, K. P. & RAVELO, A. C. 2015b. North Pacific Intermediate Water circulation enhanced by the closure of the Bering Strait. *Paleoceanography*, 30, 1287-1304.
- KOHFELD, K. E. & CHASE, Z. 2011. Controls on deglacial changes in biogenic fluxes in the North Pacific Ocean. *Quaternary Science Reviews*, 30, 3350-3363.
- KOHO, K. A., DE NOOIJER, L. J., FONTANIER, C., TOYOFUKU, T., OGURI, K., KITAZATO, H. & REICHART, G.-J. 2017. Benthic foraminiferal Mn/Ca ratios reflect microhabitat preferences. *Biogeosciences*, 14, 3067.
- KOHO, K. A., DE NOOIJER, L. J. & REICHART, G. J. 2015. Combining benthic foraminiferal ecology and shell Mn/Ca to deconvolve past bottom water oxygenation and paleoproductivity. *Geochimica et Cosmochimica Acta*, 165, 294-306.
- KORFF, L., DOBENECK, T., FREDERICHS, T., KASTEN, S., KUHN, G., GERSONDE, R. & DIEKMANN, B. 2016. Cyclic magnetite dissolution in Pleistocene sediments of the abyssal northwest Pacific Ocean: Evidence for glacial oxygen depletion and carbon trapping. *Paleoceanography*, 31, 600-624.
- KRISTJÁNSDÓTTIR, G. B., LEA, D. W., JENNINGS, A. E., PAK, D. K. & BELANGER, C. 2007. New spatial Mg/Ca-temperature calibrations for three Arctic, benthic foraminifera and reconstruction of north Iceland shelf temperature for the past 4000 years. *Geochemistry, Geophysics, Geosystems*, 8, Q03P21.
- KRYLOV, A. A., ANDREEVA, I. A., VOGT, C., BACKMAN, J., KRUPSKAYA, V. V., GRIKUROV, G. E., MORAN, K. & SHOJI, H. 2008. A shift in heavy and clay mineral provenance indicates a middle Miocene onset of a perennial sea ice cover in the Arctic Ocean. *Paleoceanography*, 23, PA1S06.
- KUEHN, H., LLEMBKE-JENE, L., GERSONDE, R., ESPER, O., LAMY, F., ARZ, H., KUHN, G. & TIEDEMANN, R. 2014. Laminated sediments in the Bering Sea reveal atmospheric teleconnections to Greenland climate on millennial to decadal timescales during the last deglaciation. *Climate of the Past*, 10, 2215-2236.
- KUHLBRODT, T., GRIESEL, A., MONTOYA, M., LEVERMANN, A., HOFMANN, M. & RAHMSTORF, S. 2007. On the driving processes of the Atlantic meridional overturning circulation. *Reviews of Geophysics*, 45, RG2001.
- KUNZENDORF, H., PLUGER, W. L. & FRIEDRICH, G. H. 1983. Uranium in Pacific deep-sea sediments and manganese nodules. *Journal of Geochemical Exploration*, 19, 147-162.
- LADD, C. 2014. Seasonal and interannual variability of the Bering Slope Current. *Deep Sea Research Part II: Topical Studies in Oceanography*, 109, 5-13.
- LADD, C., STABENO, P. J. & O'HERN, J. E. 2012. Observations of a Pribilof eddy. *Deep Sea Research Part I: Oceanographic Research Papers*, 66, 67-76.
- LAM, P. J. & BISHOP, J. K. B. 2008. The continental margin is a key source of iron to the HNLC North Pacific Ocean. *Geophysical Research Letters*, 35, L07608.

- LAM, P. J., ROBINSON, L. F., BLUSZTAJN, J., LI, C., COOK, M. S., MCMANUS, J. F. & KEIGWIN, L. D. 2013. Transient stratification as the cause of the North Pacific productivity spike during deglaciation. *Nature Geoscience*, 6, 622.
- LASKAR, J., ROBUTEL, P., JOUTEL, F., GASTINEAU, M., CORREIA, A. & LEVRARD, B. 2004. A long-term numerical solution for the insolation quantities of the Earth. *Astronomy & Astrophysics*, 428, 261-285.
- LAWRENCE, K. T., HERBERT, T. D., BROWN, C. M., RAYMO, M. E. & HAYWOOD, A. M. 2009. High-amplitude variations in North Atlantic sea surface temperature during the early Pliocene warm period. *Paleoceanography*, 24, PA2218.
- LAWRENCE, K. T., SOSDIAN, S., WHITE, H. E. & ROSENTHAL, Y. 2010. North Atlantic climate evolution through the Plio-Pleistocene climate transitions. *Earth and Planetary Science Letters*, 300, 329-342.
- LAZAR, K. B. & POLYAK, L. 2016. Pleistocene benthic foraminifers in the Arctic Ocean: Implications for sea-ice and circulation history. *Marine Micropaleontology*, 126, 19-30.
- LEA, D. W., MARTIN, P. A., PAK, D. K. & SPERO, H. J. 2002. Reconstructing a 350 kyr history of sea level using planktonic Mg/Ca and oxygen isotopic records from a Cocos Ridge core. *Quaternary Science Reviews*, 21, 283-293.
- LEA, D. W., MASHIOTTA, T. A. & SPERO, H. J. 1999. Controls on magnesium and strontium uptake in planktonic foraminifera determined by live culturing. *Geochimica et Cosmochimica Acta*, 63, 2369-2379.
- LEA, D. W., PAK, D. K. & PARADIS, G. 2005. Influence of volcanic shards on foraminiferal Mg/Ca in a core from the Galápagos region. *Geochemistry, Geophysics, Geosystems*, 6, Q11P04.
- LEAR, C. H., BILLUPS, K., RICKABY, R. E. M., DIESTER-HAASS, L., MAWBNEY, E. M. & SOSDIAN, S. M. 2016. Breathing more deeply: Deep ocean carbon storage during the mid-Pleistocene climate transition. *Geology*, 44, 1035-1038.
- LEAR, C. H., COXALL, H. K., FOSTER, G. L., LUNT, D. J., MAWBNEY, E. M., ROSENTHAL, Y., SOSDIAN, S. M., THOMAS, E. & WILSON, P. A. 2015. Neogene ice volume and ocean temperatures: Insights from infaunal foraminiferal Mg/Ca paleothermometry. *Paleoceanography*, 30, 1437-1454.
- LEAR, C. H., ELDERFIELD, H. & WILSON, P. A. 2000. Cenozoic Deep-Sea Temperatures and Global Ice Volumes from Mg/Ca in Benthic Foraminiferal Calcite. *Science*, 287, 269-272.
- LEAR, C. H., MAWBNEY, E. M. & ROSENTHAL, Y. 2010. Cenozoic benthic foraminiferal Mg/Ca and Li/Ca records: Toward unlocking temperatures and saturation states. *Paleoceanography*, 25, PA4215.
- LEAR, C. H. & ROSENTHAL, Y. 2006. Benthic foraminiferal Li/Ca: Insights into Cenozoic seawater carbonate saturation state. *Geology*, 34, 985-988.
- LEAR, C. H., ROSENTHAL, Y. & SLOWEY, N. 2002. Benthic foraminiferal Mg/Ca-paleothermometry: a revised core-top calibration. *Geochimica et Cosmochimica Acta*, 66, 3375-3387.
- LEAR, C. H., ROSENTHAL, Y. & WRIGHT, J. D. 2003. The closing of a seaway: ocean water masses and global climate change. *Earth and Planetary Science Letters*, 210, 425-436.
- LEBLANC, K., HARE, C. E., BOYD, P. W., BRULAND, K. W., SOHST, B., PICKMERE, S., LOHAN, M. C., BUCK, K., ELLWOOD, M. & HUTCHINS, D. A. 2005. Fe and Zn effects on the Si cycle and diatom community structure

- in two contrasting high and low-silicate HNLC areas. *Deep Sea Research Part I: Oceanographic Research Papers*, 52, 1842-1864.
- LEE, J.-E., SHEN, A., FOX-KEMPER, B. & MING, Y. 2017. Hemispheric sea ice distribution sets the glacial tempo. *Geophysical Research Letters*, 44, 1008-1014.
- LEGRANDE, A. N. & SCHMIDT, G. A. 2006. Global gridded data set of the oxygen isotopic composition in seawater. *Geophysical Research Letters*, 33, L12604.
- LI, Y.-H. 1982. A brief discussion on the mean oceanic residence time of elements. *Geochimica et Cosmochimica Acta*, 46, 2671-2675.
- LIN, Q., WANG, J., ALGEO, T. J., SUN, F. & LIN, R. 2016. Enhanced framboidal pyrite formation related to anaerobic oxidation of methane in the sulfate-methane transition zone of the northern South China Sea. *Marine Geology*, 379, 100-108.
- LINGLING, X. & MIN, D. 2005. Dolomite used as raw material to produce MgO-based expansive agent. *Cement and Concrete Research*, 35, 1480-1485.
- LISIECKI, L. E. 2010. Links between eccentricity forcing and the 100,00-year glacial cycle. *Nature Geoscience*, 349-352.
- LISIECKI, L. E. & RAYMO, M. E. 2005. A Pliocene-Pleistocene stack of 57 globally distributed $\delta^{18}\text{O}$ records. *Paleoceanography*, 20, PA1003.
- LISIECKI, L. E. & RAYMO, M. E. 2007. Plio-Pleistocene climate evolution: trends and transitions in glacial cycle dynamics. *Quaternary Science Reviews*, 26, 56-69.
- LO, L., BELT, S. T., LATTAUD, J., FRIEDRICH, T., ZEEDEN, C., SCHOUTEN, S., SMIK, L., TIMMERMANN, A., CABEDO-SANZ, P., HUANG, J.-J., ZHOU, L., OU, T.-H., CHANG, Y.-P., WANG, L.-C., CHOU, Y.-M., SHEN, C.-C., CHEN, M.-T., WEI, K.-Y., SONG, S.-R., FANG, T.-H., GORBARENKO, S. A., WANG, W.-L., LEE, T.-Q., ELDERFIELD, H. & HODELL, D. A. 2018. Precession and atmospheric CO₂ modulated variability of sea ice in the central Okhotsk Sea since 130,000 years ago. *Earth and Planetary Science Letters*, 488, 36-45.
- LOCARNINI, R. A., MISHONOV, A. V., ANTONOV, J. I., BOYER, T. P. & GARCIA, H. E. 2006. World Ocean Atlas 2005, Volume 1: Temperature. In: LEVITUS, S. (ed.) *NOAA Atlas NESDIS 61*. Washington, D.C.: U.S. Government Printing Office.
- LONGERICH, H. P., JACKSON, S. E. & D., G. 1996. Laser Ablation Inductively Coupled Plasma Mass Spectrometric Transient Signal Data Acquisition and Analyte Concentration Calculation. *Journal of Analytical Atomic Spectrometry* 11, 899-904.
- LOWENSTEIN, T. K., TIMOFEEFF, M. N., BRENNAN, S. T., HARDIE, L. A. & DEMICCO, R. V. 2001. Oscillations in Phanerozoic Seawater Chemistry: Evidence from Fluid Inclusions. *Science*, 294, 1086-1088.
- LU, Z., JENKYN, H. C. & RICKABY, R. E. M. 2010. Iodine to calcium ratios in marine carbonate as a paleo-redox proxy during oceanic anoxic events. *Geology*, 38, 1107-1110.
- LUGOVSKAYA, I. G., DUBINCHUK, V. T. & BATURIN, G. N. 2007. Composition of technological sample of ferromanganese crusts from seamounts and products of its processing. *Lithology and Mineral Resources*, 42, 515-522.
- LUND, D. C., MIX, A. C. & SOUTON, J. 2011. Increased ventilation age of the deep northeast Pacific Ocean during the last deglaciation. *Nature Geoscience*, 4, 771.

- LYLE, M., BARRON, J., BRALOWER, T. J., HUBER, M., OLIVAREZ LYLE, A., RAVELO, A. C., REA, D. K. & WILSON, P. A. 2008. Pacific Ocean and Cenozoic evolution of climate. *Reviews of Geophysics*, 46, RG2002.
- LYNCH-STIEGLITZ, J. 2006. Tracers of past ocean circulation. *Treatise on geochemistry*, 6, 433-451.
- MANABE, S. & STOUFFER, R. J. 1988. Two Stable Equilibria of a Coupled Ocean-Atmosphere Model. *Journal of Climate*, 1, 841-866.
- MARCHITTO, T. M., CURRY, W. B., LYNCH-STIEGLITZ, J., BRYAN, S. P., COBB, K. M. & LUND, D. C. 2014. Improved oxygen isotope temperature calibrations for cosmopolitan benthic foraminifera. *Geochimica et Cosmochimica Acta*, 130, 1-11.
- MARCHITTO, T. M., LYNCH-STIEGLITZ, J. & HEMMING, S. R. 2005. Deep Pacific CaCO₃ compensation and glacial–interglacial atmospheric CO₂. *Earth and Planetary Science Letters*, 231, 317-336.
- MARRIOTT, C. S., HENDERSON, G. M., CROMPTON, R., STAUBWASSER, M. & SHAW, S. 2004. Effect of mineralogy, salinity, and temperature on Li/Ca and Li isotope composition of calcium carbonate. *Chemical Geology*, 212, 5-15.
- MARTIN, J. H. 1990. Glacial-interglacial CO₂ change: The Iron Hypothesis. *Paleoceanography*, 5, 1-13.
- MARTIN, P. A., LEA, D. W., ROSENTHAL, Y., SHACKLETON, N. J., SARNTHEIN, M. & PAPENFUSS, T. 2002. Quaternary deep sea temperature histories derived from benthic foraminiferal Mg/Ca. *Earth and Planetary Science Letters*, 198, 193-209.
- MARTIN, W. R. & SAYLES, F. L. 1996. CaCO₃ dissolution in sediments of the Ceara Rise, western equatorial Atlantic. *Geochimica et Cosmochimica Acta*, 60, 243-263.
- MARTIN, W. R. & SAYLES, F. L. 2006. Organic matter oxidation in deep-sea sediments: Distribution in the sediment column and implications for calcite dissolution. *Deep Sea Research Part II: Topical Studies in Oceanography*, 53, 771-792.
- MARTINEZ-BOTI, M. A., FOSTER, G. L., CHALK, T. B., ROHLING, E. J., SEXTON, P. F., LUNT, D. J., PANCOST, R. D., BADGER, M. P. S. & SCHMIDT, D. N. 2015. Plio-Pleistocene climate sensitivity evaluated using high-resolution CO₂ records. *Nature*, 518, 49-54.
- MARTÍNEZ-GARCÍA, A., ROSELL-MELÉ, A., MCCLYMONT, E. L., GERSONDE, R. & HAUG, G. H. 2010. Subpolar Link to the Emergence of the Modern Equatorial Pacific Cold Tongue. *Science*, 328, 1550-1553.
- MARTÍNEZ-GARCÍA, A., SIGMAN, D. M., REN, H., ANDERSON, R. F., STRAUB, M., HODELL, D. A., JACCARD, S. L., EGLINTON, T. I. & HAUG, G. H. 2014. Iron Fertilization of the Subantarctic Ocean During the Last Ice Age. *Science*, 343, 1347-1350.
- MATSUMOTO, K., OBA, T., LYNCH-STIEGLITZ, J. & YAMAMOTO, H. 2002. Interior hydrography and circulation of the glacial Pacific Ocean. *Quaternary Science Reviews*, 21, 1693-1704.
- MATUL, A. G. 2017. Probable limits of sea ice extent in the northwestern Subarctic Pacific during the last glacial maximum. *Oceanology*, 57, 700-706.
- MAWBEY, E. M. & LEAR, C. H. 2013. Carbon cycle feedbacks during the Oligocene-Miocene transient glaciation. *Geology*, 41, 963-966.

- MAX, L., LEMBKE-JENE, L., RIETHDORF, J. R., TIEDEMANN, R., NUERNBERG, D., KUEHN, H. & MACKENSEN, A. 2014. Pulses of enhanced North Pacific Intermediate Water ventilation from the Okhotsk Sea and Bering Sea during the last deglaciation. *Climate of the Past*, 10, 591-605.
- MAX, L., RIETHDORF, J.-R., TIEDEMANN, R., SMIRNOVA, M., LEMBKE-JENE, L., FAHL, K., NÜRNBERG, D., MATUL, A. & MOLLENHAUER, G. 2012. Sea surface temperature variability and sea-ice extent in the subarctic northwest Pacific during the past 15,000 years. *Paleoceanography*, 27, PA3213.
- MAX, L., RIPPERT, N., LEMBKE-JENE, L., MACKENSEN, A., NÜRNBERG, D. & TIEDEMANN, R. 2017. Evidence for enhanced convection of North Pacific Intermediate Water to the low-latitude Pacific under glacial conditions. *Paleoceanography*, 32, 41–55.
- MAY, T. W. & WIEDMEYER, R. H. 1998. A table of polyatomic interferences in ICP-MS. *Atomic Spectroscopy*, 19, 150-155.
- MCCLYMONT, E. L., ELMORE, A. C., KENDER, S., LENG, M. J., GREAVES, M. & ELDERFIELD, H. 2016. Pliocene-Pleistocene evolution of sea surface and intermediate water temperatures from the southwest Pacific. *Paleoceanography*, 31, 895-913.
- MCCLYMONT, E. L. & ROSELL-MELÉ, A. 2005. Links between the onset of modern Walker circulation and the mid-Pleistocene climate transition. *Geology*, 33, 389-392.
- MCCLYMONT, E. L., ROSELL-MELÉ, A., HAUG, G. H. & LLOYD, J. M. 2008. Expansion of subarctic water masses in the North Atlantic and Pacific oceans and implications for mid-Pleistocene ice sheet growth. *Paleoceanography*, 23, PA4214.
- MCCLYMONT, E. L., SOSDIAN, S. M., ROSELL-MELÉ, A. & ROSENTHAL, Y. 2013. Pleistocene sea-surface temperature evolution: Early cooling, delayed glacial intensification, and implications for the mid-Pleistocene climate transition. *Earth-Science Reviews*, 123, 173-193.
- MCCORKLE, D. C., MARTIN, P. A., LEA, D. W. & KLINKHAMMER, G. P. 1995. Evidence of a dissolution effect on benthic foraminiferal shell chemistry: $\delta^{13}\text{C}$, Cd/Ca, Ba/Ca, and Sr/Ca results from the Ontong Java Plateau. *Paleoceanography*, 10, 699-714.
- MCKAY, C., GROENEVELD, J., FILIPSSON, H. L., GALLEGO-TORRES, D., WHITEHOUSE, M. J., TOYOFUKU, T. & ROMERO, O. E. 2015. A comparison of benthic foraminiferal Mn/Ca and sedimentary Mn/Al as proxies of relative bottom-water oxygenation in the low-latitude NE Atlantic upwelling system. *Biogeosciences*, 12, 5415-5428.
- MCKAY, C. L., FILIPSSON, H. L., ROMERO, O. E., STUUT, J.-B. W. & BJÖRCK, S. 2016. The interplay between the surface and bottom water environment within the Benguela Upwelling System over the last 70 ka. *Paleoceanography*, 31, 266-285.
- MCMANUS, J., BERELSON, W. M., KLINKHAMMER, G. P., HAMMOND, D. E. & HOLM, C. 2005. Authigenic uranium: Relationship to oxygen penetration depth and organic carbon rain. *Geochimica et Cosmochimica Acta*, 69, 95-108.
- MCMANUS, J. F., FRANCOIS, R., GHERARDI, J.-M., KEIGWIN, L. D. & BROWN-LEGER, S. 2004. Collapse and rapid resumption of Atlantic meridional circulation linked to deglacial climate changes. *Nature*, 428, 834-837.

- MEDINA-ELIZALDE, M. & LEA, D. W. 2005. The Mid-Pleistocene Transition in the Tropical Pacific. *Science*, 310, 1009-1012.
- MEDINA-ELIZALDE, M., LEA, D. W. & FANTLE, M. S. 2008. Implications of seawater Mg/Ca variability for Plio-Pleistocene tropical climate reconstruction. *Earth and Planetary Science Letters*, 269, 585-595.
- MÉHEUST, M., FAHL, K. & STEIN, R. 2013. Variability in modern sea surface temperature, sea ice and terrigenous input in the sub-polar North Pacific and Bering Sea: Reconstruction from biomarker data. *Organic Geochemistry*, 57, 54-64.
- MÉHEUST, M., STEIN, R., FAHL, K. & GERSONDE, R. 2018. Sea-ice variability in the subarctic North Pacific and adjacent Bering Sea during the past 25 ka: new insights from IP25 and Uk'37 proxy records. *arktos*, 4, 8.
- MÉHEUST, M., STEIN, R., FAHL, K., MAX, L. & RIETHDORF, J.-R. 2016. High-resolution IP₂₅-based reconstruction of sea-ice variability in the western North Pacific and Bering Sea during the past 18,000 years. *Geo-Marine Letters*, 36, 101-111.
- MEHRBACH, C., CULBERSON, C. H., HAWLEY, J. E. & PYTKOWICX, R. M. 1973. MEASUREMENT OF THE APPARENT DISSOCIATION CONSTANTS OF CARBONIC ACID IN SEAWATER AT ATMOSPHERIC PRESSURE. *Limnology and Oceanography*, 18, 897-907.
- MEMBERS, N. G. I. C. P. 2007. 50 year means of oxygen isotope data from ice core NGRIP. *Supplement to: North Greenland Ice Core Project Members (2004): High-resolution record of Northern Hemisphere climate extending into the last interglacial period. Nature*, 431, 147-151, <https://doi.org/10.1038/nature02805>. PANGAEA.
- MEYER, V. D., MAX, L., HEFTER, J., TIEDEMANN, R. & MOLLENHAUER, G. 2016. Glacial-to-Holocene evolution of sea surface temperature and surface circulation in the subarctic northwest Pacific and the Western Bering Sea. *Paleoceanography*, 31, 916-927.
- MIETTINEN, A., KOÇ, N. & HUSUM, K. 2013. Appearance of the Pacific diatom *Neodenticula seminae* in the northern Nordic Seas — An indication of changes in Arctic sea ice and ocean circulation. *Marine Micropaleontology*, 99, 2-7.
- MILANKOVITCH, M. 1941. Kanon der Erdbestrahlung und seine Anwendung auf das Eiszeitenproblem. *R. Serbian Acad., Belgrade*, 133, 1-633.
- MILLER, K. G., FAIRBANKS, R. G. & MOUNTAIN, G. S. 1987. Tertiary oxygen isotope synthesis, sea level history, and continental margin erosion. *Paleoceanography*, 2, 1-19.
- MILLER, R. J., HOCEVAR, J., STONE, R. P. & FEDOROV, D. V. 2012. Structure-forming corals and sponges and their use as fish habitat in Bering Sea submarine canyons. *PLoS One*, 7, e33885.
- MILLERO, F. J. 2013. *Chemical oceanography*, CRC press.
- MILLO, C., SARNTHEIN, M., ERLLENKEUSER, H., GROOTES, P. M. & ANDERSEN, N. 2005. Methane-induced early diagenesis of foraminiferal tests in the southwestern Greenland Sea. *Marine Micropaleontology*, 58, 1-12.
- MIURA, T., SUGA, T. & HANAWA, K. 2002. Winter Mixed Layer and Formation of Dichothermal Water in the Bering Sea. *Journal of Oceanography*, 58, 815-823.
- MIX, A. C., PISIAS, N. G., RUGH, W., WILSON, J., MOREY, A. & HAGELBERG, T. K. 1995. Benthic foraminifer stable isotope record from Site 849 (0–5Ma):

- Local and global climate changes. *Proceedings of the Ocean Drilling Program, Sci. Res.*, 138, 371–412.
- MIZOBATA, K. & SAITOH, S.-I. 2004. Variability of Bering Sea eddies and primary productivity along the shelf edge during 1998–2000 using satellite multisensor remote sensing. *Journal of Marine Systems*, 50, 101–111.
- MIZOBATA, K., SAITOH, S.-I. & WANG, J. 2008. Interannual variability of summer biochemical enhancement in relation to mesoscale eddies at the shelf break in the vicinity of the Pribilof Islands, Bering Sea. *Deep Sea Research Part II: Topical Studies in Oceanography*, 55, 1717–1728.
- MIZOBATA, K., SAITOH, S. I., SHIOMOTO, A., MIYAMURA, T., SHIGA, N., IMAI, K., TORATANI, M., KAJIWARA, Y. & SASAOKA, K. 2002. Bering Sea cyclonic and anticyclonic eddies observed during summer 2000 and 2001. *Progress in Oceanography*, 55, 65–75.
- MIZOBATA, K., WANG, J. & SAITOH, S.-I. 2006. Eddy-induced cross-slope exchange maintaining summer high productivity of the Bering Sea shelf break. *Journal of Geophysical Research: Oceans*, 111, C10017.
- MOFFITT, S. E., MOFFITT, R. A., SAUTHOFF, W., DAVIS, C. V., HEWETT, K. & HILL, T. M. 2015. Paleoceanographic Insights on Recent Oxygen Minimum Zone Expansion: Lessons for Modern Oceanography. *PLoS ONE*, 10, e0115246.
- MOLNAR, P., ENGLAND, P. & MARTINOD, J. 1993. Mantle dynamics, uplift of the Tibetan Plateau, and the Indian Monsoon. *Reviews of Geophysics*, 31, 357–396.
- MOORE, J. K., DONEY, S. C., GLOVER, D. M. & FUNG, I. Y. 2001. Iron cycling and nutrient-limitation patterns in surface waters of the World Ocean. *Deep Sea Research Part II: Topical Studies in Oceanography*, 49, 463–507.
- MORAN, K., BACKMAN, J., BRINKHUIS, H., CLEMENS, S. C., CRONIN, T., DICKENS, G. R., EYNAUD, F., GATTACCECA, J., JAKOBSSON, M., JORDAN, R. W., KAMINSKI, M., KING, J., KOC, N., KRYLOV, A., MARTINEZ, N., MATTHIESSEN, J., MCINROY, D., MOORE, T. C., ONODERA, J., O'REGAN, M., PÁLIKE, H., REA, B., RIO, D., SAKAMOTO, T., SMITH, D. C., STEIN, R., ST JOHN, K., SUTO, I., SUZUKI, N., TAKAHASHI, K., WATANABE, M., YAMAMOTO, M., FARRELL, J., FRANK, M., KUBIK, P., JOKAT, W. & KRISTOFFERSEN, Y. 2006. The Cenozoic palaeoenvironment of the Arctic Ocean. *Nature*, 441, 601.
- MORDY, C. W., STABENO, P. J., LADD, C., ZEEMAN, S., WISEGARVER, D. P., SALO, S. A. & HUNT, G. L. 2005. Nutrients and primary production along the eastern Aleutian Island Archipelago. *Fisheries Oceanography*, 14, 55–76.
- MORFORD, J. L. & EMERSON, S. 1999. The geochemistry of redox sensitive trace metals in sediments. *Geochimica et Cosmochimica Acta*, 63, 1735–1750.
- MORFORD, J. L., MARTIN, W. R., KALNEJAIS, L. H., FRANÇOIS, R., BOTHNER, M. & KARLE, I.-M. 2007. Insights on geochemical cycling of U, Re and Mo from seasonal sampling in Boston Harbor, Massachusetts, USA. *Geochimica et Cosmochimica Acta*, 71, 895–917.
- MOTOI, T., CHAN, W. L., MINOBE, S. & SUMATA, H. 2005. North Pacific halocline and cold climate induced by Panamanian Gateway closure in a coupled ocean-atmosphere GCM. *Geophysical Research Letters*, 32, L10618.

- MUCCI, A. 1987. Influence of temperature on the composition of magnesian calcite overgrowths precipitated from seawater. *Geochimica et Cosmochimica Acta*, 51, 1977-1984.
- MUCCI, A. & MORSE, J. W. 1983. The incorporation of Mg²⁺ and Sr²⁺ into calcite overgrowths: influences of growth rate and solution composition. *Geochimica et Cosmochimica Acta*, 47, 217-233.
- MUDELSEE, M. 2003. Estimating Pearson's Correlation Coefficient With Bootstrap Confidence Interval From Serially Dependent Time Series. *Mathematical Geology*, 35, 651–665.
- MUDELSEE, M. & SCHULZ, M. 1997. The Mid-Pleistocene climate transition: onset of 100 ka cycle lags ice volume build-up by 280 ka. *Earth and Planetary Science Letters*, 151, 117-123.
- MUETER, F. J. & LITZOW, M. A. 2008. SEA ICE RETREAT ALTERS THE BIOGEOGRAPHY OF THE BERING SEA CONTINENTAL SHELF. *Ecological Applications*, 18, 309-320.
- MUHS, D. R., AGER, T. A., ARTHUR BETTIS III, E., MCGEEHIN, J., BEEN, J. M., BEGÉT, J. E., PAVICH, M. J., STAFFORD JR, T. W. & STEVENS, D. A. S. P. 2003. Stratigraphy and palaeoclimatic significance of Late Quaternary loess–palaeosol sequences of the Last Interglacial–Glacial cycle in central Alaska. *Quaternary Science Reviews*, 22, 1947-1986.
- MÜLLER, J., MASSE, G., STEIN, R. & BELT, S. T. 2009. Variability of sea-ice conditions in the Fram Strait over the past 30,000 years. *Nature Geoscience*, 2, 772-776.
- MÜLLER, J., ROMERO, O. E., COWAN, E. A., MCCLYMONT, E. L., FORWICK, M., ASAHI, H., MÄRZ, C., MOY, C. M., SUTO, I., MIX, A. C. & STONER, J. S. 2018. Cordilleran ice-sheet growth fueled primary productivity in the Gulf of Alaska, northeast Pacific Ocean. *Geology*, 46, 307-310.
- MÜLLER, J. & STEIN, R. 2014. High-resolution record of late glacial and deglacial sea ice changes in Fram Strait corroborates ice–ocean interactions during abrupt climate shifts. *Earth and Planetary Science Letters*, 403, 446-455.
- MÜLLER, J., WAGNER, A., FAHL, K., STEIN, R., PRANGE, M. & LOHMANN, G. 2011. Towards quantitative sea ice reconstructions in the northern North Atlantic: A combined biomarker and numerical modelling approach. *Earth and Planetary Science Letters*, 306, 137-148.
- MURRAY, J. W. 1989. Syndepositional dissolution of calcareous foraminifera in modern shallow-water sediments. *Marine Micropaleontology*, 15, 117-121.
- NAVARRO-RODRIGUEZ, A., BELT, S. T., KNIES, J. & BROWN, T. A. 2013. Mapping recent sea ice conditions in the Barents Sea using the proxy biomarker IP₂₅: implications for palaeo sea ice reconstructions. *Quaternary Science Reviews*, 79, 26-39.
- NIEBAUER, H. J., BOND, N. A., YAKUNIN, L. P. & PLOTNIKOV, V. V. 1999. An Update on the Climatology and Sea Ice of the Bering Sea edited by T.R. Loughlin and K. Ohtani. *Dynamics of the Bering Sea: A summary of Physical, Chemical, and Biological Characteristics, and a Synopsis of Research on the Bering Sea, Alaskan Sea Grant College Report No. AK-SG-99-03*, 29-59.
- NORRIS, R. D. & WILSON, P. A. 1998. Low-latitude sea-surface temperatures for the mid-Cretaceous and the evolution of planktic foraminifera. *Geology*, 26, 823-826.

- NÜRNBERG, D., BIJMA, J. & HEMLEBEN, C. 1996. Assessing the reliability of magnesium in foraminiferal calcite as a proxy for water mass temperatures. *Geochimica et Cosmochimica Acta*, 60, 803-814.
- OERLEMANS, J. 1984. On the origin of the ice ages. *Milankovitch and Climate*. Springer.
- OHKUSHI, K. I., ITAKI, T. & NEMOTO, N. 2003. Last Glacial–Holocene change in intermediate-water ventilation in the Northwestern Pacific. *Quaternary Science Reviews*, 22, 1477-1484.
- OKAZAKI, Y., KIMOTO, K., ASAHI, H., SATO, M., NAKAMURA, Y. & HARADA, N. 2014. Glacial to deglacial ventilation and productivity changes in the southern Okhotsk Sea. *Palaeogeography, Palaeoclimatology, Palaeoecology*, 395, 53-66.
- OKAZAKI, Y., SAGAWA, T., ASAHI, H., HORIKAWA, K. & ONODERA, J. 2012. Ventilation changes in the western North Pacific since the last glacial period. *Climate of the Past*, 8, 17-24.
- OKAZAKI, Y., TAKAHASHI, K., ASAHI, H., KATSUKI, K., HORI, J., YASUDA, H., SAGAWA, Y. & TOKUYAMA, H. 2005. Productivity changes in the Bering Sea during the late Quaternary. *Deep Sea Research Part II: Topical Studies in Oceanography*, 52, 2150-2162.
- OKAZAKI, Y., TIMMERMANN, A., MENVIEL, L., HARADA, N., ABE-OUCHI, A., CHIKAMOTO, M. O., MOUCHET, A. & ASAHI, H. 2010. Deepwater Formation in the North Pacific During the Last Glacial Termination. *Science*, 329, 200-204.
- OKUMURA, Y. M., DESER, C., HU, A., TIMMERMANN, A. & XIE, S.-P. 2009. North Pacific Climate Response to Freshwater Forcing in the Subarctic North Atlantic: Oceanic and Atmospheric Pathways. *Journal of Climate*, 22, 1424-1445.
- OLSEN, A., KEY, R. M., VAN HEUVEN, S., LAUVSET, S. K., VELO, A., LIN, X., SCHIRNICK, C., KOZYR, A., TANHUA, T., HOPPEMA, M., JUTTERSTRÖM, S., STEINFELDT, R., JEANSSON, E., ISHII, M., PÉREZ, F. F. & SUZUKI, T. 2016. The Global Ocean Data Analysis Project version 2 (GLODAPv2) – an internally consistent data product for the world ocean. *Earth Syst. Sci. Data*, 8, 297-323.
- OOMORI, T., KANESHIMA, H., MAEZATO, Y. & KITANO, Y. 1987. Distribution coefficient of Mg²⁺ ions between calcite and solution at 10–50°C. *Marine Chemistry*, 20, 327-336.
- OVSEPYAN, E. A., IVANOVA, E. V., LEMBKE-JENE, L., MAX, L., TIEDEMANN, R. & NÜRNBERG, D. 2017. Penultimate and last glacial oceanographic variations in the Bering Sea on millennial timescales: Links to North Atlantic climate. *Quaternary Science Reviews*, 163, 135-151.
- OVSEPYAN, E. A., IVANOVA, E. V., MAX, L., RIETHDORF, J.-R., NÜRNBERG, D. & TIEDEMANN, R. 2013. Late quaternary oceanographic conditions in the Western Bering Sea. *Oceanology*, 53, 211-222.
- PAILLARD, D., LABEYRIE, L. & YIOU, P. 1996. Macintosh Program performs time-series analysis. *Eos, Transactions American Geophysical Union*, 77, 379-379.
- PALUSZKIEWICZ, T. & NIEBAUER, H. J. 1984. Satellite observations of circulation in the eastern Bering Sea. *Journal of Geophysical Research: Oceans*, 89, 3663-3678.

- PANIERI, G., LEPLAND, A., WHITEHOUSE, M. J., WIRTH, R., RAANES, M. P., JAMES, R. H., GRAVES, C. A., CRÉMIÈRE, A. & SCHNEIDER, A. 2017. Diagenetic Mg-calcite overgrowths on foraminiferal tests in the vicinity of methane seeps. *Earth and Planetary Science Letters*, 458, 203-212.
- PARRENIN, F., CAVITTE, M. G. P., BLANKENSHIP, D. D., CHAPPELLAZ, J., FISCHER, H., GAGLIARDINI, O., MASSON-DELMOTTE, V., PASSALACQUA, O., RITZ, C., ROBERTS, J., SIEGERT, M. J. & YOUNG, D. A. 2017. Is there 1.5-million-year-old ice near Dome C, Antarctica? *The Cryosphere*, 11, 2427-2437.
- PARRENIN, F. & PAILLARD, D. 2003. Amplitude and phase of glacial cycles from a conceptual model. *Earth and Planetary Science Letters*, 214, 243-250.
- PATTAN, J. N. 1993. Manganese micronodules: A possible indicator of sedimentary environments. *Marine Geology*, 113, 331-344.
- PATTAN, J. N. & PEARCE, N. J. G. 2009. Bottom water oxygenation history in southeastern Arabian Sea during the past 140ka: Results from redox-sensitive elements. *Palaeogeography, Palaeoclimatology, Palaeoecology*, 280, 396-405.
- PEARSON, P. N., DITCHFIELD, P. W., SINGANO, J., HARCOURT-BROWN, K. G., NICHOLAS, C. J., OLSSON, R. K., SHACKLETON, N. J. & HALL, M. A. 2001. Warm tropical sea surface temperatures in the Late Cretaceous and Eocene epochs. *Nature*, 413, 481-487.
- PEARSON, P. N., FOSTER, G. L. & WADE, B. S. 2009. Atmospheric carbon dioxide through the Eocene–Oligocene climate transition. *Nature*, 461, 1110.
- PEARSON, P. N. & PALMER, M. R. 2000. Atmospheric carbon dioxide concentrations over the past 60 million years. *Nature*, 406, 695-699.
- PECKMANN, J., REIMER, A., LUTH, U., LUTH, C., HANSEN, B. T., HEINICKE, C., HOEFS, J. & REITNER, J. 2001. Methane-derived carbonates and authigenic pyrite from the northwestern Black Sea. *Marine Geology*, 177, 129-150.
- PEDERSEN, T. F. & PRICE, N. B. 1982. The geochemistry of manganese carbonate in Panama Basin sediments. *Geochimica et Cosmochimica Acta*, 46, 59-68.
- PELTO, B. M., CAISSIE, B. E., PETSCH, S. T. & BRIGHAM-GRETTE, J. 2018. Oceanographic and Climatic Change in the Bering Sea, Last Glacial Maximum to Holocene. *Paleoceanography and Paleoclimatology*, 33, 93-111.
- PENA, L. D., CACHO, I., CALVO, E., PELEJERO, C., EGGINS, S. & SADEKOV, A. 2008. Characterization of contaminant phases in foraminifera carbonates by electron microprobe mapping. *Geochemistry, Geophysics, Geosystems*, 9, Q07012.
- PENA, L. D., CALVO, E., CACHO, I., EGGINS, S. & PELEJERO, C. 2005. Identification and removal of Mn-Mg-rich contaminant phases on foraminiferal tests: Implications for Mg/Ca past temperature reconstructions. *Geochemistry, Geophysics, Geosystems*, 6, Q09P02.
- PENA, L. D. & GOLDSTEIN, S. L. 2014. Thermohaline circulation crisis and impacts during the mid-Pleistocene transition. *Science*, 345, 318-322.
- PETERSEN, J., BARRAS, C., BEZOS, A., LA, C., DE NOOIJER, L. J., MEYSMAN, F. J. R., MOURET, A., SLOMP, C. P. & JORISSEN, F. J. 2018. Mn/Ca intra- and inter-test variability in the benthic foraminifer *Ammonia tepida*. *Biogeosciences*, 15, 331-348.
- PIERRE, C., BLANC-VALLERON, M. M., CAQUINEAU, S., MÄRZ, C., RAVELO, A. C., TAKAHASHI, K. & ALVAREZ ZARIKIAN, C. 2016.

- Mineralogical, geochemical and isotopic characterization of authigenic carbonates from the methane-bearing sediments of the Bering Sea continental margin (IODP Expedition 323, Sites U1343–U1345). *Deep Sea Research Part II: Topical Studies in Oceanography*, 125-126, 133-144.
- PIERRE, C. & FOUQUET, Y. 2007. Authigenic carbonates from methane seeps of the Congo deep-sea fan. *Geo-Marine Letters*, 27, 249-257.
- PISIAS, N. G., MIX, A. C. & HEUSSER, L. 2001. Millennial scale climate variability of the northeast Pacific Ocean and northwest North America based on radiolaria and pollen. *Quaternary Science Reviews*, 20, 1561-1576.
- PISIAS, N. G. & MOORE JR, T. C. 1981. The evolution of Pleistocene climate: A time series approach. *Earth and Planetary Science Letters*, 52, 450-458.
- POLLARD, D. & DECONTO, R. M. 2009. Modelling West Antarctic ice sheet growth and collapse through the past five million years. *Nature*, 458, 329.
- RAE, J. W. B., SARNTHEIN, M., FOSTER, G. L., RIDGWELL, A., GROOTES, P. M. & ELLIOTT, T. 2014. Deep water formation in the North Pacific and deglacial CO₂ rise. *Paleoceanography*, 29, 645–667.
- RAITZSCH, M., KUHNERT, H., GROENEVELD, J. & BICKERT, T. 2008. Benthic foraminifer Mg/Ca anomalies in South Atlantic core top sediments and their implications for paleothermometry. *Geochemistry, Geophysics, Geosystems*, 9, Q05010.
- RAITZSCH, M., KUHNERT, H., HATHORNE, E. C., GROENEVELD, J. & BICKERT, T. 2011. U/Ca in benthic foraminifers: A proxy for the deep-sea carbonate saturation. *Geochemistry, Geophysics, Geosystems*, 12, Q06019.
- RATHMANN, S., HESS, S., KUHNERT, H. & MULITZA, S. 2004. Mg/Ca ratios of the benthic foraminifera *Oridorsalis umbonatus* obtained by laser ablation from core top sediments: Relationship to bottom water temperature. *Geochemistry, Geophysics, Geosystems*, 5, Q12013.
- RAYMO, M. E. 1994. The Initiation of northern Hemisphere Glaciation. *Annual Review of Earth and Planetary Sciences*, 22, 353-383.
- RAYMO, M. E., LISIECKI, L. E. & NISANCIOGLU, K. H. 2006. Plio-Pleistocene Ice Volume, Antarctic Climate, and the Global $\delta^{18}\text{O}$ Record. *Science*, 313, 492-495.
- RAYMO, M. E. & NISANCIOGLU, K. H. 2003. The 41 kyr world: Milankovitch's other unsolved mystery. *Paleoceanography*, 18, 1011.
- RAYMO, M. E., OPPO, D. W. & CURRY, W. 1997. The Mid-Pleistocene climate transition: A deep sea carbon isotopic perspective. *Paleoceanography*, 12, 546-559.
- RAYMO, M. E. & RUDDIMAN, W. F. 1992. Tectonic forcing of late Cenozoic climate. *Nature*, 359, 117-122.
- RAYMO, M. E., RUDDIMAN, W. F., SHACKLETON, N. J. & OPPO, D. W. 1990. Evolution of Atlantic-Pacific $\delta^{13}\text{C}$ gradients over the last 2.5 m.y. *Earth and Planetary Science Letters*, 97, 353-368.
- REGENBERG, M., NÜRNBERG, D., STEPH, S., GROENEVELD, J., GARBE-SCHÖNBERG, D., TIEDEMANN, R. & DULLO, W. C. 2006. Assessing the effect of dissolution on planktonic foraminiferal Mg/Ca ratios: Evidence from Caribbean core tops. *Geochemistry, Geophysics, Geosystems*, 7, Q07P15.
- RELLA, S. F., TADA, R., NAGASHIMA, K., IKEHARA, M., ITAKI, T., OHKUSHI, K. I., SAKAMOTO, T., HARADA, N. & UCHIDA, M. 2012. Abrupt changes of intermediate water properties on the northeastern slope of the Bering Sea during the last glacial and deglacial period. *Paleoceanography*, 27, PA3203.

- RIAL, J. A. 2004. Abrupt climate change: chaos and order at orbital and millennial scales. *Global and Planetary Change*, 41, 95-109.
- RIETHDORF, J. R., MAX, L., NÜRNBERG, D., LEMBKE-JENE, L. & TIEDEMANN, R. 2013a. Deglacial development of (sub) sea surface temperature and salinity in the subarctic northwest Pacific: Implications for upper-ocean stratification. *Paleoceanography*, 28, 91-104.
- RIETHDORF, J. R., NÜRNBERG, D., MAX, L., TIEDEMANN, R., GORBARENKO, S. A. & MALAKHOV, M. I. 2013b. Millennial-scale variability of marine productivity and terrigenous matter supply in the western Bering Sea over the past 180 kyr. *Clim. Past*, 9, 1345-1373.
- ROBBINS, L. L., HANSEN, M. E., KLEYPAS, J. A. & MEYLAN, S. C. 2010. CO2calc—A user-friendly seawater carbon calculator for Windows, Max OS X, and iOS (iPhone). *U.S. Geological Survey Open-File Report 2010*, 1280, 17 p.
- ROBERTS, H. H. & AHARON, P. 1994. Hydrocarbon-derived carbonate buildups of the northern Gulf of Mexico continental slope: A review of submersible investigations. *Geo-Marine Letters*, 14, 135-148.
- RODIONOV, S. N., BOND, N. A. & OVERLAND, J. E. 2007. The Aleutian Low, storm tracks, and winter climate variability in the Bering Sea. *Deep Sea Research Part II: Topical Studies in Oceanography*, 54, 2560-2577.
- ROHLING, E. J., FOSTER, G. L., GRANT, K. M., MARINO, G., ROBERTS, A. P., TAMISIEA, M. E. & WILLIAMS, F. 2014. Sea-level and deep-sea-temperature variability over the past 5.3 million years. *Nature*, 508, 477.
- ROSENTHAL, Y., BOYLE, E. A., LABEYRIE, L. & OPPO, D. 1995. Glacial enrichments of authigenic Cd and U in subantarctic sediments: A climatic control on the elements' oceanic budget? *Paleoceanography*, 10, 395-413.
- ROSENTHAL, Y., BOYLE, E. A. & SLOWEY, N. 1997. Temperature control on the incorporation of magnesium, strontium, fluorine, and cadmium into benthic foraminiferal shells from Little Bahama Bank: Prospects for thermocline paleoceanography. *Geochimica et Cosmochimica Acta*, 61, 3633-3643.
- ROSENTHAL, Y., LEAR, C. H., OPPO, D. W. & LINSLEY, B. K. 2006. Temperature and carbonate ion effects on Mg/Ca and Sr/Ca ratios in benthic foraminifera: Aragonitic species *Hoeglundina elegans*. *Paleoceanography*, 21, PA1007.
- ROSENTHAL, Y. & LOHMANN, G. P. 2002. Accurate estimation of sea surface temperatures using dissolution-corrected calibrations for Mg/Ca paleothermometry. *Paleoceanography*, 17, 16-1-16-6.
- ROSENTHAL, Y., LOHMANN, G. P., LOHMANN, K. C. & SHERRELL, R. M. 2000. Incorporation and preservation of Mg in Globigerinoides sacculifer: implications for reconstructing the temperature and $18\text{O}/16\text{O}$ of seawater. *Paleoceanography*, 15, 135-145.
- RUDDIMAN, W. F. & RAYMO, M. E. 1988. Northern Hemisphere climate regimes during the past 3 Ma: possible tectonic connections. *Philosophical Transactions of the Royal Society of London B*, 318, 411-430.
- RUDDIMAN, W. F., RAYMO, M. E., MARTINSON, D. G., CLEMENT, B. M. & BACKMAN, J. 1989. Pleistocene evolution: Northern hemisphere ice sheets and North Atlantic Ocean. *Paleoceanography*, 4, 353-412.
- RUSSELL, A. D., HÖNISCH, B., SPERO, H. J. & LEA, D. W. 2004. Effects of seawater carbonate ion concentration and temperature on shell U, Mg, and Sr

- in cultured planktonic foraminifera. *Geochimica et Cosmochimica Acta*, 68, 4347-4361.
- RUSSON, T., ELLIOT, M., SADEKOV, A., CABIOCH, G., CORRÈGE, T. & DE DECKKER, P. 2010. Inter-hemispheric asymmetry in the early Pleistocene Pacific warm pool. *Geophysical Research Letters*, 37, L11601.
- SAENKO, O. A., SCHMITTNER, A. & WEAVER, A. J. 2004. The Atlantic–Pacific Seesaw. *Journal of Climate*, 17, 2033-2038.
- SAGAWA, T. & IKEHARA, K. 2008. Intermediate water ventilation change in the subarctic northwest Pacific during the last deglaciation. *Geophysical Research Letters*, 35, L24702.
- SAKAMOTO, T., IKEHARA, M., AOKI, K., IJIMA, K., KIMURA, N., NAKATSUKA, T. & WAKATSUCHI, M. 2005. Ice-rafted debris (IRD)-based sea-ice expansion events during the past 100kyrs in the Okhotsk Sea. *Deep Sea Research Part II: Topical Studies in Oceanography*, 52, 2275-2301.
- SANCETTA, C. A. 1983. Effect of Pleistocene glaciation upon oceanographic characteristics of the North Pacific and Bering Sea. *Deep Sea Research*, 30, 851-869.
- SANCETTA, C. A. & SILVESTRI, S. M. 1986. Pliocene-Pleistocene evolution of the North Pacific Ocean-Atmosphere system, interpreted from fossil diatoms. *Paleoceanography*, 1, 163–180.
- SANYAL, A., HEMMING, N. G., HANSON, G. N. & BROECKER, W. S. 1995. Evidence for a higher pH in the glacial ocean from boron isotopes in foraminifera. *Nature*, 373, 234.
- SARNTHEIN, M., GEBHARDT, H., KIEFER, T., KUCERA, M., COOK, M. & ERLLENKEUSER, H. 2004. Mid Holocene origin of the sea-surface salinity low in the subarctic North Pacific. *Quaternary Science Reviews*, 23, 2089-2099.
- SARNTHEIN, M., KIEFER, T., GROOTES, P. M., ELDERFIELD, H. & ERLLENKEUSER, H. 2006. Warmings in the far northwestern Pacific promoted pre-Clovis immigration to America during Heinrich event 1. *Geology*, 34, 141-144.
- SAYAG, R., TZIPERMAN, E. & GHIL, M. 2004. Rapid switch-like sea ice growth and land ice-sea ice hysteresis. *Paleoceanography*, 19, PA1021.
- SCHLITZER, R. 2011. Ocean Data View. <http://odv.awi.de>.
- SCHMIEDER, F., VON DOBENECK, T. & BLEIL, U. 2000. The Mid-Pleistocene climate transition as documented in the deep South Atlantic Ocean: initiation, interim state and terminal event. *Earth and Planetary Science Letters*, 179, 539-549.
- SCHMITTNER, A. & GALBRAITH, E. D. 2008. Glacial greenhouse-gas fluctuations controlled by ocean circulation changes. *Nature*, 456, 373.
- SCHNEIDER, A., CRÉMIÈRE, A., PANIERI, G., LEPLAND, A. & KNIES, J. 2017. Diagenetic alteration of benthic foraminifera from a methane seep site on Vestnesa Ridge (NW Svalbard). *Deep Sea Research Part I: Oceanographic Research Papers*, 123, 22-34.
- SCHRAG, D. P., ADKINS, J. F., MCINTYRE, K., ALEXANDER, J. L., HODELL, D. A., CHARLES, C. D. & MCMANUS, J. F. 2002. The oxygen isotopic composition of seawater during the Last Glacial Maximum. *Quaternary Science Reviews*, 21, 331-342.

- SCHRAG, D. P., HIGGINS, J. A., MACDONALD, F. A. & JOHNSTON, D. T. 2013. Authigenic Carbonate and the History of the Global Carbon Cycle. *Science*, 339, 540-543.
- SEKI, O., KAWAMURA, K., SAKAMOTO, T., IKEHARA, M., NAKATSUKA, T. & WAKATSUCHI, M. 2005. Decreased surface salinity in the Sea of Okhotsk during the last glacial period estimated from alkenones. *Geophysical Research Letters*, 32, L08710.
- SERREZE, M. C., HOLLAND, M. M. & STROEVE, J. 2007. Perspectives on the Arctic's Shrinking Sea-Ice Cover. *Science*, 315, 1533-1536.
- SETOYAMA, E. & KAMINSKI, M. A. 2015. Neogene benthic foraminifera from the southern Bering Sea (IODP Expedition 323). *Palaeontologia Electronica*, 18.2, 1-30.
- SEXTON, P. F. & BARKER, S. 2012. Onset of 'Pacific-style' deep-sea sedimentary carbonate cycles at the mid-Pleistocene transition. *Earth and Planetary Science Letters*, 321, 81-94.
- SEXTON, P. F. & WILSON, P. A. 2009. Preservation of benthic foraminifera and reliability of deep-sea temperature records: Importance of sedimentation rates, lithology, and the need to examine test wall structure. *Paleoceanography*, 24, PA2208.
- SEXTON, P. F., WILSON, P. A. & PEARSON, P. N. 2006. Microstructural and geochemical perspectives on planktic foraminiferal preservation: "Glassy" versus "Frosty". *Geochemistry, Geophysics, Geosystems*, 7, Q12P19.
- SHACKLETON, N. 1967. Oxygen Isotope Analyses and Pleistocene Temperatures Re-assessed. *Nature*, 215, 15-17.
- SHACKLETON, N. 1974. Attainment of isotopic equilibrium between ocean water and the benthonic foraminifera genus *Uvigerina*: isotopic changes in the ocean during the last glacial. *Colloques Internationaux du C.N.R.S.*, 219, 203-209.
- SHACKLETON, N. J. 2000. The 100,000-Year Ice-Age Cycle Identified and Found to Lag Temperature, Carbon Dioxide, and Orbital Eccentricity. *Science*, 289, 1897-1902.
- SHACKLETON, N. J., BACKMAN, J., ZIMMERMAN, H., KENT, D. V., HALL, M. A., ROBERTS, D. G., SCHNITKER, D., BALDAUF, J. G., DESPRAIRIES, A., HOMRIGHAUSEN, R., HUDDLESTUN, P., KEENE, J. B., KALTENBACK, A. J., KRUMSIEK, K. A. O., MORTON, A. C., MURRAY, J. W. & WESTBERG-SMITH, J. 1984. Oxygen isotope calibration of the onset of ice-rafting and history of glaciation in the North Atlantic region. *Nature*, 307, 620.
- SHACKLETON, N. J. & KENNETT, J. P. 1975. Paleotemperature history of the Cenozoic and the initiation of Antarctic glaciation: oxygen and carbon isotope analyses in DSDP Sites 277, 279, and 281. *Initial Reports of Deep Sea Drilling Project*, 29, 743-756.
- SHACKLETON, N. J. & OPDYKE, N. 1976. Oxygen isotope and paleomagnetic stratigraphy of Pacific core V28-239 Late Pliocene to Latest Pliocene. *Investigations of Late Quaternary Paleoceanography and Paleoclimatology*, *Geol. Soc. Am. Mere.*, 145, 449-464.
- SHAKUN, J. D., LEA, D. W., LISIECKI, L. E. & RAYMO, M. E. 2015. An 800-kyr record of global surface ocean $\delta^{18}\text{O}$ and implications for ice volume-temperature coupling. *Earth and Planetary Science Letters*, 426, 58-68.

- SHCHERBINA, A. Y., TALLEY, L. D. & RUDNICK, D. L. 2003. Direct Observations of North Pacific Ventilation: Brine Rejection in the Okhotsk Sea. *Science*, 302, 1952-1955.
- SIDDALL, M., HÖNISCH, B., WAELBROECK, C. & HUYBERS, P. 2010. Changes in deep Pacific temperature during the mid-Pleistocene transition and Quaternary. *Quaternary Science Reviews*, 29, 170-181.
- SIGMAN, D. M., JACCARD, S. L. & HAUG, G. H. 2004. Polar ocean stratification in a cold climate. *Nature*, 428, 59.
- SKINNER, L. C. 2009. Glacial-interglacial atmospheric CO₂ change: a possible "standing volume" effect on deep-ocean carbon sequestration. *Climate of the Past*, 5, 537-550.
- SKINNER, L. C., FALLON, S., WAELBROECK, C., MICHEL, E. & BARKER, S. 2010. Ventilation of the Deep Southern Ocean and Deglacial CO₂ Rise. *Science*, 328, 1147-1151.
- SKIRBEKK, K., HALD, M., MARCHITTO, T. M., JUNTILA, J., KLITGAARD KRISTENSEN, D. & AAGAARD SØRENSEN, S. 2016. Benthic foraminiferal growth seasons implied from Mg/Ca-temperature correlations for three Arctic species. *Geochemistry, Geophysics, Geosystems*, 17, 4684-4704.
- SMIK, L. & BELT, S. T. 2017. Distributions of the Arctic sea ice biomarker proxy IP₂₅ and two phytoplanktonic biomarkers in surface sediments from West Svalbard. *Organic Geochemistry*, 105, 39-41.
- SMIK, L., CABEDO-SANZ, P. & BELT, S. T. 2016. Semi-quantitative estimates of paleo Arctic sea ice concentration based on source-specific highly branched isoprenoid alkenes: A further development of the PIP₂₅ index. *Organic Geochemistry*, 92, 63-69.
- SMITH, M. P. 1986. Silver coating inhibits electron microprobe beam damage of carbonates. *Journal of Sedimentary Research*, 56, 560-561.
- SOSDIAN, S. & ROSENTHAL, Y. 2009. Deep-Sea Temperature and Ice Volume Changes Across the Pliocene-Pleistocene Climate Transitions. *Science*, 325, 306-310.
- SOSDIAN, S. M., ROSENTHAL, Y. & TOGGWEILER, J. R. 2018. Deep Atlantic Carbonate Ion and CaCO₃ Compensation During the Ice Ages. *Paleoceanography and Paleoclimatology*, 33, 546-562.
- SPRATT, R. M. & LISIECKI, L. E. 2016. A Late Pleistocene sea level stack. *Clim. Past*, 12, 1079-1092.
- SPRINGER, A. M., MCROY, C. P. & FLINT, M. V. 1996. The Bering Sea Green Belt: shelf-edge processes and ecosystem production. *Fisheries Oceanography*, 5, 205-223.
- ST. JOHN, K. E. K. & KRISSEK, L. A. 1999. Regional patterns of Pleistocene ice-rafted debris flux in the North Pacific. *Paleoceanography*, 14, 653-662.
- STABENO, P. J., SCHUMACHER, J. D. & OHTANI, K. 1999. The physical oceanography of the Bering Sea. . *Dynamics of the Bering Sea: A summary of Physical, Chemical, and Biological Characteristics, and a Synopsis of Research on the Bering Sea, Alaskan Sea Grant College Report No. AK-SG-99-03*, 1-28.
- STEIN, R., FAHL, K., SCHRECK, M., KNORR, G., NIESSEN, F., FORWICK, M., GEBHARDT, C., JENSEN, L., KAMINSKI, M., KOPF, A., MATTHIESSEN, J., JOKAT, W. & LOHMANN, G. 2016. Evidence for ice-

- free summers in the late Miocene central Arctic Ocean. *Nature Communications*, 7, 11148.
- STEPHENS, B. B. & KEELING, R. F. 2000. The influence of Antarctic sea ice on glacial-interglacial CO₂ variations. *Nature*, 404, 171-174.
- STONE, R. P. & SHOTWELL, S. K. 2007. State of deep coral ecosystems in the Alaska Region: Gulf of Alaska, Bering Sea and the Aleutian Islands. *The State of Deep Coral Ecosystems of the United States*, 65-108.
- STOYNOVA, V., SHANAHAN, T. M., HUGHEN, K. A. & DE VERNAL, A. 2013. Insights into Circum-Arctic sea ice variability from molecular geochemistry. *Quaternary Science Reviews*, 79, 63-73.
- STROEVE, J. C., SERREZE, M. C., HOLLAND, M. M., KAY, J. E., MALANIK, J. & BARRETT, A. P. 2012. The Arctic's rapidly shrinking sea ice cover: a research synthesis. *Climatic Change*, 110, 1005-1027.
- STROYNOWSKI, Z., ABRANTES, F. & BRUNO, E. 2017. The response of the Bering Sea Gateway during the Mid-Pleistocene Transition. *Palaeogeography, Palaeoclimatology, Palaeoecology*, 485, 974-985.
- STURCHIO, N. C., ANTONIO, M. R., SODERHOLM, L., SUTTON, S. R. & BRANNON, J. C. 1998. Tetravalent Uranium in Calcite. *Science*, 281, 971-973.
- SUN, H., LI, T., LIU, C., CHANG, F., SUN, R., XIONG, Z. & AN, B. 2017. Variations in the western Pacific warm pool across the mid-Pleistocene: Evidence from oxygen isotopes and coccoliths in the West Philippine Sea. *Palaeogeography, Palaeoclimatology, Palaeoecology*, 483, 157-171.
- TABOR, C. R. & POULSEN, C. J. 2016. Simulating the mid-Pleistocene transition through regolith removal. *Earth and Planetary Science Letters*, 434, 231-240.
- TACHIKAWA, K. & ELDERFIELD, H. 2002. Microhabitat effects on Cd/Ca and $\delta^{13}\text{C}$ of benthic foraminifera. *Earth and Planetary Science Letters*, 202, 607-624.
- TAKAHASHI, K. 2005. The Bering Sea and paleoceanography. *Deep Sea Research Part II: Topical Studies in Oceanography*, 52, 2080-2091.
- TAKAHASHI, K., RAVELO, A. C., ALVAREZ ZARIKIAN, C. A. & SCIENTISTS, E. 2011. Expedition 323 summary. *Proceedings of the Integrated Ocean Drilling Program*, 323.
- TALLEY, L. D. 1993. Distribution and Formation of North Pacific Intermediate Water. *Journal of Physical Oceanography*, 23, 517-537.
- TALLEY, L. D., PICKARD, G. L., EMERY, W. J. & SWIFT, J. H. 2011. Chapter 3 - Physical Properties of Seawater. *Descriptive Physical Oceanography (Sixth Edition)*. Boston: Academic Press.
- TANAKA, S. & TAKAHASHI, K. 2005. Late Quaternary paleoceanographic changes in the Bering Sea and the western subarctic Pacific based on radiolarian assemblages. *Deep Sea Research Part II: Topical Studies in Oceanography*, 52, 2131-2149.
- TANAKA, T., YASUDA, I., KUMA, K. & NISHIOKA, J. 2012. Vertical turbulent iron flux sustains the Green Belt along the shelf break in the southeastern Bering Sea. *Geophysical Research Letters*, 39, L08603.
- TEAM, R. 2015. RStudio: Integrated Development for R. Boston, MA: RStudio Inc.
- TEICHERT, B., JOHNSON, J., SOLOMON, E., GIOSAN, L., ROSE, K., KOCHERIA, M., CONNOLLY, E. & TORRES, M. 2014. Composition and origin of authigenic carbonates in the Krishna eGodavari and Mahanadi Basins, eastern continental margin of India. *Mar. Pet. Geol.*, 58, 43.

- TERAISHI, A., SUTO, I., ONODERA, J. & TAKAHASHI, K. 2016. Diatom, silicoflagellate and ebridian biostratigraphy and paleoceanography in IODP 323 Hole U1343E at the Bering slope site. *Deep Sea Research Part II: Topical Studies in Oceanography*, 125, 18-28.
- THOMAS, D. J. 2004. Evidence for deep-water production in the North Pacific Ocean during the early Cenozoic warm interval. *Nature*, 430, 65.
- THOMAS, D. J., KORTY, R., HUBER, M., SCHUBERT, J. A. & HAINES, B. 2014. Nd isotopic structure of the Pacific Ocean 70–30 Ma and numerical evidence for vigorous ocean circulation and ocean heat transport in a greenhouse world. *Paleoceanography*, 29, 454-469.
- THOMPSON, W. G. & GOLDSTEIN, S. L. 2005. Open-System Coral Ages Reveal Persistent Suborbital Sea-Level Cycles. *Science*, 308, 401-404.
- TOGGWEILER, J. R., RUSSELL, J. L. & CARSON, S. R. 2006. Midlatitude westerlies, atmospheric CO₂, and climate change during the ice ages. *Paleoceanography*, 21, PA2005.
- TORRES, M. E., MARTIN, R. A., KLINKHAMMER, G. P. & NESBITT, E. A. 2010. Post depositional alteration of foraminiferal shells in cold seep settings: New insights from flow-through time-resolved analyses of biogenic and inorganic seep carbonates. *Earth and Planetary Science Letters*, 299, 10-22.
- TREUDE, T., NIGGEMANN, J., KALLMEYER, J., WINTERSTELLER, P., SCHUBERT, C. J., BOETIUS, A. & JØRGENSEN, B. B. 2005. Anaerobic oxidation of methane and sulfate reduction along the Chilean continental margin. *Geochimica et Cosmochimica Acta*, 69, 2767-2779.
- TSUNOGAI, S., KUSAKABE, M., IIZUMI, H., KOIKE, I. & HATTORI, A. 1979. Hydrographic features of the deep water of the Bering Sea—the sea of Silica. *Deep Sea Research Part A. Oceanographic Research Papers*, 26, 641-659.
- TZEDAKIS, P. C., CRUCIFIX, M., MITSUI, T. & WOLFF, E. W. 2017. A simple rule to determine which insolation cycles lead to interglacials. *Nature*, 542, 427.
- TZIPERMAN, E. & GILDOR, H. 2003. On the mid-Pleistocene transition to 100-kyr glacial cycles and the asymmetry between glaciation and deglaciation times. *Paleoceanography*, 18, 1001.
- USAMI, K., IKEHARA, K., JENKINS, R. G. & ASHI, J. 2017. Benthic foraminiferal evidence of deep-sea sediment transport by the 2011 Tohoku-oki earthquake and tsunami. *Marine Geology*, 384, 214-224.
- USSLER, W. & PAULL, C. K. 2008. Rates of anaerobic oxidation of methane and authigenic carbonate mineralization in methane-rich deep-sea sediments inferred from models and geochemical profiles. *Earth and Planetary Science Letters*, 266, 271-287.
- VAN DER ZWAAN, G. J., DUIJNSTEE, I. A. P., DEN DULK, M., ERNST, S. R., JANNINK, N. T. & KOUWENHOVEN, T. J. 1999. Benthic foraminifers: proxies or problems?: A review of paleocological concepts. *Earth-Science Reviews*, 46, 213-236.
- VENUTI, A., FLORINDO, F., MICHEL, E. & HALL, I. R. 2007. Magnetic proxy for the deep (Pacific) western boundary current variability across the mid-Pleistocene climate transition. *Earth and Planetary Science Letters*, 259, 107-118.
- VOLKMAN, J. K. 2006. Lipid Markers for Marine Organic Matter. In: VOLKMAN, J. K. (ed.) *Marine Organic Matter: Biomarkers, Isotopes and DNA*. Berlin, Heidelberg: Springer Berlin Heidelberg.

- Waelbroeck, C., Labeyrie, L., Michel, E., Duplessy, J. C., McManus, J. F., Lambeck, K., Balbon, E. & Labracherie, M. 2002. Sea-level and deep water temperature changes derived from benthic foraminifera isotopic records. *Quaternary Science Reviews*, 21, 295-305.
- Walsh, J. J., McRoy, C. P., Coachman, L. K., Goering, J. J., Ni Hou, J. J., Whitley, T. E., Blackburn, T. H., Parker, P. L., Wirick, C. D., Shuert, P. G., Grebmeier, J. M., Springer, A. M., Tripp, R. D., Hansell, D. A., Djenedi, S., Deleersnijder, E., Henriksen, K., Lund, B. A., Andersen, P., Muller-Krager, F. E. & Dean, K. 1989. Carbon and nitrogen cycling within the Bering/Chukchi Seas: Source regions for organic matter effecting AOU demands of the Arctic Ocean. *Progress in Oceanography*, 22, 277-359.
- Walter, L. M. 1986. Relative efficiency of carbonate dissolution and precipitation during diagenesis: a progress report on the role of solution chemistry. In: Biddle, K.T. & Christie-Blick, N. (eds.) *Roles of Organic Matter in Sediment Diagenesis*. Society for Sedimentary Geology.
- Walter, L. M. & Burton, E. A. 1990. Dissolution of recent platform carbonate sediments in marine pore fluids. *American Journal of Science*, 290, 601-643.
- Wan, S., Feng, D., Chen, F., Zhuang, C. & Chen, D. 2018. Foraminifera from gas hydrate-bearing sediments of the northeastern South China Sea: proxy evaluation and application for methane release activity. *Journal of Asian Earth Sciences*, in press.
- Wang, S., Bailey, D., Lindsay, K., Moore, J. K. & Holland, M. 2014. Impact of sea ice on the marine iron cycle and phytoplankton productivity. *Biogeosciences*, 11, 4713-4731.
- Warner, M. J. & Roden, G. I. 1995. Chlorofluorocarbon evidence for recent ventilation of the deep Bering Sea. *Nature*, 373, 409.
- Warren, B. A. 1983. Why is no deep water formed in the North Pacific? *Journal of Marine Research*, 41, 327-347.
- Wassmann, P., Duarte, C. M., Agustí, S. & Sejr, M. K. 2011. Footprints of climate change in the Arctic marine ecosystem. *Global Change Biology*, 17, 1235-1249.
- Watanabe, T. & Wakatsuchi, M. 1998. Formation of 26.8–26.9 σ_{θ} water in the Kuril Basin of the Sea of Okhotsk as a possible origin of North Pacific Intermediate Water. *Journal of Geophysical Research: Oceans*, 103, 2849-2865.
- Wehrmann, L. M., Risgaard-Petersen, N., Schrum, H. N., Walsh, E. A., Huh, Y., Ikehara, M., Pierre, C., D'Hondt, S., Ferdelman, T. G., Ravelo, A. C., Takahashi, K. & Zarijian, C. A. 2011. Coupled organic and inorganic carbon cycling in the deep seafloor sediment of the northeastern Bering Sea Slope (IODP Exp. 323). *Chemical Geology*, 284, 251-261.
- Whitley, T. E. & Luchin, V. A. 1999. Summary of Chemical Distributions and Dynamics in the Bering Sea edited by T.R. Loughlin and K. Othani. *Dynamics of the Bering Sea, North Pacific Science Organization (PICES)*, published by University of Alaska Sea Grant, Fairbanks, Alaska.
- Wilson, P. A. & Norris, R. D. 2001. Warm tropical ocean surface and global anoxia during the mid-Cretaceous period. *Nature*, 412, 425-429.

- WINTON, M. 1997. The Effect of Cold Climate upon North Atlantic Deep Water Formation in a Simple Ocean–Atmosphere Model. *Journal of Climate*, 10, 37-51.
- WOODARD, S. C., ROSENTHAL, Y., MILLER, K. G., WRIGHT, J. D., CHIU, B. K. & LAWRENCE, K. T. 2014. Antarctic role in Northern Hemisphere glaciation. *Science*, 346, 847-851.
- XIAO, X., FAHL, K., MÜLLER, J. & STEIN, R. 2015. Sea-ice distribution in the modern Arctic Ocean: Biomarker records from trans-Arctic Ocean surface sediments. *Geochimica et Cosmochimica Acta*, 155, 16-29.
- XIAO, X., FAHL, K. & STEIN, R. 2013. Biomarker distributions in surface sediments from the Kara and Laptev seas (Arctic Ocean): indicators for organic-carbon sources and sea-ice coverage. *Quaternary Science Reviews*, 79, 40-52.
- YASUDA, I. 1997. The origin of the North Pacific Intermediate Water. *Journal of Geophysical Research: Oceans*, 102, 893-909.
- YU, J., ANDERSON, R. F. & ROHLING, E. J. 2014. Deep ocean carbonate chemistry and glacial-interglacial atmospheric CO₂ changes. *Oceanography*, 27, 16-25.
- YU, J. & BROECKER, W. S. 2010. Comment on “Deep-Sea Temperature and Ice Volume Changes Across the Pliocene-Pleistocene Climate Transitions”. *Science*, 328, 1480.
- YU, J., BROECKER, W. S., ELDERFIELD, H., JIN, Z., MCMANUS, J. & ZHANG, F. 2010a. Loss of Carbon from the Deep Sea Since the Last Glacial Maximum. *Science*, 330, 1084-1087.
- YU, J. & ELDERFIELD, H. 2008. Mg/Ca in the benthic foraminifera *Cibicides wuellerstorfi* and *Cibicides mundulus*: Temperature versus carbonate ion saturation. *Earth and Planetary Science Letters*, 276, 129-139.
- YU, J., ELDERFIELD, H., GREAVES, M. & DAY, J. 2007. Preferential dissolution of benthic foraminiferal calcite during laboratory reductive cleaning. *Geochemistry, Geophysics, Geosystems*, 8, Q06016.
- YU, J., FOSTER, G. L., ELDERFIELD, H., BROECKER, W. S. & CLARK, E. 2010b. An evaluation of benthic foraminiferal B/Ca and $\delta^{11}\text{B}$ for deep ocean carbonate ion and pH reconstructions. *Earth and Planetary Science Letters*, 293, 114-120.
- ZACHOS, J., PAGANI, M., SLOAN, L., THOMAS, E. & BILLUPS, K. 2001. Trends, Rhythms, and Aberrations in Global Climate 65 Ma to Present. *Science*, 292, 686-693.
- ZACHOS, J. C., DICKENS, G. R. & ZEEBE, R. E. 2008. An early Cenozoic perspective on greenhouse warming and carbon-cycle dynamics. *Nature*, 451, 279-283.
- ZHAO, M.-Y., ZHENG, Y.-F. & ZHAO, Y.-Y. 2016. Seeking a geochemical identifier for authigenic carbonate. *Nature Communications*, 7, 10885.
- ZHENG, Y., ANDERSON, R. F., VAN GEEN, A. & FLEISHER, M. Q. 2002. Remobilization of authigenic uranium in marine sediments by bioturbation. *Geochimica et Cosmochimica Acta*, 66, 1759-1772.
- ZIEGLER, M., DIZ, P., HALL, I. R. & ZAHN, R. 2013. Millennial-scale changes in atmospheric CO₂ levels linked to the Southern Ocean carbon isotope gradient and dust flux. *Nature Geoscience*, 6, 457.